NOMINAL AND EXTREME ERROR PERFORMANCE OF THE UNB3 TROPOSPHERIC DELAY MODEL

J. PAUL COLLINS
RICHARD B. LANGLEY

September 1999

TECHNICAL REPORT
NO. 204

NOMINAL AND EXTREME ERROR PERFORMANCE OF THE UNB3 TROPOSPHERIC DELAY MODEL

J. P. Collins
R. B. Langley

Department of Geodesy and Geomatics Engineering
University of New Brunswick
P.O. Box 4400
Fredericton, N.B.
Canada
E3B 5A3

August 1999

PREFACE

This report was prepared under Contract #12519 for Nav Canada (previously Transport Canada Aviation). The research was carried out in the Geodetic Research Laboratory at the University of New Brunswick, Fredericton, Canada, by Paul Collins under the supervision of Professor Richard B. Langley.

We have performed extensive testing of the tropospheric propagation delay model proposed for the GPS-WAAS avionics receiver. An extensive data set, comprising ten years of radiosonde data from across North America, was used as a benchmark against which to compare the performance of the model. The data represents a wide range of atmospheric conditions that can be expected in this region. This investigation is almost certainly the largest of its kind to date with regard to validating a particular tropospheric delay model.

As with any copyrighted material, permission to reprint or quote extensively from this report must be received from the authors. The citation to this work should appear as follows:

Collins, J. P., and R. B. Langley (1999). *Nominal and Extreme Error Performance of the UNB3 Tropospheric Delay Model.* Final contract report for Nav Canada Satellite Navigation Program Office, by the Geodetic Research Laboratory, Department of Geodesy and Geomatics Engineering Technical Report No. 204, University of New Brunswick, Fredericton, New Brunswick, Canada, 173 pp.

EXECUTIVE SUMMARY

Canada and the United States have been co-operating for many years to develop approvals for Global Positioning System (GPS) use in aviation. Under a standing agreement between the two nations, the University of New Brunswick (UNB) has been approached to produce an improved tropospheric delay model to be used in airborne Wide Area Augmentation System (WAAS) receivers and to estimate the bounds of the tropospheric delay contribution to the WAAS error budget.

Previous research work at UNB resulted in a proposed tropospheric propagation delay model for use in aircraft receivers operating in the GPS-WAAS navigation system. This model, denoted UNB3, does not require real-time input of meteorological parameters, relying instead on a look-up table to model the latitude and seasonal trend of atmospheric parameters. Such a concept is susceptible however, to both rare, anomalous conditions and local conditions that are significantly different from the average conditions at the same latitude and season.

This study has investigated the performance of the UNB3 model over an extremely wide range of atmospheric conditions. A 10-year radiosonde data set has been used as a "truth" source against which to compare the model. Because of the extremely large nature of this data set, and the requisite time required to process it, the error analysis has been confined to the error experienced in the zenith direction only. This component is expected to experience the largest error, whereas the mapping function component is known to be affected less significantly.

The nominal zenith error of the UNB3 model is -2 ± 5 cm (1σ), a level of performance that compares very well with that determined by our previous study. This confirms that only a comparatively small amount of data is needed to study the nominal error performance of any tropospheric delay model. Of course the actual error varies widely for any one time and place, but we have found from our extensive data set that only 0.0075% of the residual zenith errors equal or exceed a range of ±20 cm.

Those errors that do equal or exceed the ±20 cm range can be used to predict future "extremes". The extreme negative errors are limited by the maximum value of the wet zenith delay (~27 cm), assuming an unusually dry, tropical atmosphere and negligible error in the hydrostatic component. Fitting an extreme value distribution to the 10 values representing the largest negative errors in each year, suggests that the worst case error is a few centimetres smaller. The largest positive error is harder to determine. While probably not completely unlimited, it has not been possible to determine an analytical maximum. Empirically however, the extreme value distribution fitted to the 10 values representing the largest positive errors in each year, suggests a maximum on the order of 55 cm or more occurring at least once during an average of 25 years.

The direct impact of an unmodelled tropospheric error on the GPS vertical position determination is reduced by the dependence on the satellite geometry. Suitable elevation-angle weighting schemes reduce the impact further, provided that a majority of satellites are not congregating near the same low elevation angle. This fact, when combined with the very rare rate of occurrence, means that unmodelled tropospheric errors are almost certainly negligible for WAAS users when using the UNB3 model.

TABLE OF CONTENTS

LIST OF FIGURES

LIST OF TABLES

ACKNOWLEDGEMENTS

Grateful acknowledgement is made to Nav Canada for sponsoring this work with the support of the Federal Aviation Administration, U.S.A.. Special thanks are due Rob Butler, Steve Bellingham and Kim Lochhead for their personal contributions and to the other members of the SatNav team. We are also grateful to Art Niell (Haystack Observatory, Massachusetts Institute of Technology) for providing the ray-trace software used in this investigation.

1. INTRODUCTION

This report presents the results of our extended investigation into the performance of the UNB3 tropospheric propagation delay model. The primary focus has been the investigation of "extreme" atmospheric conditions that might adversely impact the position determination of an aircraft using the Wide Area Augmentation System (WAAS), especially one on a precision approach for landing. At the same time, we have taken the opportunity of confirming the overall performance of the model at a wide range of locations across North America.

1.1. Motivation

We have previously proposed a "hybrid" tropospheric delay model for user's of the Wide Area Augmentation System [*Collins and Langley*, 1997a]. The model uses algorithms designed to account for the time delay and path bending of Global Positioning System (GPS) signals as they propagate through the earth's electrically neutral atmosphere (primarily the troposphere). This algorithm (denoted as UNB3) will be coded into GPS receiver software for use in aircraft receiving both GPS signals and the supplementary accuracy and integrity signals from WAAS.

The time delay of the GPS signal, and the equivalent path length, is a function of the refractive index of the atmospheric gases through which the signal propagates. Although significant seasonal variations and latitudinal trends exist, atmospheric conditions are not

constant for extended periods of time. Most of the seasonal variations and latitudinal trends that do exist are due to the dispersion of atmospheric water vapour, the maximum amount of which is dependent upon the temperature. The effect of atmospheric water vapour accounts for only a small portion of the total atmospheric delay experienced by the GPS signals (~3% to 12%), however the impact is hard to model due to the nature of the gas and the rapid change of weather patterns.

The UNB3 algorithm attempts to model the seasonal variation of the atmosphere (and hence the tropospheric delay) through a look-up table of atmospheric parameter values derived from the 1966 Standard Atmosphere Supplements [*Dubin et al.*, 1966]. While this implementation appeared to work well in our previous tests, we could only work with a comparatively small data set. This limited the conclusions we could draw because of the wide-range of atmospheric conditions that can occur.

As we also reported, the UNB3 model may be susceptible to "extreme" atmospheric conditions. It is conceivable that the atmosphere might be at such a great variance from normal conditions that the model would fail to remove, or would remove too much of, a significant portion of the signal delay. It is not currently envisaged that a "first-generation" user of WAAS will have access to real-time measurements of atmospheric parameters, and hence the existence of any anomalous conditions will almost certainly not be detected. In addition, access to real-time measurements does not guarantee that such conditions will always be detected. Hence, the frequency and magnitude of such "extreme" conditions is of prime interest in this report.

The impact of unmodelled tropospheric effects is only likely to be important to an aircraft on a Category 1 (CAT I) precision approach. The wide-area nature of WAAS means that local corrections for the atmosphere are not broadcast to the users, who must therefore determine the effect autonomously. Precision approach guidance is supported only when the risk of a user height error exceeding the vertical alert limit (VAL) is less than 10^{-7}. The VAL for CAT I is 12 m, which includes all the error contributions in the GPS-WAAS system. For higher accuracy final approaches (CAT II and III), it is proposed that a local area augmentation system (LAAS) will be necessary. In these cases, local differential corrections can be used and the atmospheric effects will be significantly reduced under almost all conditions (see Appendix E1).

As a result of our previous tropospheric propagation delay work for Nav Canada, the UNB3 model has been adopted into official RTCA standards[†] and draft ICAO standards[‡] as the benchmark for WAAS receiver tropospheric determination. In addition, several external organisations in the wider field of navigation have expressed an interest in the work. As well being used in further navigation studies here at UNB [*Collins and Langley*, 1997b; *Mendes and Langley*, 1998], the UNB models have been used in Differential GPS investigations at the Lincoln Laboratories of the Massachusetts Institute of Technology [*Coster et al.*, 1998; *Misra et al.*, 1999]. The National Satellite Test Bed of the Federal Aviation Administration has also implemented our models in their WAAS testing, but the impact of their use is not currently known.

[†] RTCA/DO-229A, Minimum Operational Performance Standards for GPS/WAAS Airborne Equipment.

[‡] Report of the 3rd Meeting of the Global Navigation Satellite System Panel, ICAO, Montreal, April, 1999.

1.2. Objectives

The primary aim of this report is to identify and investigate any extreme conditions and their impact on the performance of the UNB3 model. What constitutes an "extreme" condition will be defined and described in terms of the expected impact on the position determination of the WAAS user. In addition, we will take the opportunity to further quantify the "general", or nominal, performance of the UNB3 model over a much wider portion of the earth's surface, and consequently over a greater range of climatic conditions, than was previously possible. Potential models for the residual tropospheric error that remains after applying the model are also investigated in some detail.

1.3. Overview

Section two outlines the processing methodologies and data set we have used to test the UNB3 model. Some tests on the integrity of the data will be described. Section three outlines the results with relevant analysis. Section four summarises with conclusions and recommendations.

2. METHODOLOGY AND DATA

This section of the report introduces our testing method and primary data set. The data comprises radiosonde profiles from across the North American continent and into Central America and the Caribbean. The adequacy of the data for this particular work is assessed.

2.1. Test Methodology

Our testing method closely followed that described in our previous report [*Collins and Langley*, 1997a]. We have again used tropospheric delay values computed from atmospheric profiles as a benchmark against which to compare the UNB3 model. The profiles of pressure, temperature and relative humidity are recorded by balloon-borne radiosonde instruments that ascend through the atmosphere after being released from ground weather stations.

These profiles can be used to determine the path delay a GPS signal would experience if propagating through that same sample of the atmosphere. The process by which the theoretical delay is computed is known as "ray-tracing", a technique directly analogous to the determination of optical paths of light given a description of the propagation medium. The tropospheric delay is often divided into two components: that portion due to all the atmospheric gases in hydrostatic equilibrium, known as the hydrostatic delay; and that portion due solely to water vapour, known as the wet delay. Both will be referred to

occasionally due to the inherent problems of modelling each, however our results are usually quoted for the total delay — the sum of both portions.

The error of the UNB3 model is determined by differencing the model value for the total delay from the ray-traced value. The location and time parameters required by the UNB3 model are taken from the radiosonde data. The statistics of the errors are then examined to determine the performance of the model.

2.2. Data Description and Overview

The source of the atmospheric profiles we have used is a set of 4 CD-ROM's, comprising North American radiosonde data recorded from 1946 to 1996. The production of this data set was undertaken by the Forecast Systems Laboratory (FSL) of the United States National Oceanic and Atmospheric Administration (NOAA). The data consists of radiosonde soundings at mandatory and significant levels up to 100 mbar (~16 km) taken from almost all the radiosonde sites operating in the United States, Canada, Mexico, the Caribbean and Central America in the last fifty years. We have concentrated only on the last ten full years of data available (1987-1996). This represents an average of 173 stations per year and approximately 1 million soundings in total (see Table 2.1 and Figure 2.1). A comprehensive list of the stations and detailed maps of their locations can be found in Appendix A.

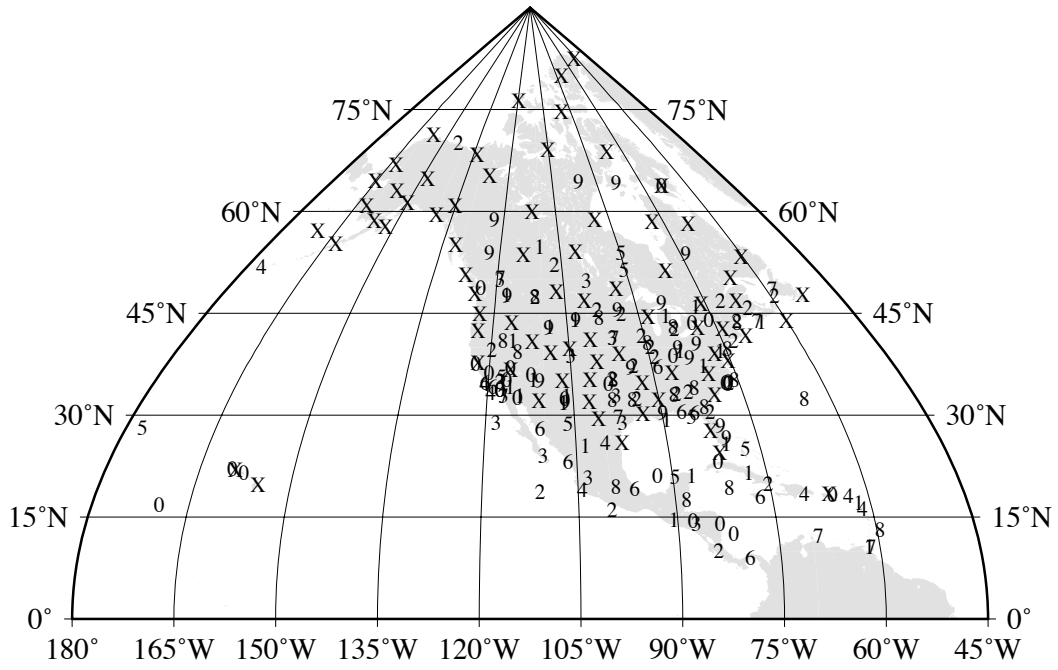

Figure 2.1. Location of radiosonde stations contributing data used in the analysis. (See text for a description of the labels. Stations Shemya, Alaska ('1'), and Keflavik, Iceland ('5'), are outside the map limits.)

Each symbol in Figure 2.1 represents the number of equivalent years of data provided by each station. An amount up to 1/2 year is represented by the symbol '0', between 1/2 and 1-1/2 years by '1', and so on, up to 9-1/2 years and over by 'X'. It should be stressed that this figure represents the amount of data equivalent to one year's worth of twice-daily balloon launches. For example, a station labelled '0' may have contributed profiles from some, or all years, of the 10 year period, but the total number is less than 365. The reason for including data from infrequently used radiosonde stations was to preclude data from being rejected arbitrarily, and because it was thought that infrequent launches may have been made during unusual atmospheric conditions.

Table 2.1. Summary of radiosonde data per year.

Year	#Stn's	#Profiles
1987	151	100327
1988	172	105362
1989	172	101032
1990	164	103263
1991	166	98435
1992	166	98108
1993	180	98089
1994	197	101214
1995	191	102532
1996	175	103289

Almost all atmospheric water vapour is found well below the 16-kilometre level and so the truncation of the CD-ROM data sets at the 100 mbar level poses no problem in accurately computing the wet delay. For the purposes of ray-tracing the hydrostatic delay however, the pressure and temperature profiles must be extended above this height. The pressure profile is assumed to follow the hydrostatic law and is easily computed once the temperature profile is extended using a suitable model profile. We have used the CIRA86 model [*Fleming et al.*, 1988] which provides monthly mean temperatures for every 5 kilometres of altitude up to 120 km at every 10 degrees of latitude. Other investigators have used a constant, global, profile derived from the U.S. Standard Atmospheres to model any missing radiosonde data. However, we feel that the CIRA model is more realistic (as well as being more up-to-date) and is independent of the Standard Atmospheres that were used to derive the UNB3 model.

The required temperature profile is computed in two steps. First, a common bi-cubic weighting function [*Junkins et al.*, 1973] is used to interpolate a profile from the two

CIRA profiles adjacent to the latitude of the radiosonde station and the two profiles adjacent to the date of the balloon launch. Second, this interpolated profile is offset by a constant temperature to match the radiosonde temperature profile at the truncation height. An example of the results for a typical temperature profile is shown in Figure 2.2.

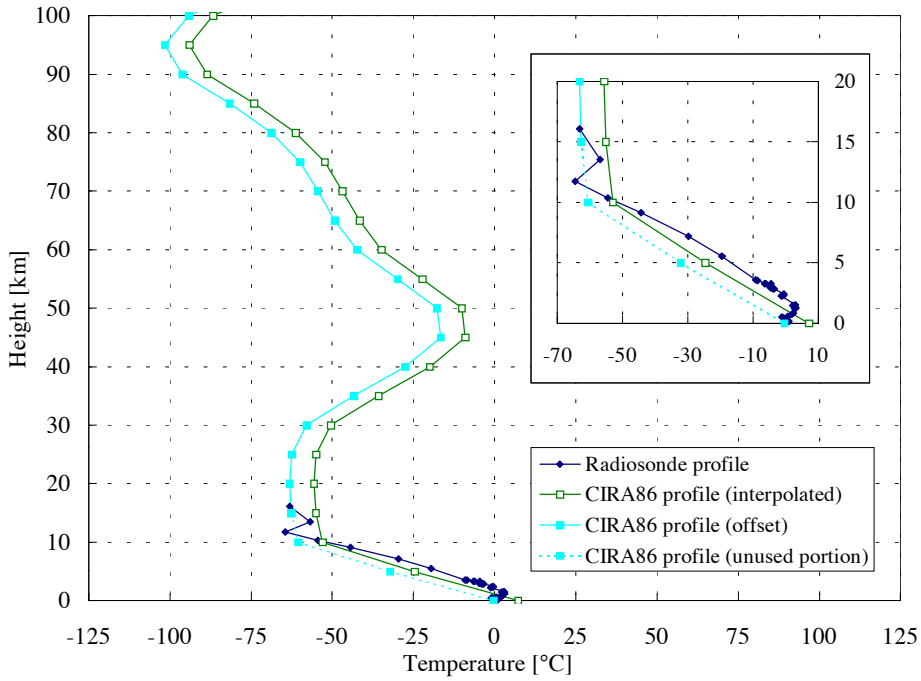

Figure 2.2. Radiosonde temperature sounding and fitted CIRA86 profile. (Balloon launched at St. John's, Newfoundland, March 3rd, 1995.)

We undertook a series of tests to determine whether this temperature extrapolation above 100 mbar was accurate to an acceptable level. A small selection of recent profiles spread across North America containing readings up to 10 or 20 mbar were obtained on-line from the University of Wyoming (http://www-das.uwyo.edu/upperair/sounding.html). Each profile was processed both in full and again after truncating and extrapolating the temperature above 100 mbar. The results of differencing the

subsequent ray-traced delays are shown in Figure 2.3. The five stations represented are 13897BNA, Nashville (Tenn.); 14607CAR, Caribou (Maine); 11903MEX, Mexico City; 18601YLT, Alert (N.W.T.); and 14531YYT, St. John's (Nfld.). The largest discrepancy between the two profiles is less than 1 cm at five degrees elevation angle. This level of accuracy is easily sufficient for our purposes, so we can conclude that our methodology with respect to extrapolating the radiosonde profiles is sound.

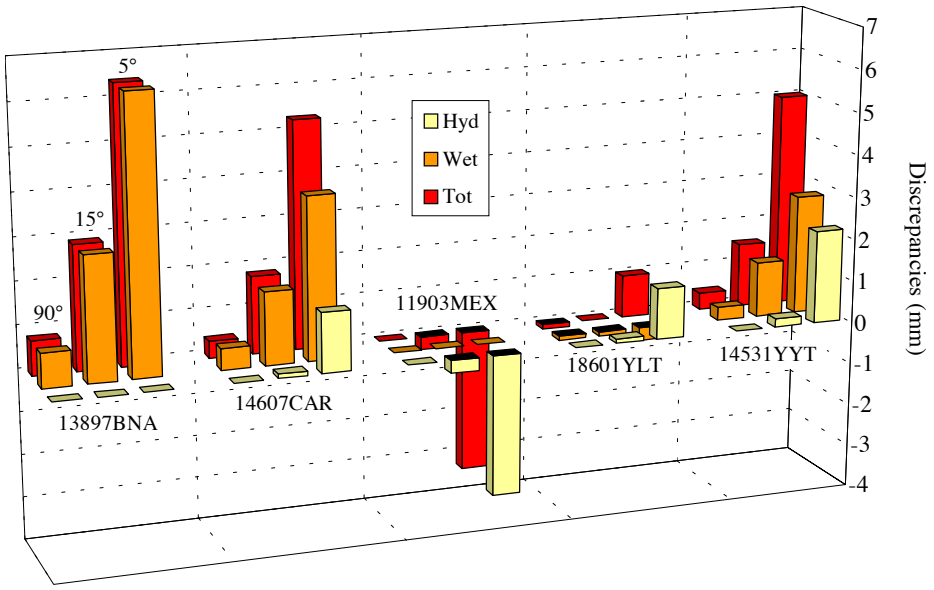

Figure 2.3. Results of ray-trace tests with full and truncated profiles. Histogram bars for each station represent hydrostatic, wet and total delay differences for elevation angles of 90, 15 and 5 degrees respectively, displayed left-to-right.

Other investigators (e.g. *Coster et al.* [1996]) have shown that, when compared to other instruments such as radiometers, ray-traced radiosonde profiles of the zenith delay are typically accurate only at the centimetre level. This reflects the inherent limitations in recording and representing any water vapour profile with a radiosonde. Because of this,

and because our truncated data limits the accuracy of the ray-trace data, all our results are only quoted at the centimetre level.

2.3. Processing Summary

Our overall processing technique consisted of three-stages: (1) pre-processing and formatting the radiosonde data; (2) ray-tracing for benchmark values; (3) model comparison. The first stage is required to extract the radiosonde data from the CD-ROM storage media and analyse the individual profiles to remove anomalous measurements that would otherwise bias the results. (A detailed description of the pre-processing error detection techniques is given in Appendix B.) The temperature profile extrapolation explained previously was also carried out at this stage. Subsequently, the data was stored in a binary file format to minimise computer storage requirements. A full year of data took approximately 30 minutes to process during this stage.

An important aspect of the subsequent ray-tracing procedure is the amount of CPU time required to compute the delay values. This is predominantly a function of the elevation angle of the ray and the step-size used to define the thickness of the initial atmospheric layer. The thickness of subsequent layers is increased to keep the change in the total delay approximately constant. Table 2.2 shows the impact of changing the step size on the accuracy of the computed delay (assuming the result for a step-size of 5 m to be correct). The CPU times pertain to zenith direction ray-traces only; the delay differences are for traces at elevation angles of 90, 15 and 5 degrees. These tests, and all

our data processing, were undertaken with a Sun Microsystems 85MHz MicroSPARC II processor. The data used here was for the year 1995 from station 23044 (El Paso, Texas – selected at random) which consisted of exactly 502 profiles.

Table 2.2. Accuracy of ray-traced delays.
(Differences are "worst-case" and relative to 5m initial step-size).

Step size (metres)	CPU time (~500 profiles)	Difference (max, mm)
5	1min:28sec	–
10	48sec	0.1
20	26sec	0.2
50	14sec	0.8
100	10sec	1.8

Hence, an equation to provide a conservative estimate of the accuracy of the ray-tracing algorithm alone would be: $0.02 \times$ step-size (mm). We therefore chose to use the 50 m value to minimise the processing time while keeping a "worst-case" accuracy of approximately 1 mm. With this value, data from one year (approximately 100,000 profiles) could be processed (that is, ray-traced in the zenith direction only) in slightly less than 1 hour.

The third processing stage performed the comparatively simple task of subtracting the model delays from the ray-traced delays and collating the results. Software was designed and written to allow the specification of an extreme value limit that would flag results and to enable the individual profiles to be extracted from the original data for further viewing and checking. The residual errors were also saved for further processing. With all these options engaged, one year of data was processed in approximately five minutes.

3. RESULTS AND ANALYSIS

Because the description follows a more logical progression, we will first deal with the model performance under general, or nominal, atmospheric conditions. From this analysis comes a definition of what constitutes an "extreme" error from which we can proceed to that specific part of our analysis.

All of our results are stated for the error in the zenith direction only. Errors at other elevation angles will be a function of the zenith errors mapped to the elevation angle plus some error in the mapping function. We have previously determined that we expect this latter portion of the error to be usually at the order of 1 cm [*Collins and Langley*, 1997a; Appendix C3]. Therefore, the majority of the tropospheric delay error will usually be determined by the error in the zenith component alone. At the same time, our results are independent of whichever mapping function is eventually chosen for the Minimum Operational Performance Standards (MOPS) for the WAAS user. We originally specified the *Niell* [1996] mapping functions, however a proposal was made to replace these with the *Black and Eisner* [1984] function for the sake of computational simplicity. While slightly less accurate, this function should not contribute more than a few centimetres of delay error, on average (see Appendix E2).

The benefits of using real-time meteorological values in modelling the tropospheric delay are often contested in both the GPS-geodetic and GPS-navigation fields. To provide a brief comparison here, the results for UNB3 are compared with those obtained

when the portion of the look-up table for pressure, temperature and water vapour is replaced by measured values recorded at the radiosonde launch points. The remaining portion of the look-up table devoted to the temperature and water-vapour lapse rates was retained. Otherwise, this model uses exactly the same algorithms as the normal UNB3 model. The results for this model, denoted UNB3(SfcMet), simulates the performance we would expect from using meteorological data recorded at an aircraft flying at predominantly low altitudes, that is with the bulk of the troposphere above it.

3.1. Model Performance Under General Conditions

To test the overall distribution of the model errors we can utilise Gaussian probability plots to compare them to a standardised Normal distribution. The distributions of all the residuals using both UNB3 models are shown in Figure 3.1 along with a theoretical Normal distribution of zero mean and 5 cm standard deviation ($N(0,5^2)$). It can be seen that an $N(0,5^2)$ distribution characterises the errors of both UNB3 models quite well up to approximately the 4σ level where the value of the residuals is almost exactly ± 20 cm. Beyond the lower 4σ level, the $N(0,5^2)$ bound for UNB3 becomes progressively more conservative because the magnitude of the negative residuals appears to be levelling off. The residuals for UNB3(SfcMet) beyond the same point are drastically underestimated. The residuals beyond the upper bound for both models are also drastically underestimated by an $N(0,5^2)$ distribution. In comparison, the current WAAS and ICAO tropospheric error bound of $N(0,12^2)$ is also plotted. This distribution clearly over-bounds even the extreme residuals, and it appears that a small reduction, to say $N(0,10^2)$ is possible.

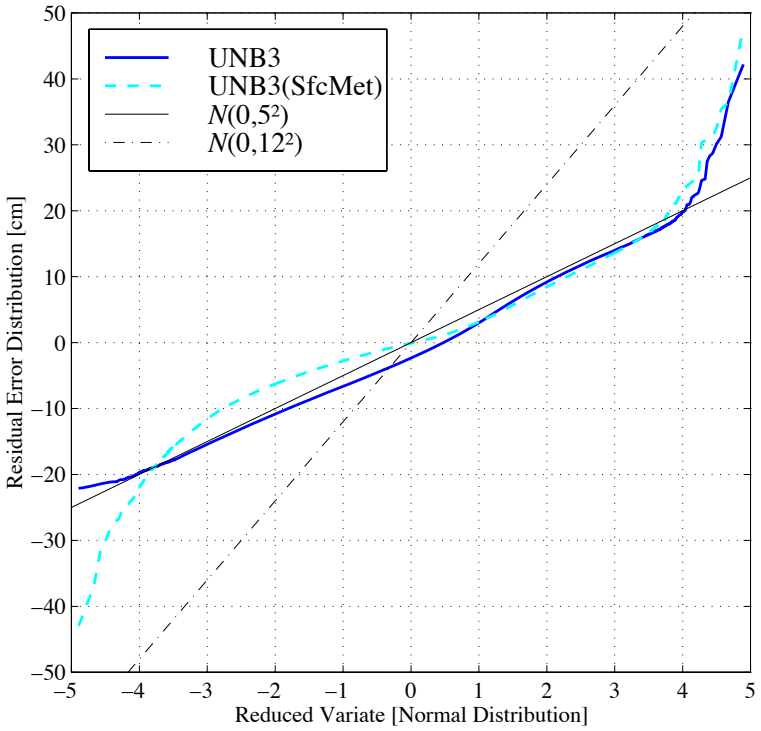

Figure 3.1. Gaussian probability plot of zenith delay residuals.

This figure indicates that care must be taken when attempting to characterise large tropospheric delay errors using distribution parameters computed directly from the data. It seems likely that the true distribution is drastically underestimated in the tails (beyond 4σ, for our data), and especially so with real-time data. The standard deviation calculated from the data can be artificially inflated to over-bound the larger residuals, however, we feel that this is a rather subjective method of characterising the residual error.

Table 3.1 shows the mean and standard deviation statistics for these two UNB3 models. The average performance of the two is very consistent from year-to-year, indicating that one-year of data, from a large number of stations, is sufficient to quantify the average, or typical, performance of a tropospheric delay model. The statistics for the

UNB3(SfcMet) model are smaller in magnitude and vary slightly less from year-to-year than those for the original UNB3 model. However, even though a near-zero mean performance is achieved, Figure 3.1 shows that there are more extreme values, and an overall asymmetric shape compared to a true Normal distribution.

Table 3.1. Statistics for UNB3 and UNB3(SfcMet) model errors. (Units in centimetres.)

Year	UNB3		UNB3(SfcMet)	
	Mean	S.D.	Mean	S.D.
1987	–1.7	5.0	0.3	3.3
1988	–2.0	5.0	0.3	3.4
1989	–1.9	4.9	0.2	3.4
1990	–1.8	4.8	0.2	3.3
1991	–1.6	4.9	0.4	3.3
1992	–1.9	4.7	0.4	3.3
1993	–1.7	4.9	0.4	3.3
1994	–1.9	4.9	0.2	3.4
1995	–1.9	5.2	0.0	3.6
1996	–2.1	5.0	0.0	3.6
All	**–1.9**	**4.9**	**0.2**	**3.4**

Unfortunately, the results in Table 3.1 do not give a complete picture of the performance of the UNB3 model. For example, it is useful to examine the performance of the model on a geographical (latitudinal) basis. Figure 3.2 shows the empirical probability density distributions of all ten years of residuals grouped by the six latitude zones used in the UNB3 model look-up table. The densities have been normalised by the number of residuals in each zone so that we can see how each zone compares to each the others. It is immediately obvious that there is a great deal of difference between how the model operates in the tropics compared to the arctic or mid-latitudes.

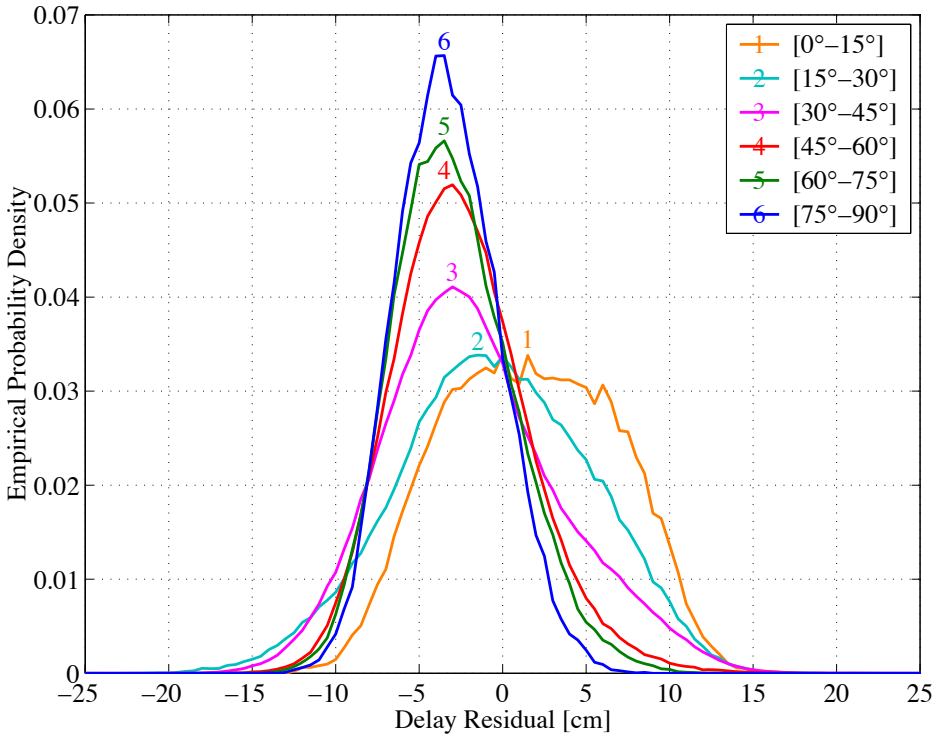

Figure 3.2. Empirical probability density function for all UNB3 residuals grouped by model zones.

As Table 3.2 confirms, the UNB3 model is quite accurate (i.e., near zero-mean, small bias), but relatively imprecise (large scatter), between 15° and 30°, while the accuracy decreases as the precision increases moving towards the polar zone. The change in precision is reflected in the changing shapes of the distributions: from the flat (negative kurtosis), tropic and arctic zones, to the peaked (positive kurtosis) mid-latitude zones. Only the residuals in the 30°–45° zone approach the shape of a Normal distribution (zero kurtosis). The symmetry of the distributions is important for the statistical representation of the errors. Unfortunately, only the tropical zones 0°–15° and 15°–30° have distributions anything like symmetric in shape. The distributions of the other zones are markedly asymmetric.

Table 3.2. Statistics for zoned residuals.
(Mean and standard deviation (S.D.) in centimetres.)

Latitude	Mean	S.D.	Skewness	Kurtosis	#residuals
0°–15°	1.6	5.1	0.00	–0.72	25741
15°–30°	–0.5	5.7	–0.09	–0.23	153891
30°–45°	–1.8	5.3	0.38	0.04	443389
45°–60°	–2.5	4.0	0.43	0.52	240938
60°–75°	–2.9	3.6	0.36	0.14	126574
75°–90°	–3.3	3.0	0.18	–0.12	21118

A better idea of the spatial variation of the model performance can be gained from examining contour plots of the residual statistics from individual stations. Figure 3.3 and Figure 3.4 represent the mean and standard deviation of the UNB3 model residuals for the data from 1992 only (selected at random). These maps are only illustrative of the annual performance of the model, and they only indicate whether the "first-order" latitudinal and seasonal components of the model are effective. (It should be noted that the particular station distribution can influence the contour patterns on these plots.)

From Figure 3.3 it appears that, on average, the UNB3 model does not remove quite enough of the delay in the Caribbean Sea area, and removes too much around the west coast of Baja California (Mexico) and Southern California (U.S.A.). From Figure 3.4, we can say that the variation in the UNB3 model error is less than 5 cm (1σ) across a large part of the North American continent, with the exception of south-western Mexico and the Mid-West and South-Eastern areas of the U.S.A. The large variation in the model performance centred on the Gulf Coast area is possibly associated with climatological variations in water vapour in that region.

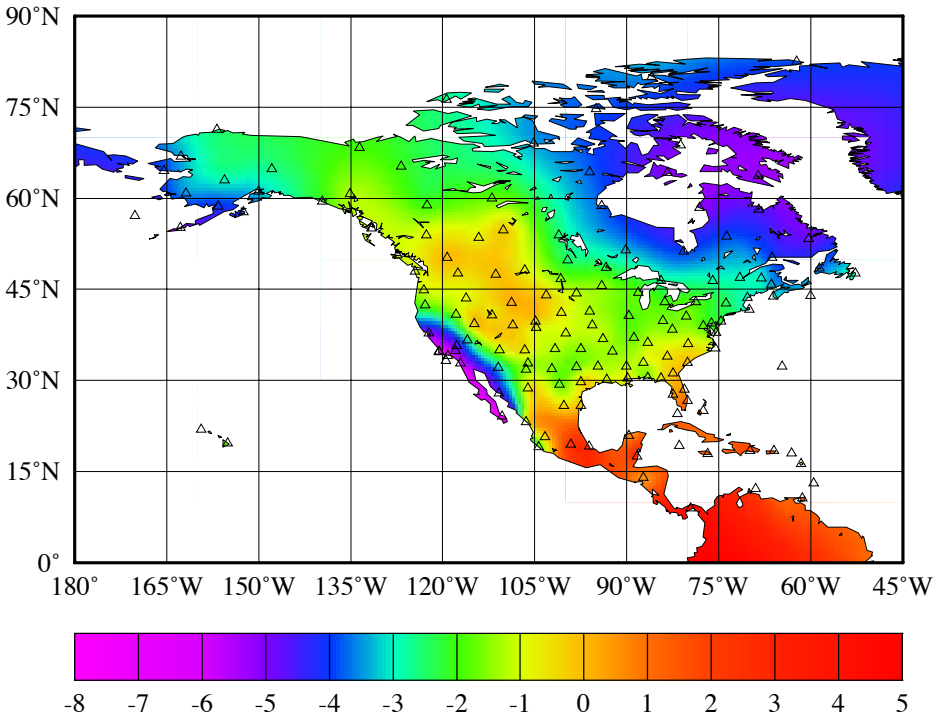

Figure 3.3. Mean UNB3 model error (cm) for 1992 data.

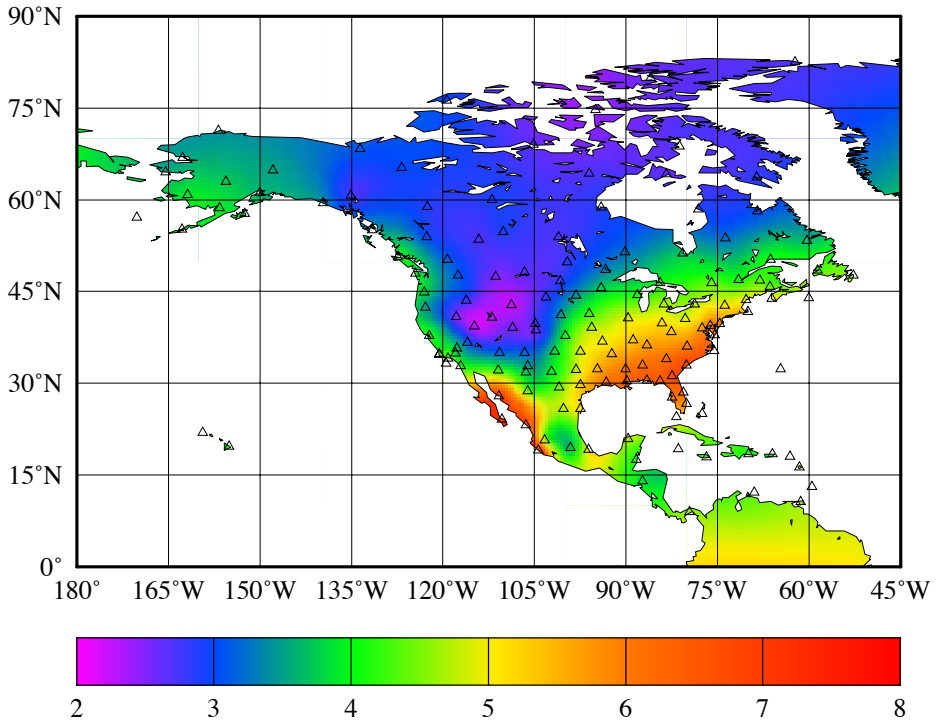

Figure 3.4. Standard deviation of UNB3 model error (cm) for 1992 data.

At this point, it is worthwhile re-examining the nature of the problem of trying to model the variation of the tropospheric delay. Figure 3.5 and Figure 3.6 are contour plots of the mean and standard deviation of the hydrostatic portion of the zenith delay computed from the radiosonde profiles. The mean plot is essentially a scaled "inverse height" terrain model, due to the pressure dependence on altitude. We can see that the variation of the hydrostatic delay over one year is very small, which again corresponds to the typically small variation in surface pressure. Figure 3.7 and Figure 3.8 indicate how well the UNB3 model has dealt with this portion of the delay. On average, only a few centimetres of the hydrostatic delay remains after applying the UNB3 model. The height variation due to the Rocky Mountains range and others appears to be adequately dealt with. The variation of the error is almost exactly the same as for the actual hydrostatic delay, which would tend to indicate that the UNB3 model is less useful at modelling the sub-seasonal, or day-to-day, variations.

The conclusion that can be drawn therefore, is that the "total delay" errors represented by Figure 3.3 and Figure 3.4 are predominantly due to mis-modelling the wet delay portion only. Figure 3.9 and Figure 3.10 show the mean and standard deviation respectively of the wet zenith delay for 1992. The pattern of the standard deviation in Figure 3.10 is almost exactly the same as Figure 3.4, although some of the magnitude has been reduced by the model. The complicated spatial pattern of water vapour below 30°N is immediately obvious. It is impossible to represent this kind of variation with a model dependent on coordinates, such as latitude, only. In the arctic north-west, the UNB3 model appears to be over-predicting the true delay by approximately a factor of two.

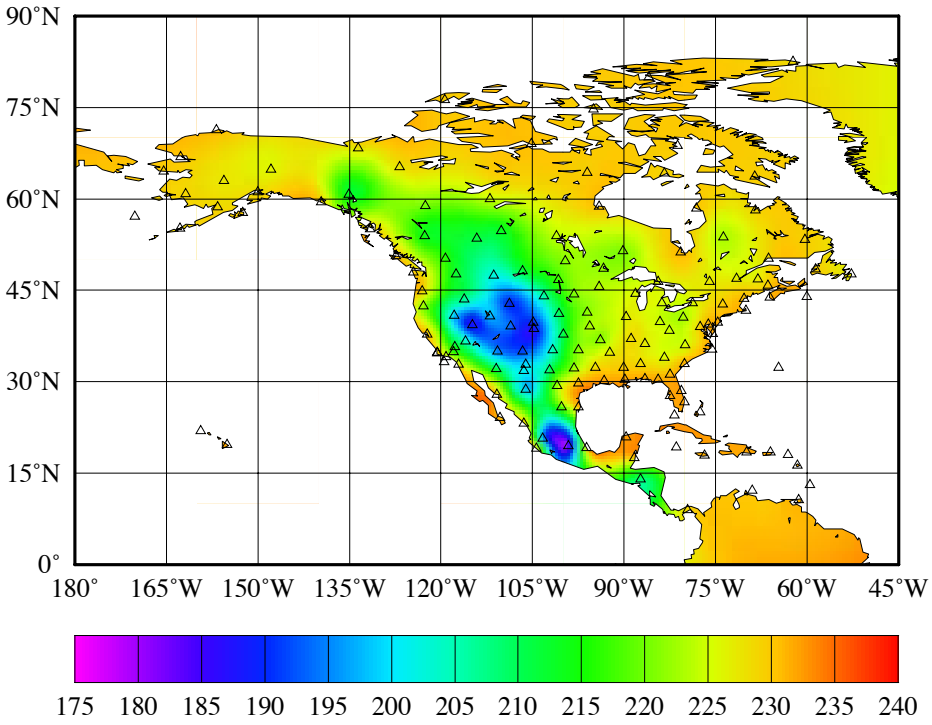

Figure 3.5. Mean hydrostatic zenith delay (cm) for 1992 data.

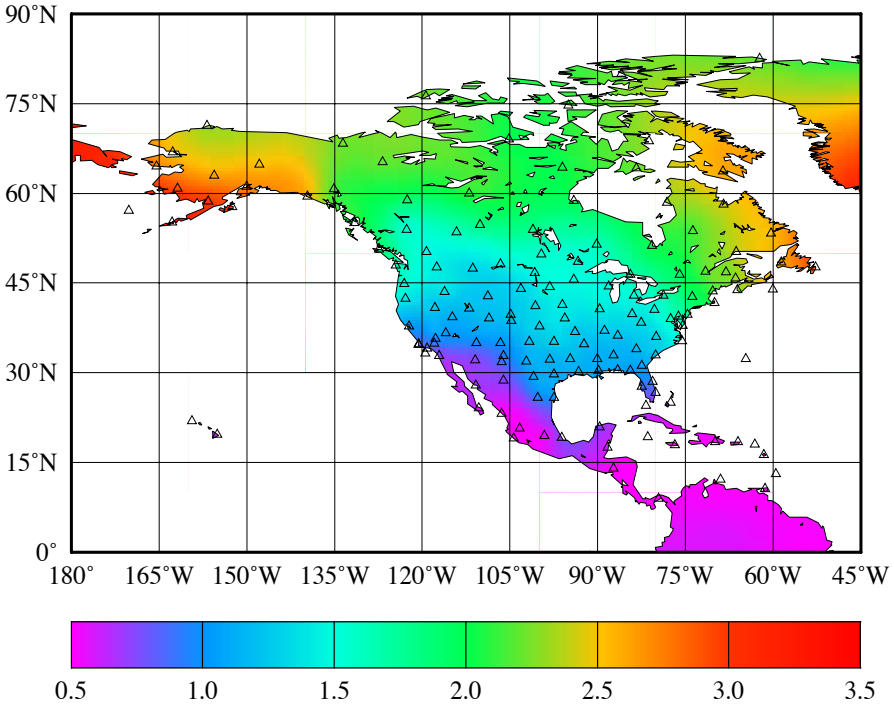

Figure 3.6. Standard deviation of hydrostatic zenith delay (cm) for 1992 data.

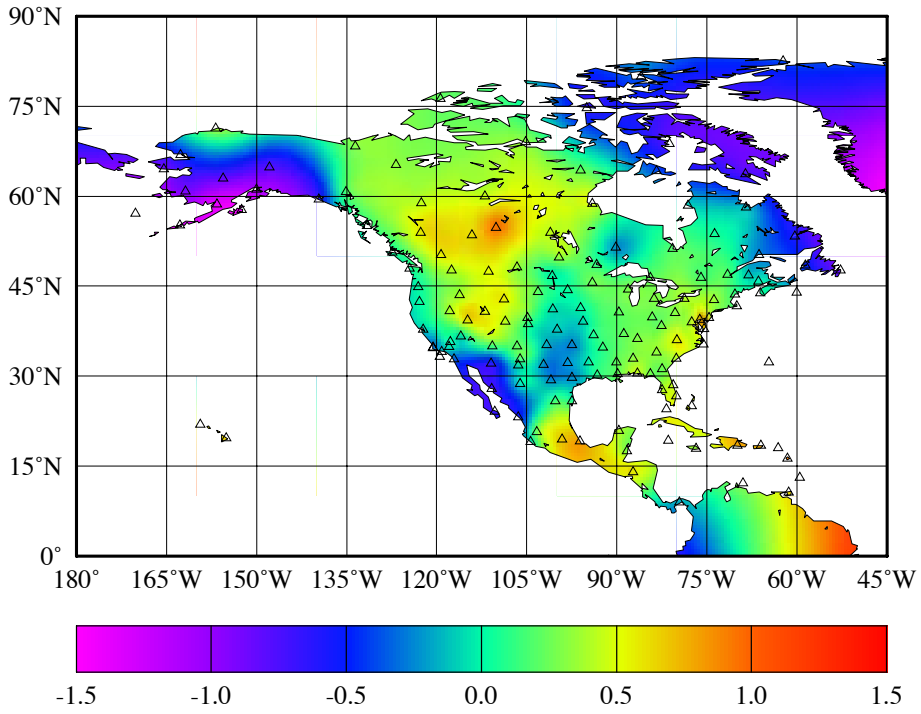

Figure 3.7. Mean hydrostatic UNB3 model error (cm) for 1992 data.

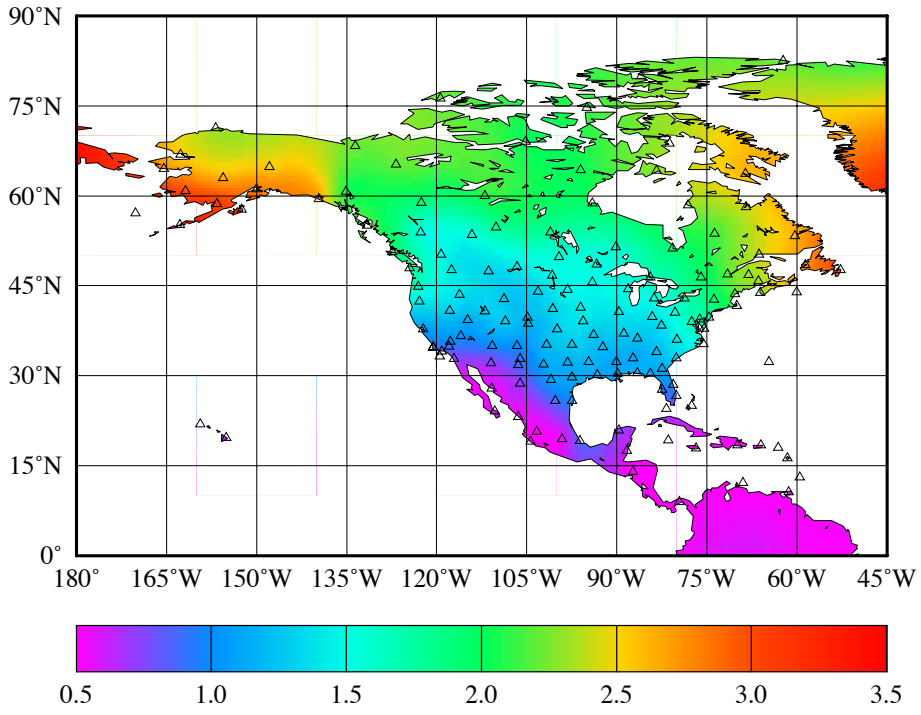

Figure 3.8. Standard deviation of hydrostatic UNB3 model error (cm) for 1992 data.

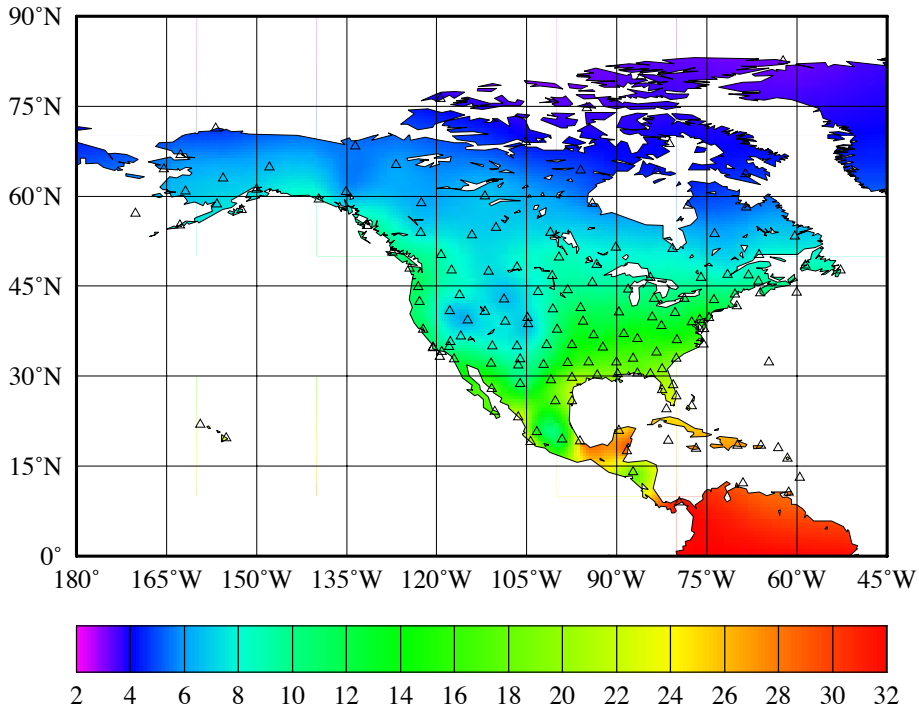

Figure 3.9. Mean wet zenith delay (cm) for 1992 data.

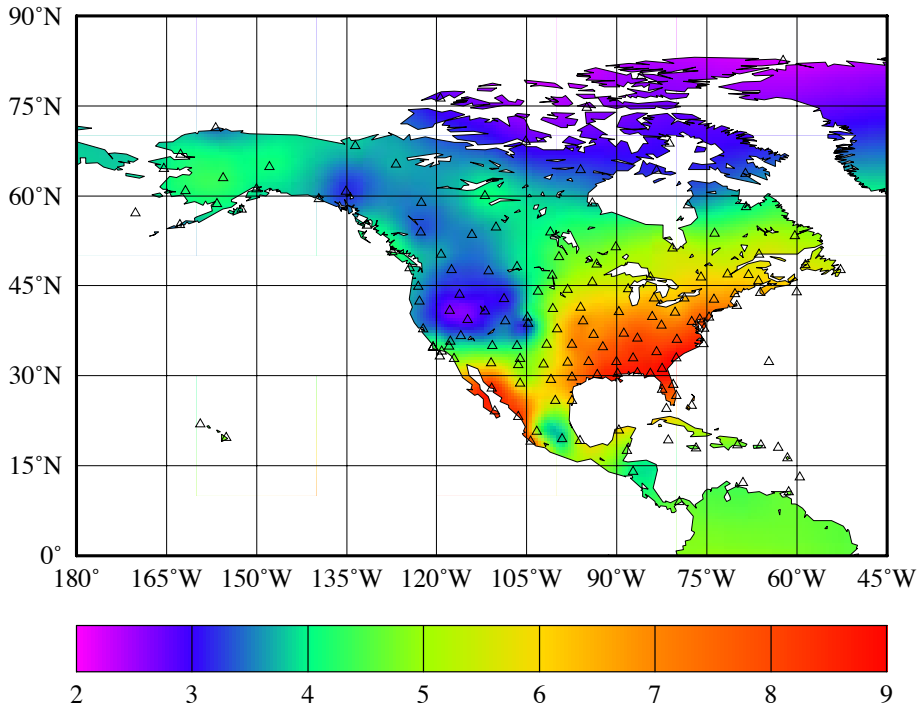

Figure 3.10. Standard deviation of the wet zenith delay (cm) for 1992 data.

As we alluded to, contour plots can be misleading when considering the tropospheric delay because of the localised variation of atmospheric water vapour. It is therefore prudent to also consider results on a station-by-station basis. The following figures show histograms of the error experienced at various radiosonde stations. At each station, the UNB3 model error computed from all the available data was separated into 10 cm bins. These correspond to the 2σ, 4σ, etc, error limits of the UNB3 model, ignoring the non-zero mean contribution. In this way, the percentage of observations falling outside a specific limit can be gauged on a station-by-station basis.

An important qualifier that must be discussed is that the data for each station should be spread evenly across a year. This is because there are still seasonal variations remaining in the errors. Statistics computed from only one or two seasons of data could therefore be biased. Hence, each histogram is accompanied by a key describing the percentage of the seasonal contribution of the residuals, i.e. how much of all the available data was recorded in the spring, summer, autumn and winter. Obviously, we would like each of these to be 25%, indicating an equal contribution.

The following diagrams (Figure 3.11 to Figure 3.18) represent some of the poorer cases of UNB3 performance around Southern California and Western Mexico. These are followed by some of the problematical cases from the South-East and Gulf Coast area of the U.S. and then several, more typical, stations from Canada. Following each set of histogram plots are scatter plots showing the actual wet zenith delay and total model residuals for the same stations.

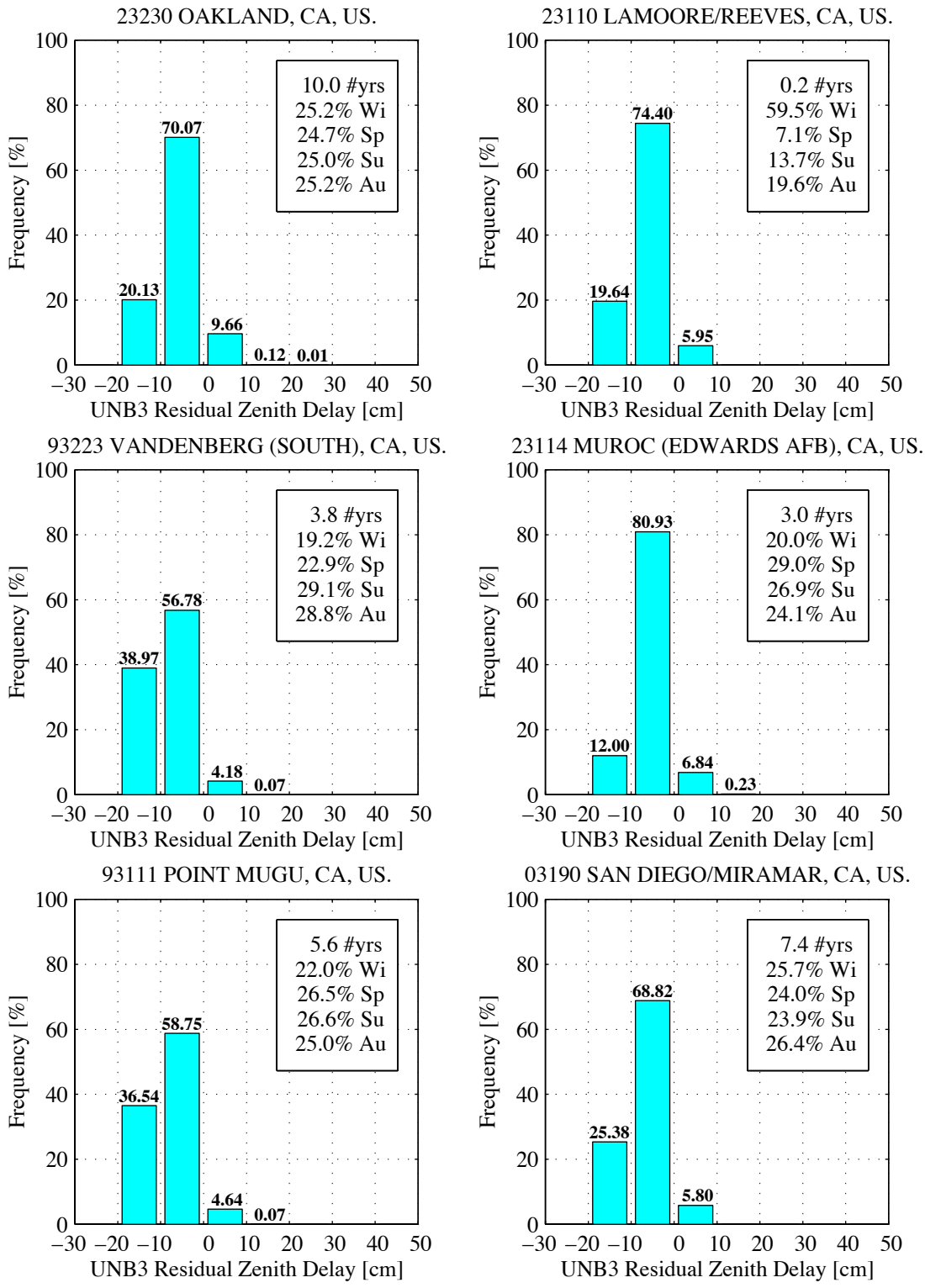

Figure 3.11. UNB3 model error histograms for Southern California stations.

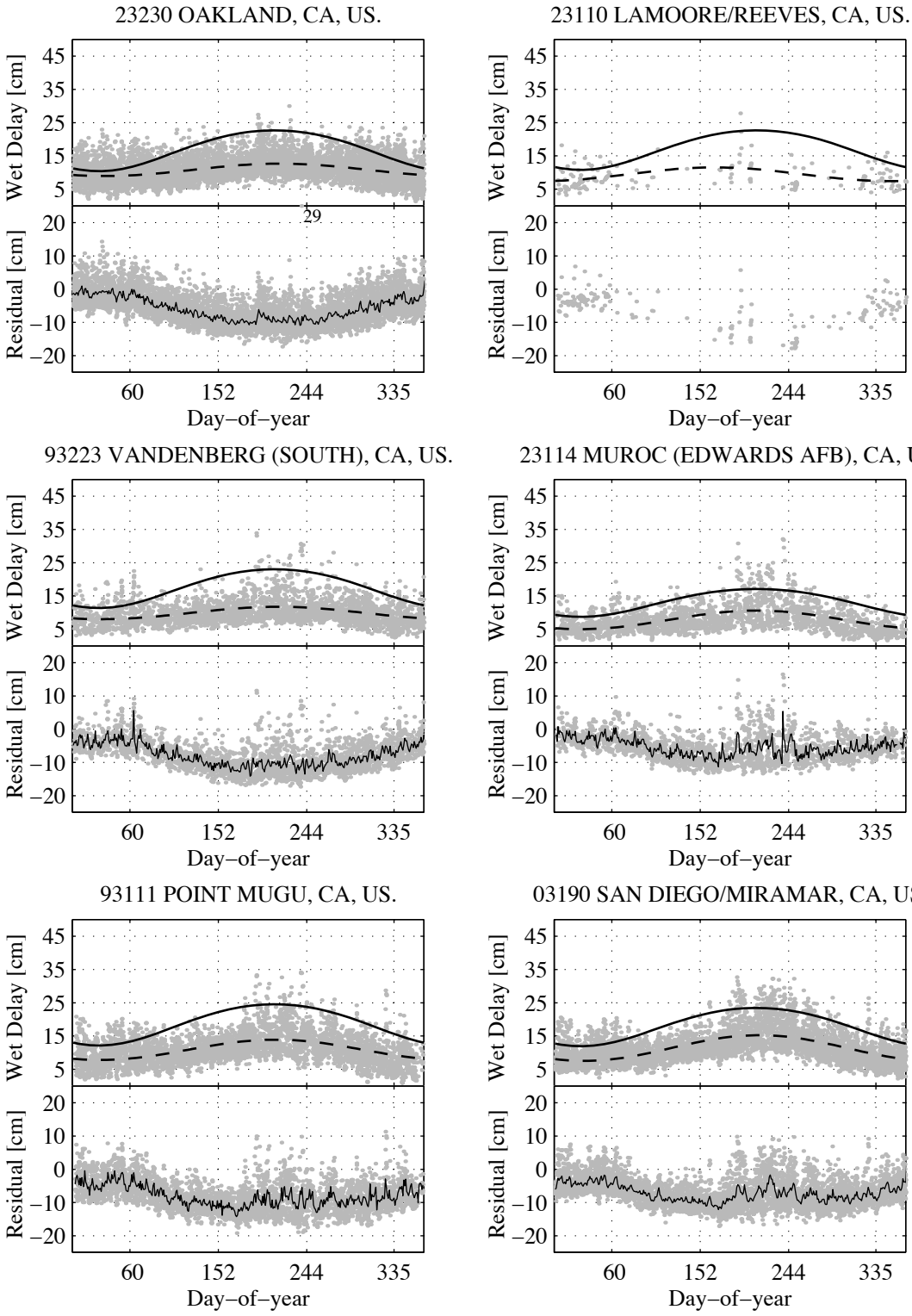

Figure 3.12. Wet zenith delays and UNB3 residuals for S-Calif. stations.

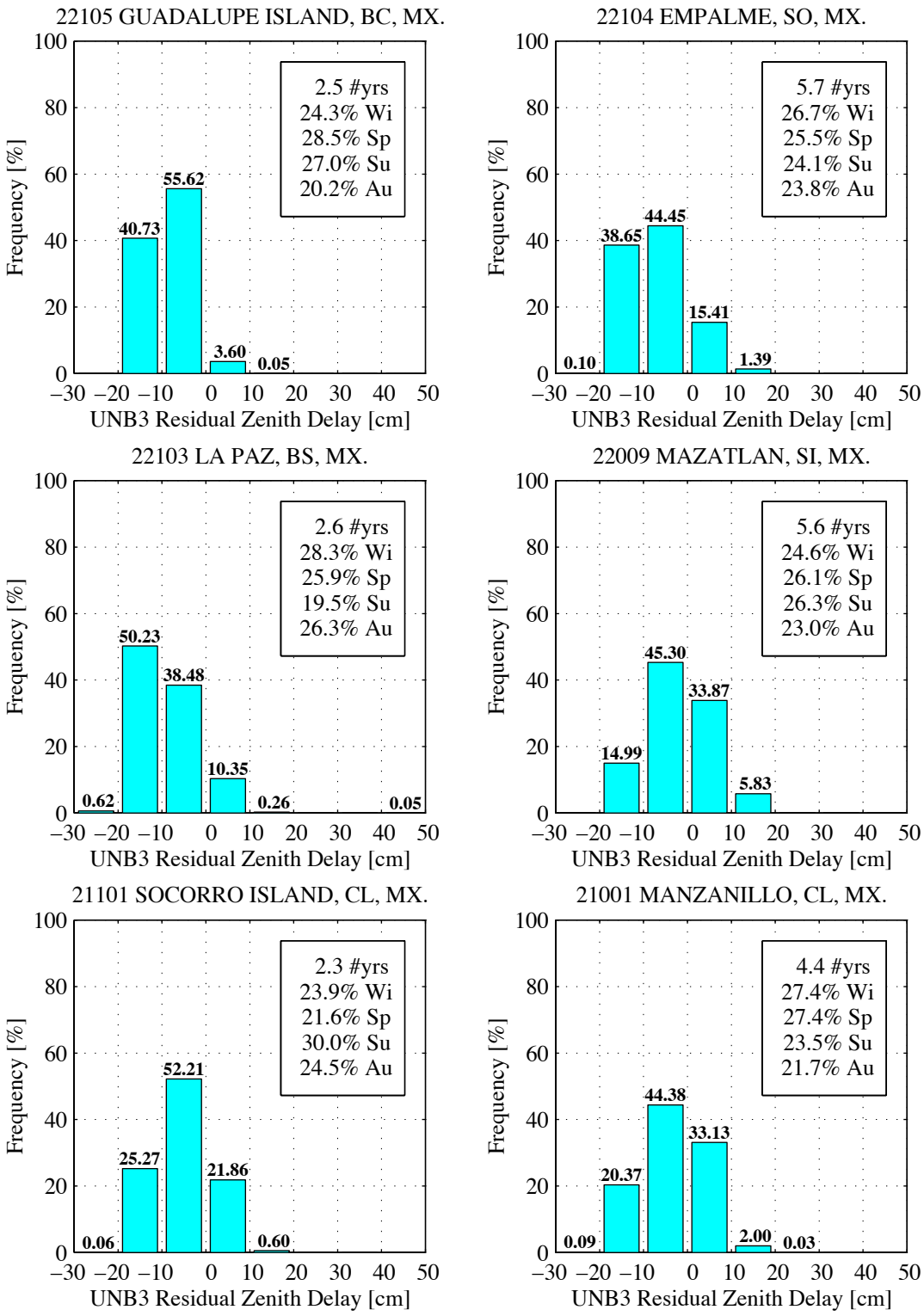

Figure 3.13. UNB3 model error histograms for Western Mexico stations.

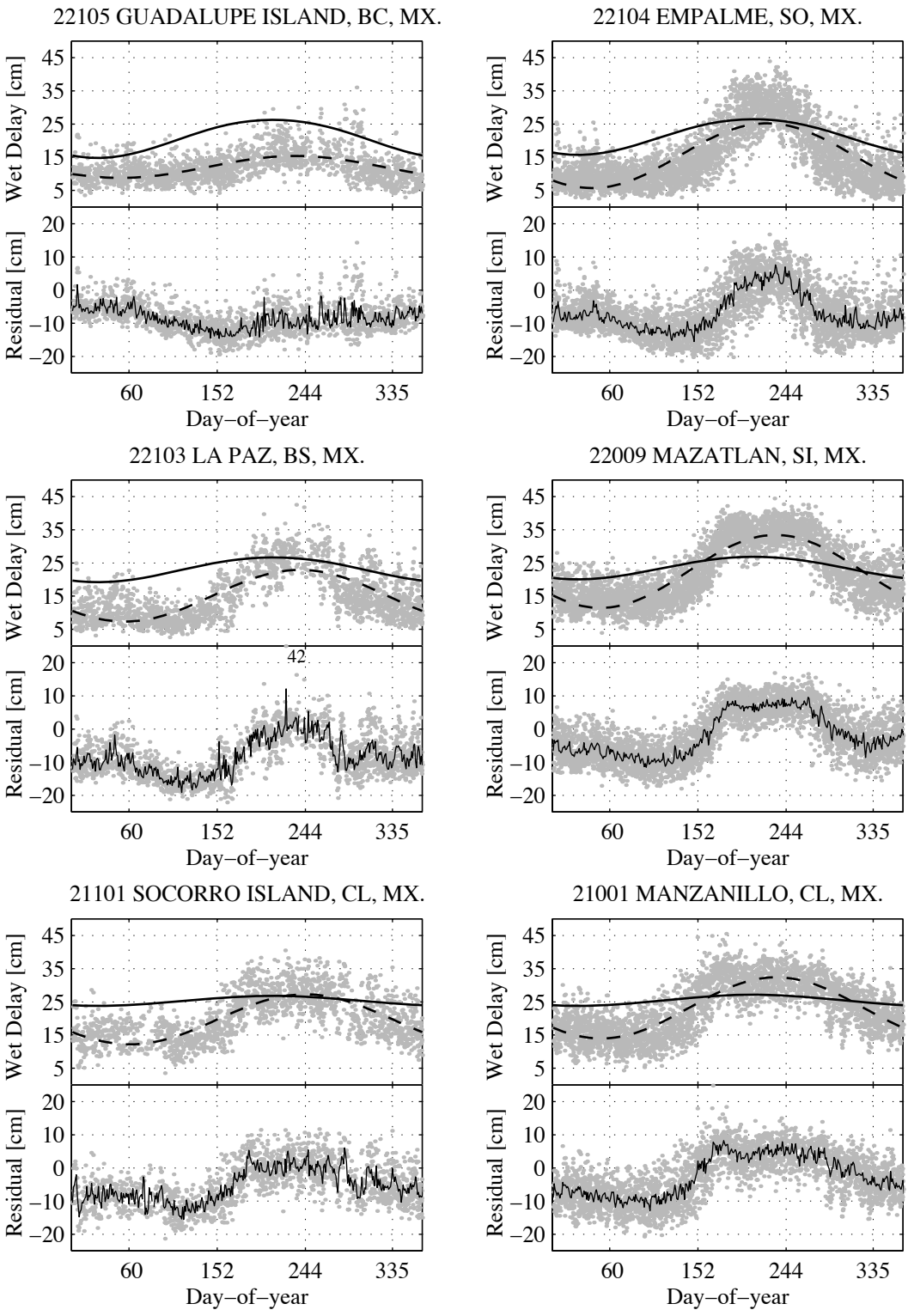

Figure 3.14. Wet zenith delays and UNB3 residuals for Western Mexico stations.

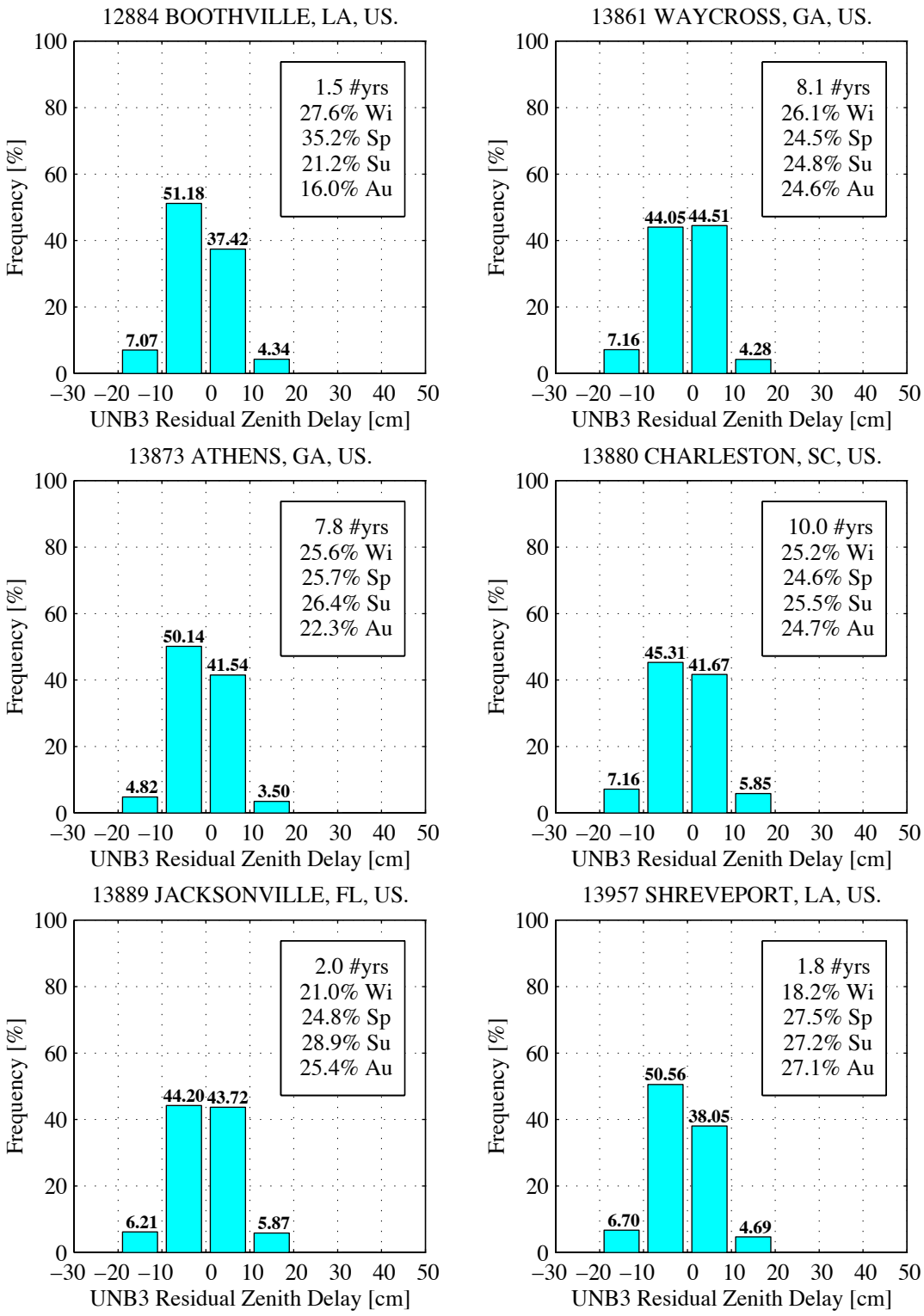

Figure 3.15. UNB3 model error histograms for South-Eastern U.S. stations.

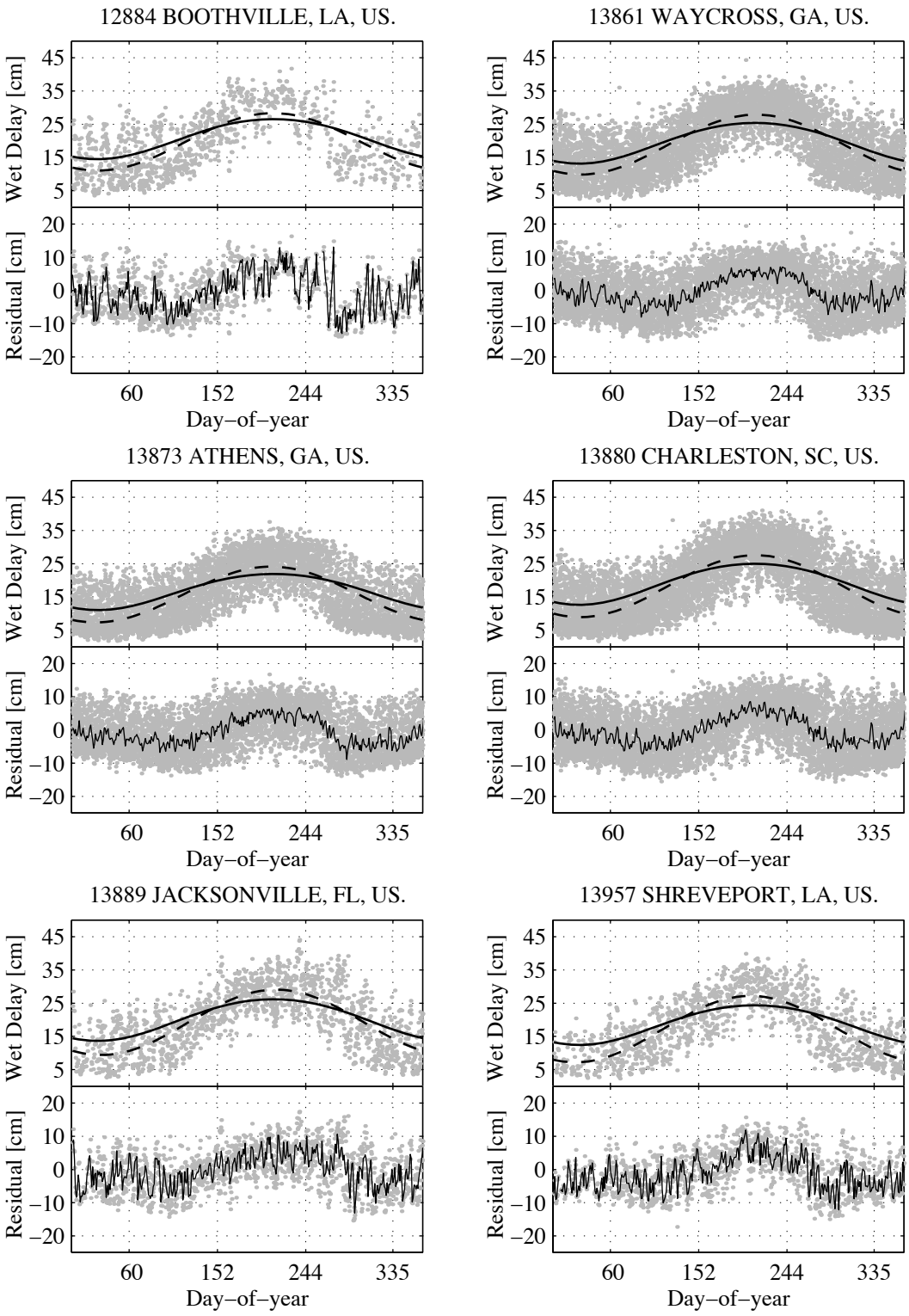

Figure 3.16. Wet zenith delays and UNB3 residuals for South-Eastern U.S. stations.

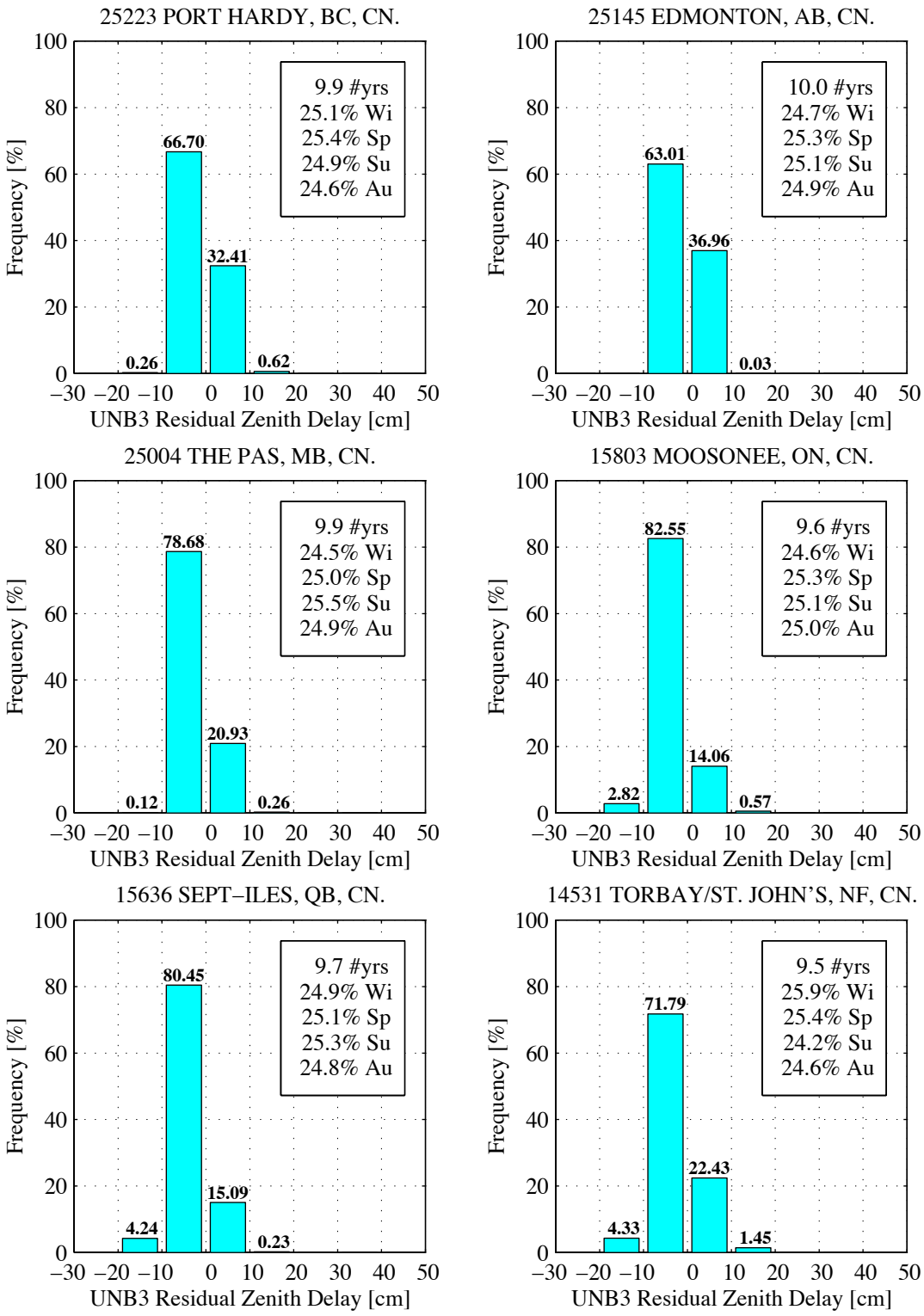

Figure 3.17. UNB3 model error histograms for Canadian stations.

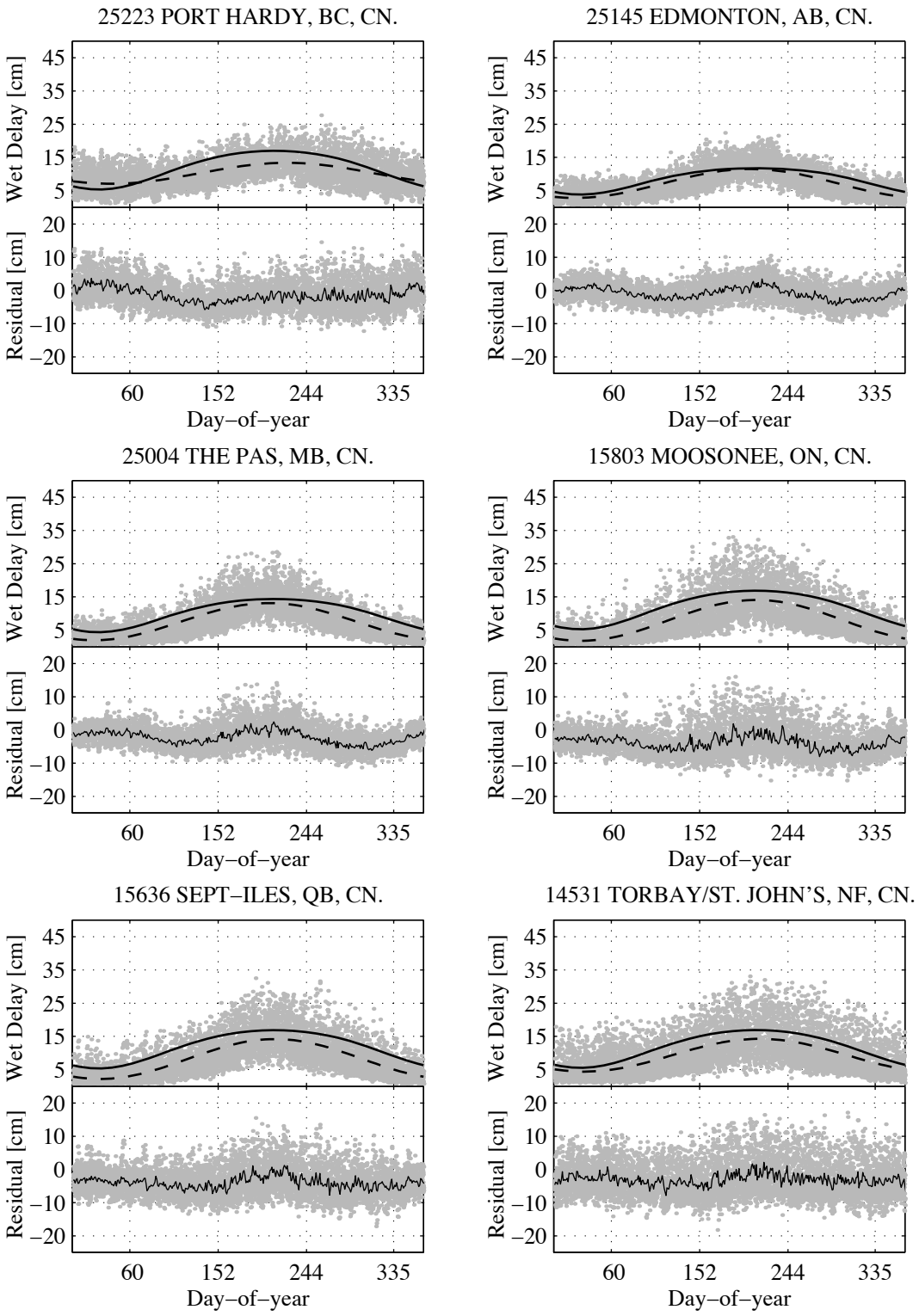

Figure 3.18. Wet zenith delays and UNB3 residuals for Canadian stations.

Histogram plots of all the stations in our data set are presented in Appendix C. Complete residual and wet zenith delay scatter plots are presented in Appendix D. The upper panels of the delay and residual plots have two curves superimposed over the delay points. These are the UNB3 model values (unbroken line) and the best-fit sinusoid in a least squares sense (broken line). The estimated parameters were the mean offset, amplitude and phase of the sinusoid, with the period fixed at 182.625 days. In the lower panels, the ensemble average (average value at discrete points of time) is superimposed over the residuals. For increasing amounts of data, this trace becomes more smooth, indicating that the mean day-to-day error is consistent over short periods of time. Large residuals outside the range of the panels are plotted on the upper limit of the lower panel and annotated with their numerical value. On both panels, the vertical grid lines approximately delineate the four seasons.

An example of the censoring problem due to incomplete sampling is visible on the second histogram of Figure 3.11. Station 23110 La Moore/Reeves has ~20% of its error greater (in a negative sense) than −10 cm, however the key indicates that this station has predominantly winter data points and in Figure 3.12 we can see that that is indeed the case. Very little data is available from the summer season and what is available is mostly greater than −10 cm in magnitude. The other Californian stations have reasonably equally distributed seasonal data and so are more reliable. All of these stations have more than 10% of residuals greater than −10 cm. The worst two, Vandenberg (South) and Point Mugu have almost 40% of their residuals greater than −10 cm.

The stations in Western Mexico (Figure 3.13 and Figure 3.14) are, if anything, worse. Station La Paz is the worst in this area with over 50% of residuals greater than −10 cm. The main reason here is that the UNB3 model for the wet zenith delay has a much larger mean and a much smaller amplitude than the actual delays experienced. The dampening of the amplitude visible in Figure 3.14 is due to the fact that the station locations are approaching 15°N latitude where the UNB3 model has a constant value for the wet zenith delay.

The results for the South-East and Gulf Coast area of the U.S. are problematical because, while the UNB3 model closely follows the true delay, the large scatter means there can still be some large errors. Of the stations plotted in Figure 3.15 and Figure 3.16, only Athens has less than 10% of its residuals greater than ±10 cm. The Canadian stations in Figure 3.17 and Figure 3.18 are examples of much better results. Very few residuals are greater than ±10 cm and the UNB3 model succeeds in removing almost all of the seasonal trends, leaving only a constant bias and the inherent day-to-day scatter.

In an attempt to summarise the model performance of the worst stations, we can consider Figure 3.19. This 3D map and bar plot primarily shows the distribution of stations that have 10% or more residuals greater than 2σ (±10 cm). The size of the columns is proportional to the actual percentage of residuals that exceed the ±10 cm range. The concentration of large errors around Southern California and Western Mexico is again emphasised, as are the lesser problems in the South-Eastern U.S. Stations with between 5% and 10% of errors greater than 2σ are plotted as squares, and are generally

located in a long arc stretching down the eastern seaboard from St. John's, Nfld., to Florida and around the Gulf of Mexico. A few more can be found in the Mid-Western U.S. It should be noted that there are also several Alaskan stations that fall within these same criteria (the largest are 25704 Adak, 11.3%, and 45715 Shemya, 13.1%), however they have not been plotted for clarity.

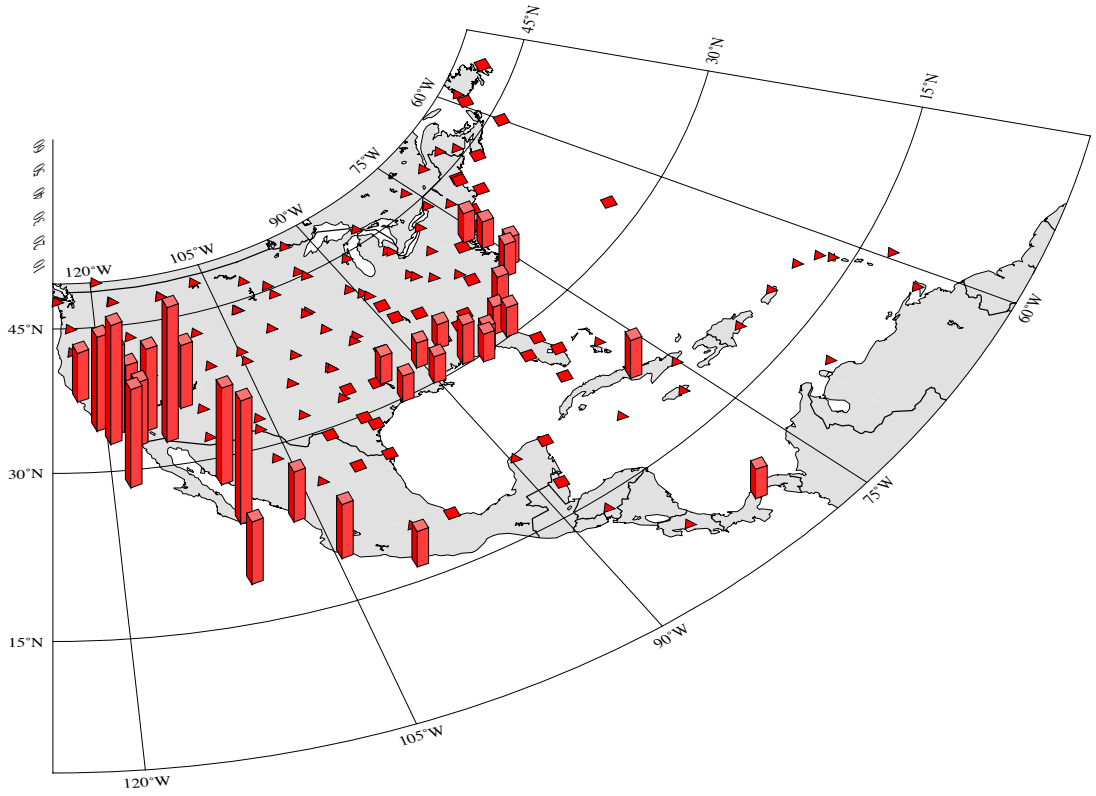

Figure 3.19. Location of stations with 10% or more residuals outside the range ±10 cm (columns); stations with between 5% and 10% of residuals outside the range ±10 cm (squares); and remaining stations (triangles). (Vertical scale in percentage points; the largest bar is for station 03125 Yuma Proving Ground, ≈56%.)

3.1.1. Formulation of a Residual Delay Error Model

We have seen that at certain times (and at certain places) there can remain a considerable unmodelled portion of the tropospheric delay after application of the UNB3 error model. This is an unavoidable consequence of the lack of real-time data and the nature of the atmosphere. An appropriate error model is therefore required to properly weight the tropospheric error contribution in the determination of the user's position. In addition, the probability of an unacceptably large error due to the troposphere must be monitored. In WAAS, this is done through the Vertical Protection Limit (VPL) equation.

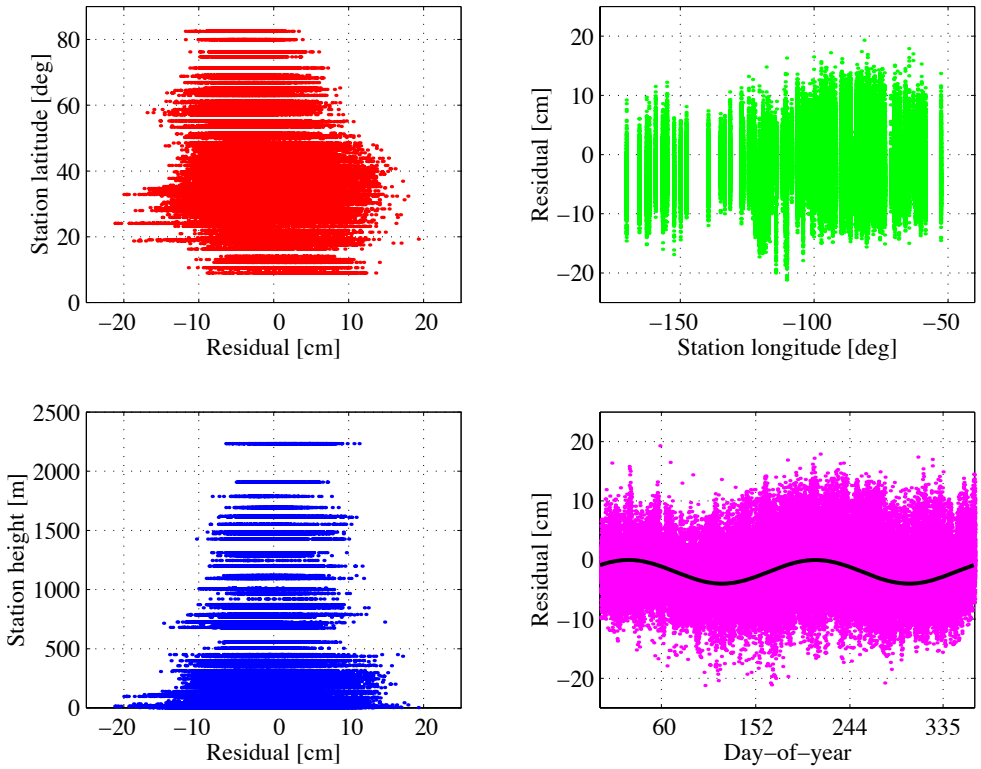

Figure 3.20. Residual scatter plots as a function of station location components and day-of-year for the 1992 data.

Ideally, and if necessary, we would like the residual error model to be some function of the same parameters that drive the UNB3 model; that is, latitude, height and day-of-year and other similar readily-available parameters such as longitude. To this end, Figure 3.20 shows the UNB3 model residuals for all of the 1992 data plotted against the latitude, longitude and height of the radiosonde stations and against the day-of-year of the radiosonde launches. It is clear that the only distinct, quasi-random, variations are in the day-of-year plot. There does appear to be an overall decrease in the magnitude of the residuals with an increase in the station height, but the trend is not as consistent as for the day-of-year, which reveals a strong semi-annual variation that can be approximated with a sine curve.

We need to consider a very important aspect about the residuals as a function of the day-of-year. The process that governs the behaviour of this time-series appears to be non-stationary. This means that some, or all, of the statistics that describe the process are time-dependent. Special considerations must be taken when computing the statistics of a non-stationary time series. The general procedure [*Bendat and Piersol*, 1986], is to hypothesise a general model that combines a non-random (deterministic) function with a stationary random process that is zero-mean Gaussian. Figure 3.20 suggests that the mean is non-stationary and the variance is stationary (i.e. constant around the sine curve), and it seems reasonable to propose the following process:

$$\{x(t)\} = y(t) + \{u(t)\}, \qquad (3.1)$$

where $x(t)$ is a sample record of the process at time t, $\{u(t)\}$ is a stationary random process and $y(t)$ is a deterministic function. The random process $\{u(t)\}$ is defined to be zero mean Gaussian, with standard deviation σ_N. This function $x(t)$ is a very simple type of non-stationary process and the mean and standard deviation of it are easy to define:

$$\begin{aligned} \bar{x}(t) &= E[\{x(t)\}] \\ &= E[y(t) + \{u(t)\}] \\ &= E[y(t)] + E[\{u(t)\}] \\ &= y(t) \end{aligned} \qquad (3.2)$$

and

$$\begin{aligned} \sigma^2(t) &= E[\{x(t)\}^2] - E[\{x(t)\}]^2 \\ &= E[y(t)^2] + E[\{u(t)\}^2] - 2 \cdot E[y(t)] \cdot E[\{u(t)\}] - \bar{x}(t)^2 \\ &= y(t)^2 + \sigma_N^2 - y(t)^2 \\ &= \sigma_N^2 \end{aligned} \qquad (3.3)$$

where $E[\cdot]$ is the statistical expectation operator. The expected value of a zero mean Gaussian process is zero, and the expected square value is the variance of the process. Consequently, for the root-mean-square (RMS) value:

$$\mathrm{RMS}(t) = \sqrt{\bar{x}(t)^2 + \sigma(t)^2} = \sqrt{y(t)^2 + \sigma_N^2} \,. \qquad (3.4)$$

Equation (3.4) is the formula required in the WAAS VPL equation. We can now attempt to define $y(t)$ and σ_N.

Because the variation of $y(t)$ appears to be much slower than the slowest variation in $\{u(t)\}$, we should be able to separate the deterministic function from the random process. From examining the plot of the residuals, a sine-curve model of the same form as the UNB3 model should be suitable, i.e.:

$$y(t) = \mu - \psi \cos\left([t - \varphi] \frac{2\pi}{\lambda} \right), \qquad (3.5)$$

where μ is a constant offset; ψ is the amplitude; φ is the phase offset from zero; and λ is the wavelength. The simple fitting technique we used is a least-squares adjustment of all the residuals from each year.

Given that the residuals from each zone of the UNB3 model display a different empirical distribution, we tried fitting equation (3.5) to the residuals of each zone separately. As Figure 3.21 shows, the constant and amplitude results vary by several centimetres from zone to zone. While most of the phase values are reasonably similar, there is an approximate half-cycle change between the 0°–15° zone and the 15°–30° zone. This is almost certainly a consequence of the UNB3 model specifying a constant value for the wet zenith delay in this zone. There is no obvious way to represent this change in a practical model; hence, we have grouped together all the yearly residuals from all the stations to compute the final model.

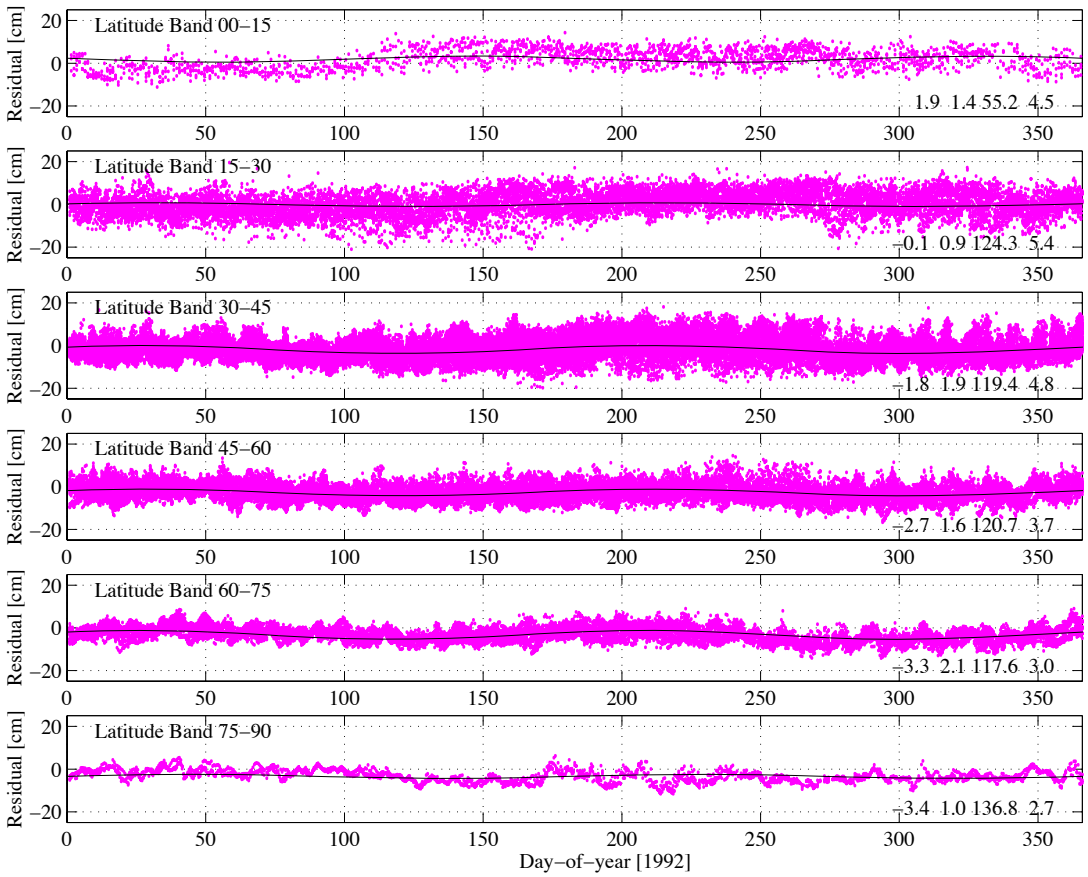

Figure 3.21. Sine-curve error model fit by latitude zones of the UNB3 model (1992 data). Values in the lower-right corner of each panel represent the results of a least squares fit of the constant (cm), amplitude (cm) and phase (doy) parameters respectively. The wavelength is fixed at 182.625 days. The fourth value is the RMS (cm) of the post-fit residuals.

The first attempt at solving for the parameters of equation (3.5) included the wavelength of the sine curve. However, the mean result turned out to be ~211 days (from a range of values between ~184 and ~229), the use of which would cause a step in the function at the end-of-year changeover because it is not a multiple of 365.25 days. Hence, a second run was performed after fixing the wavelength to 182.625 days. These results are presented in Table 3.3.

Table 3.3. Results of least-squares fit to yearly residuals.

Year	Constant (μ, cm)	Amplitude (ψ, cm)	Phase (φ, doy)	Residual RMS (cm)	No. of iterations
1987	−1.7	1.7	114.2	4.8	11
1988	−2.0	2.2	120.4	4.7	7
1989	−1.9	2.0	123.0	4.6	5
1990	−1.8	1.8	122.5	4.7	6
1991	−1.5	1.6	114.2	4.8	8
1992	−1.9	1.6	119.7	4.6	8
1993	−1.7	1.9	119.1	4.7	8
1994	−1.9	1.9	117.7	4.7	7
1995	−1.9	1.9	123.3	5.0	6
1996	−2.1	1.7	114.6	4.9	9
Mean	**−1.8**	**1.8**	**118.9**	**4.7**	7.5
S.D.	**0.2**	**0.2**	**3.6**	**0.1**	

The constant values are almost exactly equivalent to the statistical means of the residuals (cf. Table 3.1). The residual RMS values are only slightly smaller than the equivalent standard deviations, which indicates that the UNB3 errors are only weakly non-stationary. The value for the phase offset in Table 3.3 does not appear to be very meaningful at first glance, however we can arrive at an interesting result if we adjust the results algebraically. By inverting the sign of the amplitude and adjusting the phase by half a cycle, we then obtain a value of $\varphi = 27.6$, which is almost exactly equal to the phase value of 28 specified in the UNB3 model. Whether this is just a coincidence is not clear, however it seems obvious that we should use the same value. Rounding the constant and amplitude values to the centimetre level gives a final equation:

$$y(t) = -2 + 2\cos\left([t - 28]\frac{2\eth}{182.625} \right) \text{ (cm).} \qquad (3.6)$$

Given that the UNB3 model residuals are approximately normally distributed anyway, we would expect the residuals from the error model to be more closely normally distributed. As Figure 3.22 shows, this appears to be the case, although the improvement is only marginal. We are therefore justified in using the mean RMS of the residuals from Table 3.3, $\sigma_N = 5$ cm, as the standard deviation of the Gaussian process in equation (3.1).

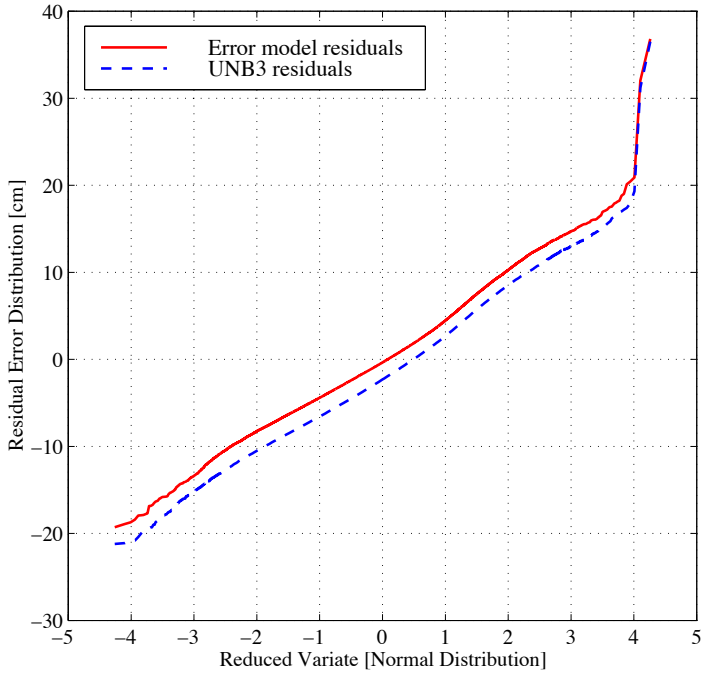

Figure 3.22. Gaussian probability plot of UNB3 and sine curve error model residuals for the 1992 data.

While using equation (3.6) would provide a rigorous approach to modelling the residual error, it is worthwhile performing a brief numerical analysis to assess its impact. Substituting a value of $2\sigma_N$ into equation (3.4), the maximum and minimum values of the RMS are 10.8 and 10.0 cm respectively. This small range is due to the dominance of the variance component in the mean square error. The range of the mean value function $y(t)$

is only [0, –4] cm and makes almost no impact on the RMS calculation (~8% at most). It is not unrealistic therefore to fall back on our previous results and merely state that the UNB3 model residuals are approximately zero-mean Gaussian with a standard deviation of 5 cm.

Investigators at Stanford University have suggested one other parameter that the error may be proportional to — that of the actual wet delay [*Bellingham*, 1998]. While we obviously do not have access to this value in real-time applications, our model value is a good approximation. We investigated the Stanford-proposed error model, which uses the square value of the model wet delay, using our previous data set of only thirteen stations (one year of profiles); the results are presented in Appendix E3. Figure 3.23 shows the corresponding results for our current 1992 data set. Surprisingly, the best-fit linear regression to this data is almost exactly equivalent to the one performed with only the thirteen stations. The regression equation for this data is:

$$\mathrm{RMS}^2 = 17.7 + \left(\frac{d_{wet}^z}{5.25} \right)^2 \mathrm{cm}^2, \qquad (3.7)$$

where d_{wet}^z (cm) is the UNB3 model value of the wet zenith delay. However, as Figure 3.23 clearly shows, the application of this type of equation cannot be recommended because it is a very poor model of the residual error.

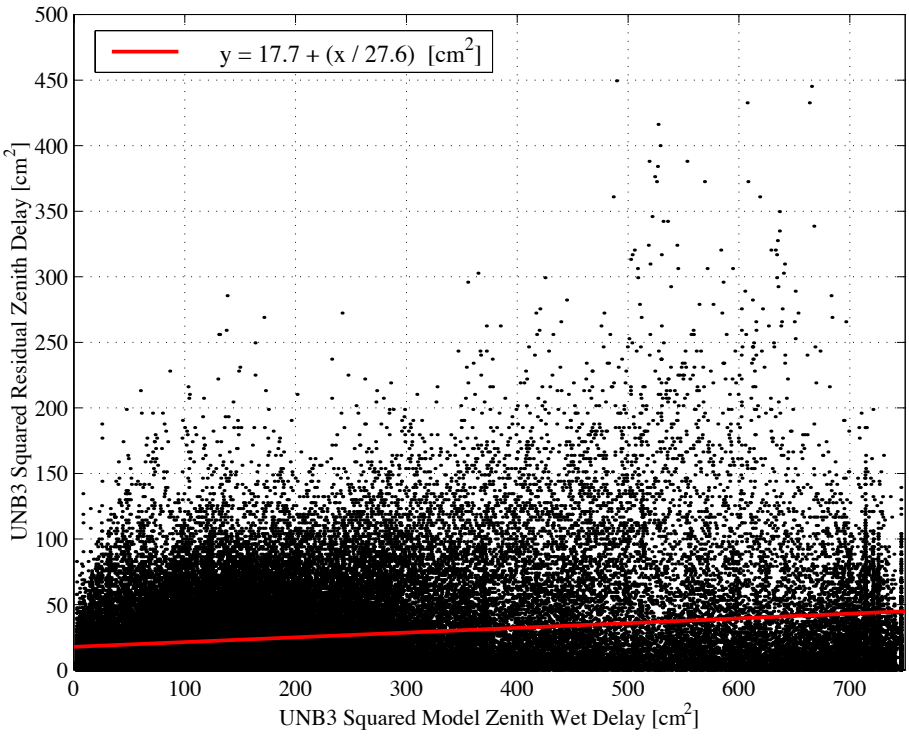

Figure 3.23. Scatter plot of the squared residual errors as a function of the squared UNB3 model wet zenith delays (1992 data).

The idea of using the model value of the delay to drive an error model is worth considering further, because it is a function of all the parameters we would like to use — the latitude, the height and the day-of-year. To this end, Figure 3.24 shows the model residuals plotted directly against the model wet zenith delays. The overall trend appears to be slightly parabolic, however, by grouping the residuals as a function of the model wet zenith delay we can compute empirical estimates of the 68% and 95% limits. As Figure 3.24 shows, these are not at all parabolic, and would be difficult to represent with a simple function.

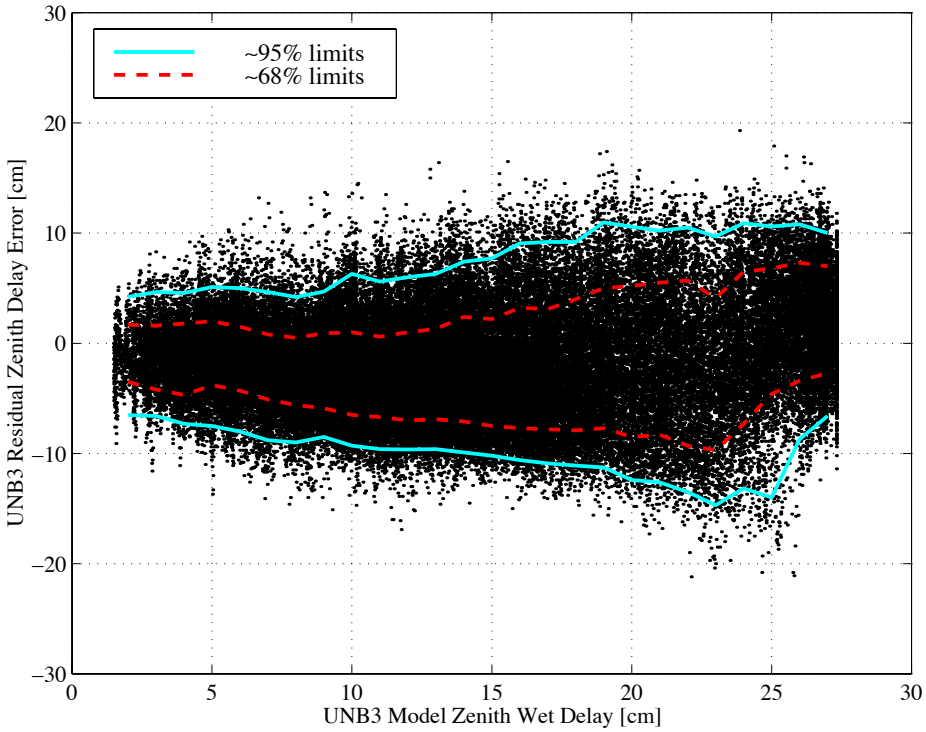

Figure 3.24. Scatter plot of residual errors as a function of the UNB3 model wet zenith delay (1992 data).

Figure 3.25 shows the empirical 68% and 95% limits computed from each of the 10 years of data. The mean values of these limits are also shown. A look-up table could be used to store the exact values of the mean limits, but for the sake of simplicity, it is also possible to represent them using an "over-bounding" equation. The negative limits are larger in magnitude than the positive limits and so were used for a linear regression through the model values from 2 cm to 23 cm, ignoring the reverse trend beyond 23 cm. The consistent pattern of the residuals beyond this point could be a function of both the model, because the "tropical" values of the wet zenith delay are constant at mean-sea-level, and the lack of a broad sample of stations from that zone.

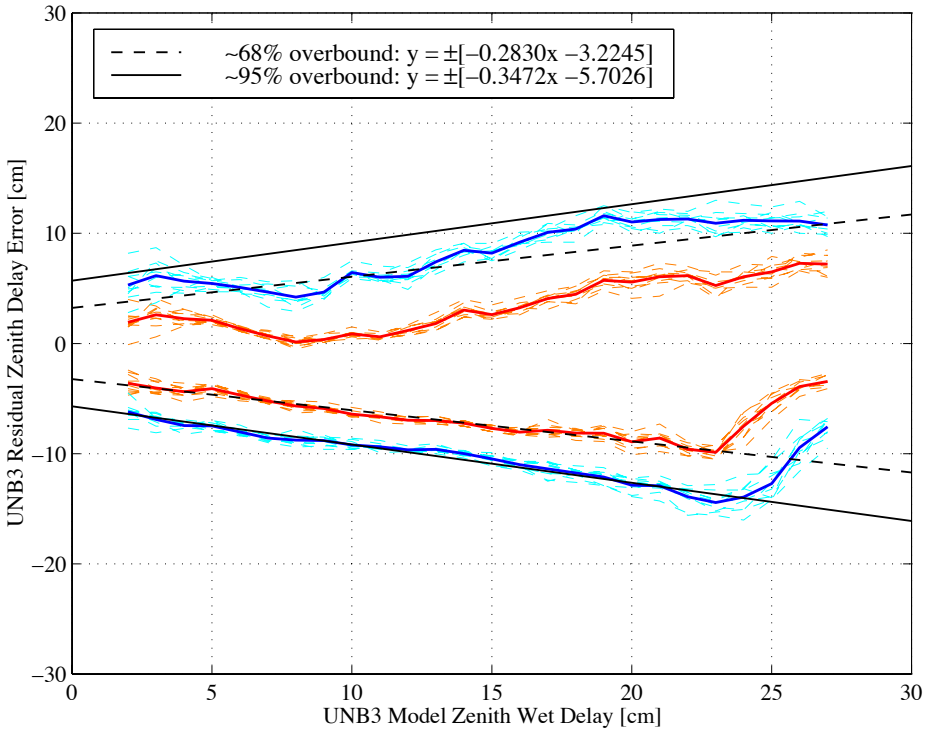

Figure 3.25. Empirical estimates of the 68% and 95% limits of all the residuals per year as a function of the UNB3 model wet zenith delay. Mean limits and "over-bounding" linear approximations are also shown.

Therefore, if a simple estimate of the UNB3 model residual error is required, the following equations are recommended:

$$\sigma_{68\%} = \pm\left[3.22 + \left(\frac{d^{z}_{wet}}{3.53}\right)\right] \text{ cm}, \qquad (3.8)$$

$$\sigma_{95\%} = \pm\left[5.70 + \left(\frac{d^{z}_{wet}}{2.88}\right)\right] \text{ cm}, \qquad (3.9)$$

where d^{z}_{wet} (cm) is the UNB3 model value of the wet zenith delay.

3.2. Model Performance Under Extreme Conditions

The results from Section 3.1 suggest that it is convenient to use a "non-extreme" range of ±20 cm for the UNB3 models. A zenith delay error equal to the cut-off values of ±20 cm could lead to a potential ±2 m bias in a computed position height (see Section 3.2.2). The numbers of residuals per year exceeding this range from the UNB3 models are given in Table 3.4. In total, there are 76 residuals from the UNB3 model that equal or exceed the ±20 cm range out of 1,011,651 profiles. This is equivalent to approximately 0.0075%. Correspondingly, 99.99249% of the residuals are within the non-extreme range.

Table 3.4. Number of residuals exceeding ±20 cm for UNB3 and UNB3(SfcMet) models.

Year	UNB3		UNB3(SfcMet)	
	−Max	+Max	−Max	+Max
1987	0	3	1	5
1988	0	8	1	19
1989	0	1	3	6
1990	0	4	0	7
1991	1	1	2	3
1992	9	2	0	5
1993	10	1	4	7
1994	8	3	9	5
1995	9	8	17	13
1996	4	4	25	10
Total	**76**		**142**	

Table 3.4 shows that the UNB3(SfcMet) model is much more susceptible to extremes than the UNB3 model (as was indicated previously in Figure 3.1). In general, the same

extremes show up for both models, however the UNB3(SfcMet) model is sensitive to measured values of surface temperature and water vapour that, when combined with the empirical profile parameter, are unrepresentative of the true water vapour profile.

It should be noted that some of the extremes experienced with UNB3(SfcMet) might be due to incorrect surface measurements. All the initially detected "extreme" profiles were checked and several were rejected as unlikely. Unfortunately, without detailed knowledge of the actual weather conditions at each station, it is not possible to be completely sure about all the remaining extremes. It is worth pointing out however, that poor instrument quality is a potentially important factor when using actual meteorological data. The impact cannot always be quantified and the errors rectified. Hence, we feel that the remaining extremes described here are representative of using actual real-time meteorological data with a tropospheric delay model.

Because wide-area differential aircraft receivers generally do not have access to real-time measurements of the atmosphere, we will again concentrate solely on the original UNB3 model using the look-up table. As Table 3.4 shows, there is no obvious gain to be made, with regard to extreme errors, in replacing a good meteorological look-up table with real-time values. The small improvement in overall bias (c.f. Table 3.1) is negligible in comparison to other potential error sources, such as multipath and the residual ionosphere.

The location of stations with extreme residuals are shown in Figure 3.26. Stations with at least one positive extreme (a residual greater than +20 cm zenith delay error) are

shown as a triangle and labelled with a station identification number to the right. Stations with at least one negative extreme (a residual magnitude greater than –20 cm zenith delay error) are shown as an inverted triangle and labelled to the left. Parenthetical numbers indicate more than one extreme over the ten-year period.

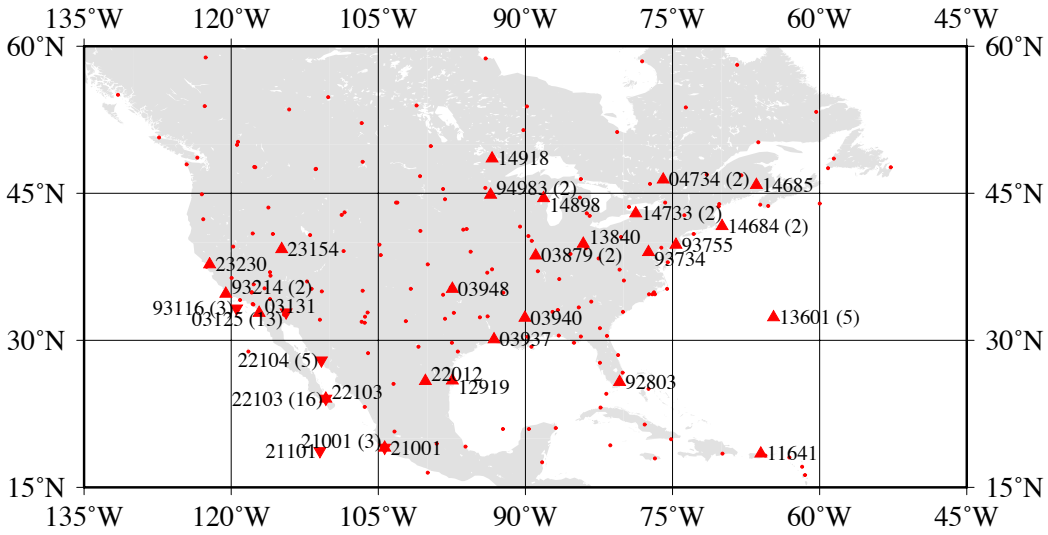

Figure 3.26. Location of radiosonde stations with "extreme" delay errors.

Figure 3.26 indicates that the negative extremes are confined to the Baja California, Sonora and Sinaloa regions of Mexico and the southern tips of California and Arizona. All of these stations are also present in Figure 3.19, indicating the correlation of the extremes with an area of poor overall performance of the model. The number and location of the positive extremes are geographically more scattered than the negative extremes, although concentrations do occur. Bermuda (station number 13601), for example, seems particularly prone to extreme conditions, a possible consequence of the weather associated with its mid-Atlantic location.

It is useful to examine a plot of the extremes versus day-of-year, especially to understand the pattern of negative extremes. Figure 3.27 shows that most of the negative extremes occur during the late spring. Examining the residual time series for stations in the west of Mexico (see Figure 3.14) indicates that the climate is dry and relatively constant through this season. Unfortunately, the UNB3 model is biased toward larger delays in this general location, and at the same time, the sinusoidal variation in the day-of-year is increasing. Hence, the error for these stations is prone to exceed the ±20 cm error limit. In contrast, the positive extremes are more confined to the summer season, although the second and third largest extremes occurred outside this period, in the winter. Unlike the majority of negative extremes, the positive extremes are outliers in the station's time series, suggesting the influence of short period, transient weather systems.

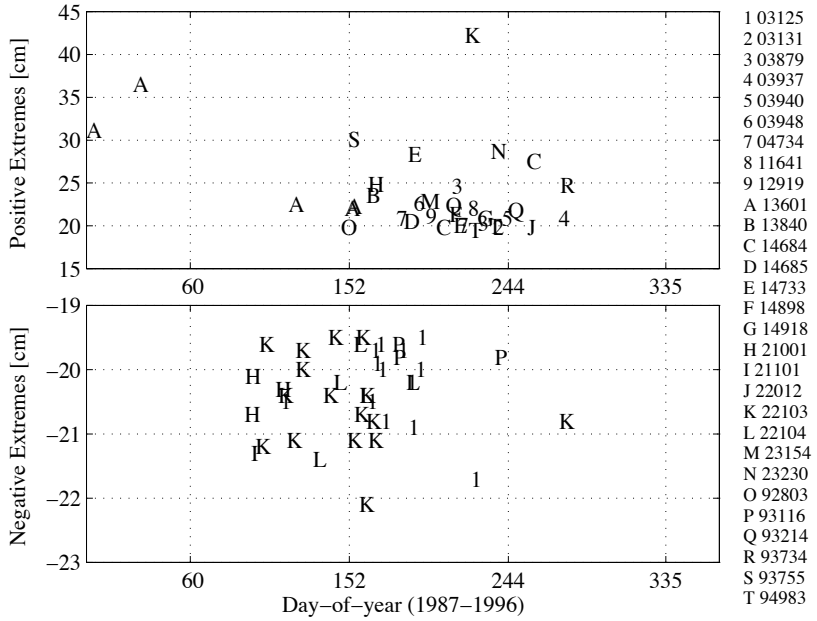

Figure 3.27. Time of extremes during yearly period. Key to the right links the character codes with the station identification numbers used in Figure 3.26.

To examine the maximum extreme residuals more closely, we have plotted the first and last ten ordered residuals (in terms of magnitude) for each year in Figure 3.28. This plot shows that the largest positive extreme varies widely from year to year, and may not exceed +20 cm by much, as in 1993 for example. This indicates the danger of using only one year's-worth of data to study extremes. The number of extremes per year also varies. The largest extreme in our data set (42 cm) occurred in 1995 at station 22103 (La Paz, Mexico) during the passage of a tropical cyclone (Hurricane Flossie). This value represents a wet zenith delay of over 70 cm, which is extremely large. We have attempted to verify the validity of both this, and the other extremes, with an independent data source. However, the availability and accessibility of data from other techniques that adequately sample the atmosphere is very limited.

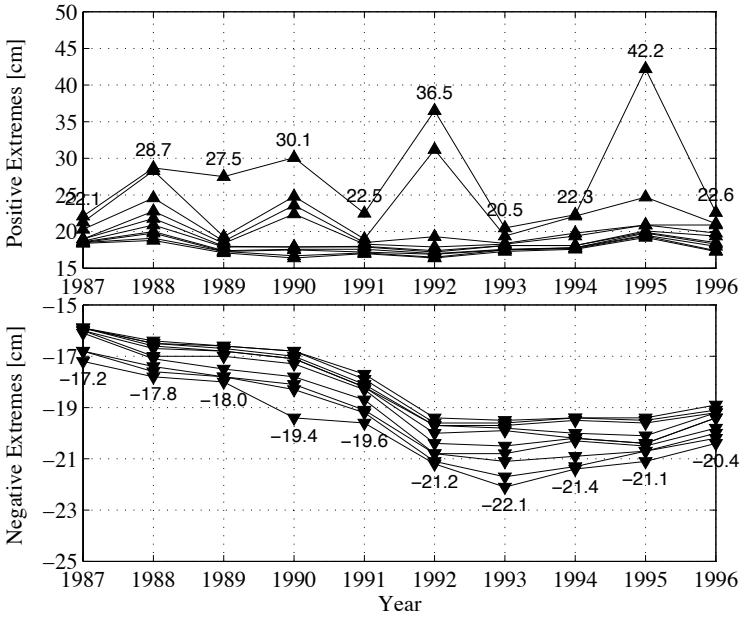

Figure 3.28. Ten largest positive and negative errors each year. The magnitude of the maximum residual in each year is labelled (in cm).

The negative extremes follow a very intriguing pattern, one that changes approximately with the total number of stations operating each year. Figure 3.26 reveals that stations 03125 (Yuma, Ariz.) and 22103 (La Paz, Mexico) contribute almost two-thirds of these residuals and it should be pointed out that neither station provided data before 1992 and 1991 respectively. It is quite possible that if data from these stations had been available for the remaining years, the pattern of the negative extremes would be quite different.

3.2.1. Extreme Value Prediction

It is possible to examine extreme residuals separately using what are known as extreme value distributions (Gumbel, Frechet and Weibull distributions). These distributions are the limiting forms that most common distributions take when only considering the largest or smallest values from a number of sample sets. It is not necessary to know the underlying distribution in order to consider the distribution of the extreme values [*Castillo*, 1988].

An extreme value probability plot has the potential to provide a lot of useful information. Figure 3.29 and Figure 3.30 show the extreme value probability plots for both the largest yearly positive and negative extremes respectively. Of the three distributions, the positive extremes fit a Frechet distribution best and the negative extremes fit a Weibull distribution best.

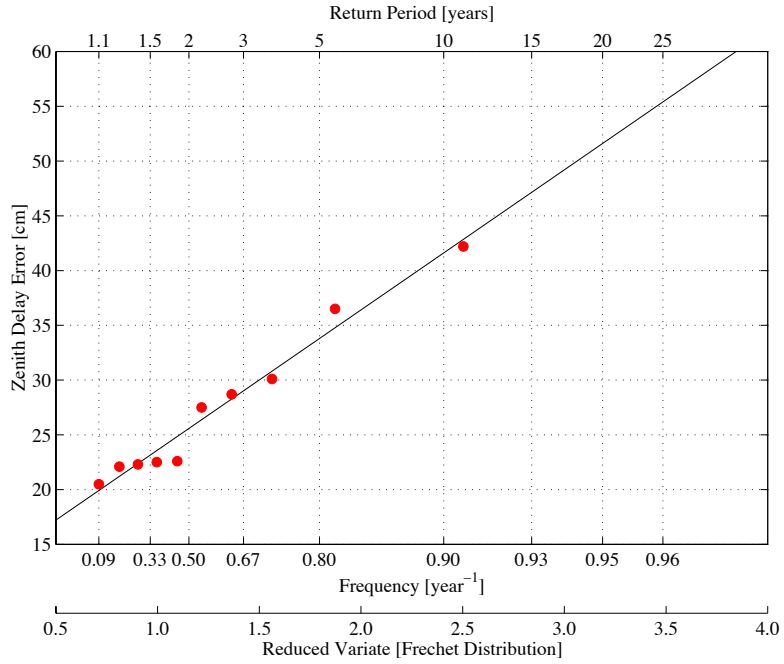

Figure 3.29. Extreme value cumulative probability plot for positive extremes.

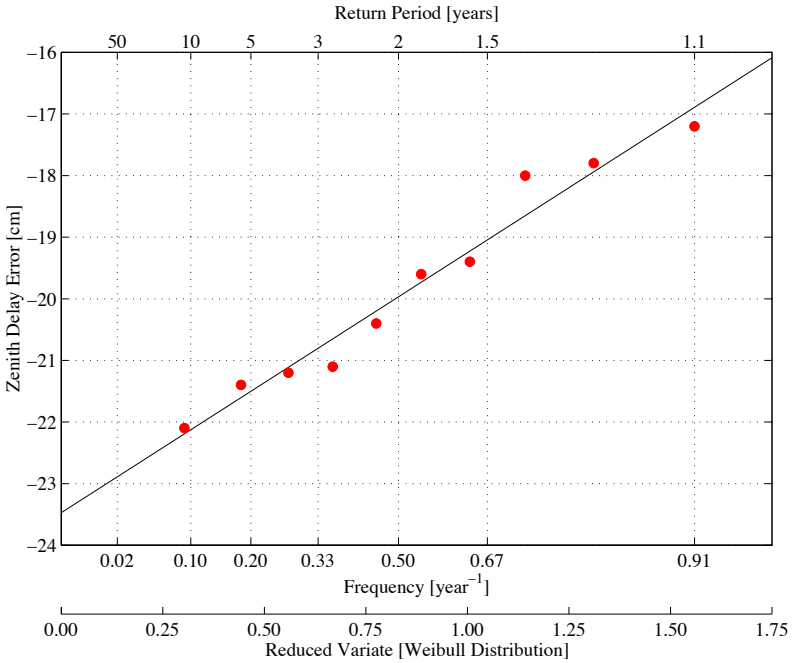

Figure 3.30. Extreme value cumulative probability plot for negative extremes.

The power in these plots lies in the ability to extrapolate and estimate the return periods of future extremes. The return period is defined as the average interval between occurrences of an event, and is merely the inverse of the expected frequency of occurrence. The probability of an event occurring at or before its return period is ~63%. By using the largest value in each year, the return periods are defined with units of years. It should be pointed out that the use of extreme value statistics usually requires a set of at least 20 samples from which to draw the extreme values. With only ten years of data in our sample, the confidence in these results is not high. However, we are able to give a good example of the application of extreme value statistics.

If the positive extremes do follow the Frechet distribution, then an average return period of 25 years is forecast for an extreme zenith delay value of at least 55 cm (with a probability of 63%). The forecast return period for an extreme zenith delay error less (i.e. greater in absolute value) than –23 cm is 50 years (with a probability of 63%). Both the Frechet and Weibull distributions are specified with threshold values. For example, the Frechet threshold is a lower limit, and for the positive extremes is approximately 11 cm, which indicates that an error at least this large will occur every year.

If we assume no error in the hydrostatic delay, the maximum wet zenith delay value of the UNB3 model (~27 cm) limits the magnitude of the negative extremes. This error would occur with a dry, or nearly dry, atmosphere in the tropics. Thus, we could specify this value as the threshold in the Weibull distribution; however, we have tried to use the data itself to identify the value. This approach appears to work because the Weibull

distribution best-fit specifies a cut-off value of −23.5 cm. The slight difference between this value and the theoretical one suggests either insufficient data, or indicates that the maximum zenith wet delay error will never be reached because some water vapour (and, therefore, a few centimetres' worth of wet zenith delay) is always present in the atmosphere.

The problem of the possible under-sampling of the negative extremes from stations Yuma and La Paz will not affect the results stated in the last paragraph. The frequency of occurrence of very large negative extremes could be larger than those estimated by our data, but the upper limit provide by the model and the nature of the atmosphere's water vapour will not change.

3.2.2. Impact On Position Determination

The impact of an unmodelled tropospheric range delay on the GPS position determination is complicated by the elevation angle dependence of the error. The value will not be constant for all the satellites in view and hence the vertical dilution of precision (VDOP) cannot be reliably used. The most rigorous way to study the impact is to undertake position simulations, replacing the GPS range with the tropospheric range delay bias. In this way, we can predict how the error is mapped into the position coordinates.

We have computed position solution biases for all the stations with extreme residuals. Broadcast ephemerides were used from 1997 to provide satellite constellations for six

hours around the time of the radiosonde launches. In theory, the extreme residuals we have seen could occur at any time of year at the stations, however to perform position simulations for each day of the year would be too time consuming. In addition, we have assumed that the tropospheric error remains constant over short periods of several hours. These are very broad assumptions, but as we shall see, it is possible to derive a general relationship between tropospheric delay error and the resulting position bias.

Two kinds of position solution simulations were performed — a regular unweighted least-squares solution and a weighted least-squares solution using the squared inverse of the mapping function to down-weight any low-elevation-angle errors. In WAAS, the unweighted least-squares method is permitted for en-route and non-precision approaches, but the weighted method must be used in the precision approach mode [*Bellingham*, 1999]. The position biases were computed every two minutes. For almost all of the position solutions, the weighted vertical biases were from one-third to two-thirds smaller than the unweighted vertical biases. In general, the weighted solution reduced the extreme vertical bias to the metre level or less. The horizontal biases for both solutions were always much smaller — at or below the decimetre level.

It was discovered that for one particular time period at one station, the satellite constellation was dominated by low-elevation-angle satellites. Over this period (approximately 10 minutes), the weighted and unweighted position solutions converged towards equivalent values (~1.5 m). This can be seen in Figure 3.31, along with the correlation between the unweighted vertical position bias and the maximum tropospheric

delay error. The residual zenith error for this station was approximately +21 cm and there is one time period where the unweighted vertical bias approaches +2 m.

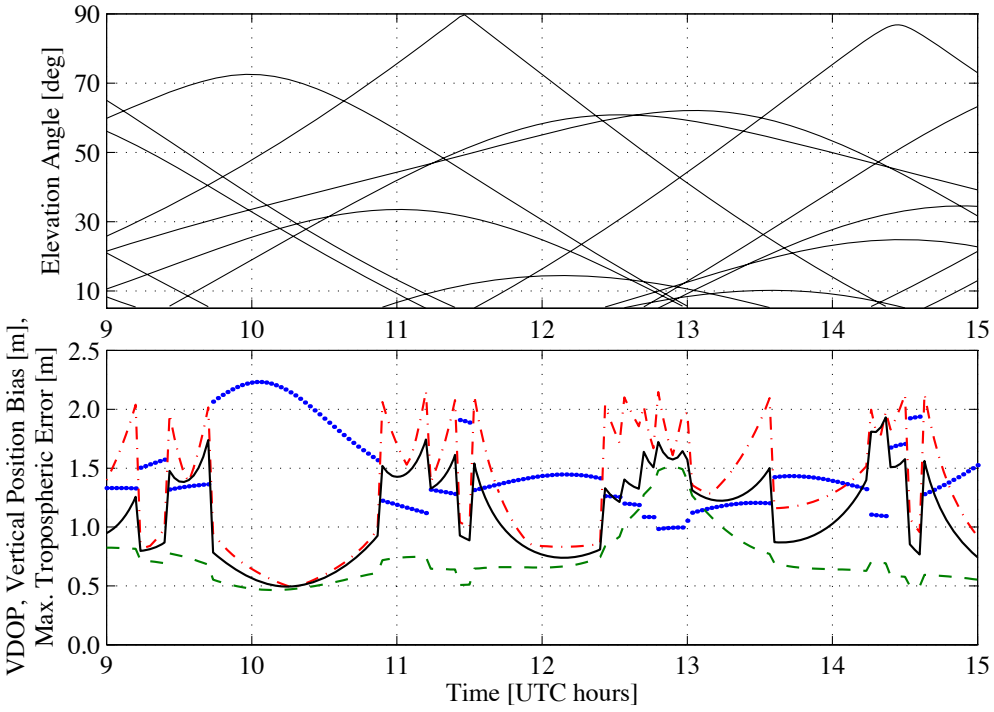

Figure 3.31. Satellite constellation and simulated vertical position biases from a zenith delay error of 21 cm at station 12919, Brownsville, Texas, July 18, 1997. Unweighted solution bias (—); weighted solution bias (– –); maximum tropospheric error (error at lowest elevation satellite) (– ·); VDOP (· · ·).

It is also clear from Figure 3.31 that the VDOP value is approximately inversely proportional to the height bias. This arises from the fact that the amount of tropospheric bias varies in proportion to the secant of the elevation angle. A good VDOP indicates a solution comprised of at least several satellites at low-elevation-angles, with a few placed closer to the zenith. Unfortunately in this configuration, the amount of tropospheric delay influencing the solution is at a maximum because of the elevation angle dependence of the error. It is in this context that weighting the observations by the

tropospheric mapping function helps reduce the impact of the low-elevation-angle satellites.

This analysis indicates that the amount of vertical position bias resulting from any unmodelled tropospheric range delay is approximately equal to the maximum residual tropospheric delay present in the solution. Because of the elevation-angle dependence of the delay, this position bias will essentially be the delay error from the lowest-elevation angle satellite. Given the expected zenith delay error, an approximate mapping function value will give the correct result. At an elevation angle of 5 degrees, the mapping function value is roughly 10. With this figure, the value of the maximum possible vertical height error can be easily calculated.

As we have discussed previously, the size of the maximum bias in the computed position will be limited in one direction because of the upper limit of the UNB3 model's wet zenith delay. A negative tropospheric bias indicates that the tropospheric delay model prediction was too large. By effectively shortening the range, the computed position will be higher than the true position. Hence, an aircraft flying below its intended height can only ever be approximately 3 m too low at most due to tropospheric delay mis-modelling. For an aircraft flying above its intended height (the situation in Figure 3.31), given an unfavourable satellite constellation and unusual weather conditions, vertical position biases of up to 3 or 4 metres are possible for wide-area differential users, due solely to mis-modelled tropospheric delays. Rare errors of at least 5 metres are predicted by the extreme value theory.

4. CONCLUSIONS AND RECOMMENDATIONS

We have studied the performance of the UNB3 tropospheric delay model against a comprehensive data set of radiosonde profiles. These profiles represent a vast range of atmospheric conditions across the North American continent over a period of ten years. The following sections present our conclusions and recommendations for future work.

4.1. Conclusions

We have confirmed that the average performance of the UNB3 model is at the several centimetre level only in the zenith direction (-1.9 ± 4.9 (1σ) cm). This level of performance is consistent from year to year. The distribution of all the model errors examined here is approximately Normal, but representing them adequately is complicated by site-specific biases and errors. Individual sites can experience mean biases on the order of ±10 cm, although the level of scatter remains generally similar everywhere. The sample standard deviation can be artificially inflated to bound, or over-bound some of the larger residuals. While this is a rather subjective method and not statistically rigorous, our results suggest that a zero-mean Normal distribution with 10 cm standard deviation ($N(0,10^2)$) would be suitable. A more comprehensive, yet relatively simple method relies on the predicted wet delay component of the total delay. An approximately linear relationship between the magnitude of the predicted wet delay and the expected error has been derived (equations 3.8 and 3.9).

Atmospheric conditions that generate "extreme" zenith errors greater than or equal to ±20 cm are very rare (<0.008% of the profiles investigated here). Positive extremes are slightly rarer and appear to occur more randomly in space and time. Negative extremes occur primarily at stations that experience relatively poor model performance rather than rare atmospheric conditions. The atmospheric conditions at these stations are only "unusual" in that they are biased from the average conditions experienced at similar latitudes and seasons. In addition, some of these stations are comparatively under-sampled compared to most of the other stations in our data set.

For example, the station that provides the second highest number of negative extremes (03125 Yuma Proving Ground) does so from a very limited data set (433 profiles from 4 years) compared to the majority of stations. If data from a full ten years of twice-daily radiosonde launches were available from this site (over 7,300 profiles), the results for the negative extremes could be significantly different. This means that, for example, the prediction of future extremes from the extreme value fit to the Weibull distribution could be unreliable. However, the maximum possible negative error remains unchanged, due to the upper limit of the predicted wet delay.

The impact of extreme atmospheric conditions on the GPS vertical position determination is reduced by the dependence on the satellite geometry. For an unweighted least-squares determination of vertical position, the error induced by any unmodelled portion of the tropospheric delay approaches the magnitude of the error experienced at the lowest elevation-angle satellite. This amount can be reduced by between one- and

two-thirds by suitable weighting schemes, as long as satellites do not congregate at the same elevation angle. In such cases the error can increase toward the unweighted-solution error.

4.2. Recommendations

The results at Yuma are symptomatic of localised atmospheric conditions that are significantly different from the average conditions at the same latitude. This means that the latitude-only dependence of the UNB3 model causes the residuals to be biased at most of the stations in Southern California, Arizona and Western Mexico. Almost all of the negative extremes experienced in these areas could be removed by improving the model performance. Such improvements would at least require the introduction of a seasonal variation to the wet delay in the 0°–15° zone of the model's look-up table. It is likely however, that some type of longitudinal-based variation would have to be introduced to make a significant difference.

Other improvements could also be applied to the whole breadth of the model's coverage so that some of the remaining station-to-station biases and variations could be reduced. Some of these variations are quite substantial, and the non-stationary nature of the residuals poses particular problems in the rigorous statistical treatment of the model errors. The goal of any improvements should be to try to attain a more consistent, zero-mean, model performance. It should be noted that due to the dominant effect of water vapour compared to the hydrostatic gases, our tropospheric delay model is, in effect, a

model of the atmospheric precipitable water content. This is an important parameter in weather forecasting and future work should consider any relevant advances in this field.

The small error due to the hydrostatic gases could be further reduced if altimeter readings of the barometric pressure could be fed into the model. This could reduce the hydrostatic component error to near zero, aside from inaccuracies due to the actual recording of the pressure value. If, at the same time, temperature measurements could also be made available, then an upper limit on the wet zenith delay could be calculated by computing a saturated, or near-saturated water vapour profile, as the aircraft descends on final approach. The provision of relative humidity measurements would allow an approximation of the true profile to be made, for the ultimate accuracy. Careful testing would be required to see if this would make a significant difference however, given the generally small impact of any residual tropospheric error on the final position computation.

REFERENCES

Bellingham, S. (1998). Personal communication. Satellite Navigation Program Office, Nav Canada, Ottawa, Ontario, 11th February.

Bellingham, S. (1999). Personal communication. Satellite Navigation Program Office, Nav Canada, Ottawa, Ontario, 2nd May.

Bendat, J.S. and A.G. Piersol (1986). *Random Data: Analysis and Measurement Procedures*. Wiley-Interscience, New York.

Black, H.D. and A. Eisner (1984). "Correcting satellite doppler data for tropospheric effects." *Journal of Geophysical Research*, Vol. 89, No. D2, pp. 2616-2626.

Castillo, E. (1988). *Extreme Value Theory in Engineering*. Academic Press, Inc., San Diego.

Collins, J.P. and R.B. Langley (1997a). *A Tropospheric Delay Model for the User of the Wide Area Augmentation System*. Final contract report prepared for Nav Canada, Department of Geodesy and Geomatics Engineering Technical Report No. 187, University of New Brunswick, Fredericton, N.B., Canada.

Collins, J.P. and R.B. Langley (1997b). "Estimating the residual tropospheric delay for airborne differential GPS positioning." *Proceedings of ION GPS-97*, Kansas City, Missouri, September 16-19, pp. 1197-1206.

Coster, A.J., A.E. Niell, F.S. Solheim, V.B. Mendes, P.C. Toor, K.P. Buchmann and C.A. Upham (1996). "Measurements of precipitable water vapor by GPS, radiosondes and a microwave water vapor radiometer." *Proceedings of ION GPS-96*, Kansas City, Missouri, September 17-20, pp. 625-634.

Coster, A.J, M.M. Pratt, B.P. Burke and P.N. Misra (1998). "Characterization of atmospheric propagation errors for DGPS." *Proceedings of the ION 54th Annual Meeting*, Denver, Colorado, June 1-3, pp. 327-336.

Dubin, M., N. Sissenwine and S. Teweles (1966). *U.S. Standard Atmosphere Supp–lements, 1966*. U.S. Committee on Extension to the Standard Atmosphere. U.S. Government Printing Office, Washington, DC.

Fleming, E.L., S. Chandra, M.R. Schoeberl and J.J. Barnet, (1988). *Monthly Mean Global Climatology of Temperature, Wind, Geopotential Height and Pressure for 0-120 km*. NASA TM-100697, Goddard Space Flight Center, Greenbelt, Maryland, U.S.A.

Junkins, J.L., G.W. Miller and J.R. Jancaitis (1973). "A weighting function approach to modeling of irregular surfaces." *Journal of Geophysical Research*, Vol. 78, No. 11, pp. 1794-1803.

Mendes, V.B. and R.B. Langley (1998). "Tropospheric zenith delay prediction accuracy for airborne GPS high-precision positioning." *Proceedings of the ION 54th Annual Meeting*, Denver, Colorado, June 1-3, pp. 337-348.

Misra, P., B.P. Burke and M.M Pratt (1999). "GPS performance in navigation." *Proceedings of the IEEE*, Vol. 87, No.1, pp. 65-85.

Niell, A.E. (1996). "Global mapping functions for the atmosphere delay at radio wavelengths." *Journal of Geophysical Research*, Vol. 101, No. B2, pp. 3227-3246.

APPENDIX A.

STATION INFORMATION AND LOCATIONS

The following table lists all the stations that provided data processed for this report. It is based on a meta-data file provided with the CD-ROM's and hence some of the country and state abbreviations are non-standard. The exceptions are the US state abbreviations, and the majority of the Canadian provinces. A full table of country abbreviations, as well as Canadian provinces and Mexican states are listed separately after the main table. Maps showing the locations of all the stations are also presented.

Table A.1. Station identification codes, coordinates, name and location.

FAA[1]	WBAN[2]	WMO[3]	Lat. [deg]	Lon. [deg]	Hgt. [m]	Station Name	State/Province	Country[4]
NPC	01003	78730	14.05	83.57	20	Puerto Cabezas		NK
EPZ	03020	72364	31.90	106.70	1257	Santa Teresa	NM	US
1Y7	03125	72280	32.87	114.33	131	Yuma Proving Ground	AZ	US
SAN	03131	72290	32.82	117.13	124	San Diego/Montgomery	CA	US
UCC	03133	72385	36.95	116.05	1195	Yucca Flat	NV	US
999	03145	99999	32.58	114.62	65	Yuma	AZ	US
DRA	03160	72387	36.62	116.02	1007	Desert Rock/Mercury	NV	US
BYS	03182	74611	35.28	116.62	716	Bicycle Lake	CA	US
NKX	03190	72293	32.87	117.15	147	San Diego/Miramar	CA	US
EDW	03197	72381	34.90	117.92	724	Edwards AFB	CA	US
REV	03198	72489	39.57	119.80	1516	Reno	NV	US
PAH	03816	72435	37.07	88.77	126	Paducah	KY	US
HTS	03860	72425	38.37	82.55	246	Huntington	WV	US
SLO	03879	72433	38.65	88.97	175	Salem	IL	US
CKL	03881	72229	32.90	87.25	140	Centerville	AL	US
LCH	03937	72240	30.12	93.22	5	Lake Charles	LA	US
JAN	03940	72235	32.32	90.07	91	Jackson	MS	US
UMN	03946	72349	36.88	93.90	438	Monett	MO	US
OUN	03948	72357	35.23	97.47	362	Norman	OK	US
GGG	03951	72247	32.35	94.65	124	Longview	TX	US
1M1	03952	72340	34.83	92.27	172	North Little Rock	AR	US
FTD	03990	72249	32.80	97.30	196	Fort Worth	TX	US

cont....

TFX	04102	72776	47.45	111.38	1130	Great Falls	MT	US
LKN	04105	72582	40.87	115.73	1608	Elko	NV	US
OTX	04106	72786	47.68	117.63	728	Spokane International Apt.	WA	US
YMW	04734	71722	46.38	75.97	170	Maniwaki	QB	CN
DTX	04830	72632	42.70	83.47	329	Detroit/Pontiac	MI	US
ILX	04833	74560	40.15	89.33	178	Lincoln	IL	US
APX	04837	72634	44.55	84.43	448	Gaylord/Alpena	MI	US
BLB	10701	78806	8.98	79.60	66	Balboa (Albrook AFB)		PN
ROL	10809	78762	9.98	84.22	920	San José		CR
BDI	11501	78954	13.07	59.50	47	Seawell		BA
CGU	11621	78967	10.68	61.62	2	Trinidad/Chaguaramas		TR
SDQ	11629	78486	18.47	69.88	14	Santo Domingo		DR
JNR	11630	78535	18.25	65.55	12	Roosevelt Roads	PR	US
KPP	11634	78970	10.58	61.35	12	Trinidad/Piarco		TR
JSJ	11641	78526	18.43	66.00	3	San Juan	PR	US
FFR	11642	78897	16.27	61.52	8	Pointe-à-Pitre		GU
ACC	11643	78988	12.20	68.97	54	Curaçao		NA
ACM	11645	78866	18.05	63.12	3	Saint Martin		AN
KPA	11647	78861	17.12	61.78	4	Saint John (Coolidge AFB)		AN
UGM	11706	78367	19.90	75.15	6	Guantánamo		CU
KJP	11715	78397	17.93	76.78	1	Kingston		JA
KCR	11813	78384	19.30	81.37	3	Grand Cayman		CI
KSP	11814	80001	12.58	81.72	1	San Andres Island		CL
HTG	11817	78720	14.03	87.23	1014	Tegucigalapa		HO
ZBZ	11818	78583	17.53	88.30	5	Belize City		BE
GUA	11901	78641	14.53	90.57	1496	Guatemala City		GU
MEX	11903	76679	19.43	99.07	2234	Mexico City		MX
VER	11904	76692	19.17	96.12	13	Veracruz	VR	MX
999	11906	76805	16.50	99.93	3	Acapulco	GR	MX
CUN	11907	76595	21.03	86.92	10	Cancun	QR	MX
CMW	12711	78355	21.42	77.87	122	Camagüey		CU
YNN	12717	78073	25.05	77.47	2	Nassau		BM
AQQ	12832	72220	29.73	85.03	7	Apalachicola	FL	US
EYW	12836	72201	24.55	81.75	1	Key West	FL	US
TBW	12842	72210	27.70	82.40	13	Tampa Bay	FL	US
PBI	12844	72203	26.68	80.12	6	West Palm Beach	FL	US
HAV	12864	78325	23.15	82.35	49	Havana		CU
XMR	12868	74794	28.48	80.55	5	Cape Kennedy	FL	US
MID	12878	76644	20.95	89.65	11	Mérida	YC	MX
BVE	12884	72232	29.33	89.40	1	Boothville	LA	US
VCT	12912	72255	28.85	96.92	33	Victoria	TX	US
BRO	12919	72250	25.90	97.43	7	Brownsville	TX	US
CRP	12924	72251	29.77	97.50	14	Corpus Christi	TX	US
XKF	13601	78016	32.37	64.68	25	Bermuda		BU
999	13701	74002	39.47	76.17	18	Aberdeen Proving Ground	MD	US
GSO	13723	72317	36.08	79.95	277	Greensboro	NC	US

cont.…

NKT	13754	72309	34.90	76.88	11	Cherry Point	NC	US
DAY	13840	72429	39.87	84.12	298	Dayton	OH	US
999	13841	72426	39.42	83.82	317	Wilmington	OH	US
VPS	13858	72221	30.52	86.58	20	Valparaiso (Elgin AFB)	FL	US
AYS	13861	72213	31.25	82.40	44	Waycross	GA	US
AHN	13873	72311	33.95	83.32	246	Athens	GA	US
CHS	13880	72208	32.90	80.03	15	Charleston	SC	US
JAX	13889	72206	30.43	81.70	10	Jacksonville	FL	US
BNA	13897	72327	36.25	86.57	180	Nashville	TN	US
SEP	13901	72260	32.22	98.18	399	Stephenville	TX	US
FSI	13945	72355	34.65	98.40	369	Fort Sill AFB	OK	US
SHV	13957	72248	32.45	93.83	84	Shreveport	LA	US
OKC	13967	72353	35.40	97.60	392	Oklahoma City	OK	US
DDC	13985	72451	37.77	99.97	791	Dodge City	KS	US
SGF	13995	72440	37.23	93.40	394	Springfield	MO	US
TOP	13996	72456	39.07	95.62	268	Topeka	KS	US
YJT	14503	71815	48.53	58.55	60	Stephenville (Harmon AFB)	NF	CN
WZB	14526	71197	47.57	59.17	40	Port-Aux-Basques	NF	CN
YYT	14531	71801	47.67	52.75	140	Torbay/St. John's	NF	CN
CAR	14607	72712	46.87	68.02	191	Caribou	ME	US
YSA	14642	71600	43.93	60.02	4	Sable Island	NS	CN
CHH	14684	74494	41.67	69.97	16	Chatham	MA	US
YCX	14685	71701	45.83	66.43	52	Gagetown	NB	CN
WOS	14693	71399	43.72	65.25	30	Shelbourne	NS	CN
GTB	14715	74370	44.05	75.73	214	Ft. Drum (Wheeler Sack AFB)	NY	US
BUF	14733	72528	42.93	78.73	218	Buffalo	NY	US
ALB	14735	72518	42.75	73.80	86	Albany	NY	US
PWM	14764	72606	43.65	70.32	20	Portland	ME	US
FNT	14826	72637	42.97	83.73	236	Flint/Bishop	MI	US
PIA	14842	72532	40.67	89.68	200	Peoria	IL	US
Y62	14847	72734	46.47	84.37	221	Sault Ste. Marie	MI	US
GRB	14898	72645	44.48	88.13	210	Green Bay	WI	US
INL	14918	72747	48.57	93.38	359	International Falls	MN	US
STC	14926	72655	45.55	94.08	315	Saint Cloud/Whitney	MN	US
ABR	14929	72659	45.45	98.42	397	Aberdeen	SD	US
HON	14936	72654	44.38	98.22	392	Huron	SD	US
YYR	15601	71816	53.30	60.37	36	Goose Bay	NF	CN
YZV	15636	71811	50.22	66.27	52	Sept-Îles	QB	CN
YVP	15641	71906	58.10	68.42	60	Kuujjuaq	QB	CN
YPH	15704	71907	58.45	78.12	7	Inukjuak	QB	CN
YAH	15708	71823	53.75	73.67	307	La Grande IV	QB	CN
YMO	15803	71836	51.27	80.65	10	Moosonee	ON	CN
YTL	15806	71848	53.83	89.87	222	Trout Lake	ON	CN
YYQ	15901	71913	58.75	94.07	29	Churchill	MB	CN
WPL	15907	71845	51.47	90.20	373	Pickle Lake	ON	CN
IKF	16201	4018	63.97	22.60	50	Keflavík		IL

cont.…

YFB	16603	71909	63.75	68.53	21	Frobisher Bay	NW	CN
YVN	16607	71909	63.75	68.55	21	Iqaluit	NW	CN
YZS	16801	71915	64.20	83.37	57	Coral Harbour	NW	CN
YUX	16895	71081	68.78	81.25	7	Hall Beach/Hall Lake	NW	CN
YBK	16910	71926	64.30	96.00	49	Baker Lake	NW	CN
YRB	17901	71924	74.72	94.98	40	Resolute	NW	CN
YLT	18601	71082	82.50	62.33	66	Alert	NW	CN
YEU	18801	71917	79.98	85.93	10	Eureka	NW	CN
999	21001	76654	19.07	104.33	3	Manzanillo	CL	MX
999	21002	76642	20.97	92.32	2	Triangulos Reefs		MX
SIC	21101	76723	18.72	110.95	34	Socorro Island	CL	MX
ITO	21504	91285	19.72	155.07	10	Hilo	HI	US
999	21603	91275	16.73	169.52	3	Johnston Island		US
MCV	22007	76225	28.70	106.07	1428	Chihuahua	CH	MX
MZT	22009	76458	23.18	106.42	4	Mazatlán	SI	MX
DRT	22010	72261	29.37	100.92	313	Del Rio	TX	US
MTY	22012	76394	25.87	100.20	450	Monterrey	NL	MX
999	22013	76612	20.68	103.33	1551	Guadalajara	JL	MX
TRC	22014	76382	25.53	103.45	1150	Torreón	CO	MX
LAP	22103	76405	24.07	110.33	14	La Paz	BS	MX
GYM	22104	76256	27.95	110.80	12	Empalme	SO	MX
IGP	22105	76151	28.87	118.25	23	Guadalupe Island	BN	MX
YEV	22258	71957	68.32	133.53	103	Inuvik	NW	CN
BKH	22501	91162	22.03	159.78	5	Barking Sands	HI	US
HNG	22519	91176	21.45	157.78	3	Kaneohe Bay	HI	US
LIH	22536	91165	21.98	159.35	36	Lihue/Kauai	HI	US
MDY	22701	91066	28.22	177.35	3	Midway Island		US
HMN	23002	74732	32.85	106.08	1246	Alamogordo (Holloman AFB)	NM	US
MAF	23023	72265	31.93	102.20	873	Midland	TX	US
999	23039	72269	32.40	106.35	1216	White Sands/Las Cruces	NM	US
ELP	23044	72270	31.80	106.40	1199	El Paso	TX	US
AMA	23047	72363	35.23	101.70	1095	Amarillo	TX	US
ABQ	23050	72365	35.05	106.62	1619	Albuquerque	NM	US
DEN	23062	72469	39.77	104.88	1611	Denver	CO	US
GJT	23066	72476	39.12	108.53	1472	Grand Junction	CO	US
999	23110	74702	36.33	119.97	73	Lamoore/Reeves	CA	US
EDW	23114	72381	34.92	117.90	725	Muroc (Edwards AFB)	CA	US
ELY	23154	72486	39.28	114.85	1908	Ely	NV	US
TUS	23160	72274	32.12	110.93	788	Tuscon	AZ	US
INW	23194	72374	35.02	110.73	1487	Winslow	AZ	US
OAK	23230	72493	37.75	122.22	6	Oakland	CA	US
BIS	24011	72764	46.77	100.75	503	Bismarck	ND	US
LND	24021	72576	42.82	108.73	1695	Lander	WY	US
LBF	24023	72562	41.13	100.68	847	North Platte	NE	US
RIW	24061	72672	43.06	108.47	1688	Riverton	WY	US
RAP	24090	72662	44.05	103.07	966	Rapid City	SD	US

cont….

SLC	24127	72572	40.77	111.97	1288	Salt Lake City	UT	US
WMC	24128	72583	40.90	117.80	1312	Winnemucca	NV	US
BOI	24131	72681	43.57	116.22	871	Boise	ID	US
GTF	24143	72775	47.48	111.35	1118	Great Falls	MT	US
GEG	24157	72785	47.63	117.53	720	Spokane	WA	US
MFR	24225	72597	42.37	122.87	397	Medford	OR	US
SLE	24232	72694	44.92	123.02	61	Salem	OR	US
YQD	25004	71867	53.97	101.10	273	The Pas	MB	CN
YXE	25021	71866	52.16	106.68	504	Saskatoon	SK	CN
WSE	25145	71119	53.55	114.10	766	Edmonton	AB	CN
YVR	25152	71115	50.23	119.28	556	Vernon	BC	CN
WIQ	25154	71124	54.80	110.08	703	Primrose Lake	AB	CN
YXS	25206	71896	53.88	122.68	675	Prince George	BC	CN
YZT	25223	71109	50.68	127.37	17	Port Hardy	BC	CN
YYE	25262	71945	58.83	122.60	377	Fort Nelson	BC	CN
ANN	25308	70398	55.03	131.57	37	Annette Island	AK	US
YAK	25339	70361	59.52	139.67	10	Yakutat	AK	US
ADQ	25501	70350	57.75	152.48	4	Kodiak	AK	US
AKN	25503	70326	58.68	156.65	15	King Salmon	AK	US
CDB	25624	70316	55.20	162.72	30	Cold Bay	AK	US
ADK	25704	70454	51.88	176.65	5	Adak (Davis AFB)	AK	US
SNP	25713	70308	57.15	170.22	10	St. Paul Island	AK	US
YCB	26005	71925	69.10	105.12	25	Cambridge Bay	NW	CN
YSM	26118	71934	60.03	111.95	203	Fort Smith	NW	CN
YVQ	26214	71043	65.28	126.75	95	Norman Wells	NW	CN
YXY	26316	71964	60.72	135.07	704	Whitehorse	YK	CN
ANC	26409	70273	61.17	150.02	45	Anchorage	AK	US
FAI	26411	70261	64.82	147.87	135	Fairbanks	AK	US
MCG	26510	70231	62.97	155.62	103	Mcgrath	AK	US
BET	26615	70219	60.78	161.80	36	Bethel	AK	US
OTZ	26616	70133	66.87	162.63	5	Kotzebue	AK	US
OME	26617	70200	64.50	165.43	5	Nome	AK	US
YMD	27101	71072	76.23	119.33	58	Mould Bay	NW	CN
BTI	27401	70086	70.13	143.63	15	Barter Island	AK	US
BRW	27502	70026	71.30	156.78	12	Point Barrow	AK	US
SYA	45715	70414	52.72	-174.10	37	Shemya	AK	US
FLG	53103	72376	35.23	111.82	2179	Flagstaff	AZ	US
SIL	53813	72233	30.33	89.82	8	Slidell	LA	US
MDN	53814	74468	38.80	85.40	266	Jefferson Proving Ground	IN	US
FFC	53819	72215	33.35	84.56	246	Peachtree City	GA	US
BMX	53823	72230	33.10	86.70	178	Birmingham	AL	US
RNK	53829	72318	37.20	80.41	648	Roanoke/Blacksburg	VA	US
YWA	54706	71625	45.95	77.32	130	Petawawa	ON	CN
YOY	54724	71716	46.90	71.50	178	Valcartier	QB	CN
GYX	54762	74389	43.89	70.25	125	Gray	ME	US
MFL	92803	72202	25.75	80.38	4	Miami	FL	US

cont….

NZJ	93101	69014	33.66	117.73	116	El Toro	CA	US
NID	93104	74612	35.68	117.68	681	Inyokern/China Lake	CA	US
NTD	93111	72391	34.10	119.12	2	Point Mugu	CA	US
NTK	93114	99999	33.68	117.80	197	Tustin	CA	US
NSI	93116	72291	33.25	119.45	174	San Nicolas Island	CA	US
999	93121	99999	34.22	116.05	538	Twentynine Palms	CA	US
VBG	93214	72393	34.75	120.57	100	Vandenberg (North)	CA	US
HGT	93218	69002	36.00	112.23	317	Jolon/Hunter Liggett	CA	US
999	93222	74504	37.50	122.50	43	Pillar Point	CA	US
VBG	93223	74606	34.67	120.58	112	Vandenberg (South)	CA	US
NCA	93727	72309	34.70	77.38	5	New River	NC	US
HAT	93729	72304	35.27	75.55	4	Cape Hatteras	NC	US
IAD	93734	72403	38.98	77.47	85	Sterling (Wash. Dulles)	VA	US
WAL	93739	72402	37.93	75.48	13	Wallops Island	VA	US
NJM	93743	72309	34.68	77.03	7	Bogue Field	NC	US
ACY	93755	72407	39.75	74.67	23	Atlantic City	NJ	US
MHX	93768	72305	34.70	76.80	11	Morehead City/Newport	NC	US
TLH	93805	72214	30.38	84.37	25	Tallahasee	FL	US
GGW	94008	72768	48.20	106.62	693	Glasgow	MT	US
FCS	94018	72468	38.70	104.77	1788	Fort Carson	CO	US
UNR	94043	72662	44.07	103.21	1037	Rapid City	SD	US
YLW	94151	71203	49.97	119.38	430	Kelowna	BC	CN
UIL	94240	72797	47.95	124.55	56	Quillayute	WA	US
WQI	94620	71603	43.87	66.05	9	Yarmouth	NS	CN
OKX	94703	72501	40.87	72.87	20	Brookhaven	NY	US
PIT	94823	72520	40.53	80.23	360	Pittsburgh	PA	US
OVN	94918	72553	41.37	96.02	400	North Omaha	NE	US
YLO	94921	71853	49.82	99.65	382	Shilo	MB	CN
OAX	94980	72558	41.32	96.37	350	Omaha/Valley	NE	US
DVN	94982	74455	41.60	90.57	229	Davenport	IA	US
MPX	94983	72649	44.83	93.55	287	Minneapolis	MN	US
YYJ	99992	71200	48.65	123.43	19	Victoria	BC	CN
WTO	99997	71638	43.58	79.47	187	Toronto	ON	CN
HSC	99998	78718	14.38	87.62	626	Soto Cano		HO

[1]Three-letter codes allocated by the Federal Aviation Administration (FAA) and National Weather Service (NWS) for identification purposes. Not unique.
[2]Five-digit Weather Bureau, Army and Navy (WBAN) numbers allocated by the National Climatic Data Center (NCDC)
[3]Five-digit numbers allocated by the World Meteorological Organisation (WMO) for identification purposes.
[4]See Table A.2, *et seq*.

Table A.2. Country abbreviations.

Country	Abbreviation
Anguilla	AN
Barbados	BA
Belize	BE
Bahamas	BM
Bermuda	BU
Canada	CN
Cayman Islands	CI
Colombia	CO
Costa Rica	CR
Cuba	CU
Dominican Republic	DR
Guatemala	GA
Guadeloupe	GU
Honduras	HO
Iceland	IL
Jamaica	JA
Mexico	MX
Netherlands Antilles	NA
Nicaragua	NK
Panama	PN
Trinidad and Tobago	TR
United States of America	US

Table A.3. Canadian provinces and abbreviations.

Canadian Provinces	Abbreviation
Alberta	AB
British Columbia	BC
Manitoba	MB
New Brunswick	NB
Newfoundland	NF
Northwest Territories	NW
Nova Scotia	NS
Ontario	ON
Quebec	QB
Saskatchewan	SK
Yukon	YK

Table A.4. Mexican provinces and abbreviations.

Mexican Provinces	Abbreviation
Baja California	BN
Baja California Sur	BS
Chihuahua	CH
Coahuila	CO
Colima	CL
Guerrero	GR
Jalisco	JL
Nuevo León	NL
Quintana Roo	QR
Sinaloa	SI
Sonora	SO
Veracruz	VR
Yucatán	YC

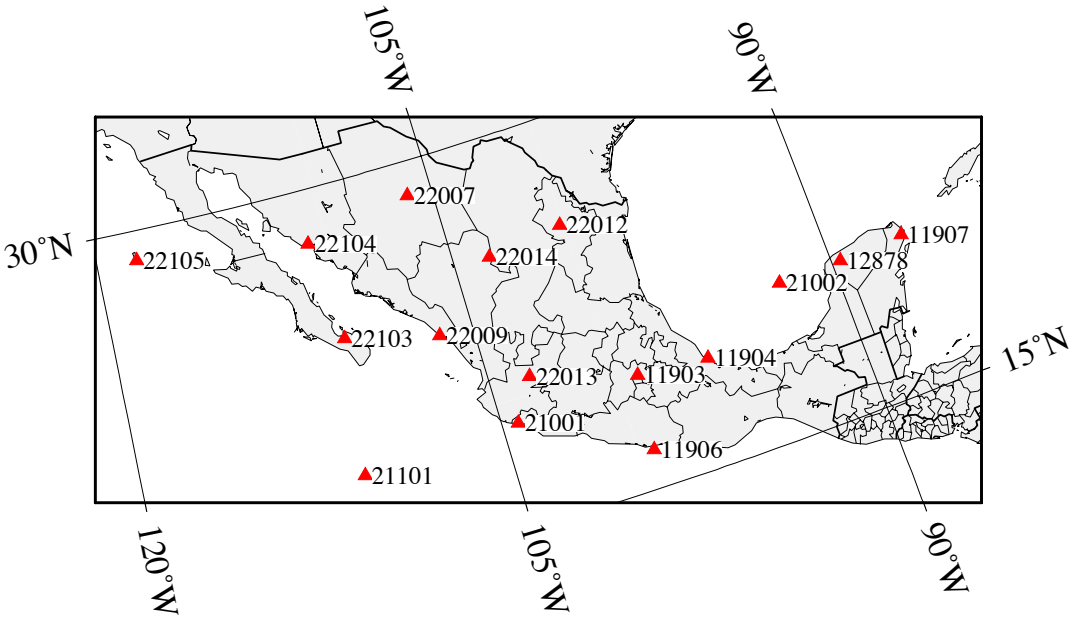

Figure A.1. Distribution of radiosonde stations in Mexico.
(Oblique Mercator projection.)

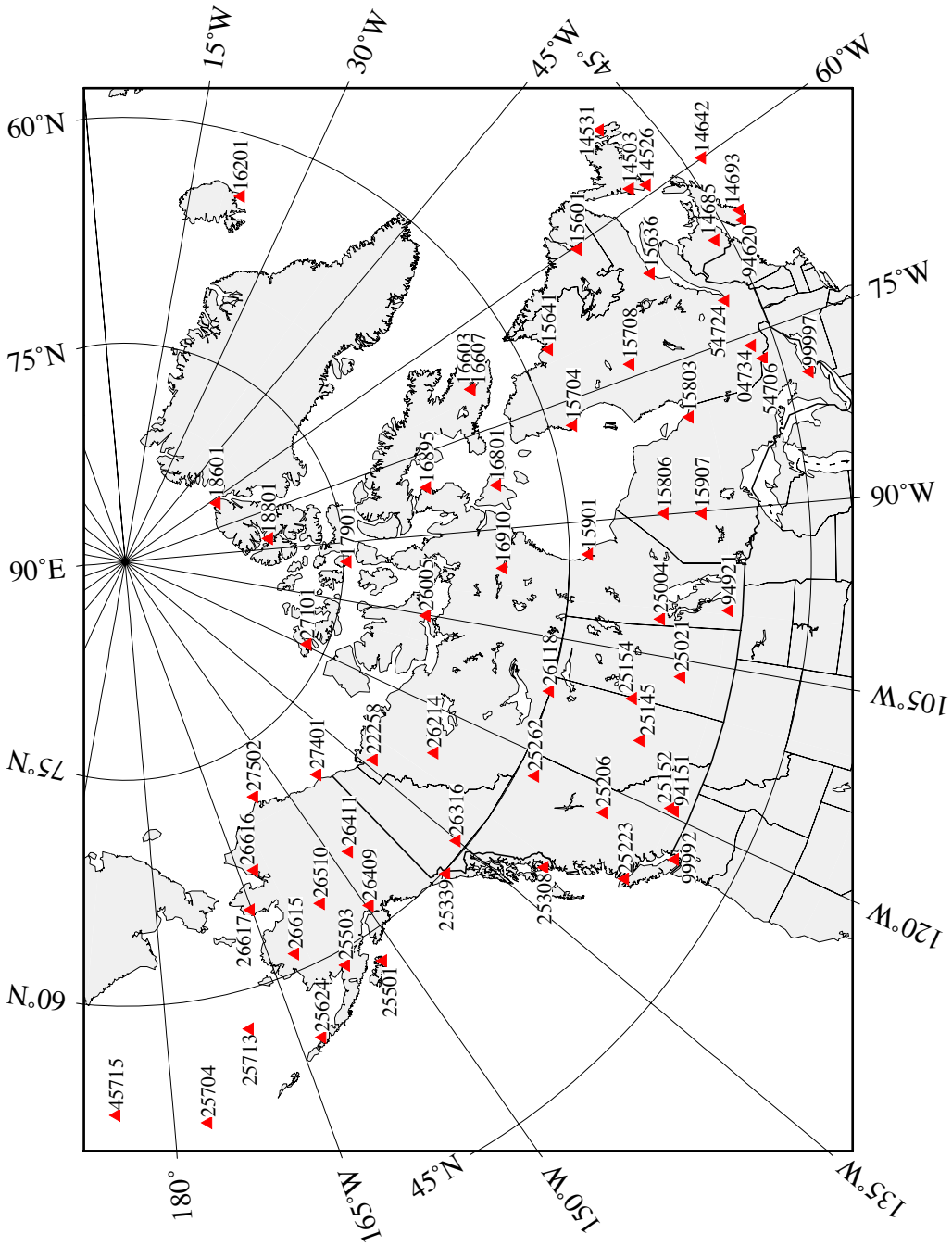

Figure A.2. Distribution of radiosonde stations in Canada, Alaska and Iceland.
(Stereographic equal-angle projection.)

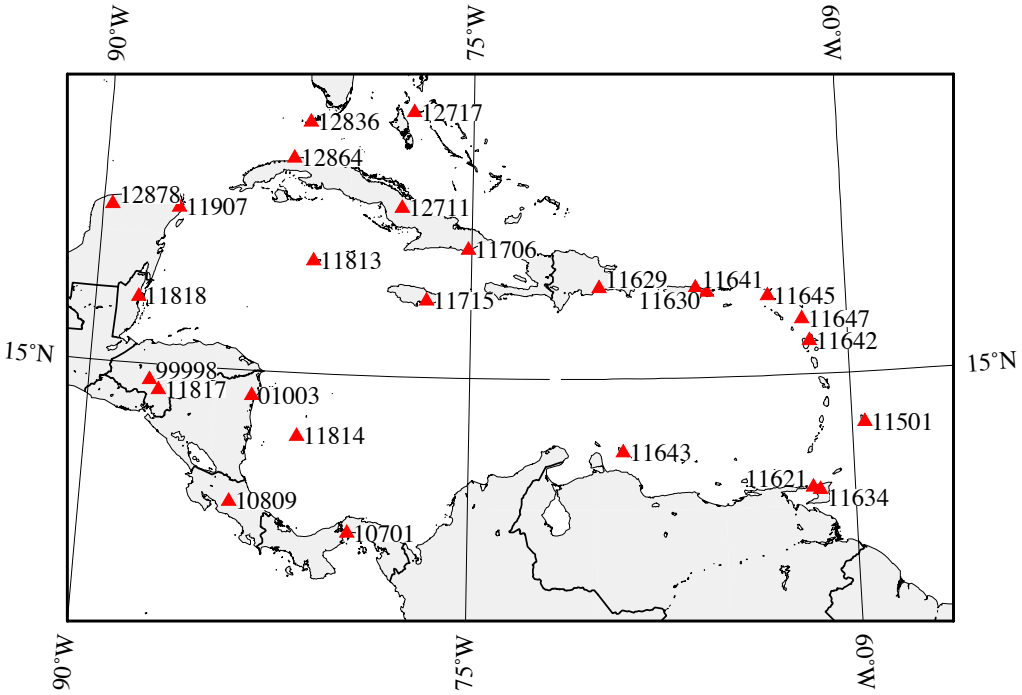

Figure A.3. Distribution of radiosonde stations in the Caribbean and Central America.
(Oblique Mercator projection.)

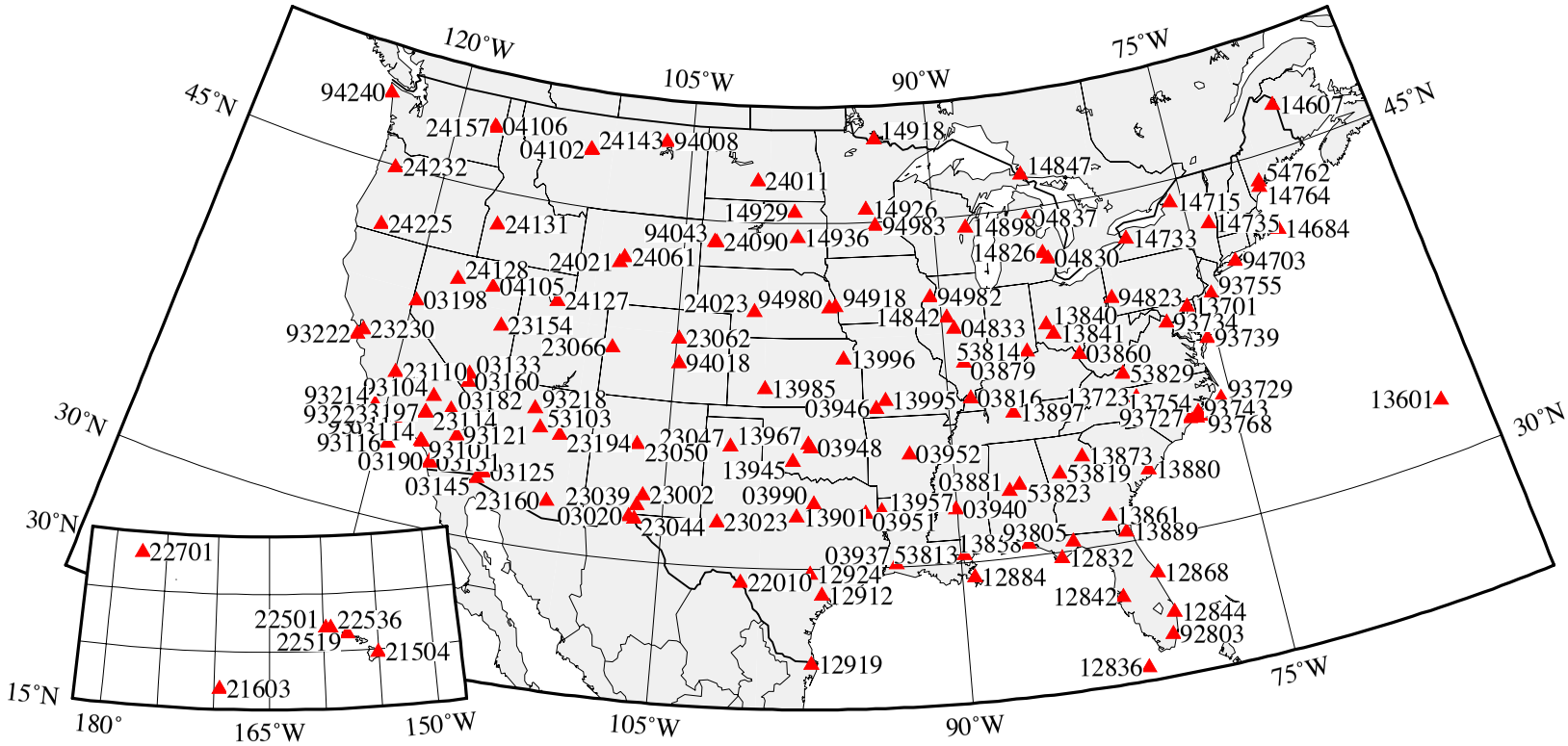

Figure A.4. Distribution of radiosonde stations in the contiguous United States, Hawaii and Bermuda.
(Lambert conic conformal projection.)

APPENDIX B.

QUALITY CONTROL OF RADIOSONDE DATA

The quality control of radiosonde data is a very heuristic procedure, but a necessary one due to the potential existence of erroneous measurements. The measurements of the three fundamental variables of pressure, temperature and relative humidity can be susceptible to two kinds of errors: biases and outliers. The FSL data sets have already been subjected to extensive quality control tests, however we found several measurement outliers that gave significantly biased values for the ray-traced zenith delays.

Pressure measurements are extremely accurate, generally to the sub-millibar level at low altitudes, although the FSL data set only provides values rounded to the nearest millibar. Temperature and humidity measurements are susceptible to errors due to inherent instrumental limitations [*Elliot and Gaffen*, 1991; *Larsen et al.*, 1993; *Nash*, 1993; *Gaffen*, 1994]. One fundamental problem is the inability of most older humidity sensors to work properly in conditions of less than 20% relative humidity [*Wade*, 1994]. In most cases, it appears that these measurements have been removed from the FSL data set, although some remain in data from Canadian and Mexican stations. Fortunately, the potential impact of an error on the wet zenith delay at the 20% relative humidity level is small. Table B.1 shows the calculated delay for two thick layers of the atmosphere experiencing constant humidity and temperature conditions. Errors greater than a few centimetres only occur at high temperatures, not during the cold, dry, conditions usually associated with the problem.

Table B.1. Wet zenith delay (cm) for constant 20% relative humidity, isothermal conditions in atmospheric layers of depth 1- and 2-km.

T (C)	e (mbar)	1 km	2 km
–30	0.1	~0.0	0.1
0	1.2	0.6	1.2
30	8.5	3.5	7.0

An additional problem can also occur in very saturated conditions when the sensors do not properly record the humidity above 90% [*Wade and Schwartz*, 1993]. Again, the impact on the wet zenith delay for even thick layers of the atmosphere is comparatively small (see Table B.2). Both these tables show that we must ray-trace through a very thick atmospheric layer before errors in the relative humidity would significantly impact the wet delay determination. The conditions described by these two tables are highly unusual, and the validity of any layer exhibiting these conditions would have to be considered in the context of the remaining portion of the profile.

Table B.2. Wet zenith delay difference (cm) between 90% and 100% relative humidity, for isothermal conditions in atmospheric layers of depth 1- and 2-km.

T (C)	Δrh (%)	1 km	2 km
–30	10	~0.0	0.1
0	10	0.3	0.6
30	10	1.8	3.5

Despite the generally recognised problems with radiosonde data, very few comprehensive and explicit directions for quality control procedures appear in the literature. Such procedures appear to be undertaken on an individual basis (see e.g.,

Serreze et al., [1995]). For our data set, the quality control procedures were derived heuristically, based on a broad understanding of the instrumental problems and the physics of the atmosphere, combined with a general feel for the quality of the data. Hence, for each radiosonde sounding:

- The surface values of pressure, temperature and water vapour partial pressure were compared to a moving average of the six previous values to determine any outliers. Extreme values outside a specified range around the moving average were replaced with the moving average value.

- Dew-point temperatures (T_d) outside the acceptable range ($\equiv [0, 100]\%$ relative humidity) were replaced with interpolated values. The interpolation variable used was the dew-point depression ($T–T_d$), to avoid problems when interpolating over temperature inversions.

- Individual lines were rejected if:

  - The total pressure was missing (did not in fact occur), increased with height or was repeated;

  - Temperature differences with respect to the CIRA profile above 15 km exceeded 25 degrees;

  - Two consecutive temperature gradients, with opposing sign, both exceeded the dry adiabatic lapse rate (previous sounding was removed);

- A temperature gradient greater than the autoconvective lapse rate (≈35°C/km) was encountered. This was modified to three times this value in the first 1 km above the surface, because it seemed to preclude an unacceptably large number of soundings.

- A specific humidity value greater than 0.01 g/kg occurred above the 500 mbar pressure level (often due to incorrect temperature readings).

- Soundings were rejected outright for any of the following reasons:

  - Any of the profile header lines were missing;

  - The surface height was drastically inconsistent with the recorded pressure;

  - No water vapour measurements were made in the first 2 km above the surface;

  - More than 25% of lines had bad temperature readings;

  - Less than 50% of the remaining lines below 500 mbar had water vapour readings (would generally preclude successful interpolation);

  - More than 90% of the sounding was wholly saturated;

  - There were less than 8 lines in total (approximately equal to the number of mandatory reporting levels below 100 mbar);

  - If water vapour measurements did not reach 550 mbar and the extrapolated water vapour profile represented more than 20% of the total;

- If a very thick layer (>4km) contributed more than 30 cm of wet delay.

Water vapour measurements were extended beyond the last recorded value by computing the so-called "lambda" value to represent the average water vapour decrease with height. Water vapour "measurements" were then computed using this parameter normalised by the last recorded relative humidity value. This ensured that relative humidity did not increase with height.

References:

Elliot, W.P. and D.J. Gaffen (1991). "On the utility of radiosonde humidity archives for climate studies." *Bulletin American Meteorological Society*, Vol. 72, No. 10, pp. 1507-1520.

Gaffen, D.J. (1994). "Temporal inhomogeneities in radiosonde temperature records." *Journal of Geophysical Research*, Vol. 99, No. D2, pp. 3667-3676.

Larsen, J.C., E.W. Chiou, W.P. Chu, M.P. McCormick, L.R. McMaster, S. Oltmans and D. Rind (1993). "A comparison of the Stratospheric Aerosol and Gas Experiment II tropospheric water vapor to radiosonde measurements." *Journal of Geophysical Research*, Vol. 98, No. D3, pp. 4897-4917.

Nash, J. (1993). "Characteristic errors in radiosonde temperature observations identified in the WMO radiosonde comparisons." *Proceedings of the Eighth Symposium on Meteorological Observations and Instrumentation*, American Meteorological Society, Anaheim, Calif., 17-22 January, pp. 98-103.

Serreze, M.C., R.G. Barry and J.E. Walsh (1995). "Atmospheric water vapour characteristics at 70ºN." *Journal of Climate*, Vol. 8, April, pp. 719-731.

Wade, C.G. and B. Schwartz (1993). "Radiosonde humidity observations near saturation." *Proceedings of the Eighth Symposium on Meteorological Observations and Instrumentation*, American Meteorological Society, Anaheim, Calif., 17-22 January, pp. 44-49.

Wade, C.G. (1994). "An evaluation of problems affecting the measurement of low relative humidity on the United States radiosonde." *Journal of Atmospheric and Oceanic Technology*, Vol. 11, June, pp. 687-700.

APPENDIX C.

UNB3 MODEL RESIDUAL HISTOGRAMS

These diagrams represent the UNB3 model zenith delay residual errors grouped into 10 cm bins, on a station-by-station basis for the whole ten-year data set. The frequency percentage is explicitly labelled at the top of each bar, principally for the easy identification of extreme errors. The approximate, annually equivalent, amount of data (assuming twice-daily balloon launches) and the percentage seasonal contribution are shown in the key to each histogram.

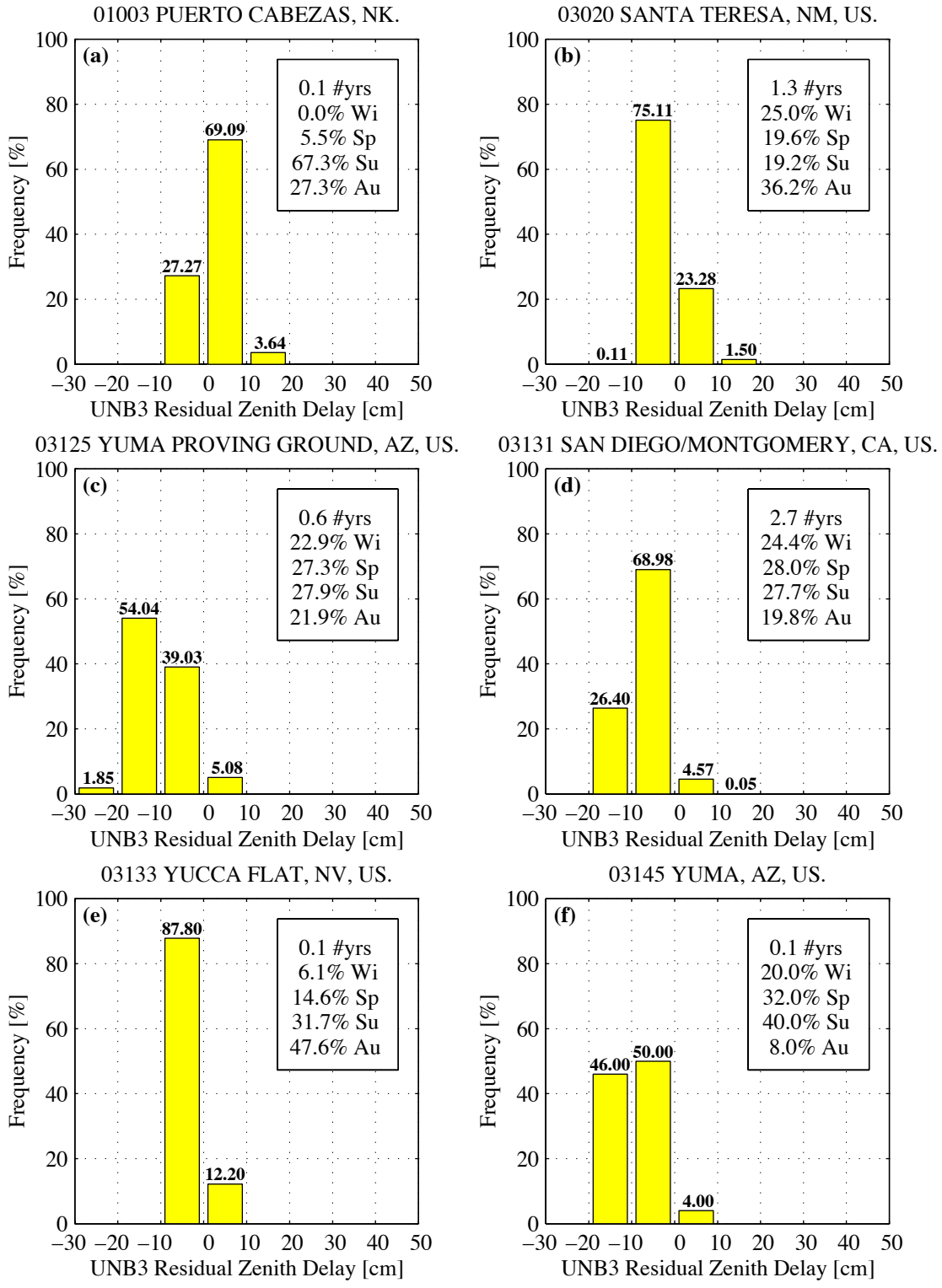

Figure C.1a–f. UNB3 model error histograms for stations 01003, 03020, 03125, 03131, 03133, and 03145.

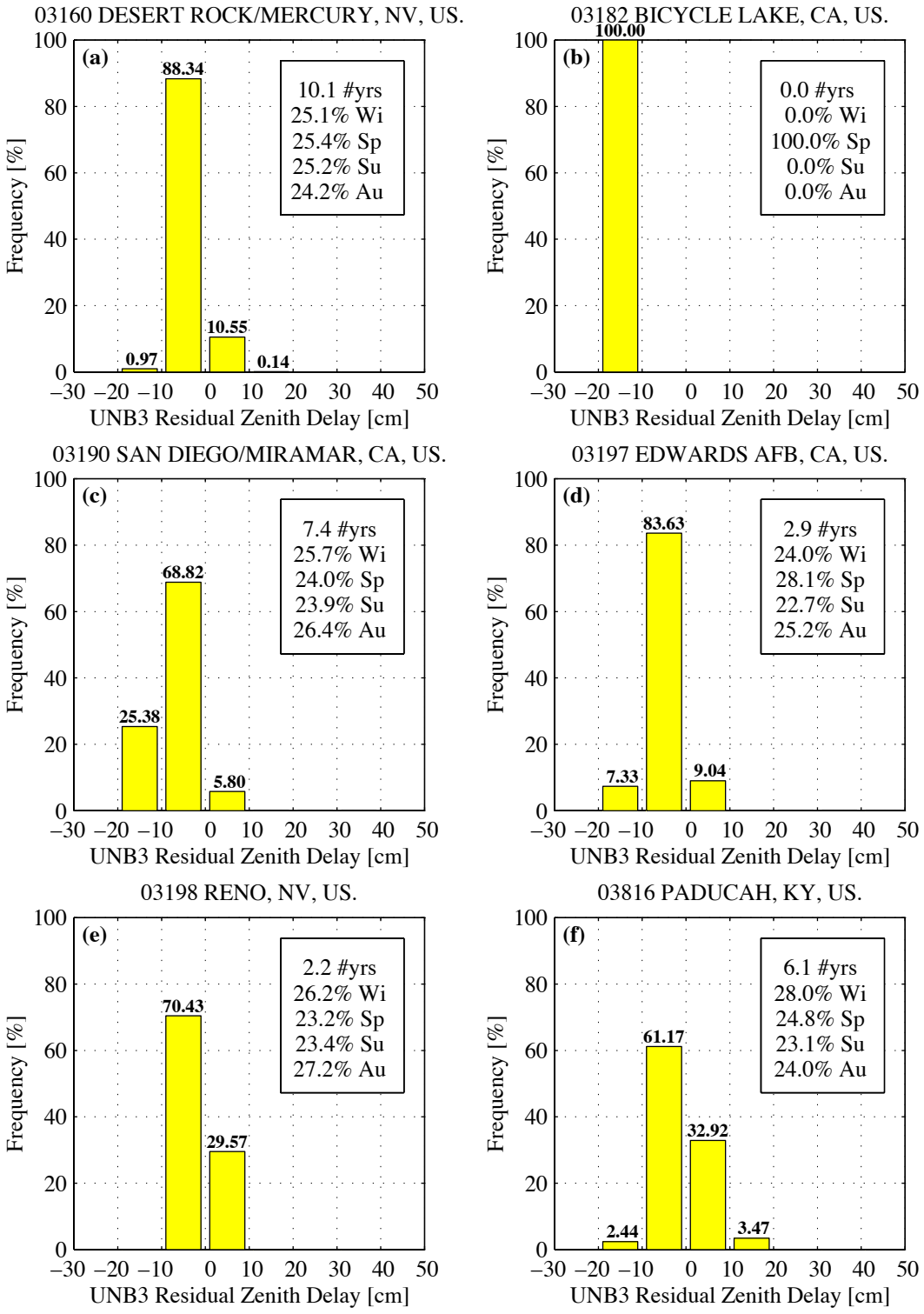

Figure C.2a–f. UNB3 model error histograms for stations 03160, 03182, 03190, 03197, 03198, and 03816.

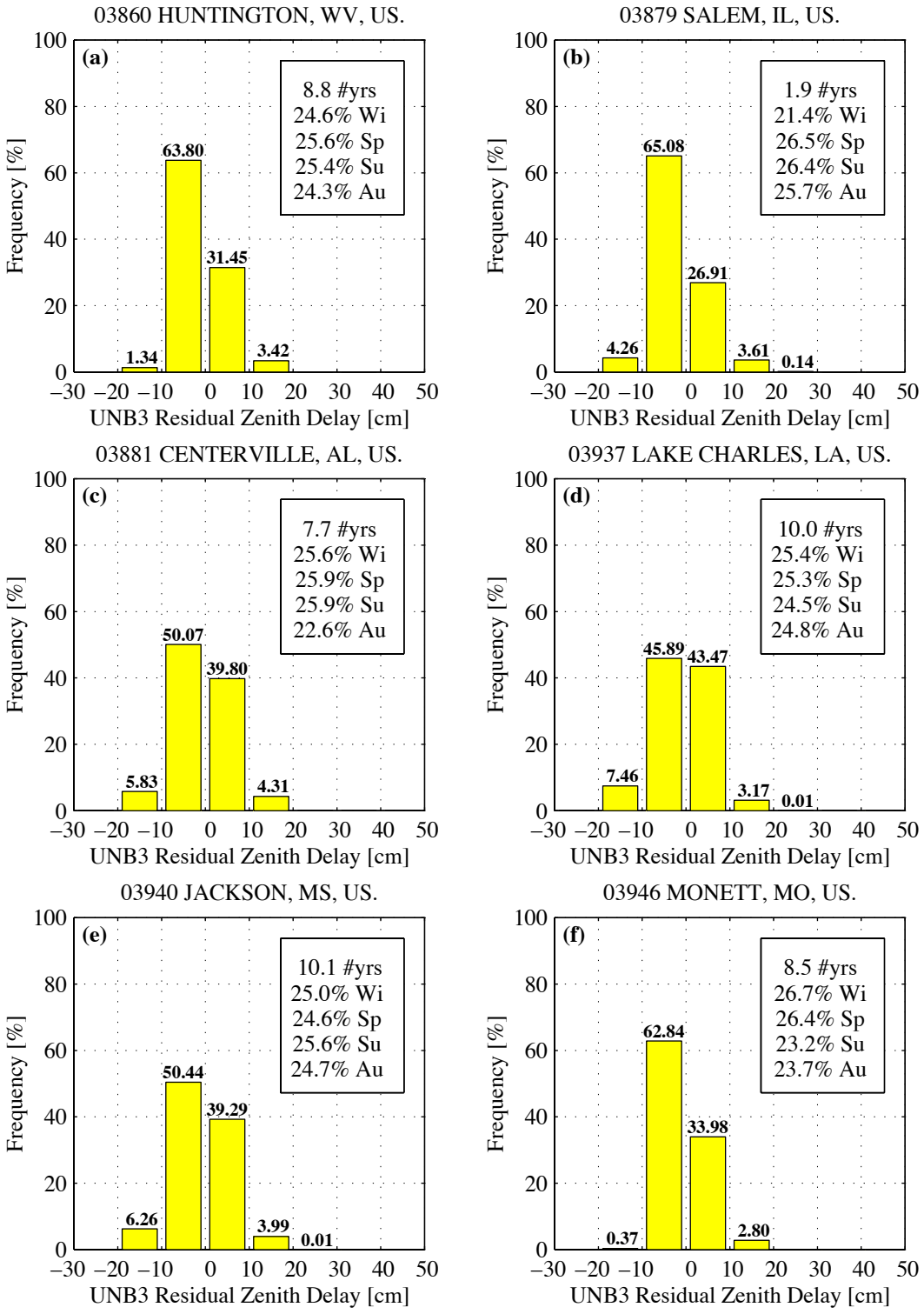

Figure C.3a–f. UNB3 model error histograms for stations 03860, 03879, 03881, 03937, 03940, and 03946.

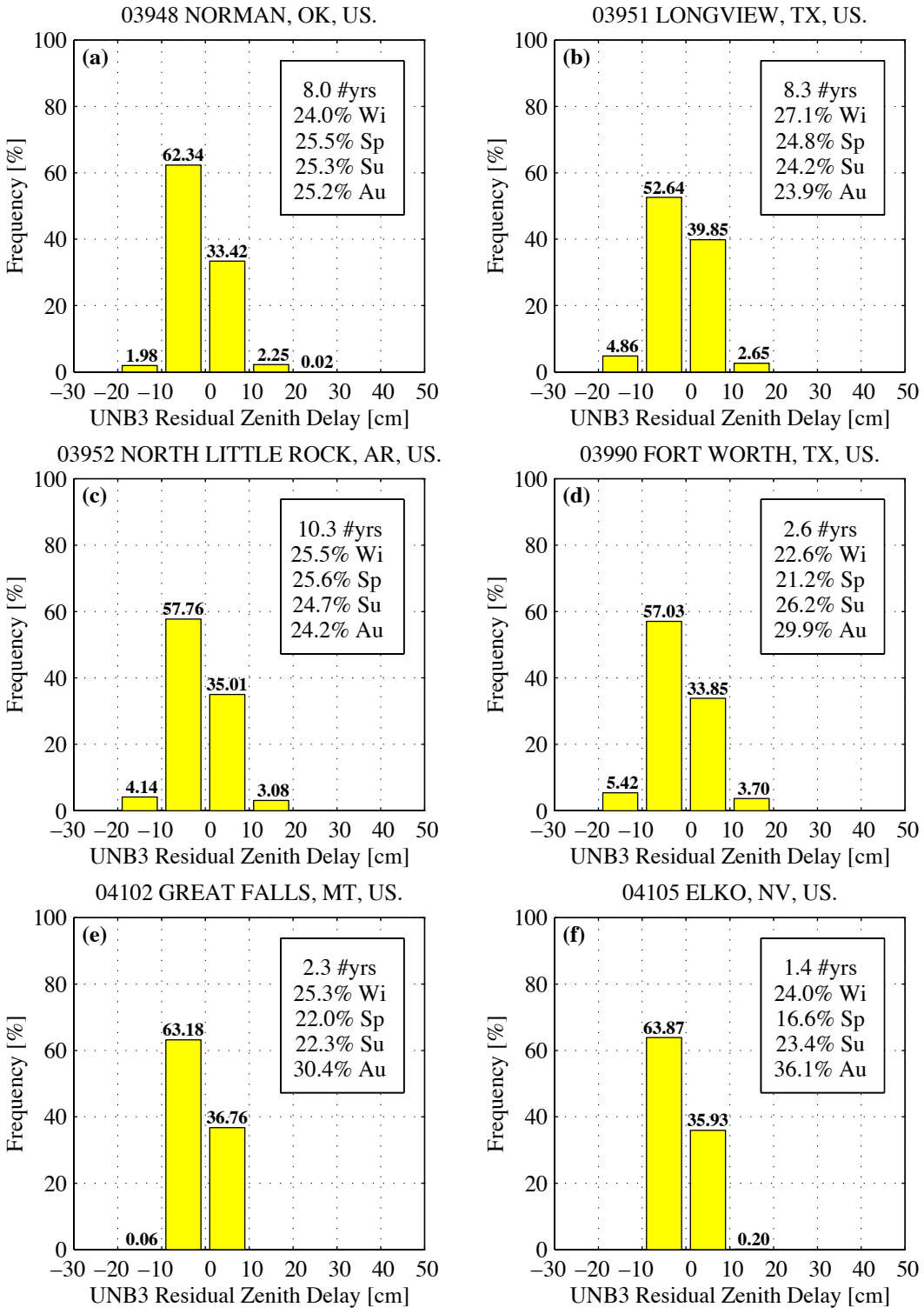

Figure C.4a–f. UNB3 model error histograms for stations 03948, 03951, 03952, 03990, 04102, and 04105.

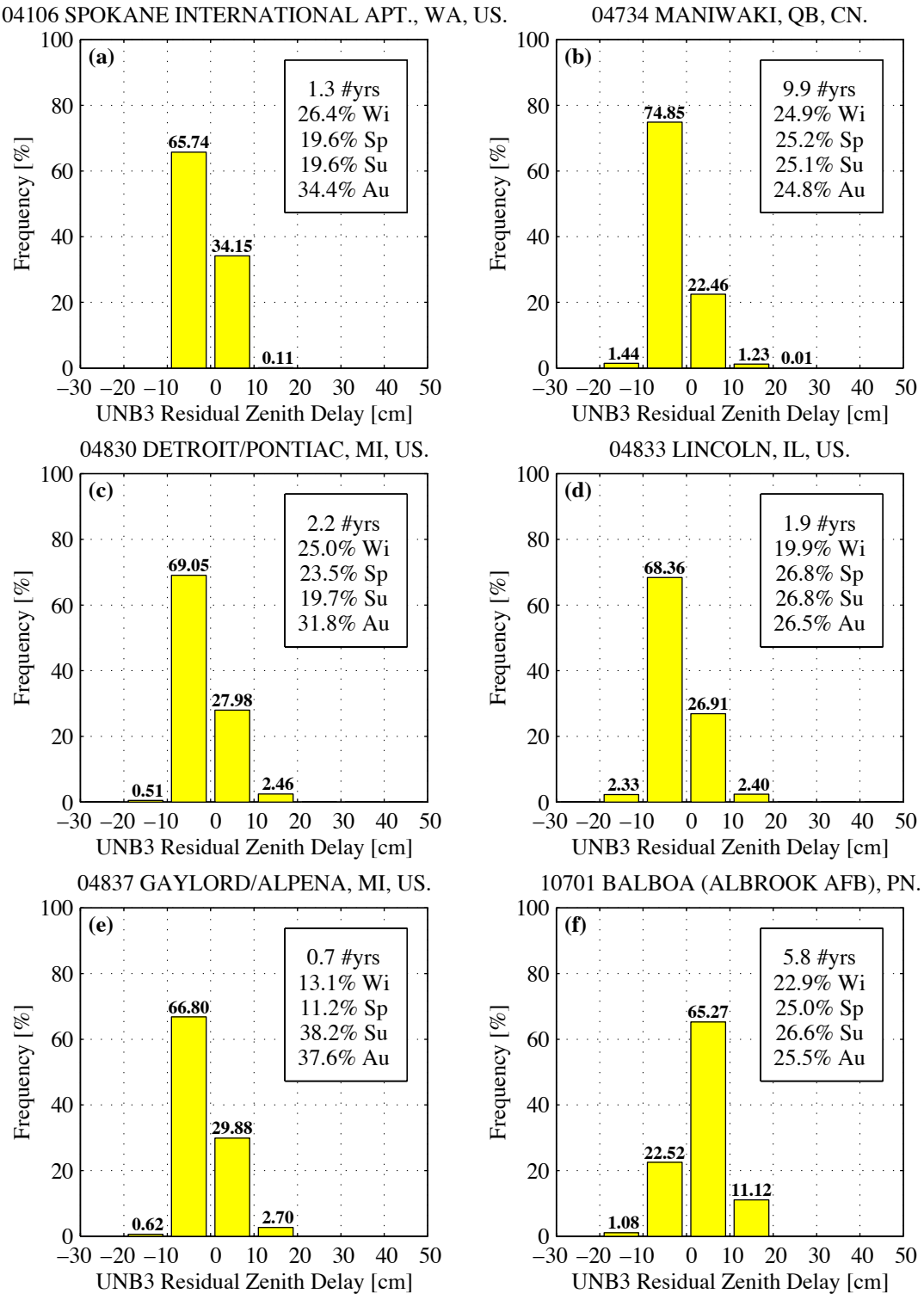

Figure C.5a–f. UNB3 model error histograms for stations 04106, 04734, 04830, 04833, 04837, and 10701.

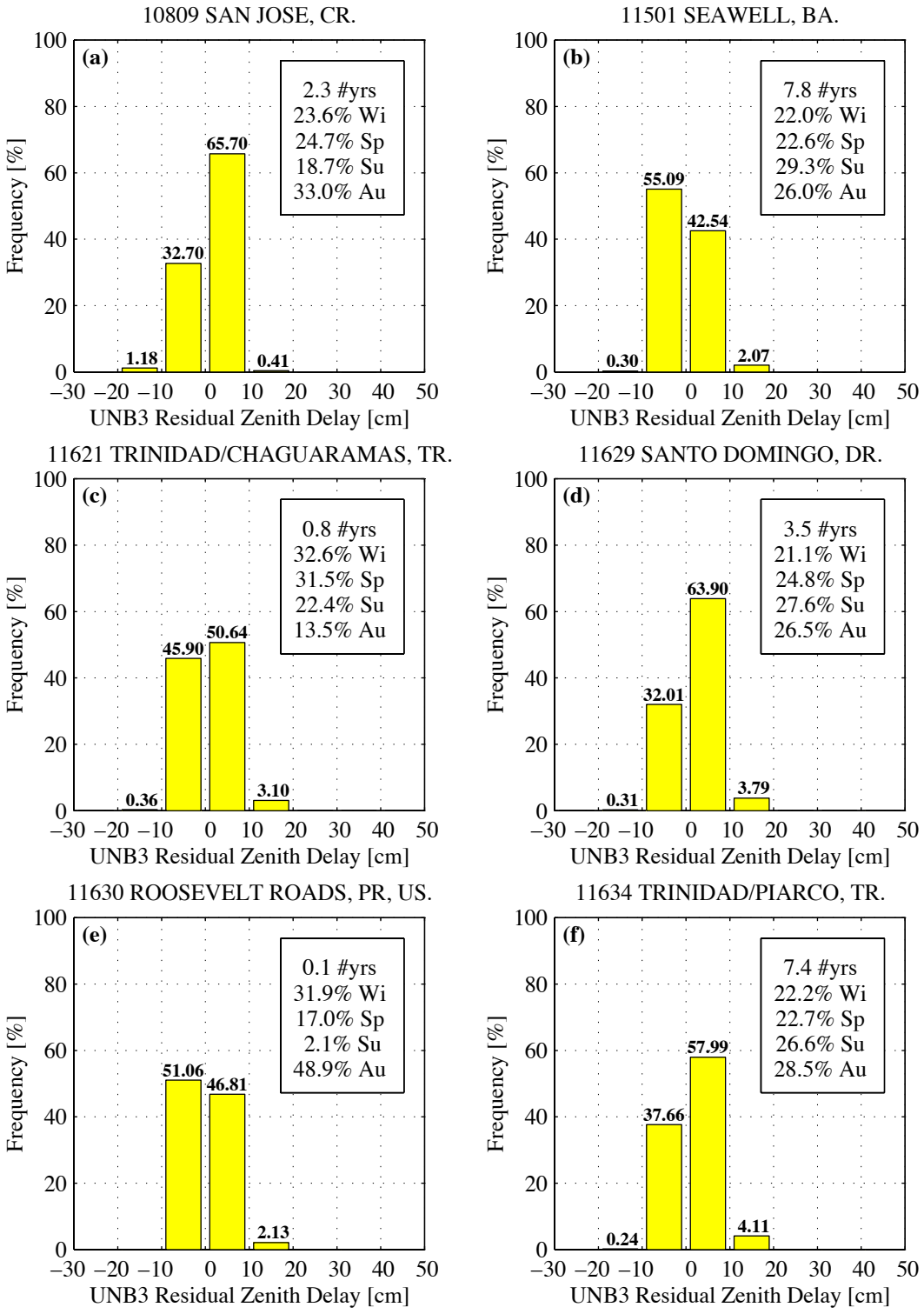

Figure C.6a–f. UNB3 model error histograms for stations 10809, 11501, 11621, 11629, 11630, and 11634.

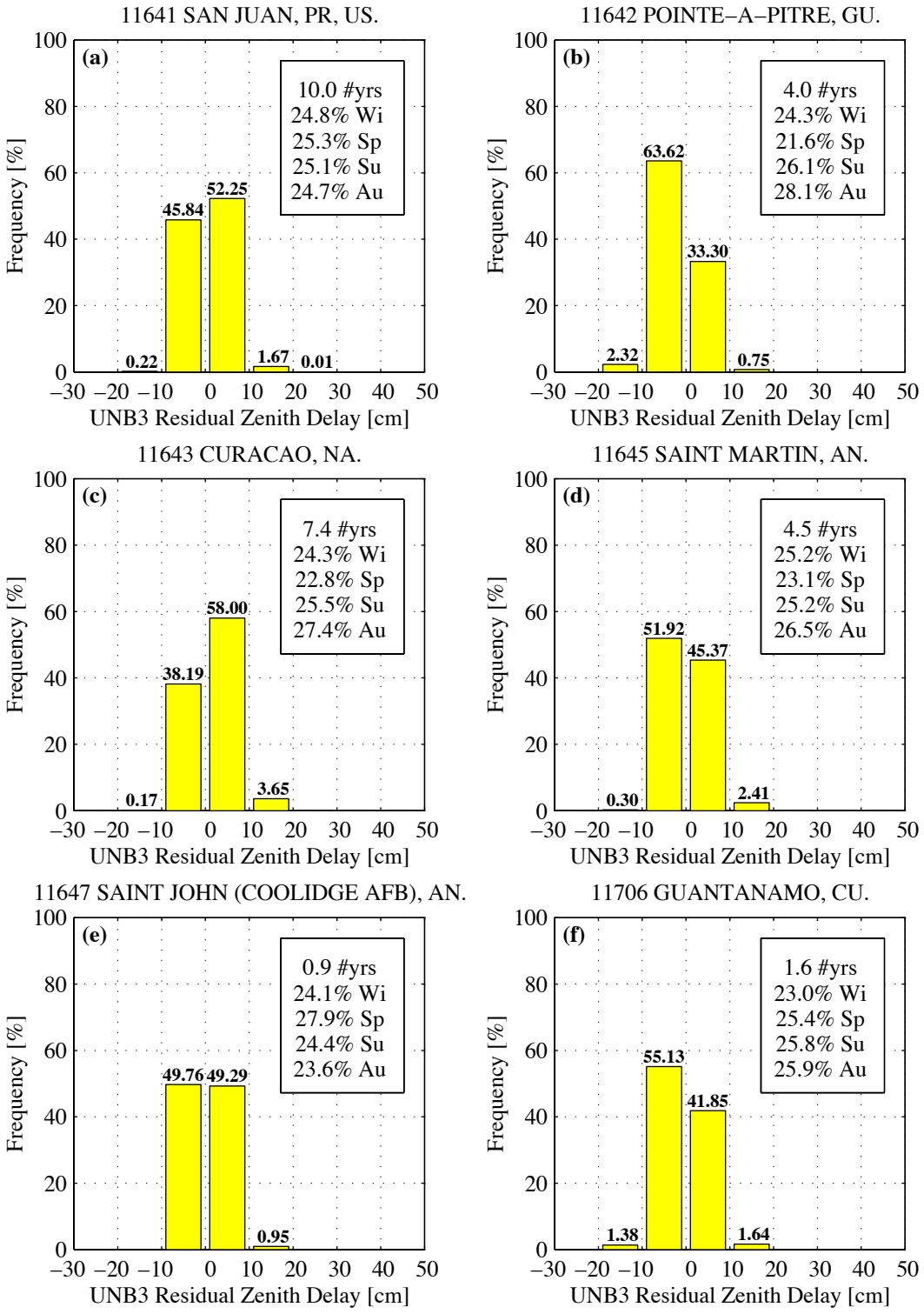

Figure C.7a–f. UNB3 model error histograms for stations 11641, 11642, 11643, 11645, 11647, and 11706.

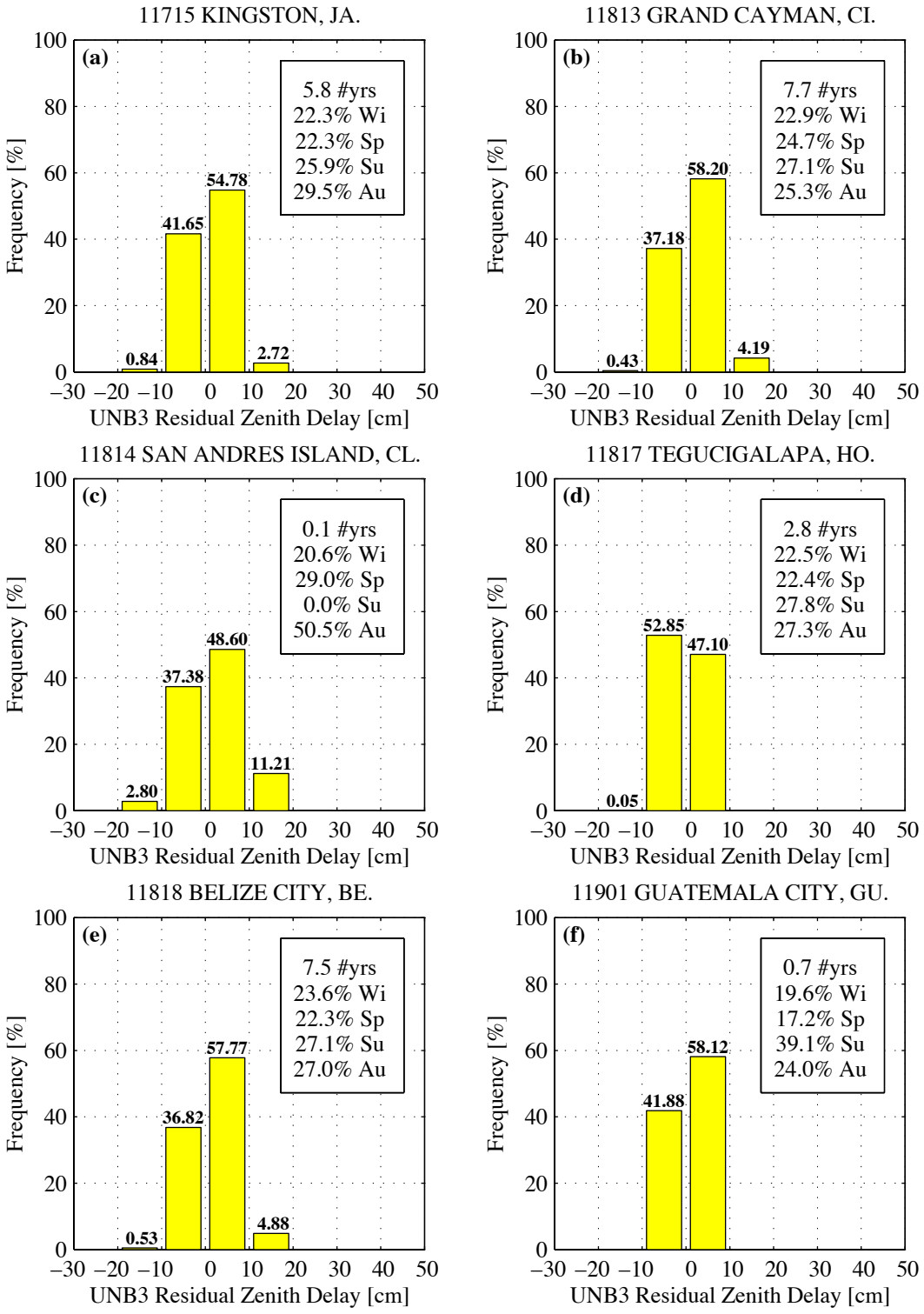

Figure C.8a–f. UNB3 model error histograms for stations 11715, 11813, 11814, 11817, 11818, and 11901.

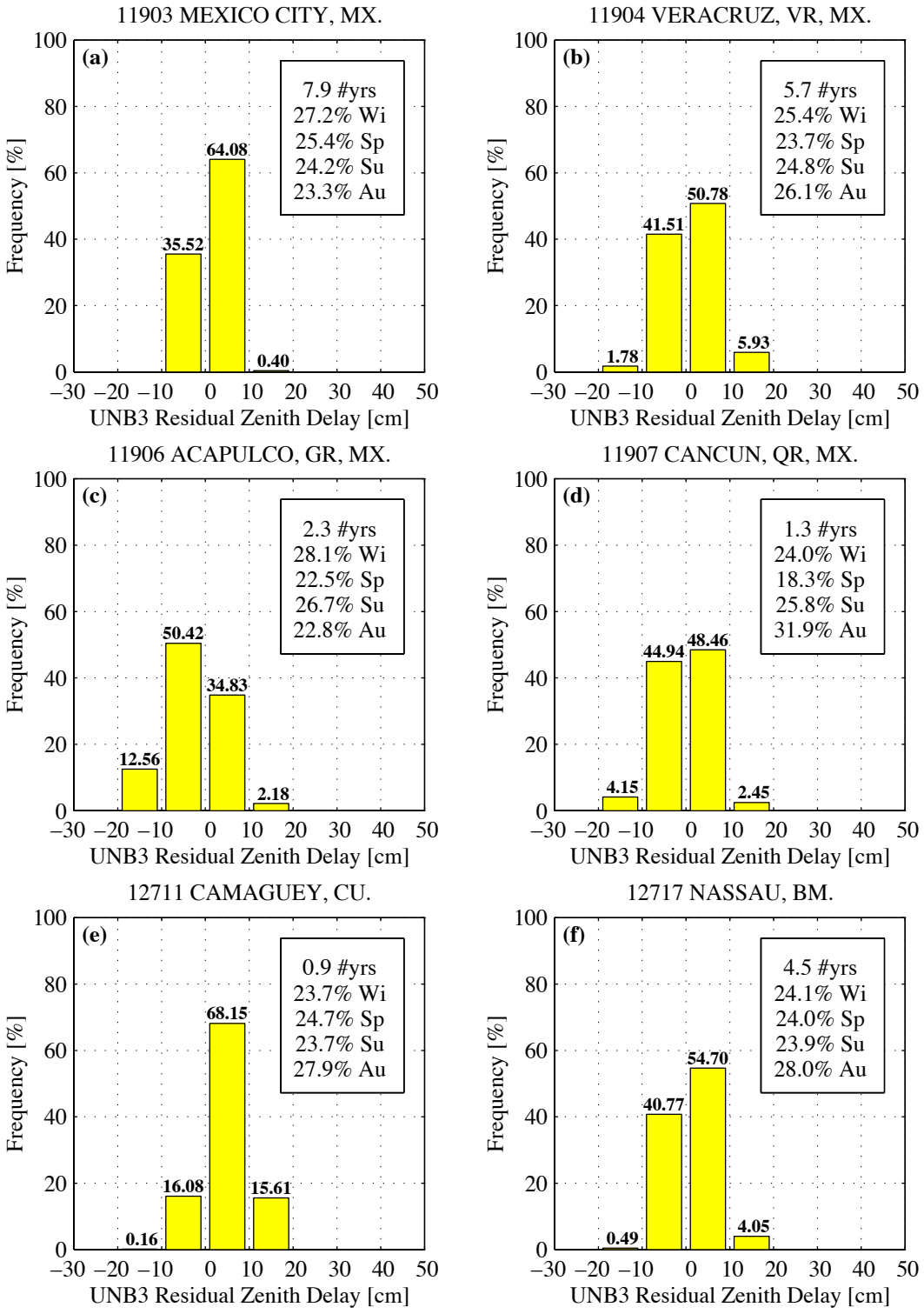

Figure C.9a–f. UNB3 model error histograms for stations 11903, 11904, 11906, 11907, 12711, and 12717.

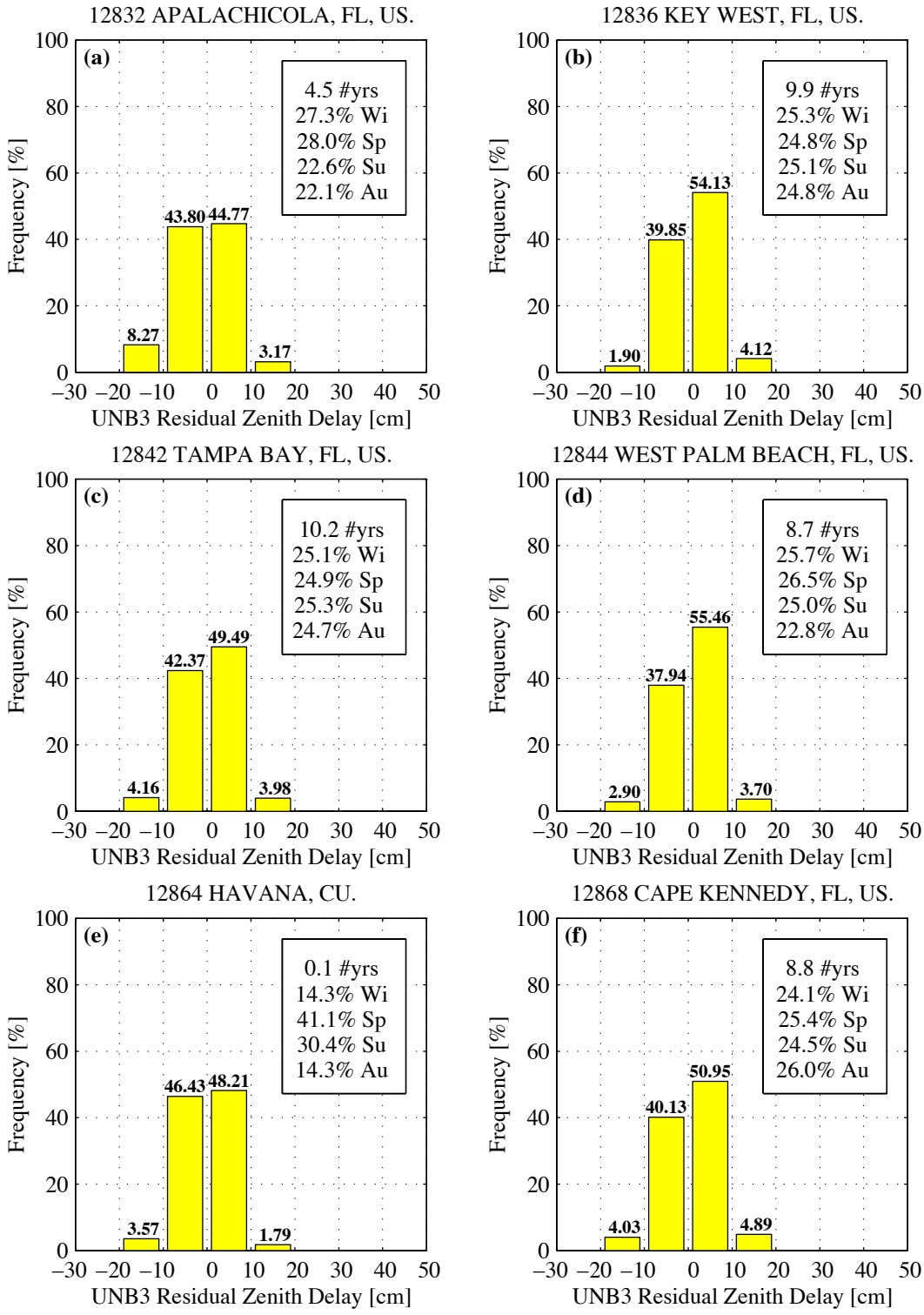

Figure C.10a–f. UNB3 model error histograms for stations 12832, 12836, 12842, 12844, 12864, and 12868.

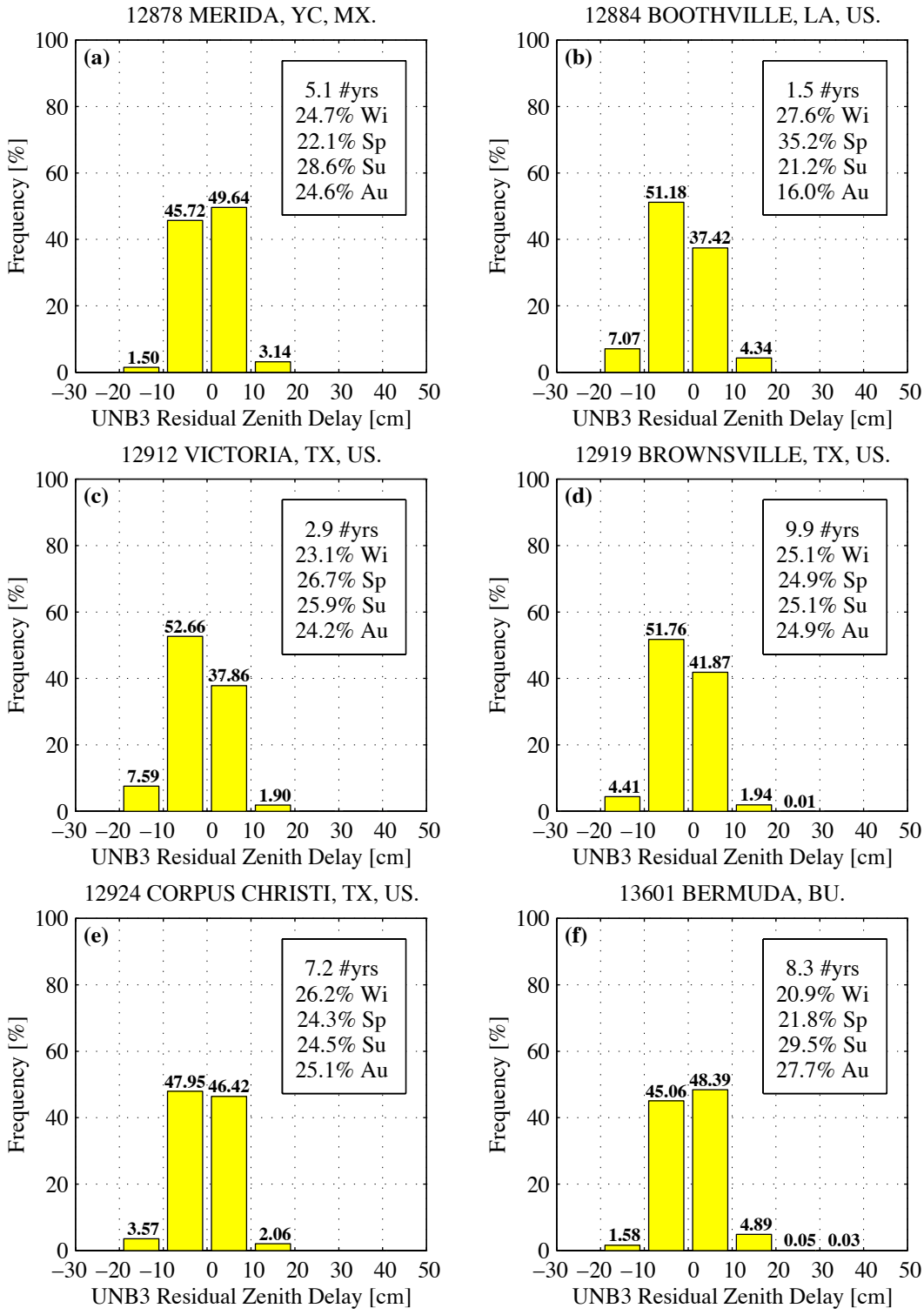

Figure C.11a–f. UNB3 model error histograms for stations 12878, 12884, 12912, 12919, 12924, and 13601.

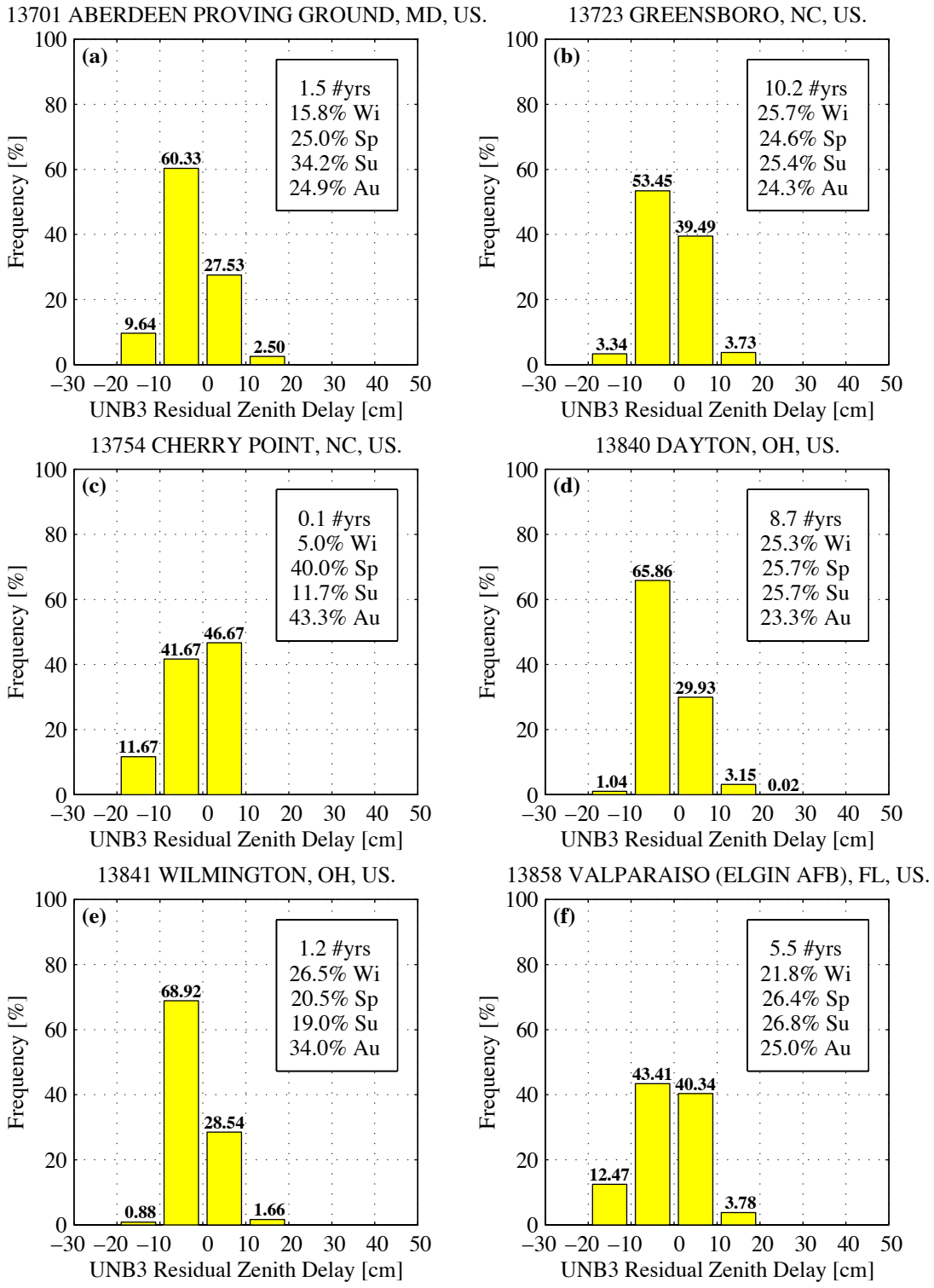

Figure C.12a–f. UNB3 model error histograms for stations 13701, 13723, 13754, 13840, 13841, and 13858.

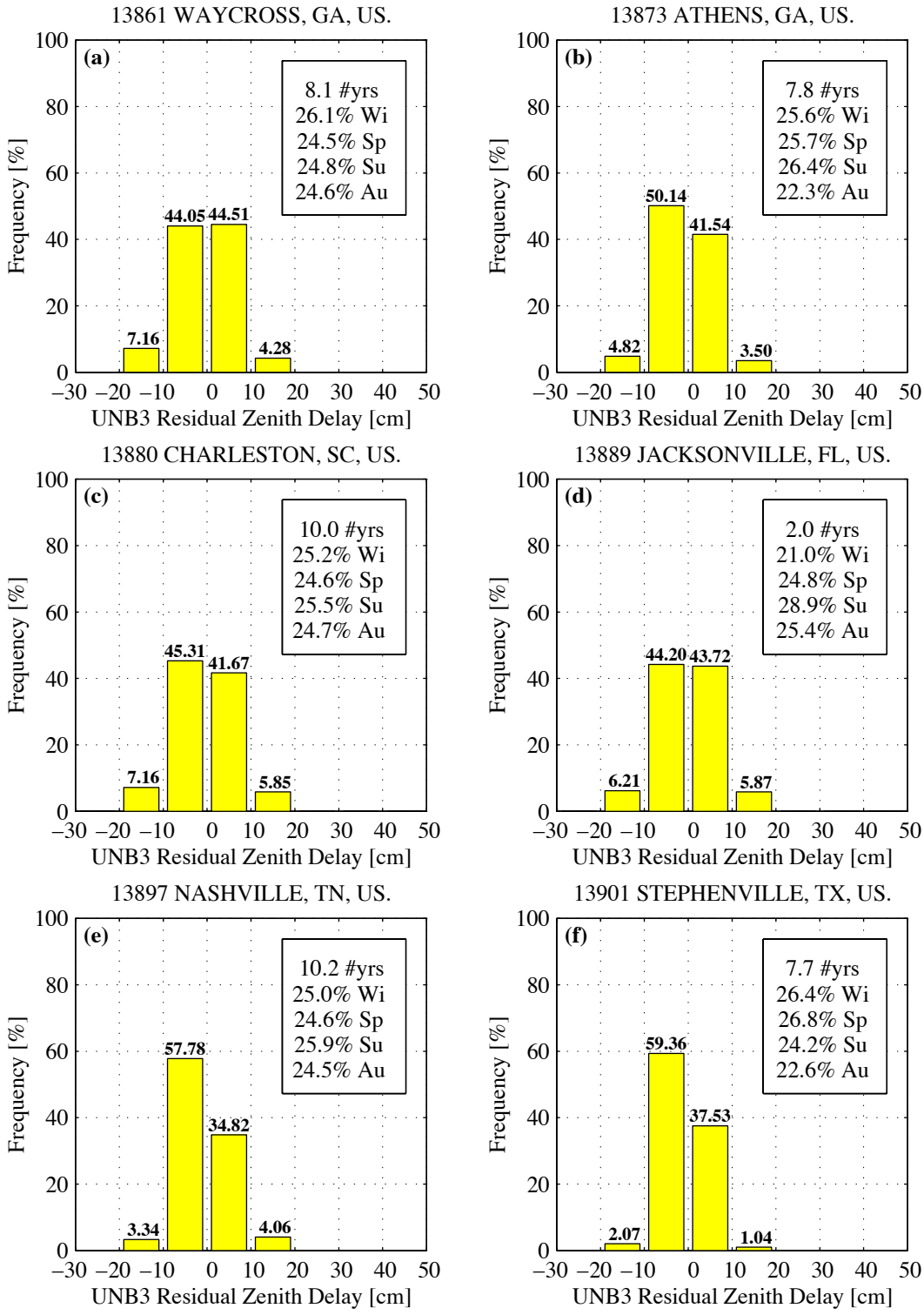

Figure C.13a–f. UNB3 model error histograms for stations 13861, 13873, 13880, 13889, 13897, and 13901.

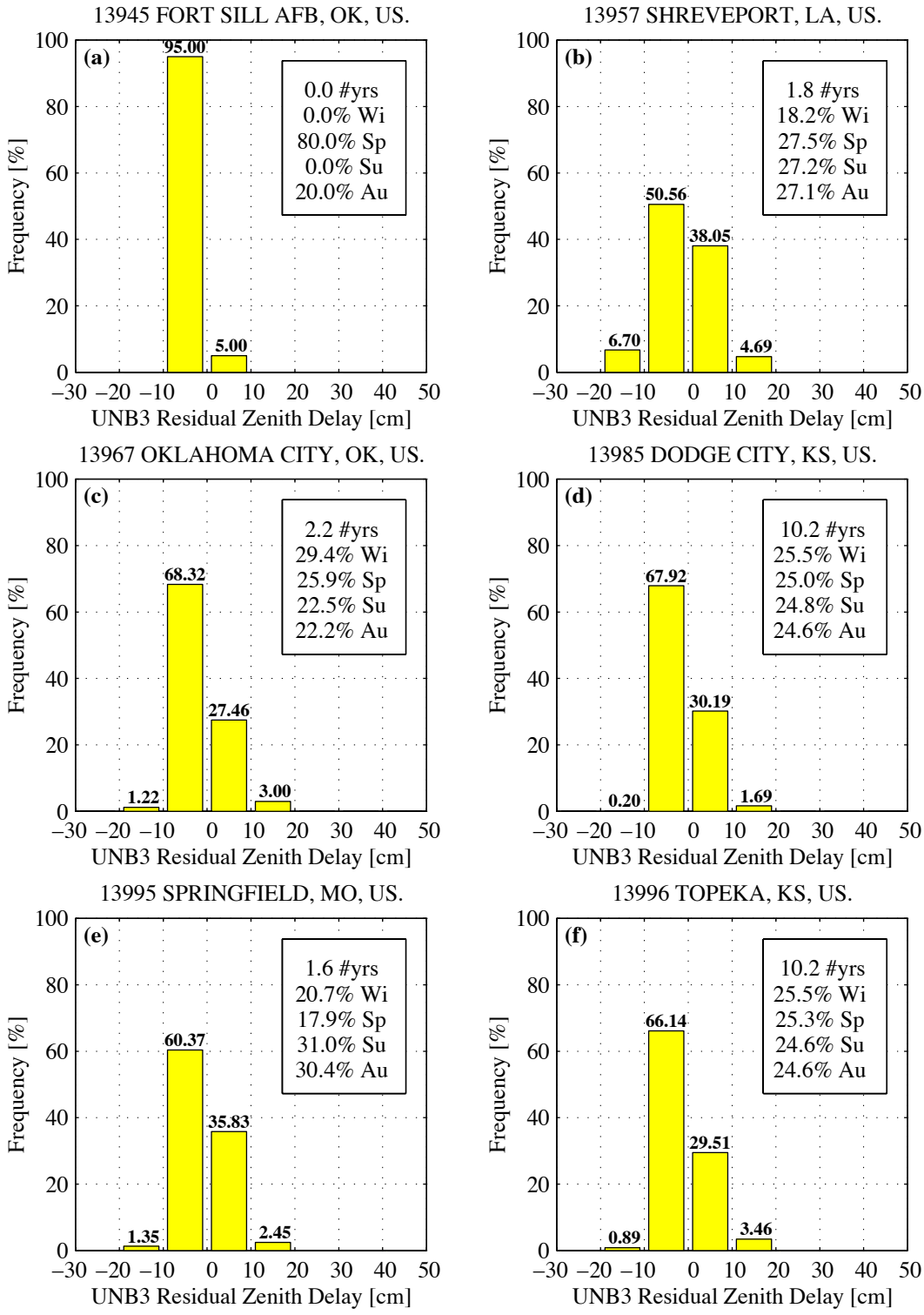

Figure C.14a–f. UNB3 model error histograms for stations 13945, 13957, 13967, 13985, 13995, and 13996.

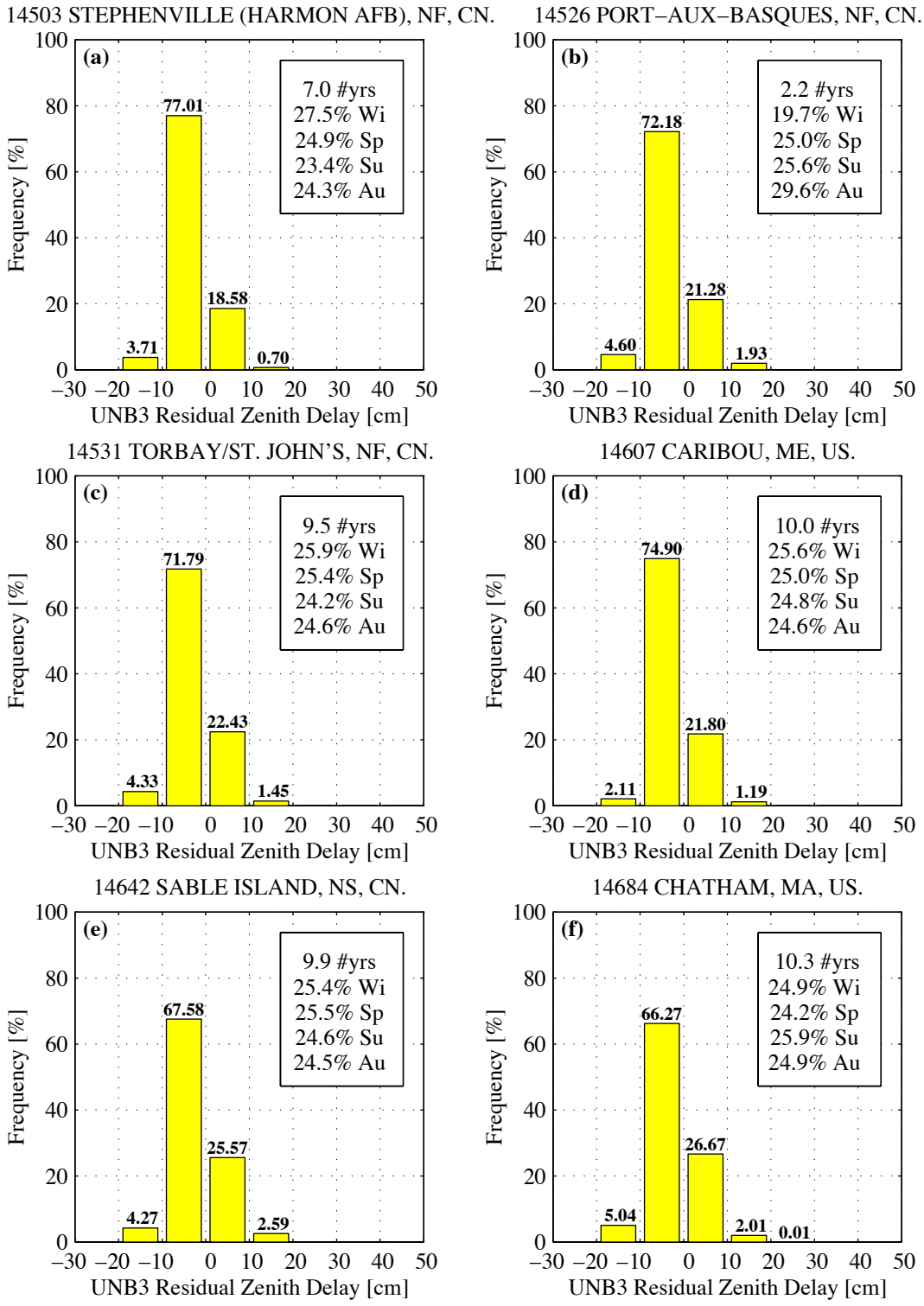

Figure C.15a–f. UNB3 model error histograms for stations 14503, 14526, 14531, 14607, 14642, and 14684.

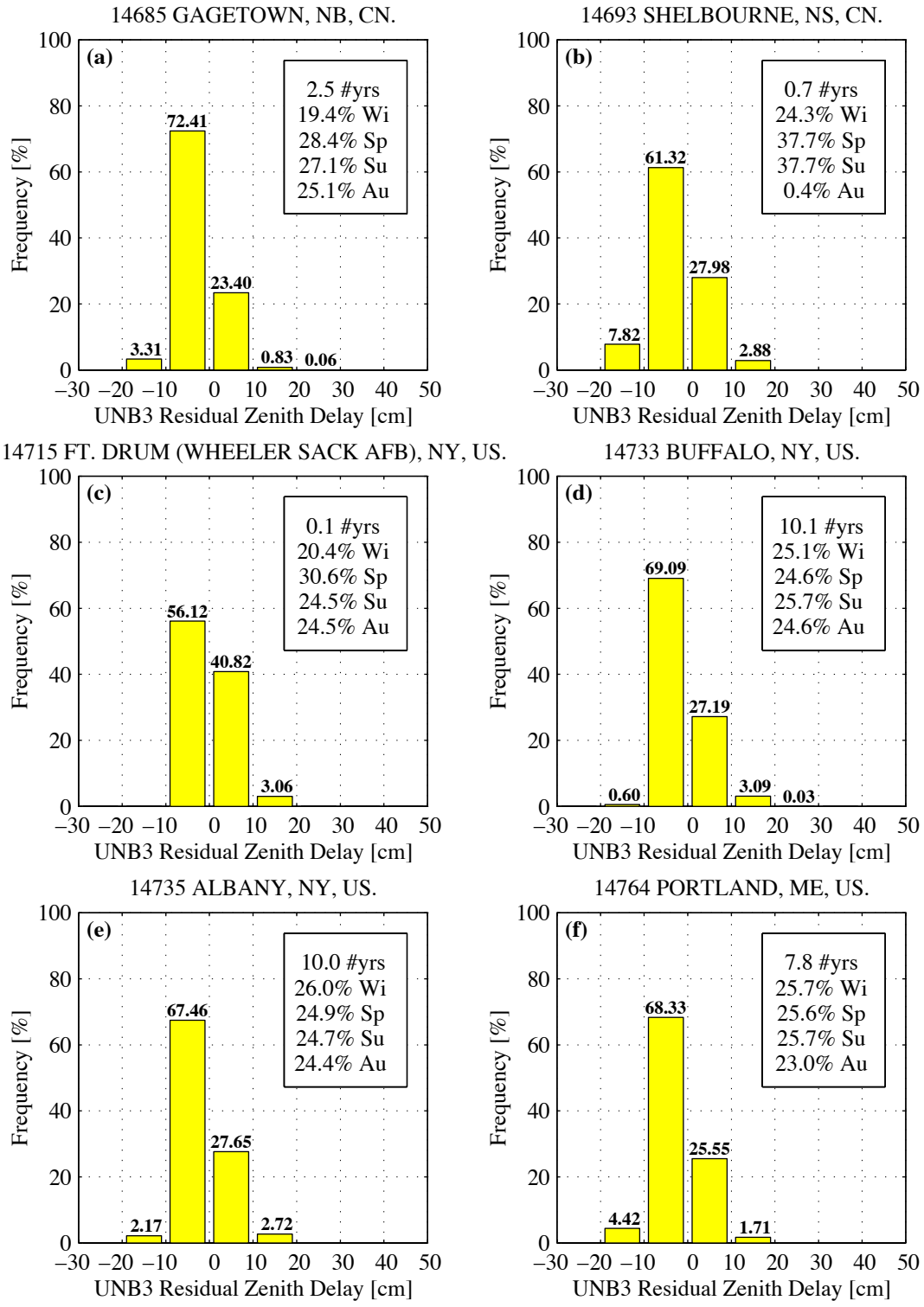

Figure C.16a–f. UNB3 model error histograms for stations 14685, 14693, 14715, 14733, 14735, and 14764.

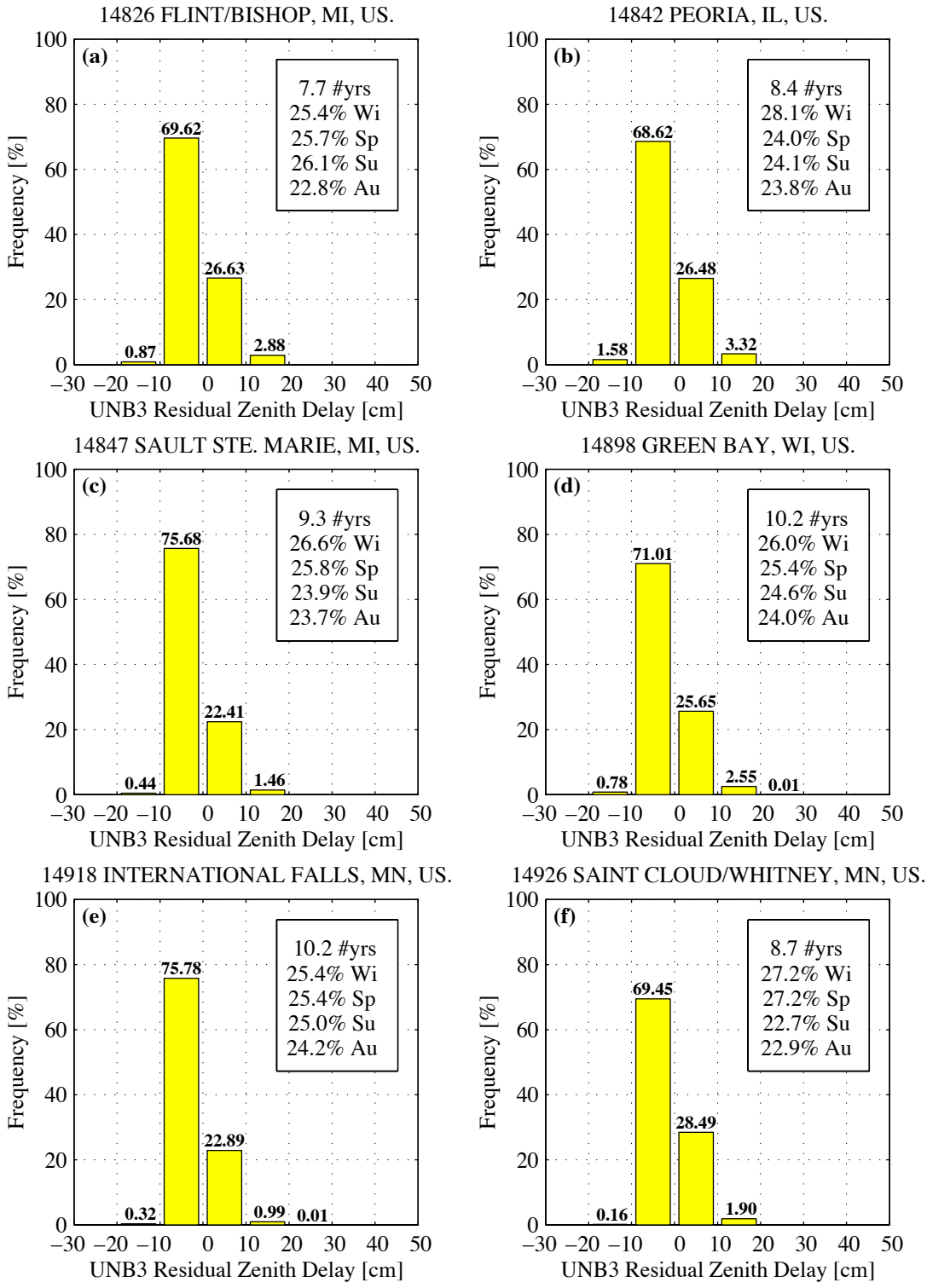

Figure C.17a–f. UNB3 model error histograms for stations 14826, 14842, 14847, 14898, 14918, and 14926.

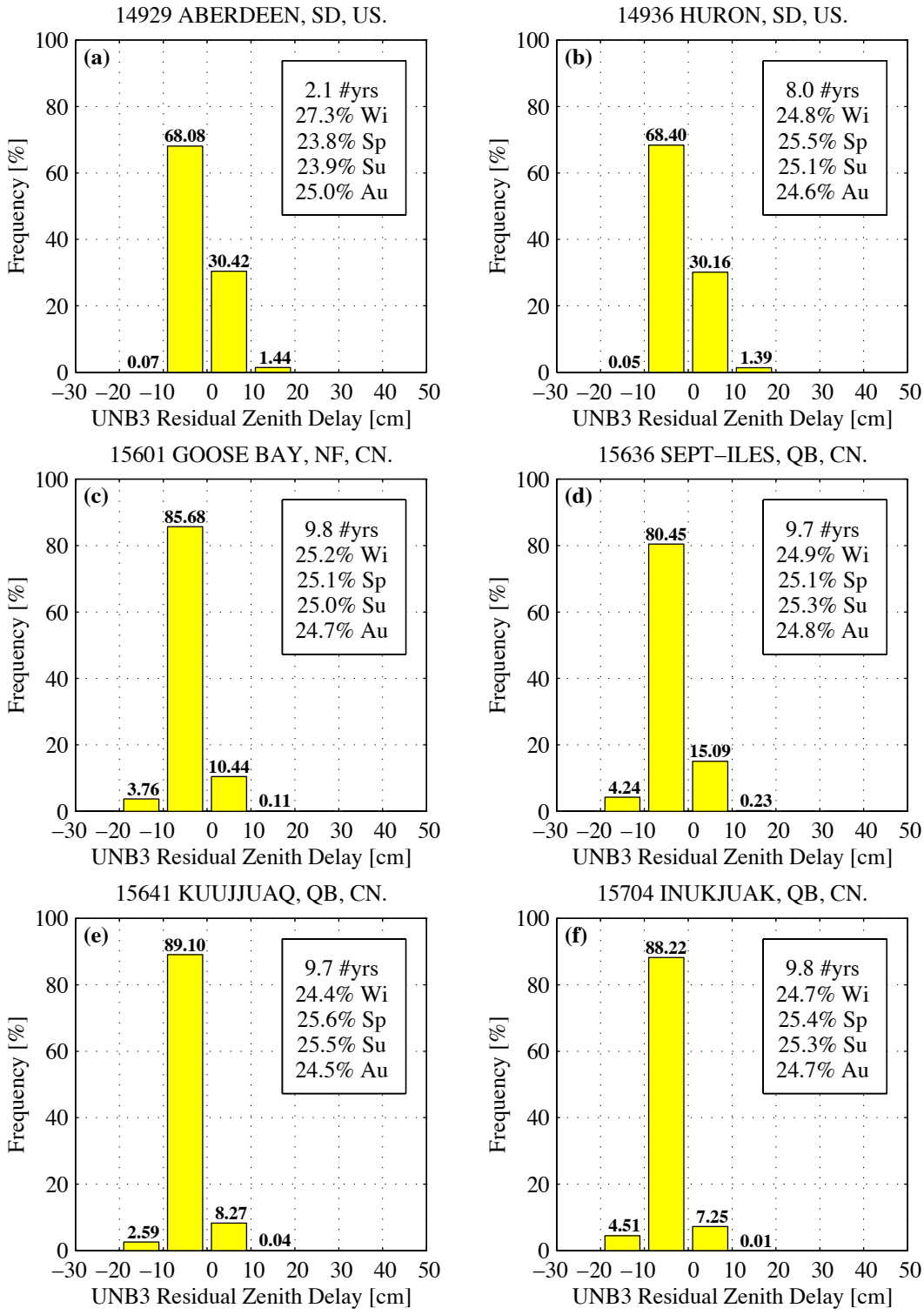

Figure C.18a–f. UNB3 model error histograms for stations 14929, 14936, 15601, 15636, 15641, and 15704.

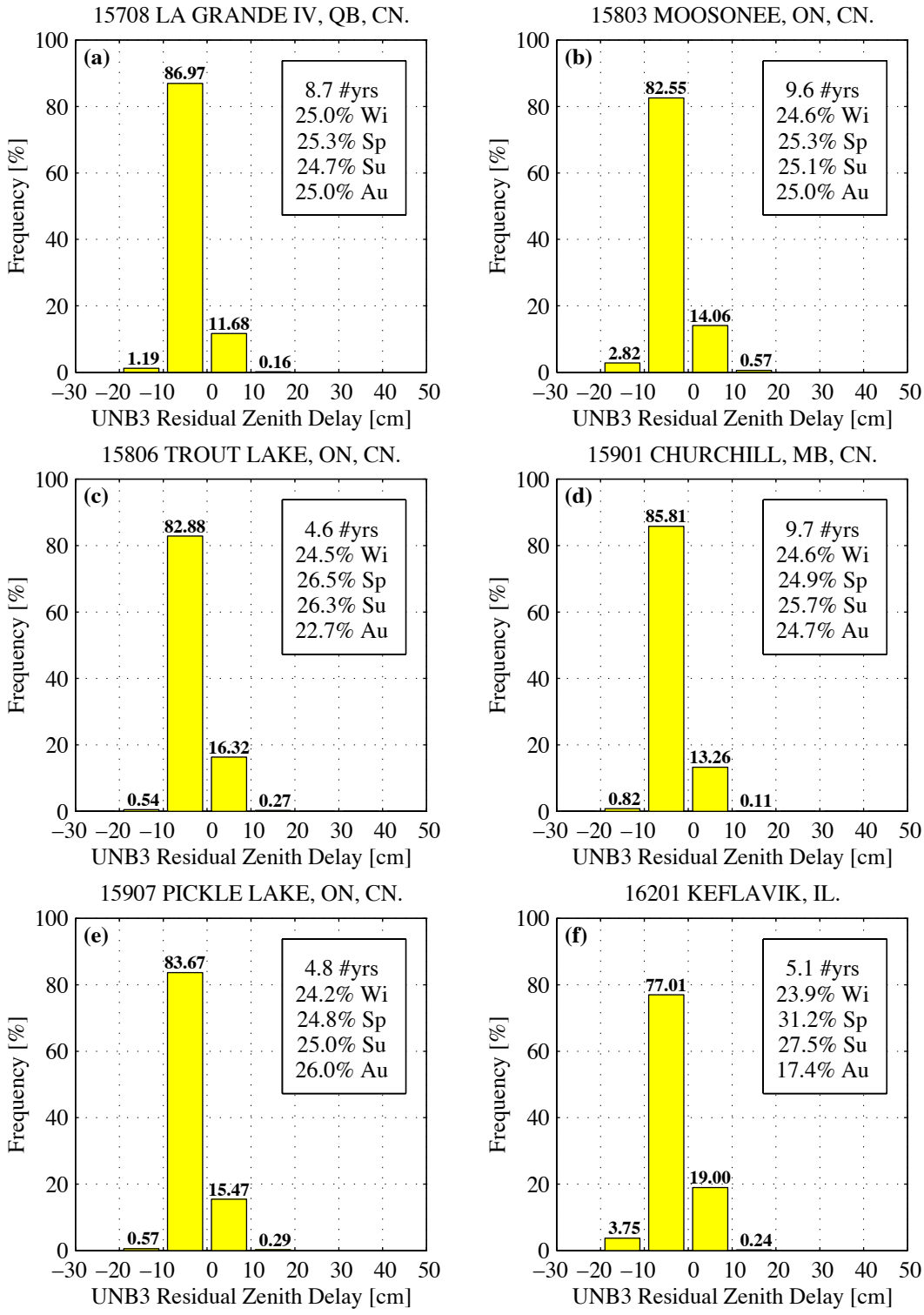

Figure C.19a–f. UNB3 model error histograms for stations 15708, 15803, 15806, 15901, 15907, and 16201.

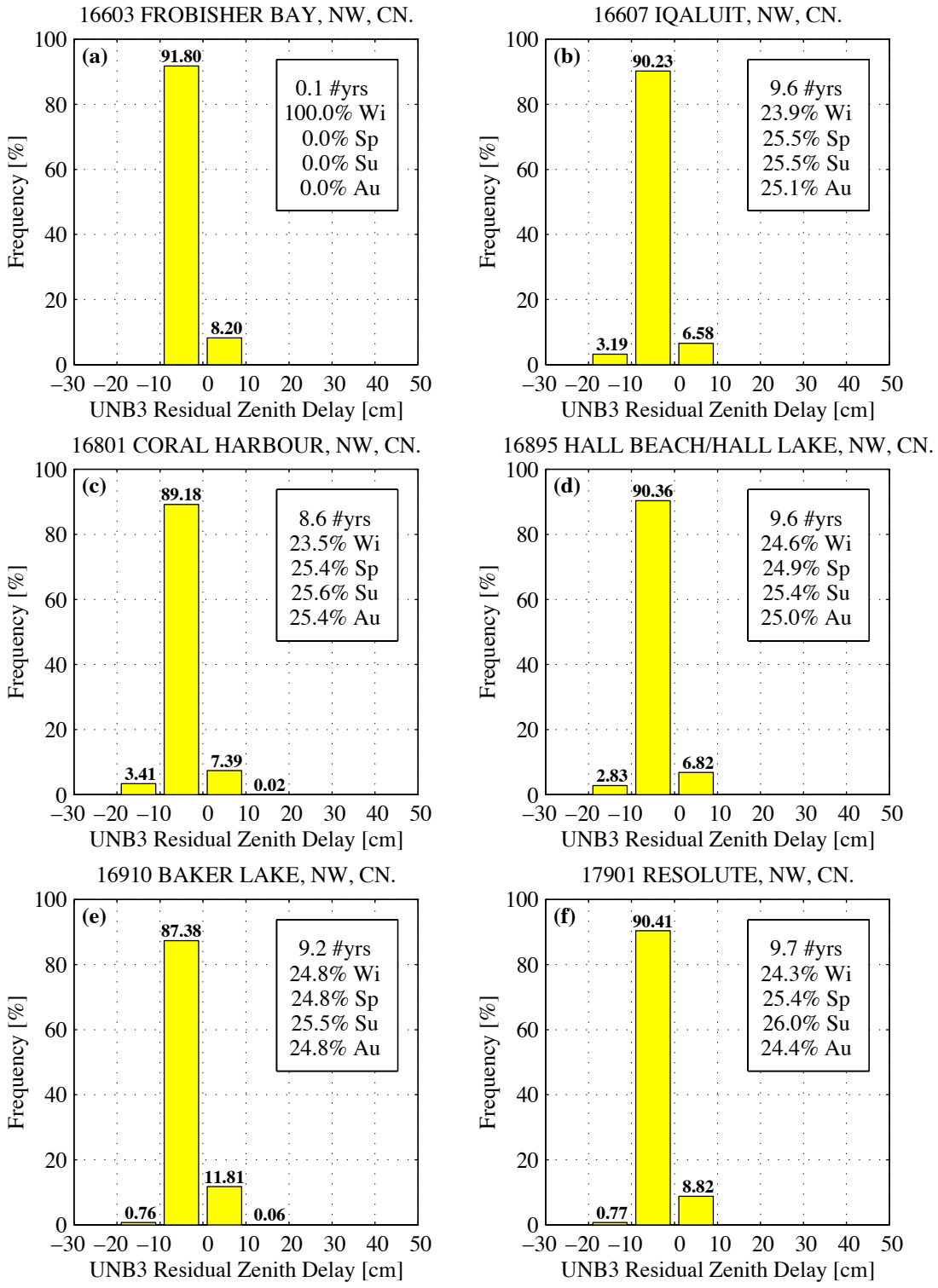

Figure C.20a–f. UNB3 model error histograms for stations 16603, 16607, 16801, 16895, 16910, and 17901.

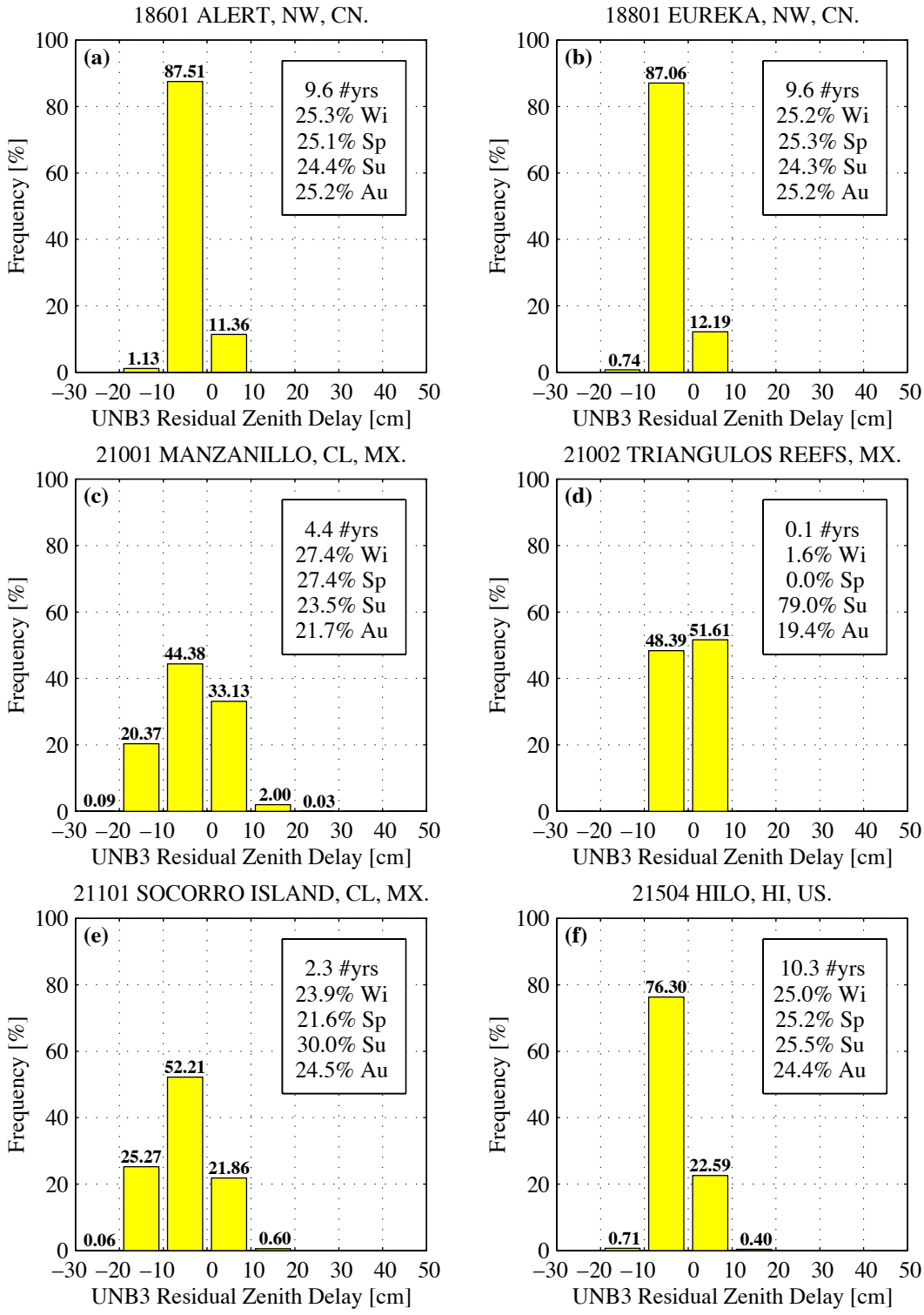

Figure C.21a–f. UNB3 model error histograms for stations 18601, 18801, 21001, 21002, 21101, and 21504.

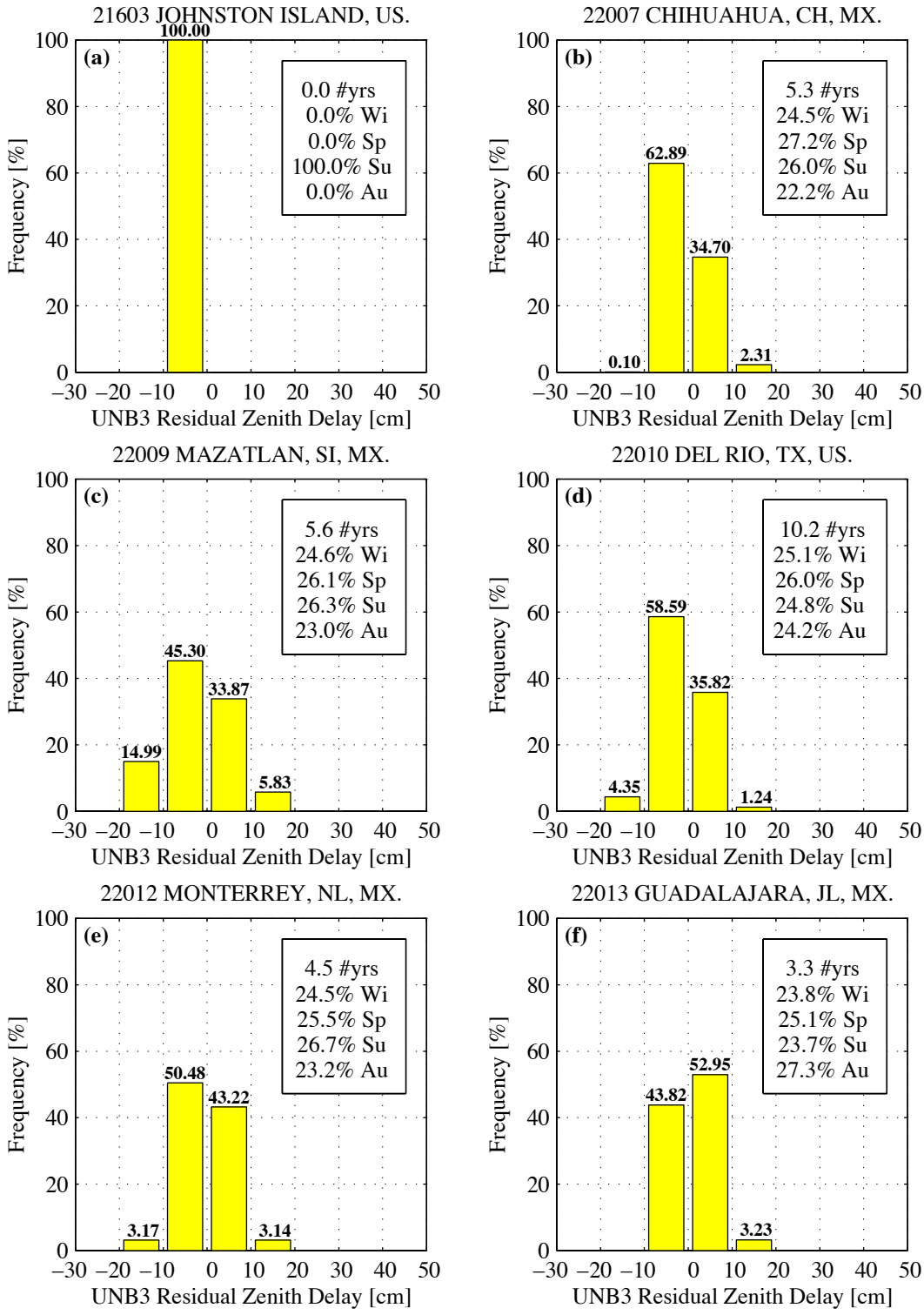

Figure C.22a–f. UNB3 model error histograms for stations 21603, 22007, 22009, 22010, 22012, and 22013.

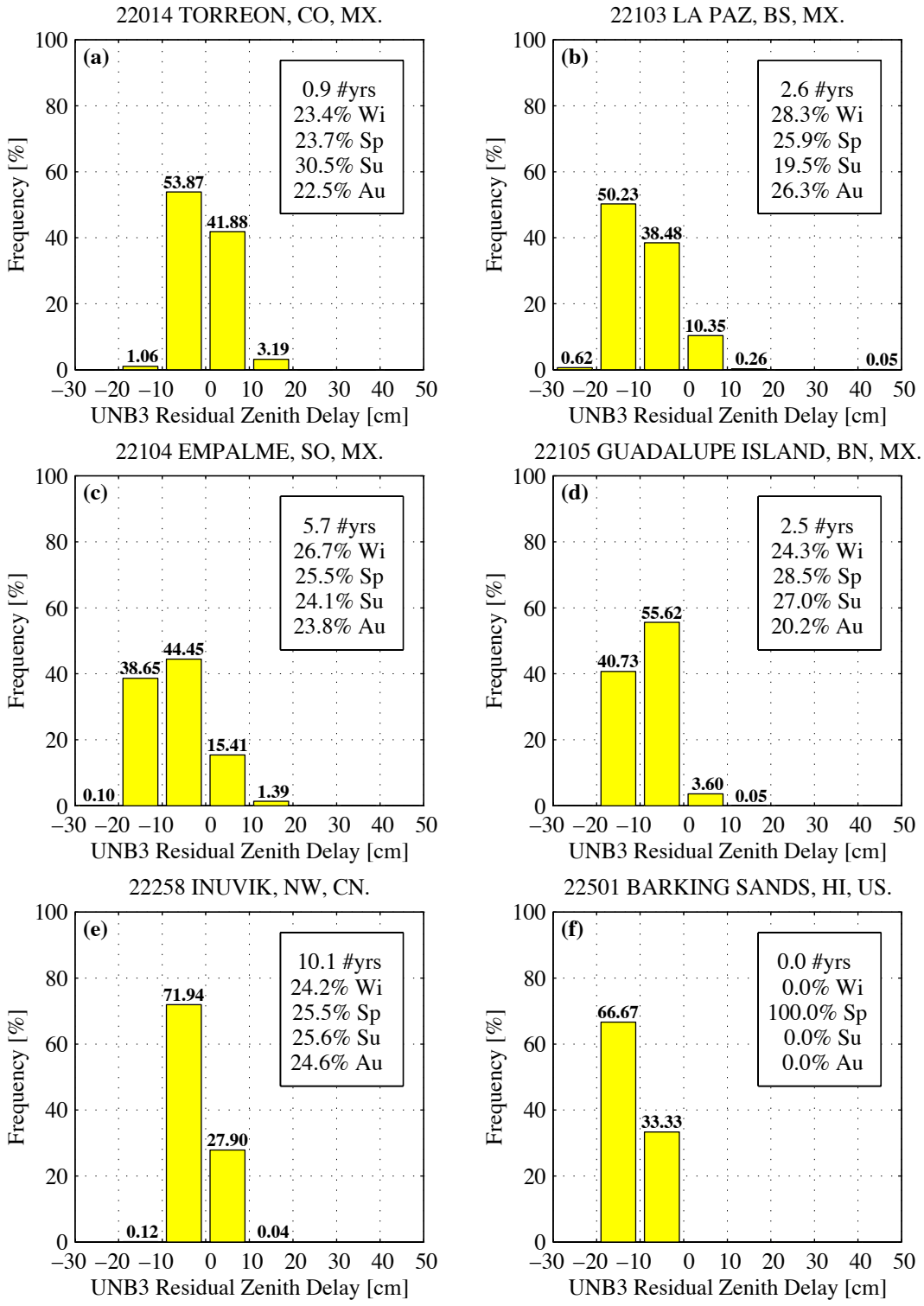

Figure C.23a–f. UNB3 model error histograms for stations 22014, 22103, 22104, 22105, 22258, and 22501.

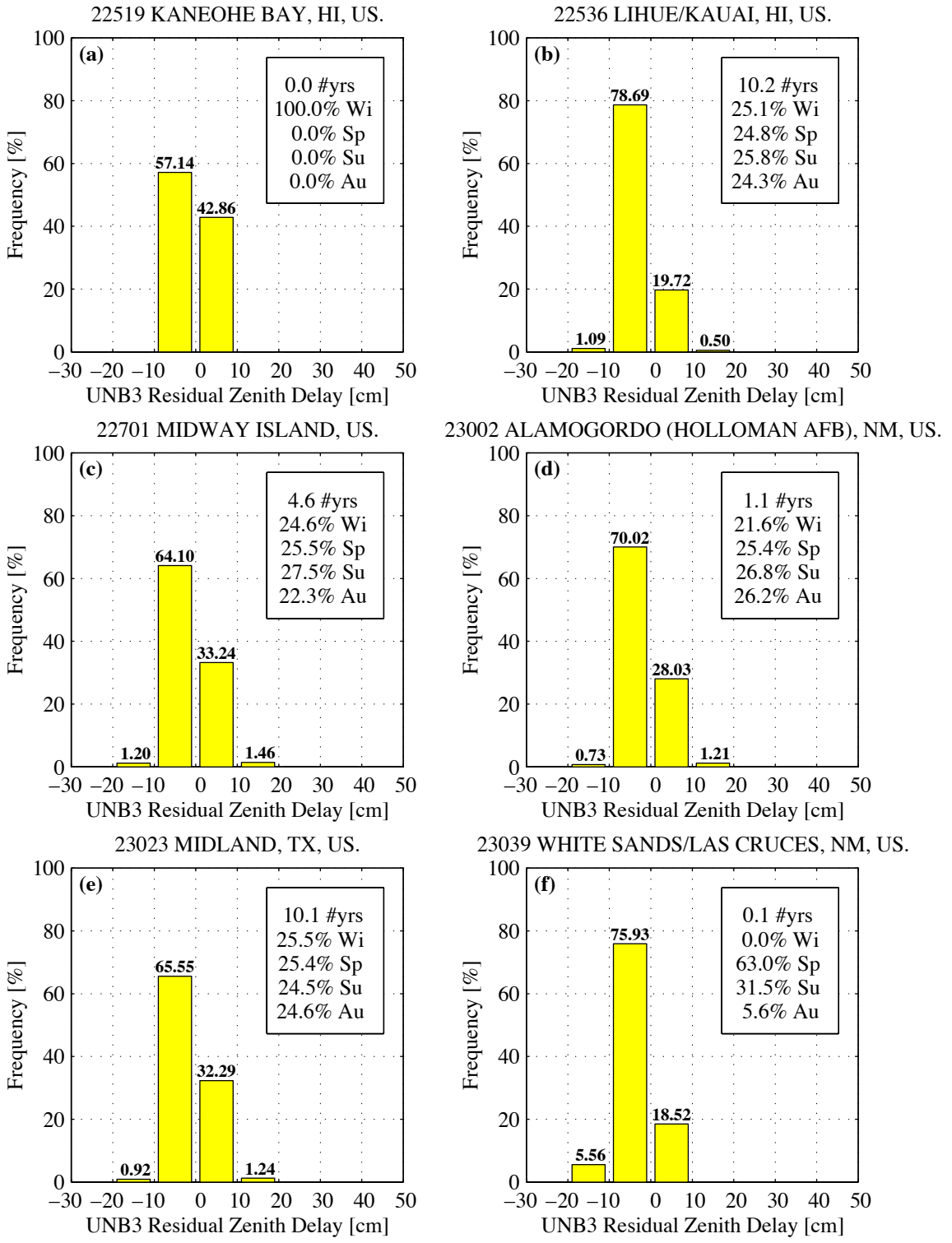

Figure C.24a–f. UNB3 model error histograms for stations 22519, 22536, 22701, 23002, 23023, and 23039.

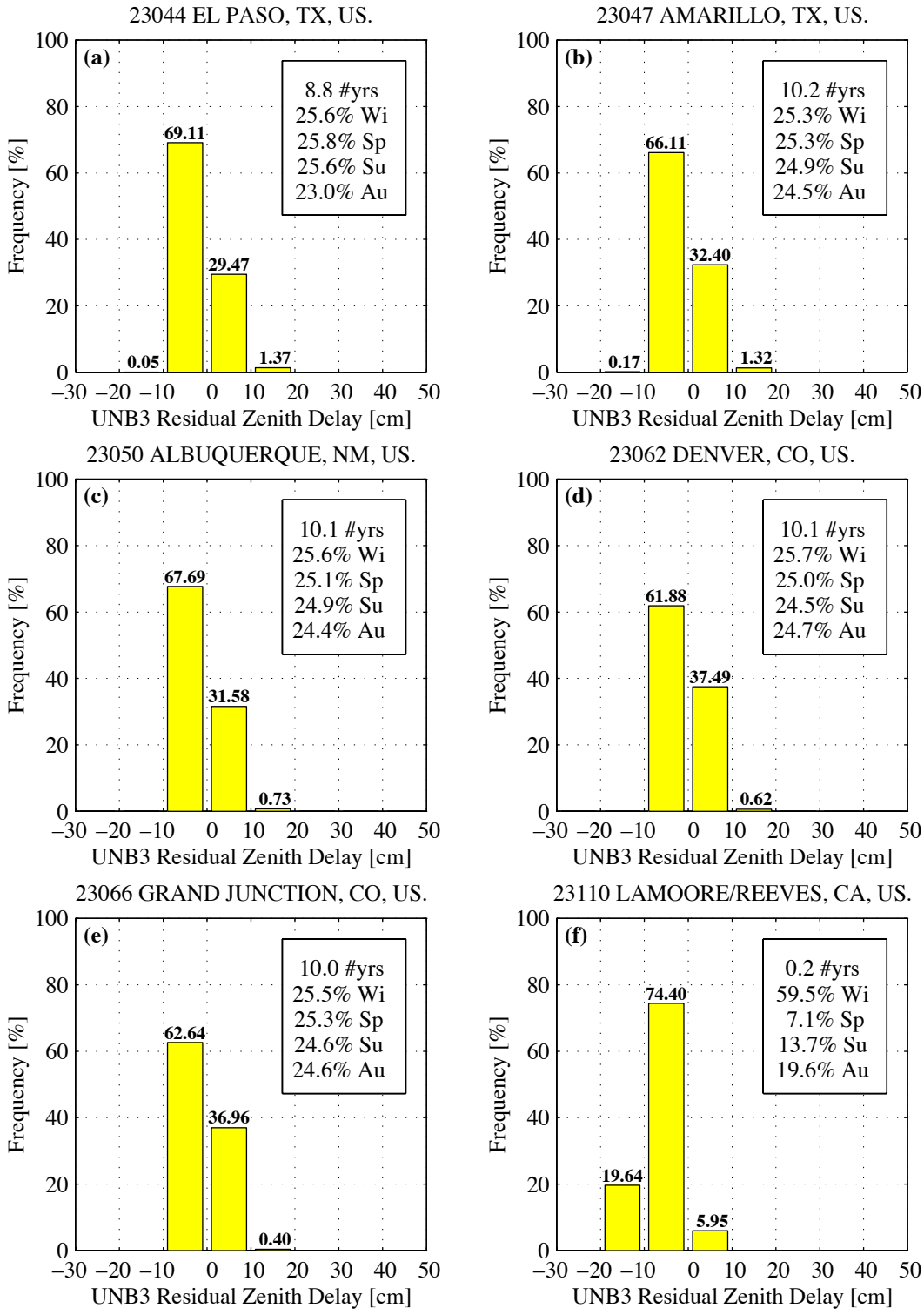

Figure C.25a–f. UNB3 model error histograms for stations 23044, 23047, 23050, 23062, 23066, and 23110.

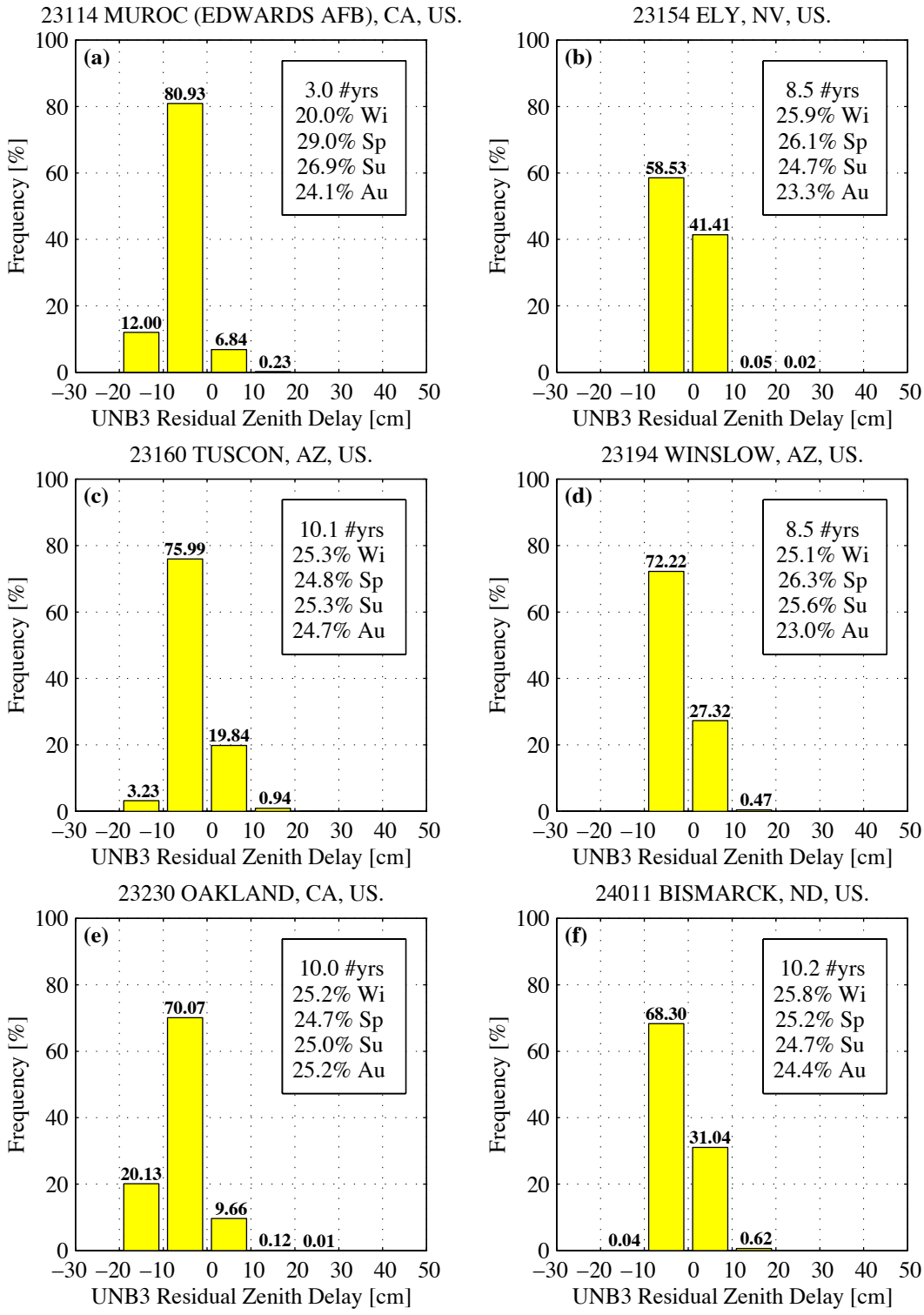

Figure C.26a–f. UNB3 model error histograms for stations 23114, 23154, 23160, 23194, 23230, and 24011.

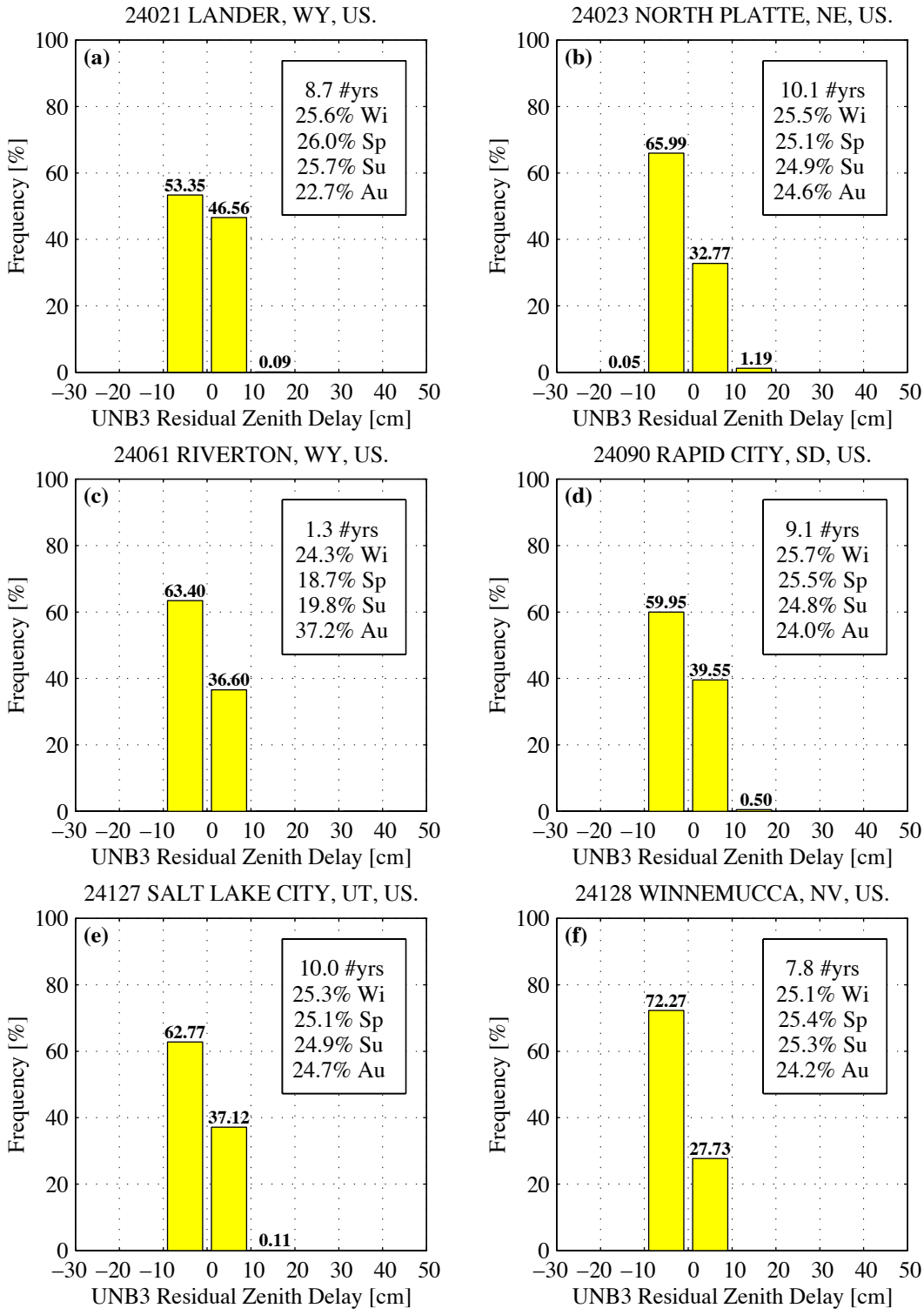

Figure C.27a–f. UNB3 model error histograms for stations 24021, 24023, 24061, 24090, 24127, and 24128.

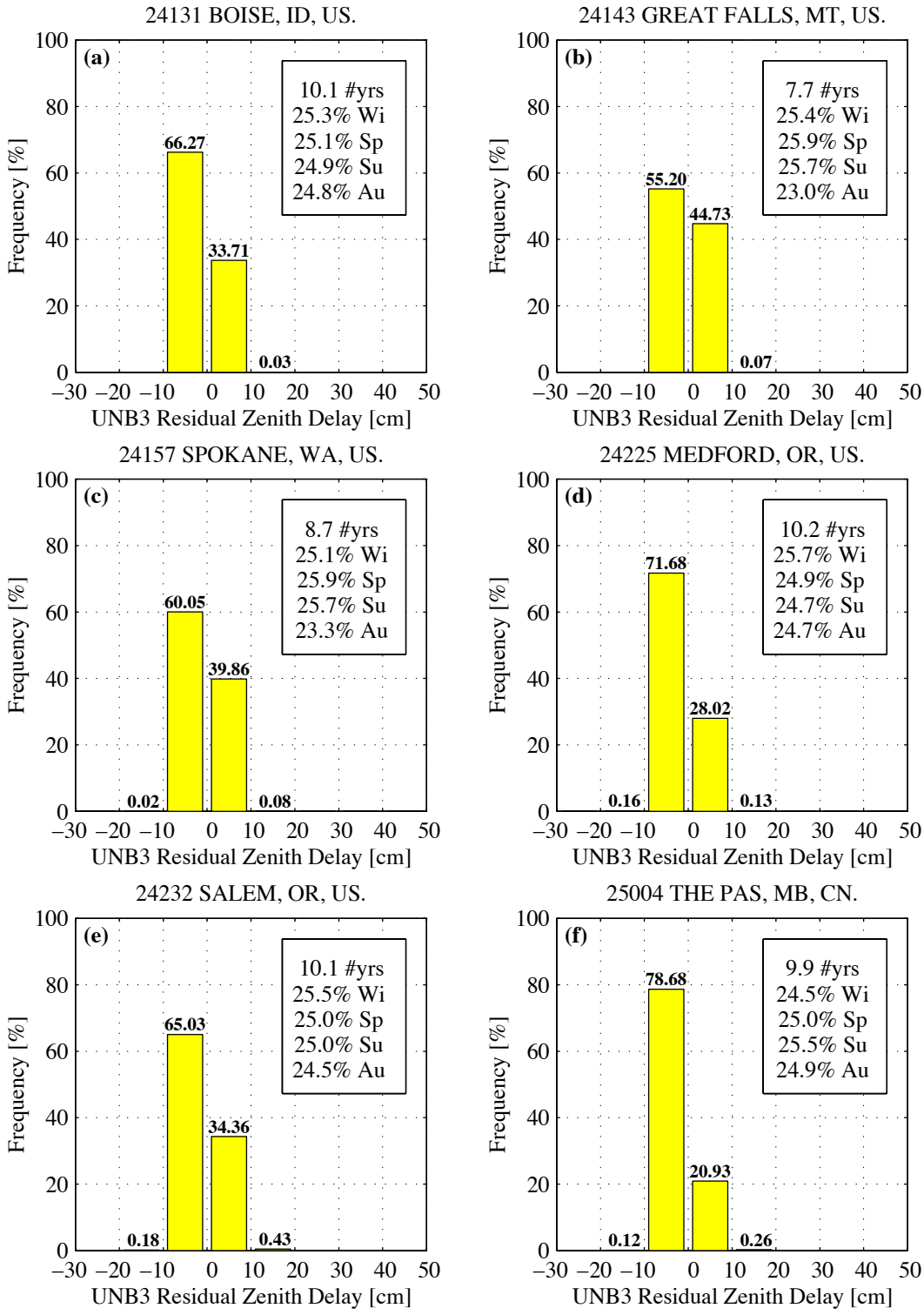

Figure C.28a–f. UNB3 model error histograms for stations 24131, 24143, 24157, 24225, 24232, and 25004.

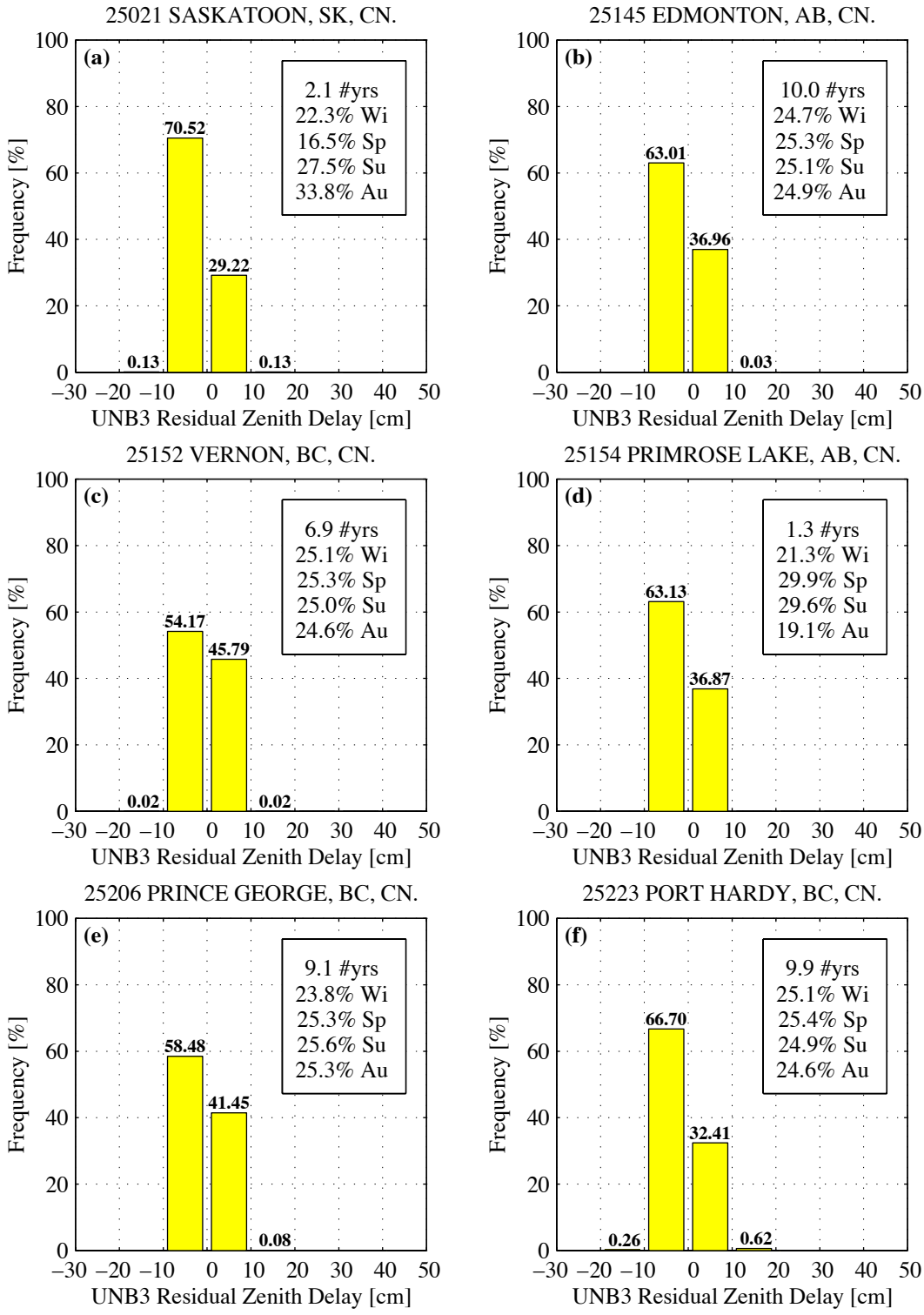

Figure C.29a–f. UNB3 model error histograms for stations 25021, 25145, 25152, 25154, 25206, and 25223.

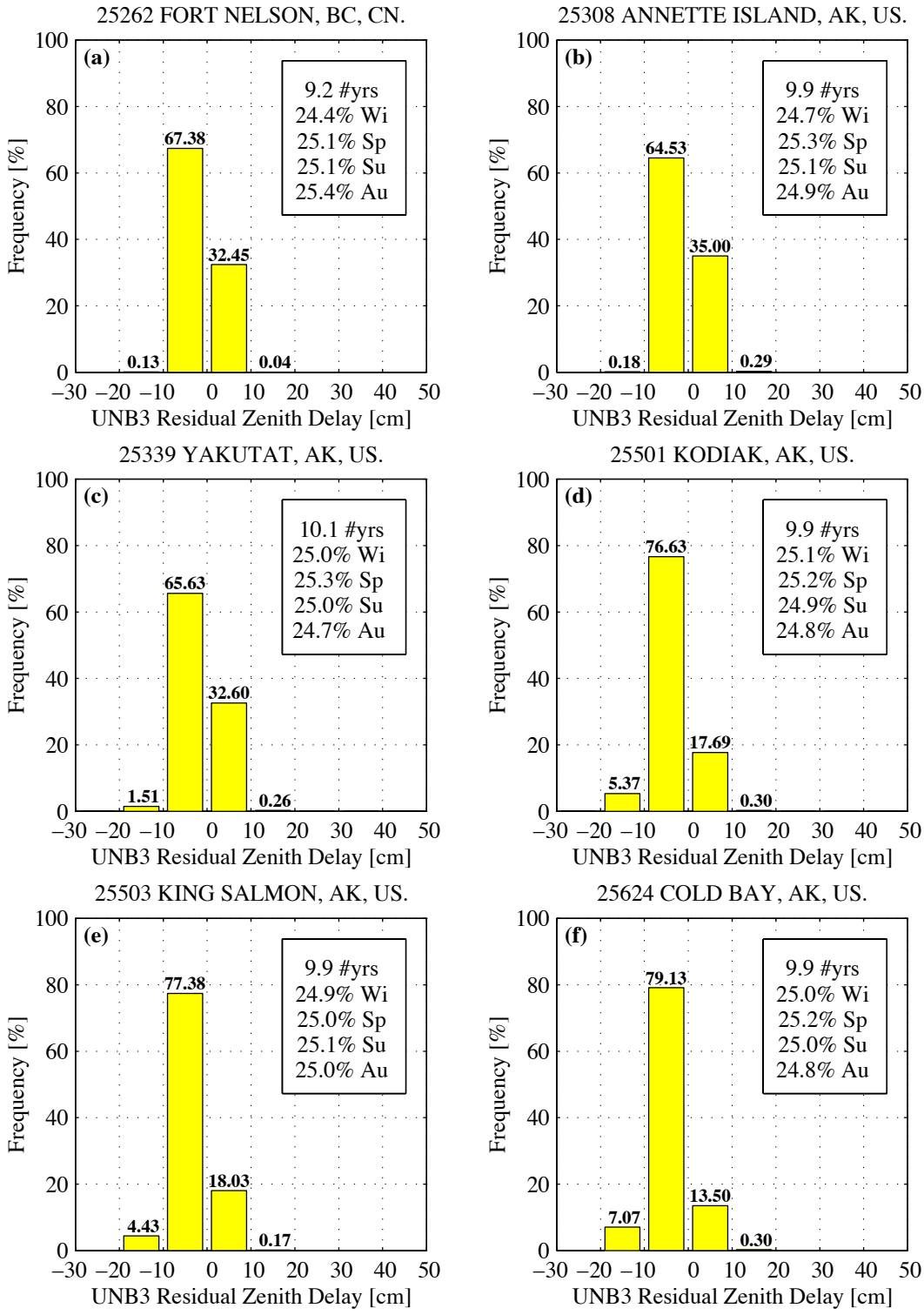

Figure C.30a–f. UNB3 model error histograms for stations 25262, 25308, 25339, 25501, 25503, and 25624.

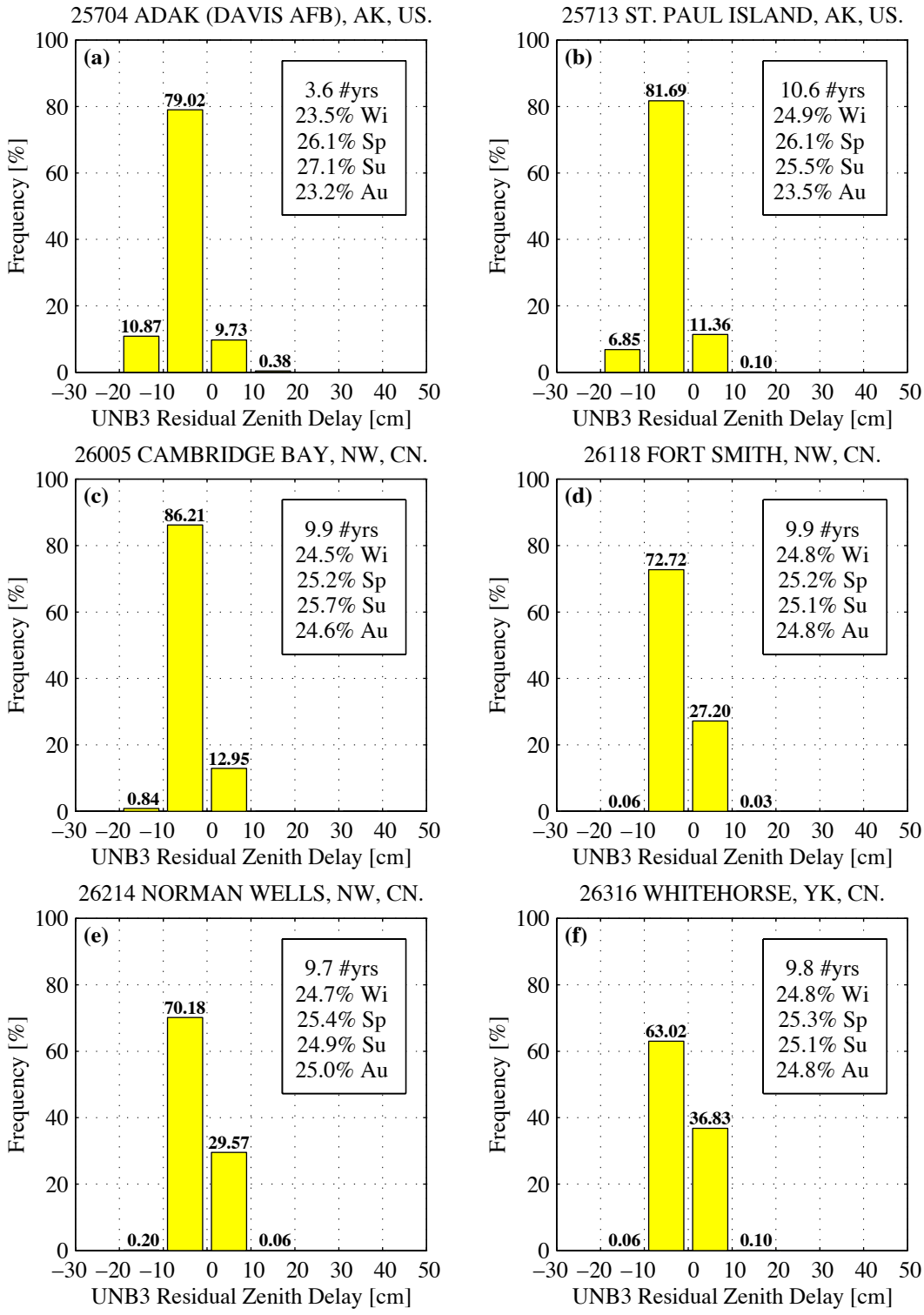

Figure C.31a–f. UNB3 model error histograms for stations 25704, 25713, 26005, 26118, 26214, and 26316.

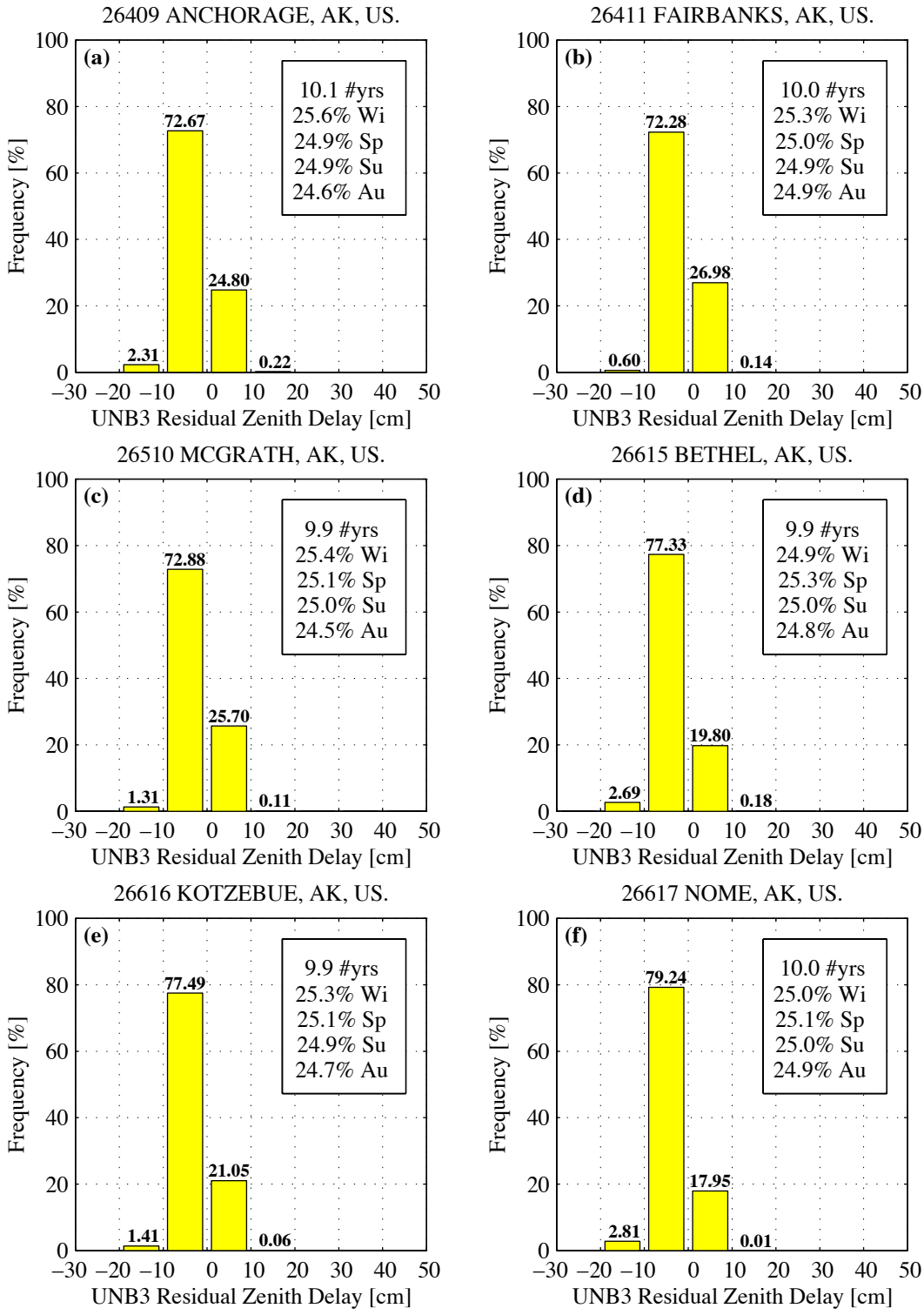

Figure C.32a–f. UNB3 model error histograms for stations 26409, 26411, 26510, 26615, 26616, and 26617.

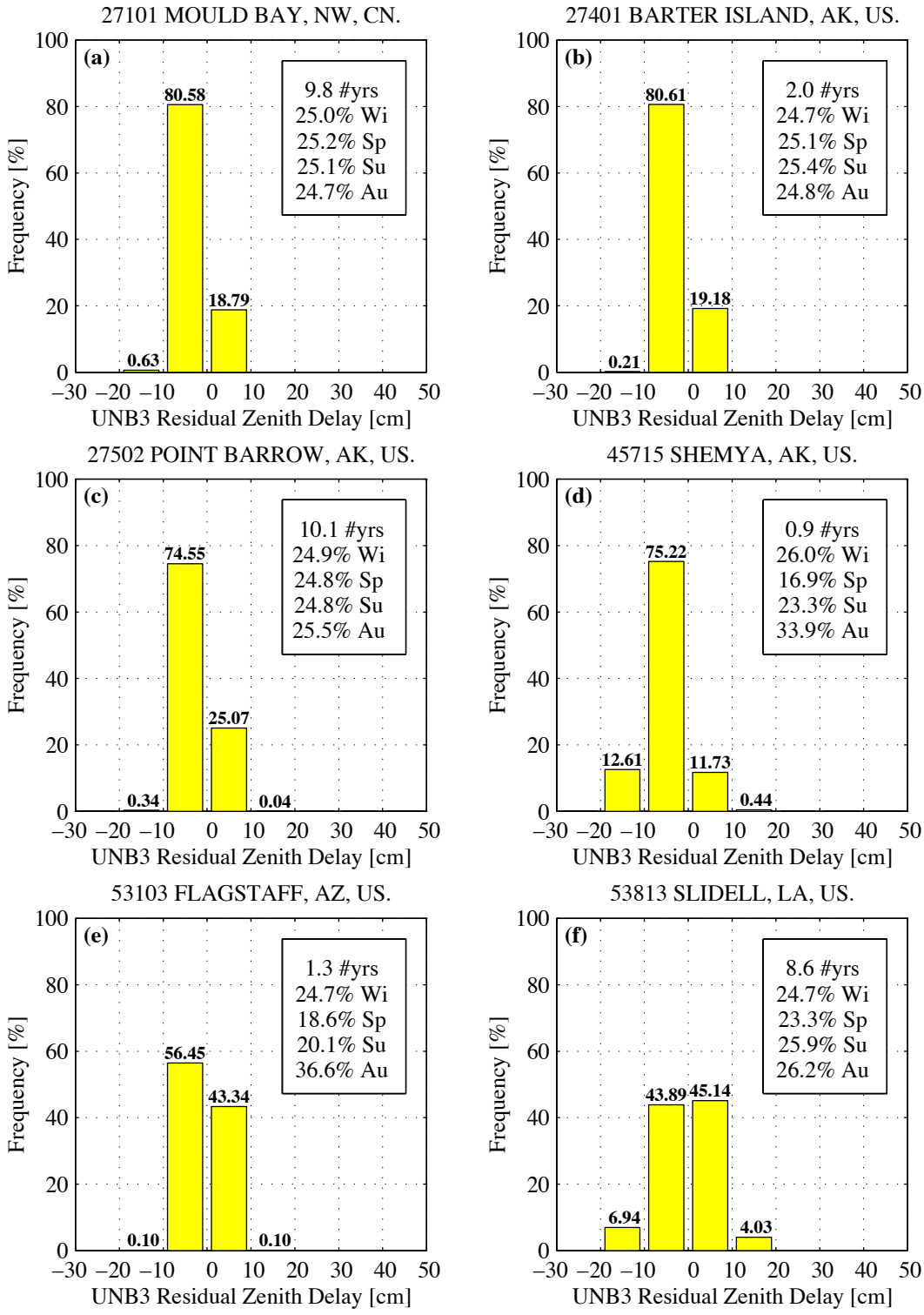

Figure C.33a–f. UNB3 model error histograms for stations 27101, 27401, 27502, 45715, 53103, and 53813.

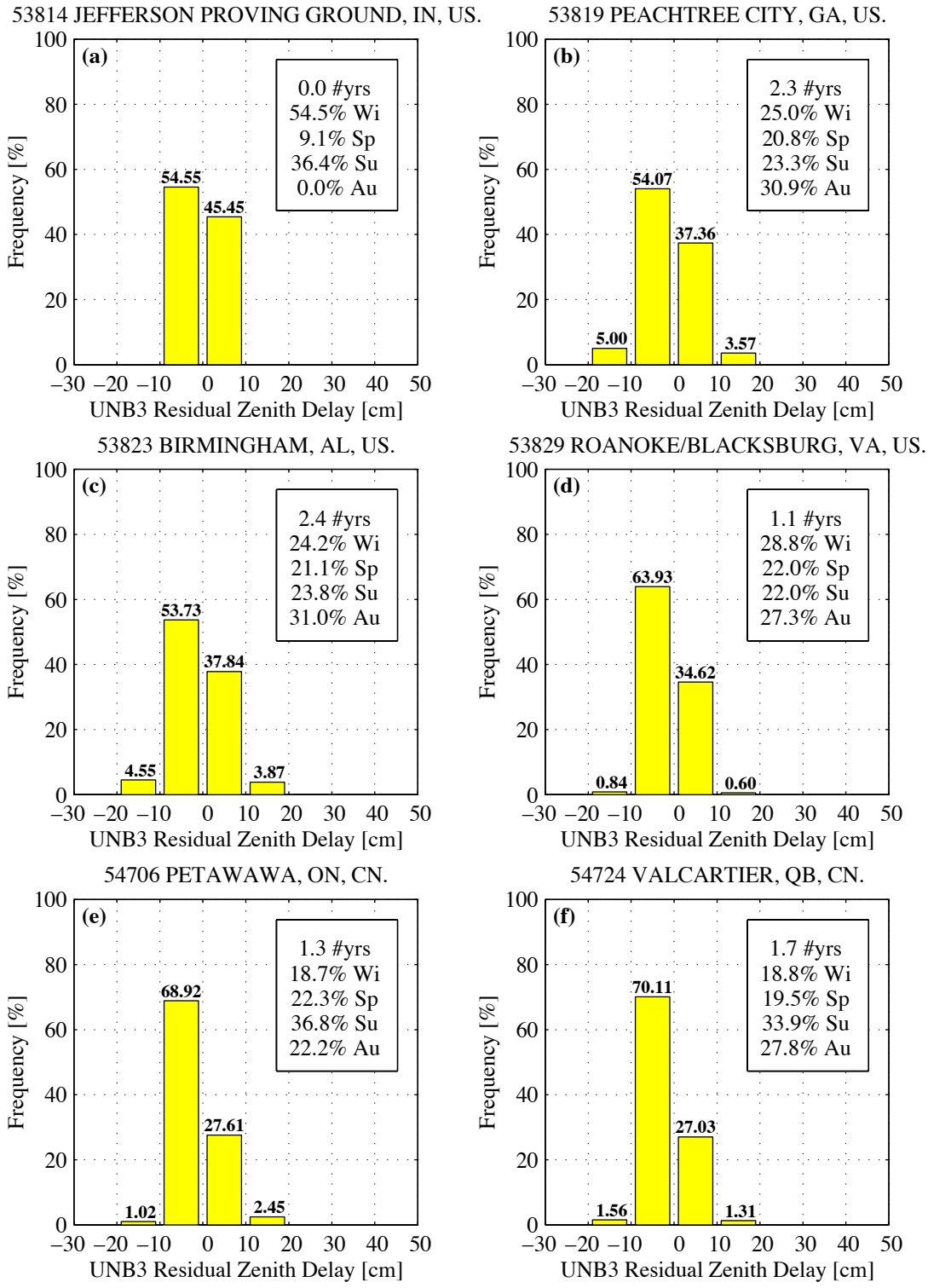

Figure C.34a–f. UNB3 model error histograms for stations 53814, 53819, 53823, 53829, 54706, and 54724.

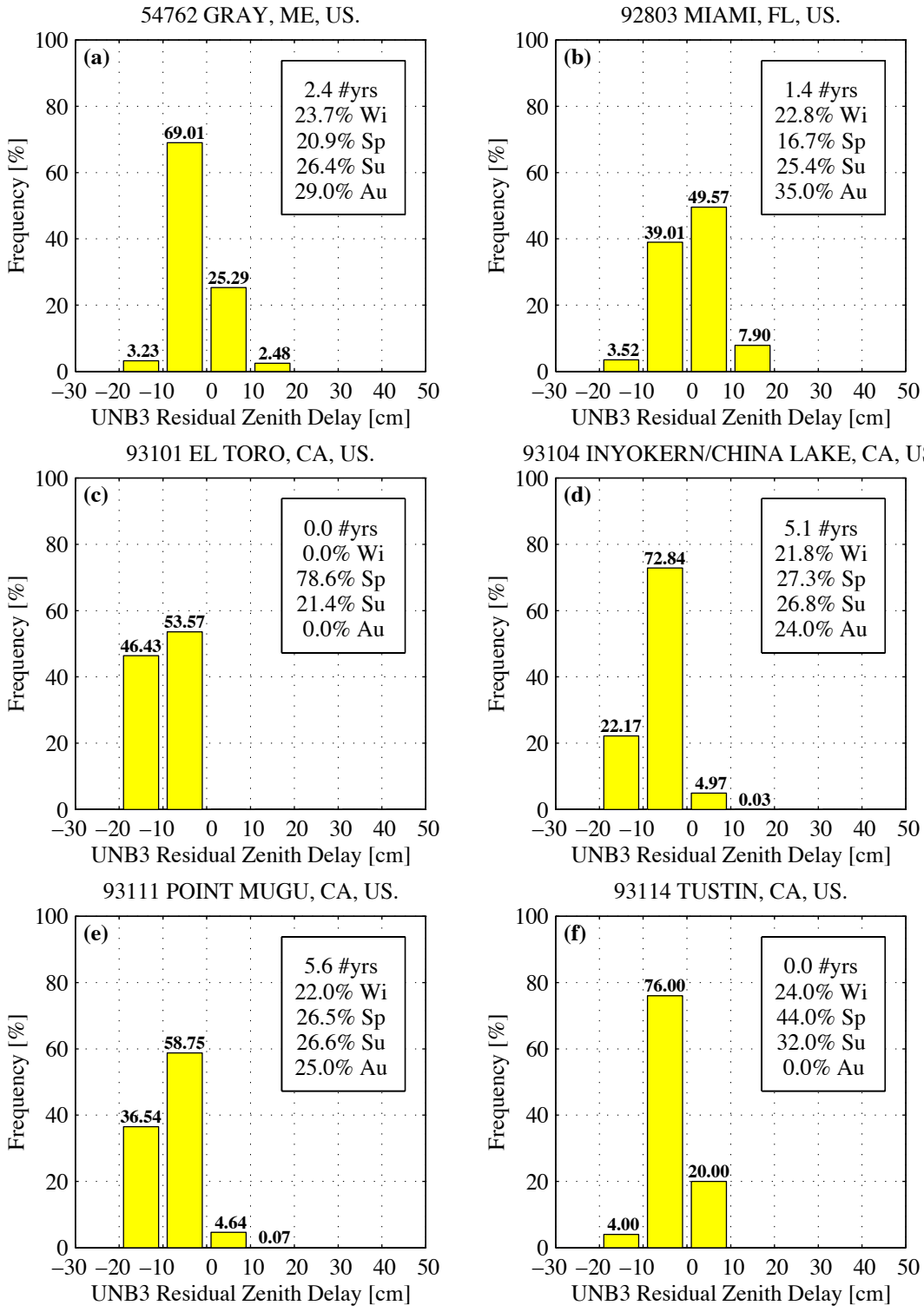

Figure C.35a–f. UNB3 model error histograms for stations 54762, 92803, 93101, 93104, 93111, and 93114.

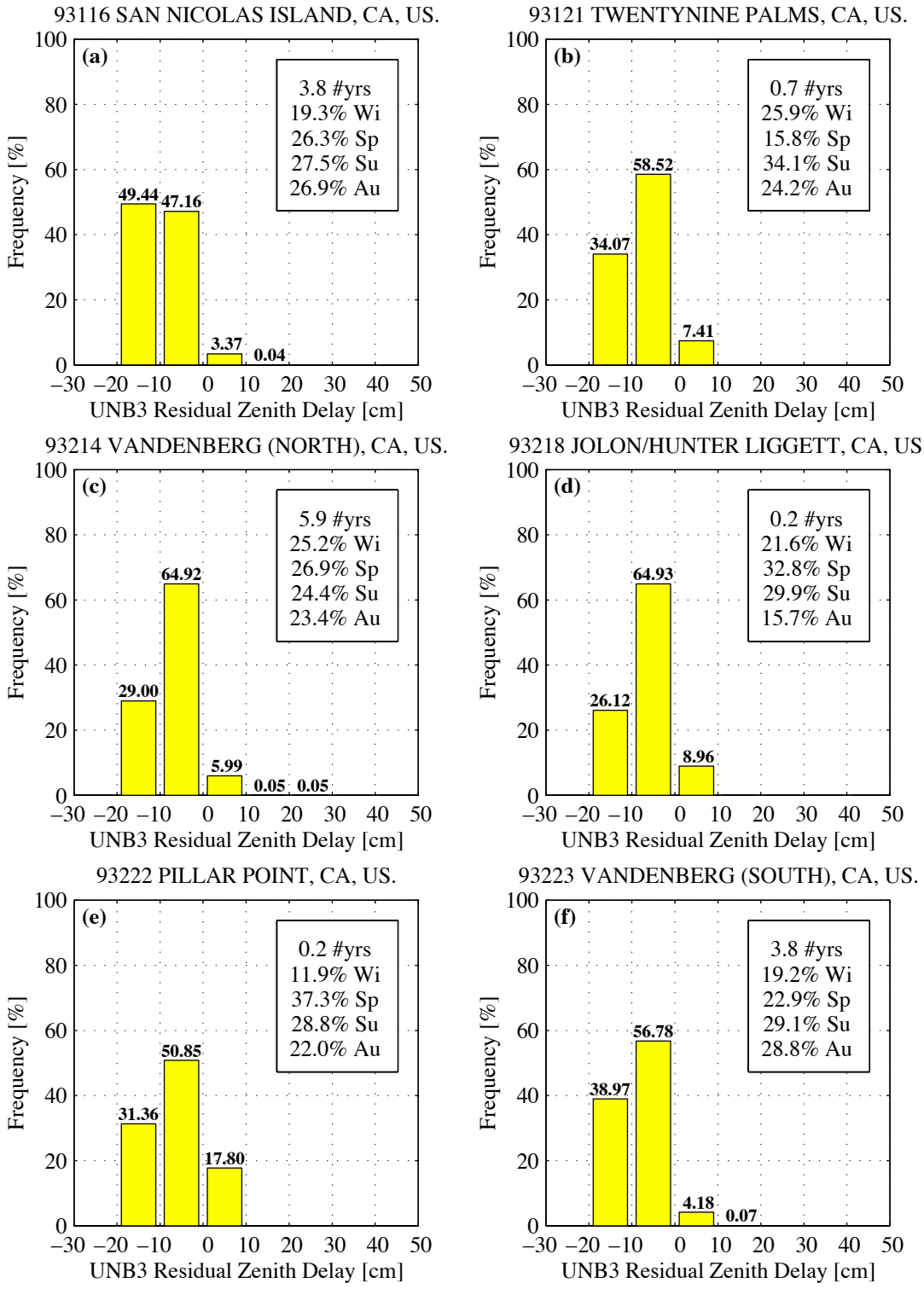

Figure C.36a–f. UNB3 model error histograms for stations 93116, 93121, 93214, 93218, 93222, and 93223.

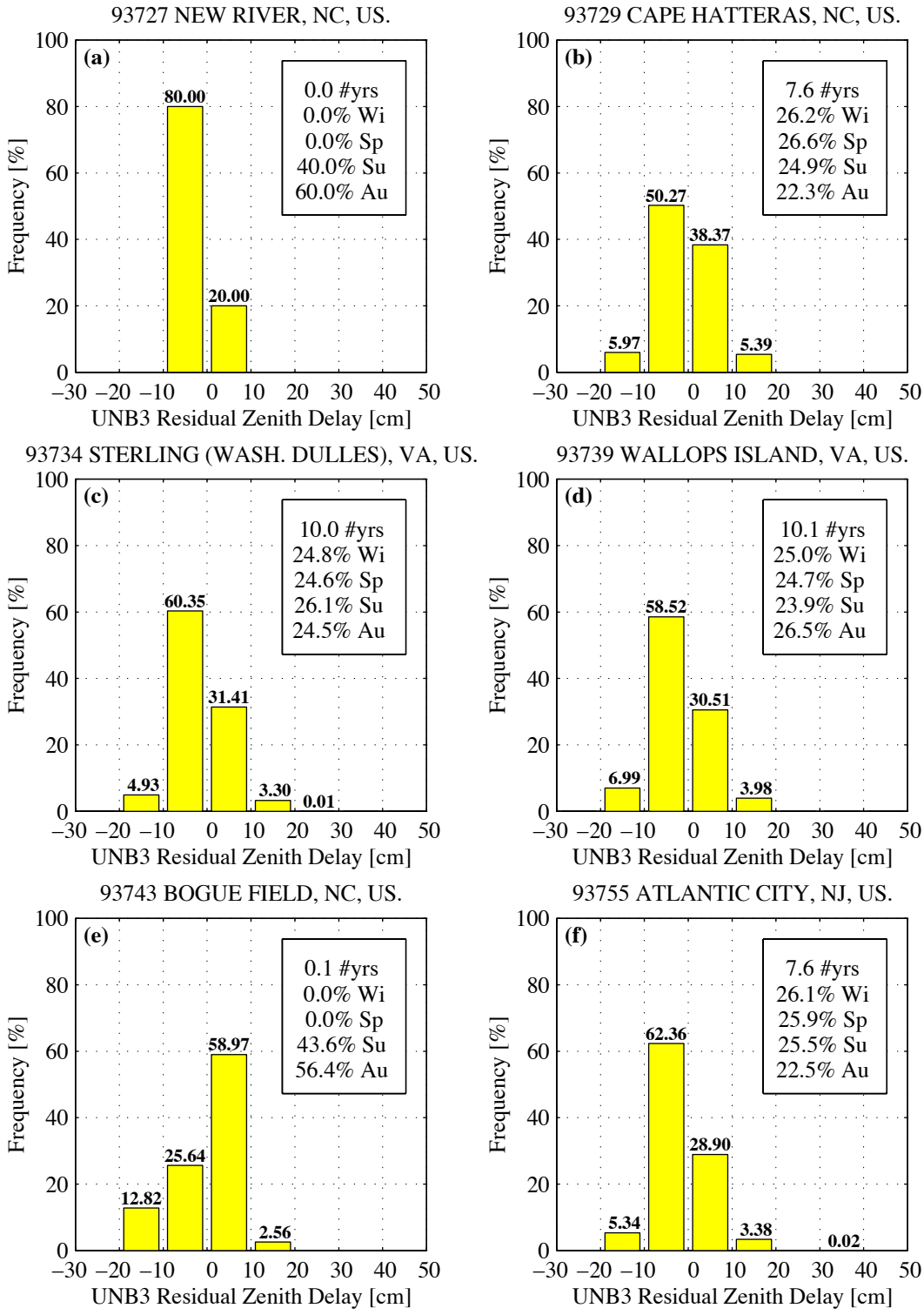

Figure C.37a–f. UNB3 model error histograms for stations 93727, 93729, 93734, 93739, 93743, and 93755.

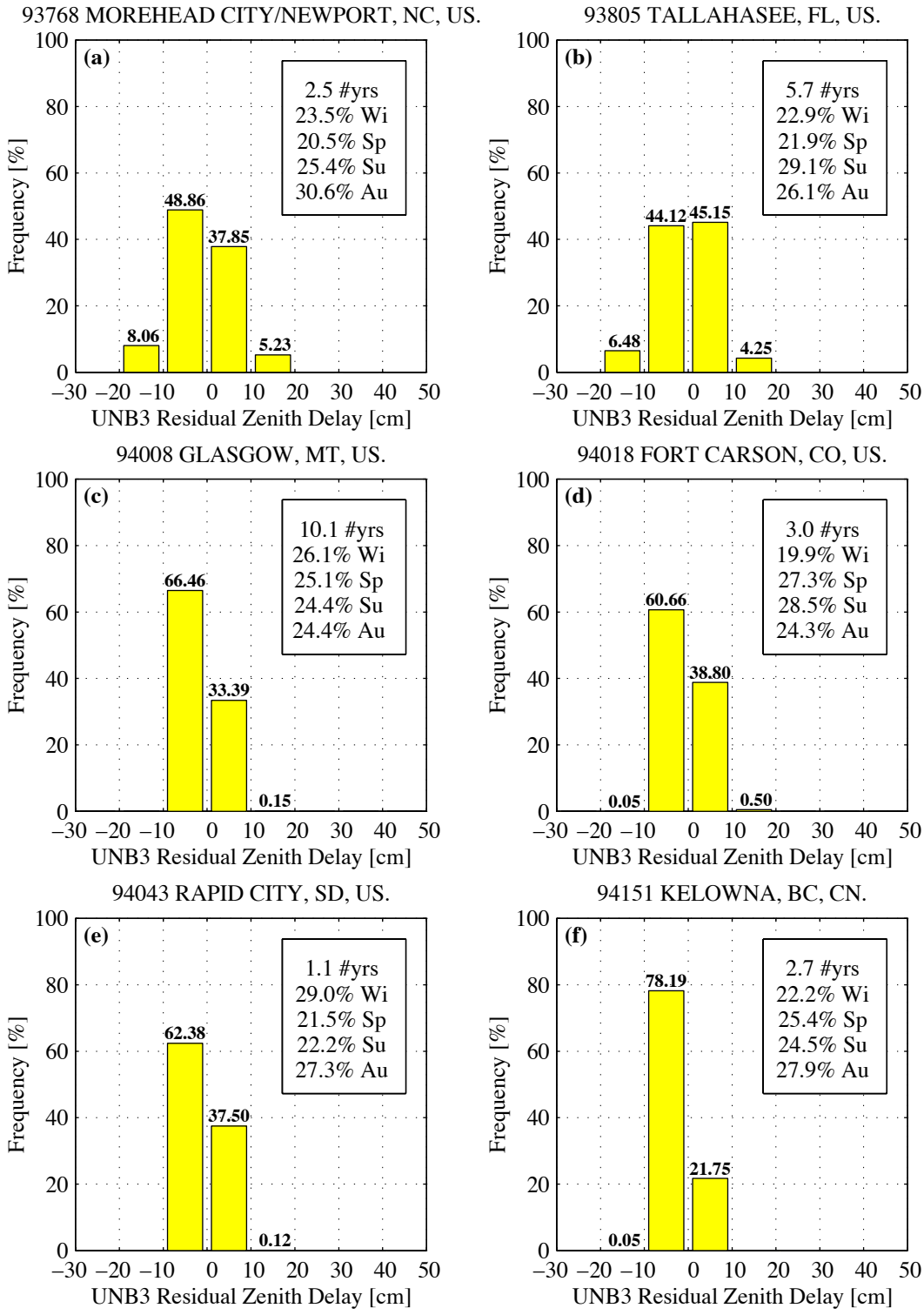

Figure C.38a–f. UNB3 model error histograms for stations 93768, 93805, 94008, 94018, 94043, and 94151.

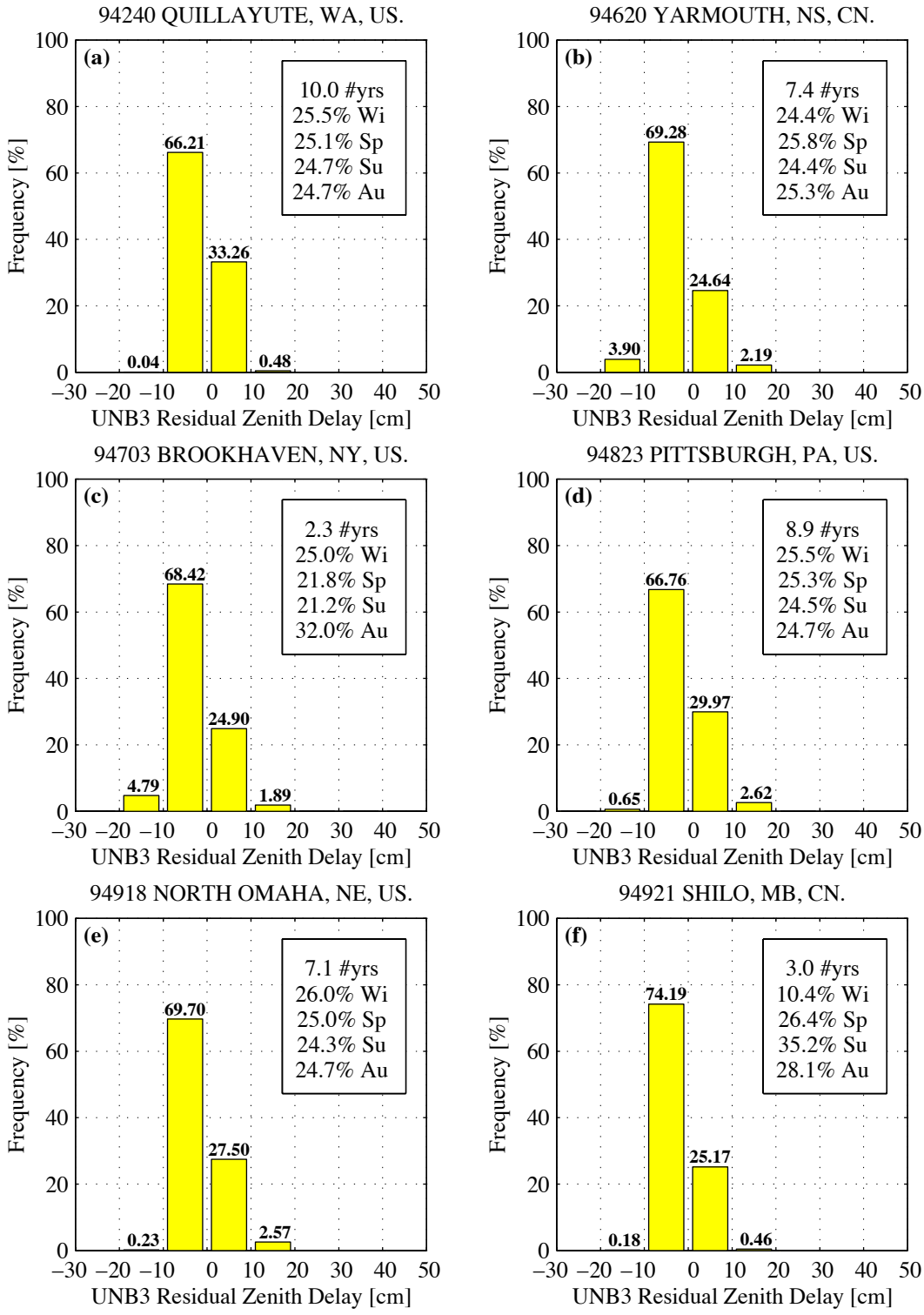

Figure C.39a–f. UNB3 model error histograms for stations 94240, 94620, 94703, 94823, 94918, and 94921.

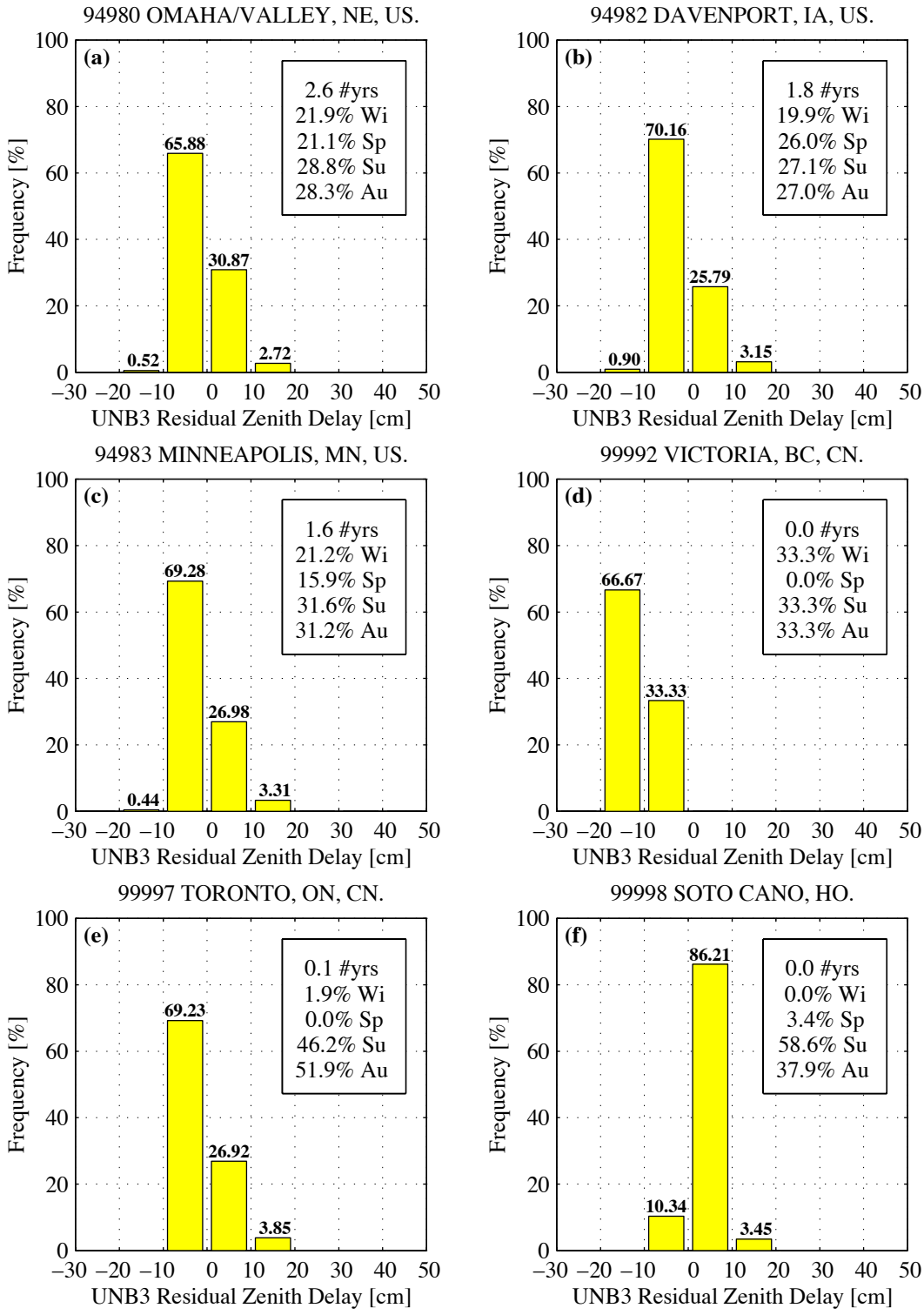

Figure C.40a–f. UNB3 model error histograms for stations 94980, 94982, 94983, 99992, 99997, and 99998.

APPENDIX D.

WET DELAY AND MODEL RESIDUAL SCATTER PLOTS

The following diagrams present both the measured wet zenith delay, and the full UNB3 model residual (including the small hydrostatic portion), on a station-by-station basis for the whole ten-year data set. The actual zenith delays caused by the atmospheric water vapour are displayed in the upper portion of each figure, over which are superimposed two curves. The unbroken curve represents the UNB3 model values for the station as a function of its location and the time-of-year. The broken curve represents the best-fit sinusoid (in a least-squares sense) to the data. This curve is of the same formulation as equation (3.5) and the values for the mean (μ), amplitude (ψ) and phase offset (ϕ), rounded to the nearest centimetre and day-of-year, are recorded down the right-hand vertical axis.

The lower portion of each figure displays the model errors, with the mean (μ) and standard deviation (σ) statistics recorded down the right-hand vertical axis. The broken horizontal lines represent the $\mu+2\sigma$ and $\mu-2\sigma$ ($\approx$95%) limits computed from these statistics (note that the sign of the mean is retained). The numerical values of these limits are labelled adjacent to each line.

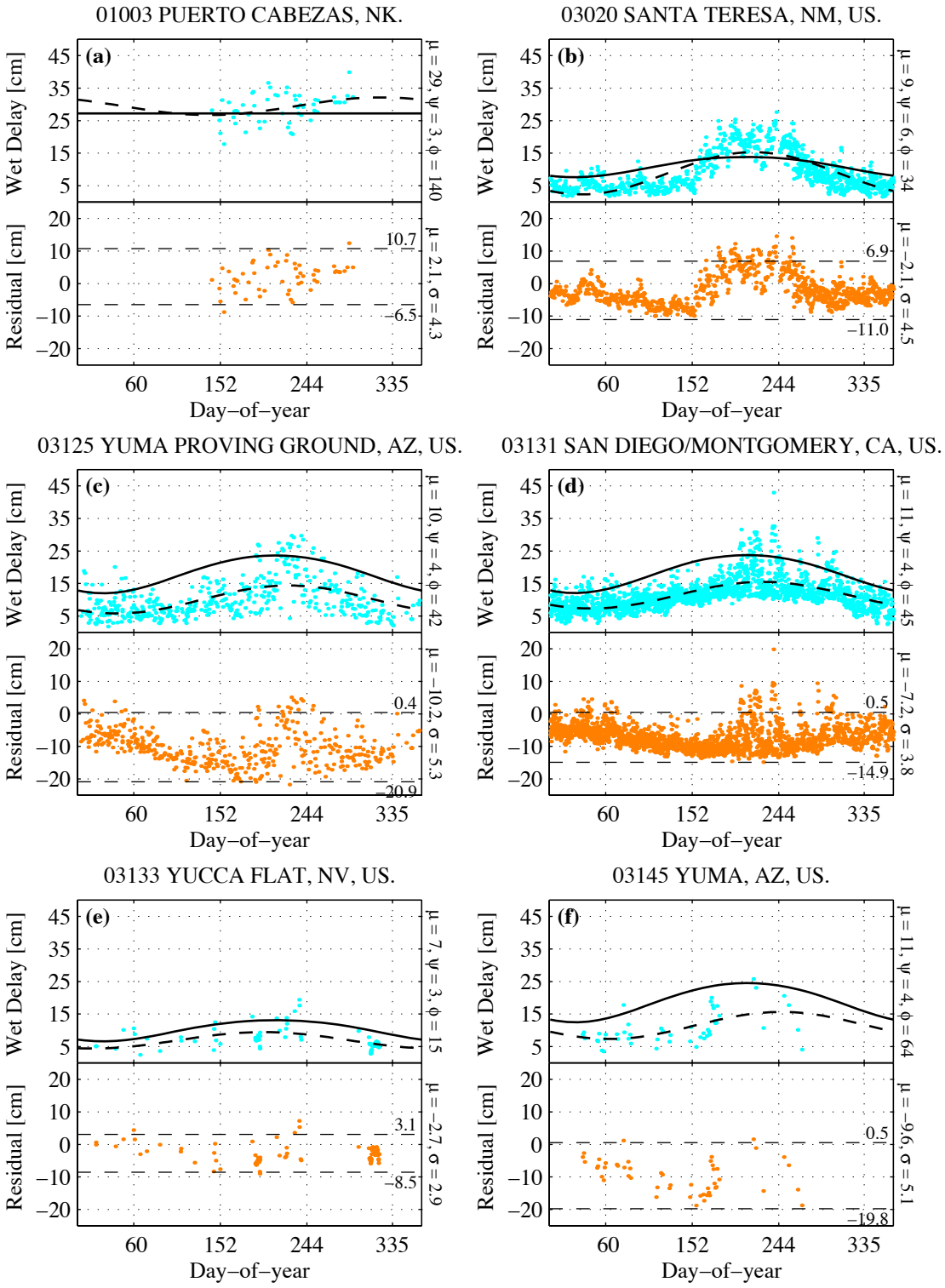

Figure D.1a–f. Wet zenith delays and UNB3 residuals for stations 01003, 03020, 03125, 03131, 03133, and 03145.

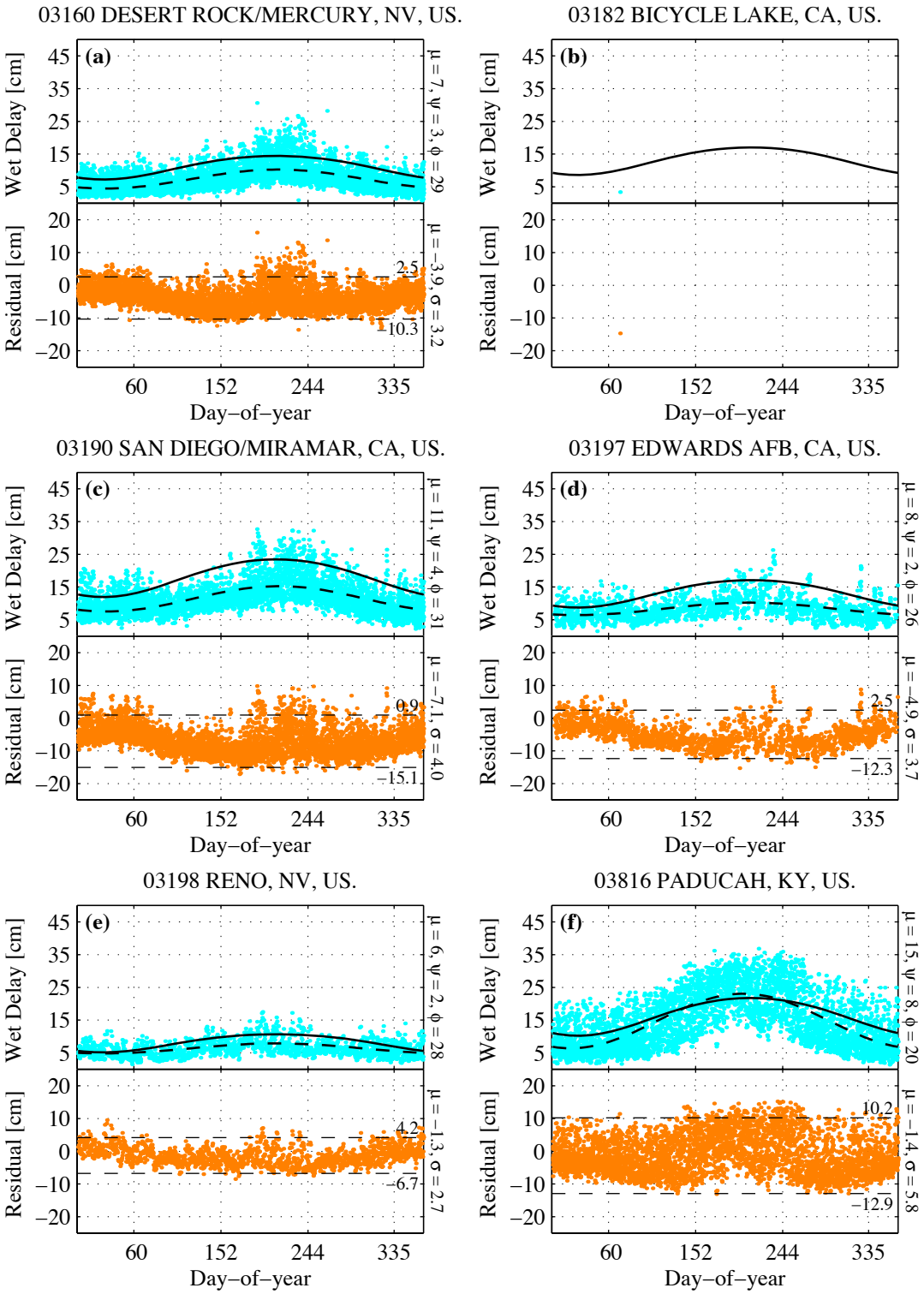

Figure D.2a–f. Wet zenith delays and UNB3 residuals for stations 03160, 03182, 03190, 03197, 03198, and 03816.

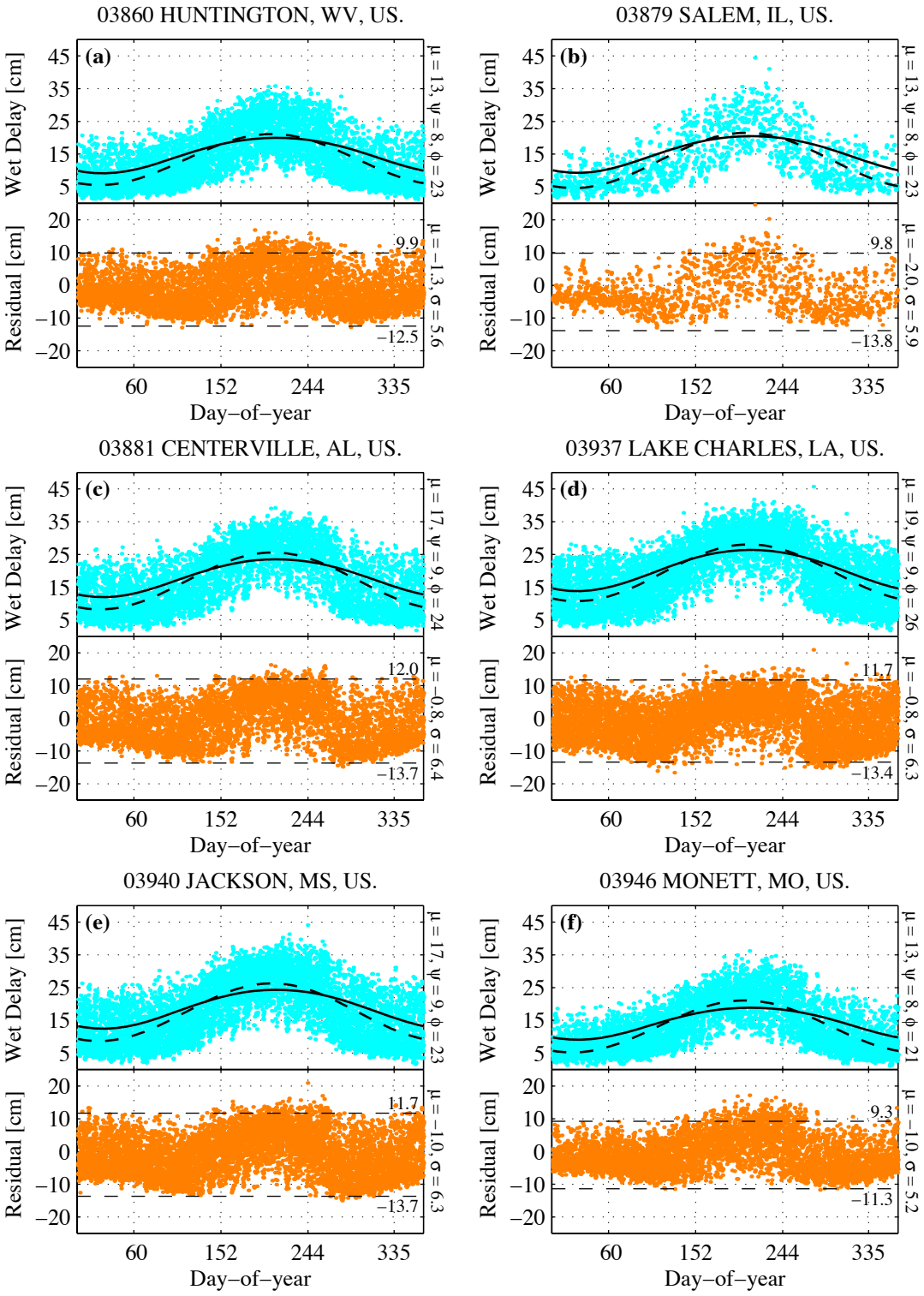

Figure D.3a–f. Wet zenith delays and UNB3 residuals for stations 03860, 03879, 03881, 03937, 03940, and 03946.

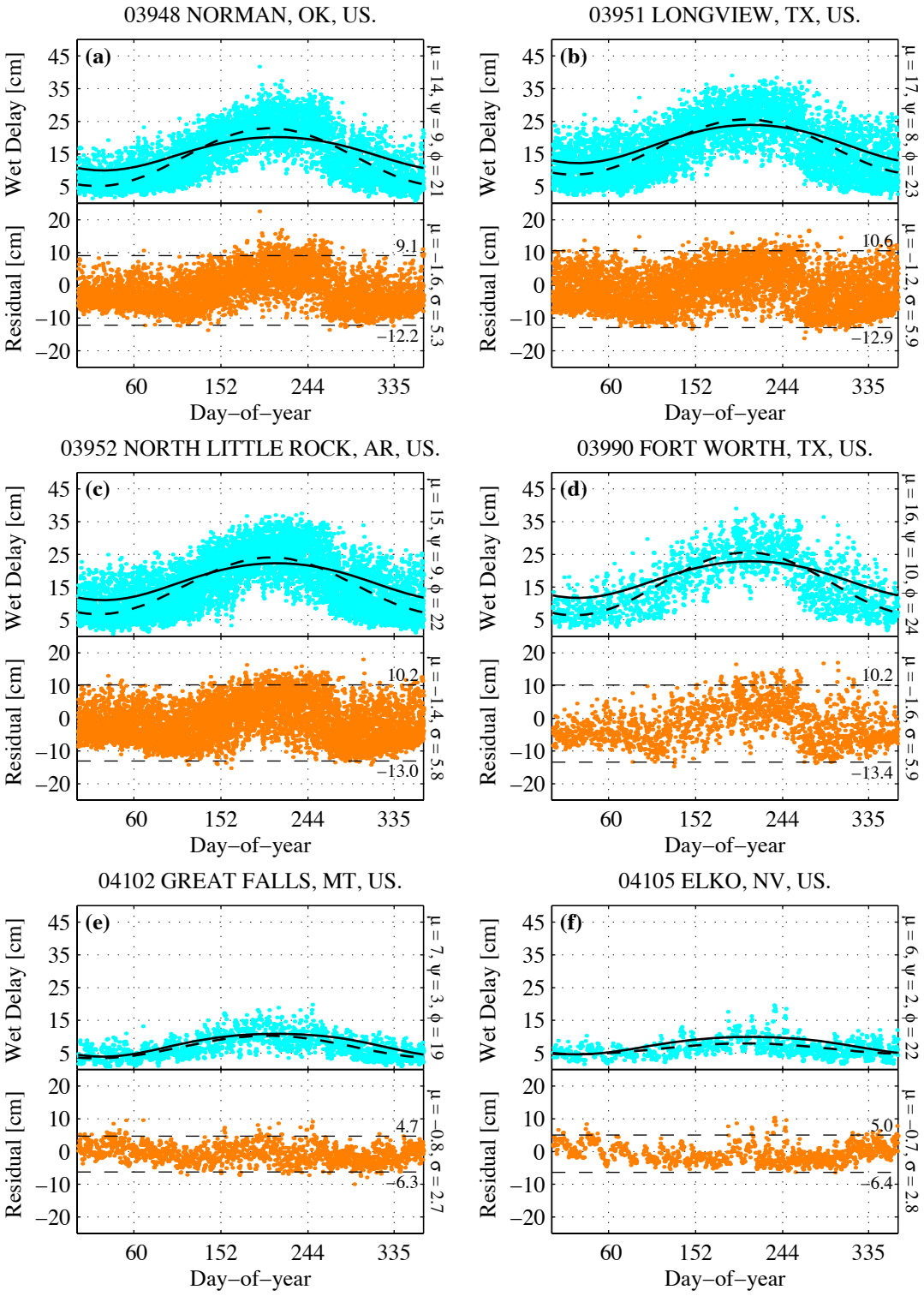

Figure D.4a–f. Wet zenith delays and UNB3 residuals for stations 03948, 03951, 03952, 03990, 04102, and 04105.

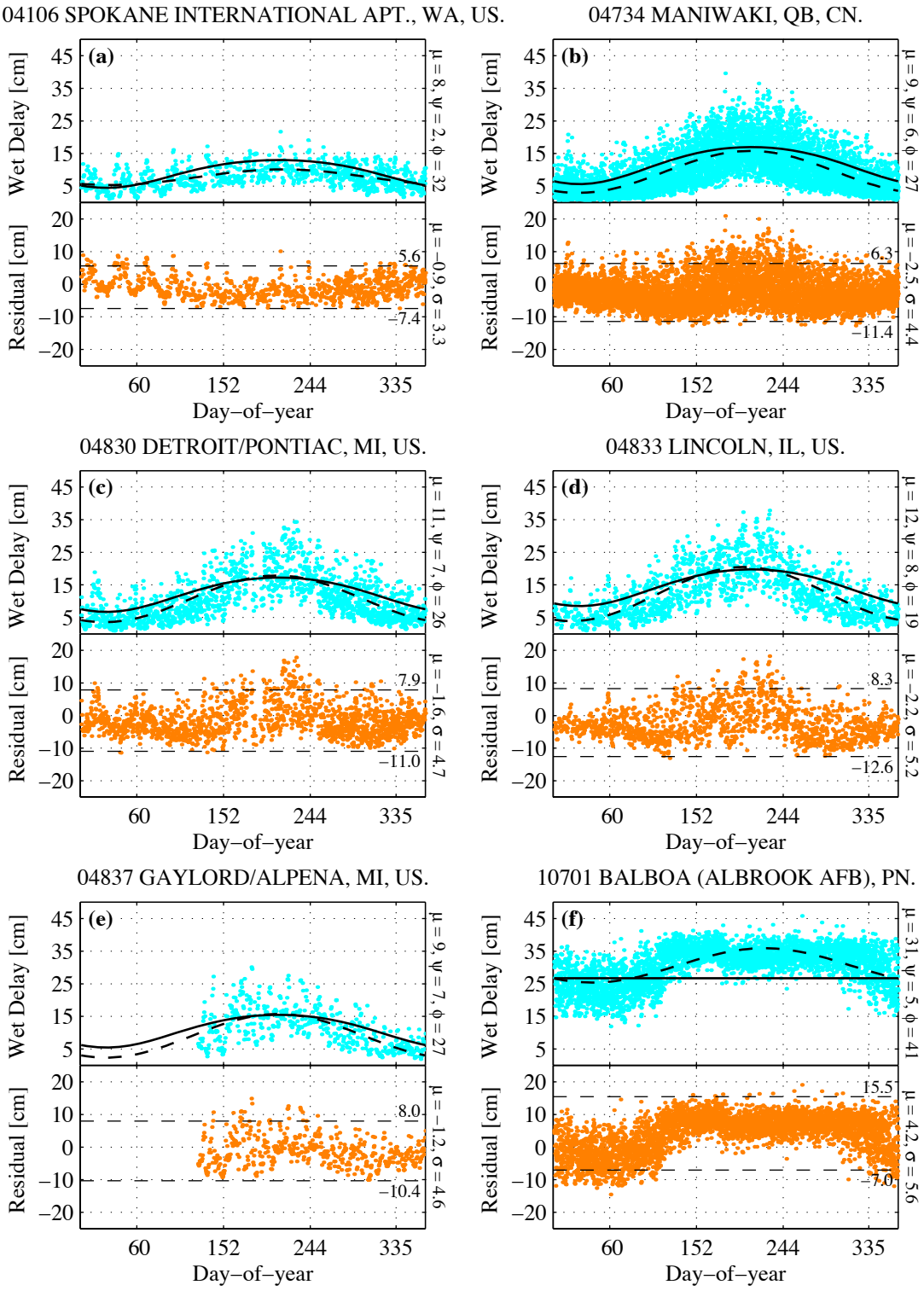

Figure D.5a–f. Wet zenith delays and UNB3 residuals for stations 04106, 04734, 04830, 04833, 04837, and 10701.

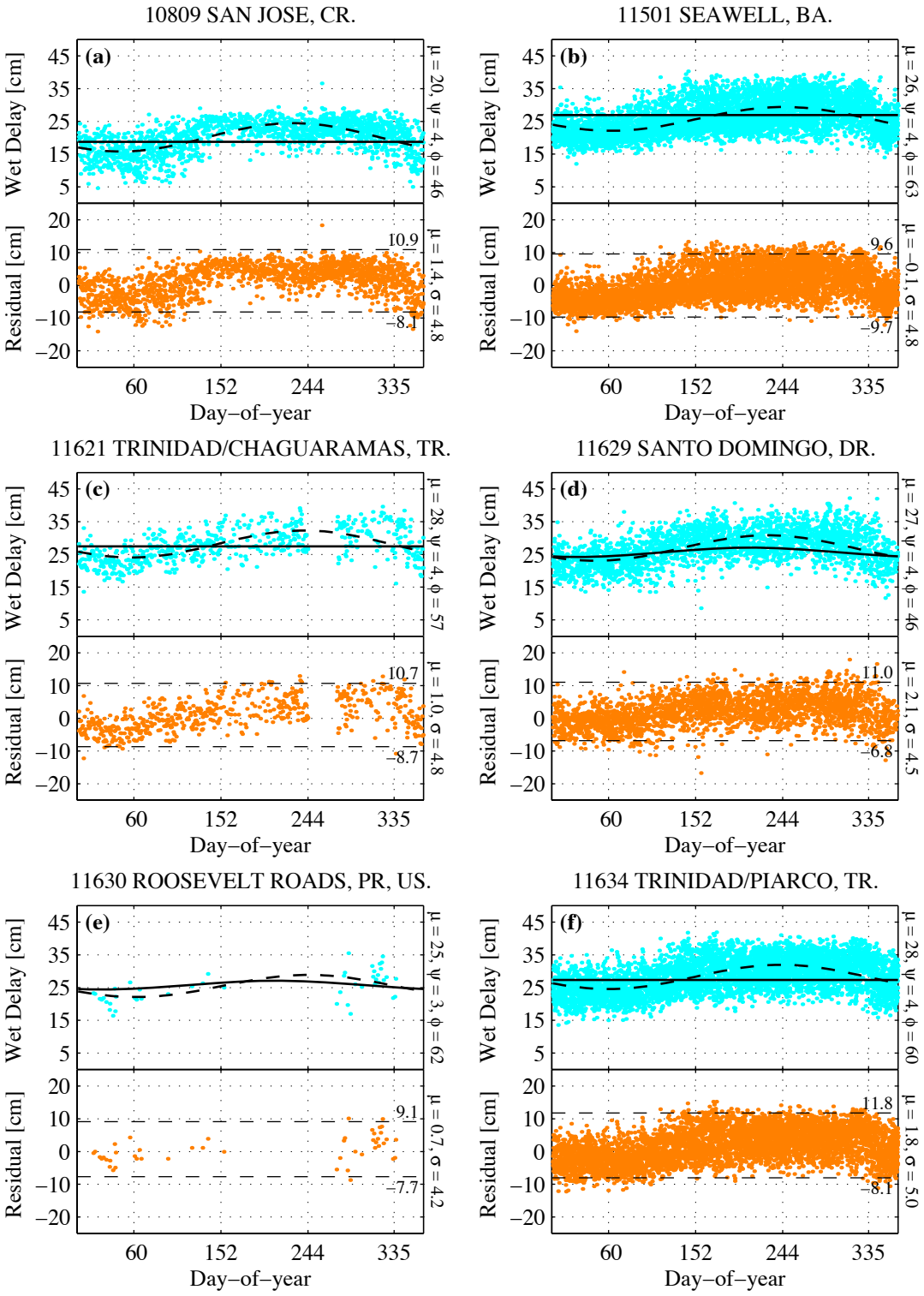

Figure D.6a–f. Wet zenith delays and UNB3 residuals for stations 10809, 11501, 11621, 11629, 11630, and 11634.

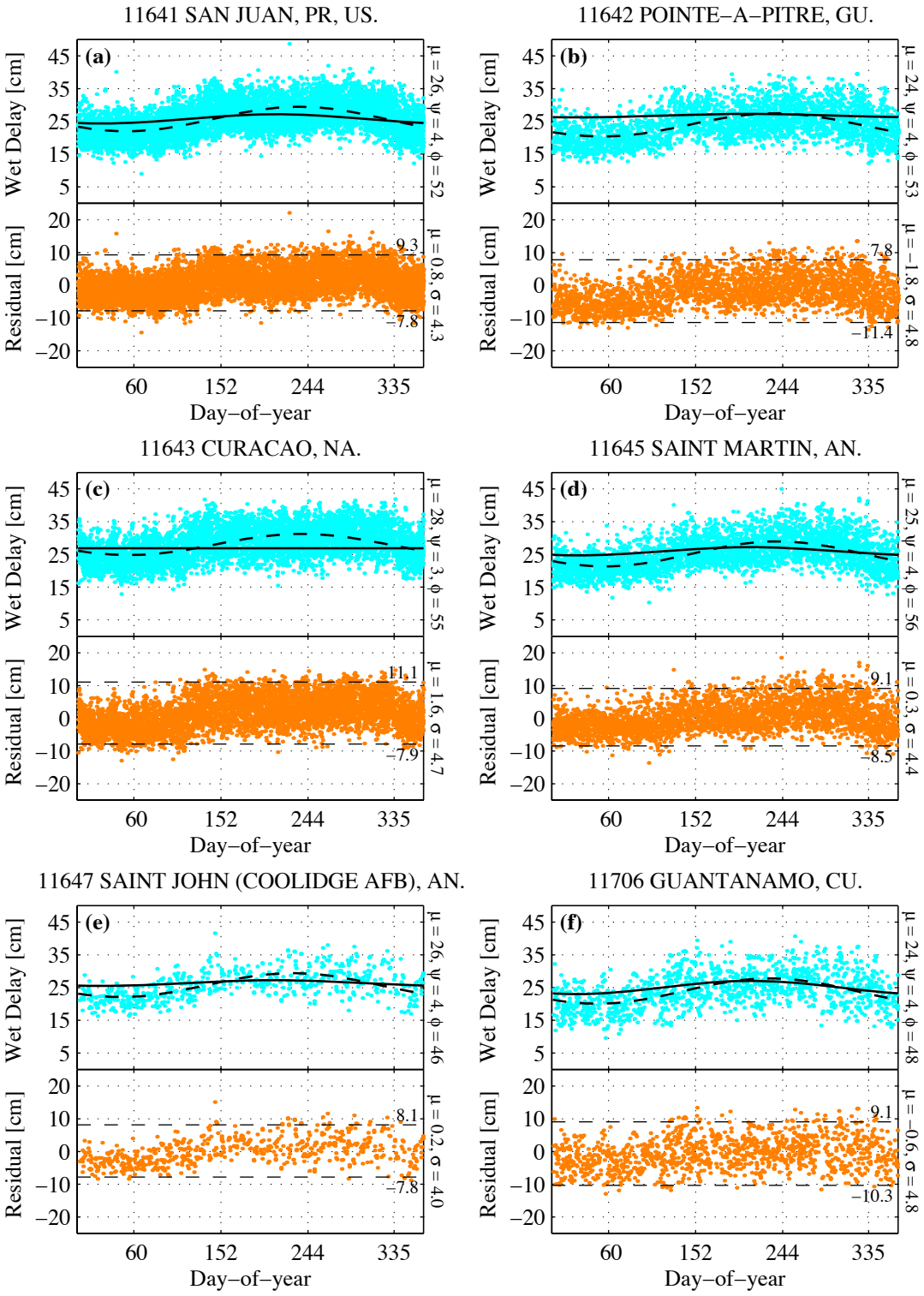

Figure D.7a–f. Wet zenith delays and UNB3 residuals for stations 11641, 11642, 11643, 11645, 11647, and 11706.

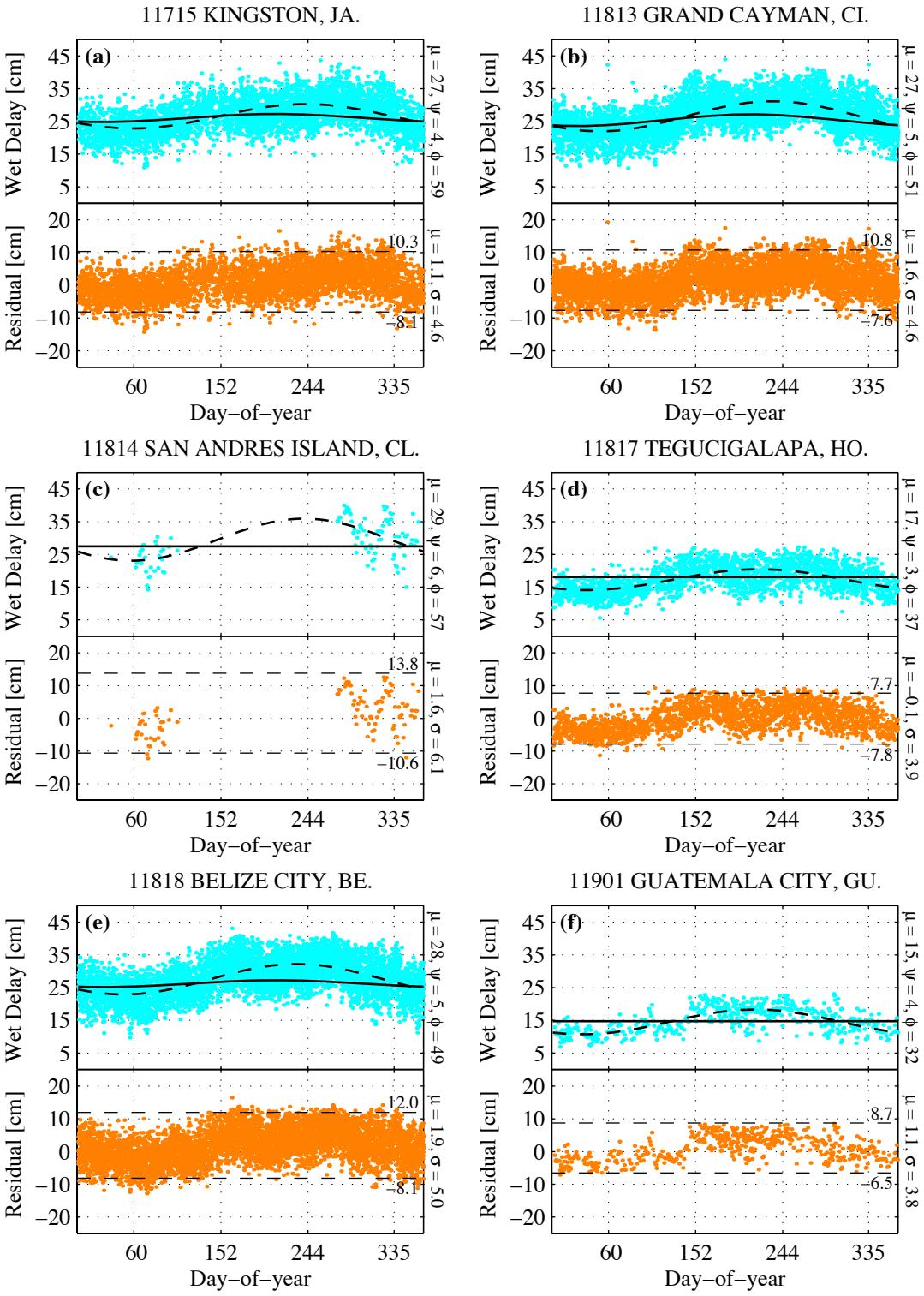

Figure D.8a–f. Wet zenith delays and UNB3 residuals for stations 11715, 11813, 11814, 11817, 11818, and 11901.

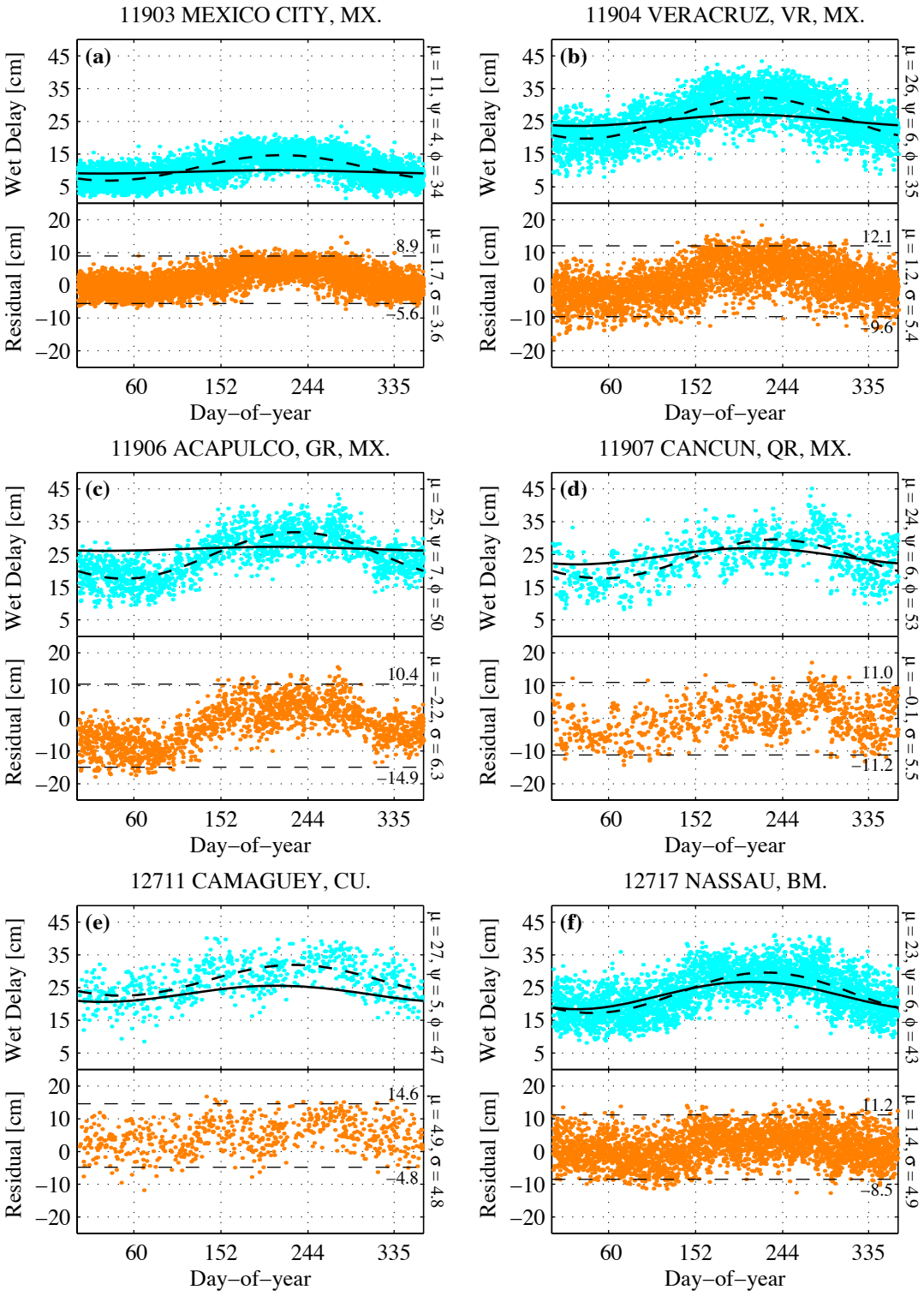

Figure D.9a–f. Wet zenith delays and UNB3 residuals for stations 11903, 11904, 11906, 11907, 12711, and 12717.

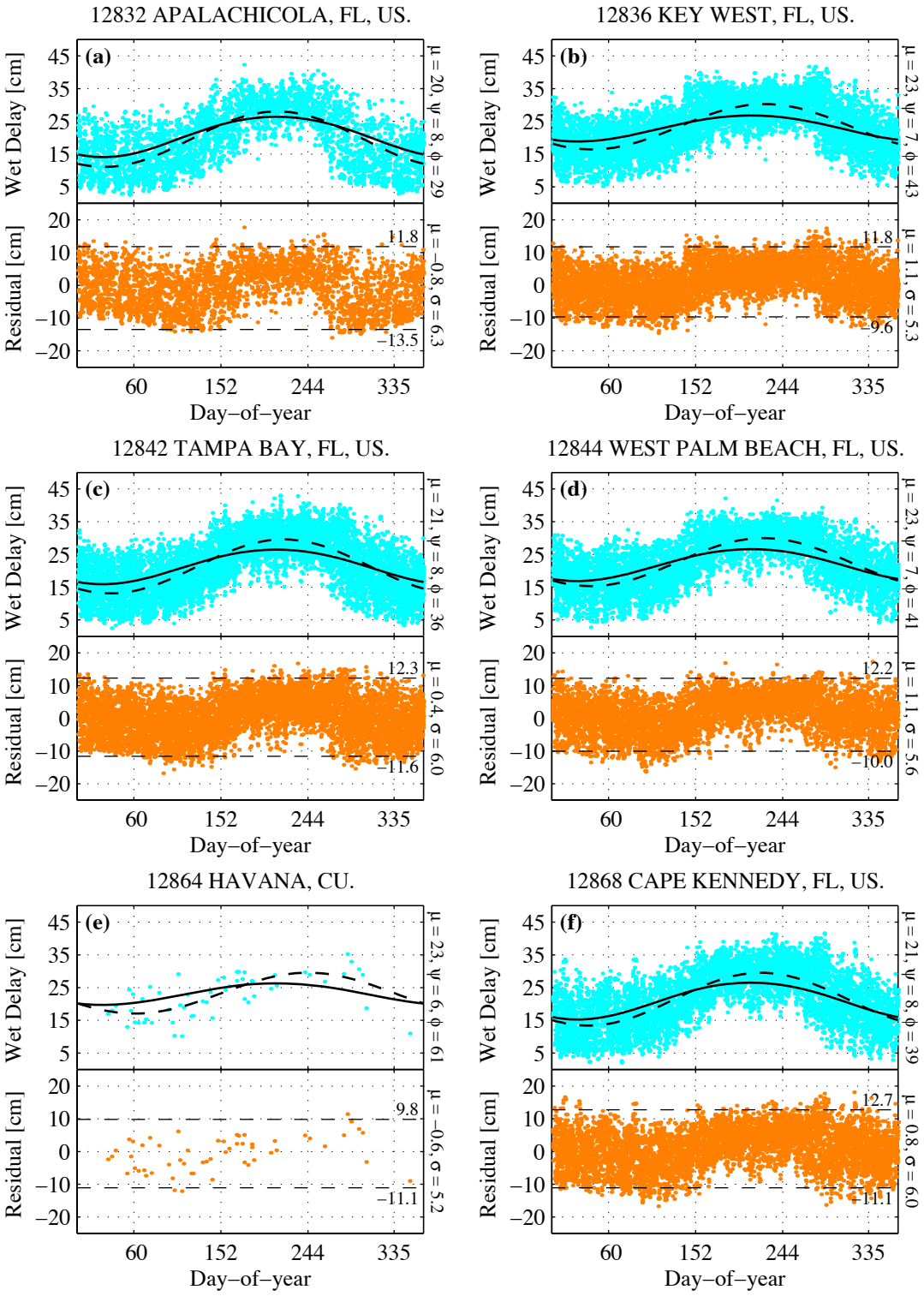

Figure D.10a–f. Wet zenith delays and UNB3 residuals for stations 12832, 12836, 12842, 12844, 12864, and 12868.

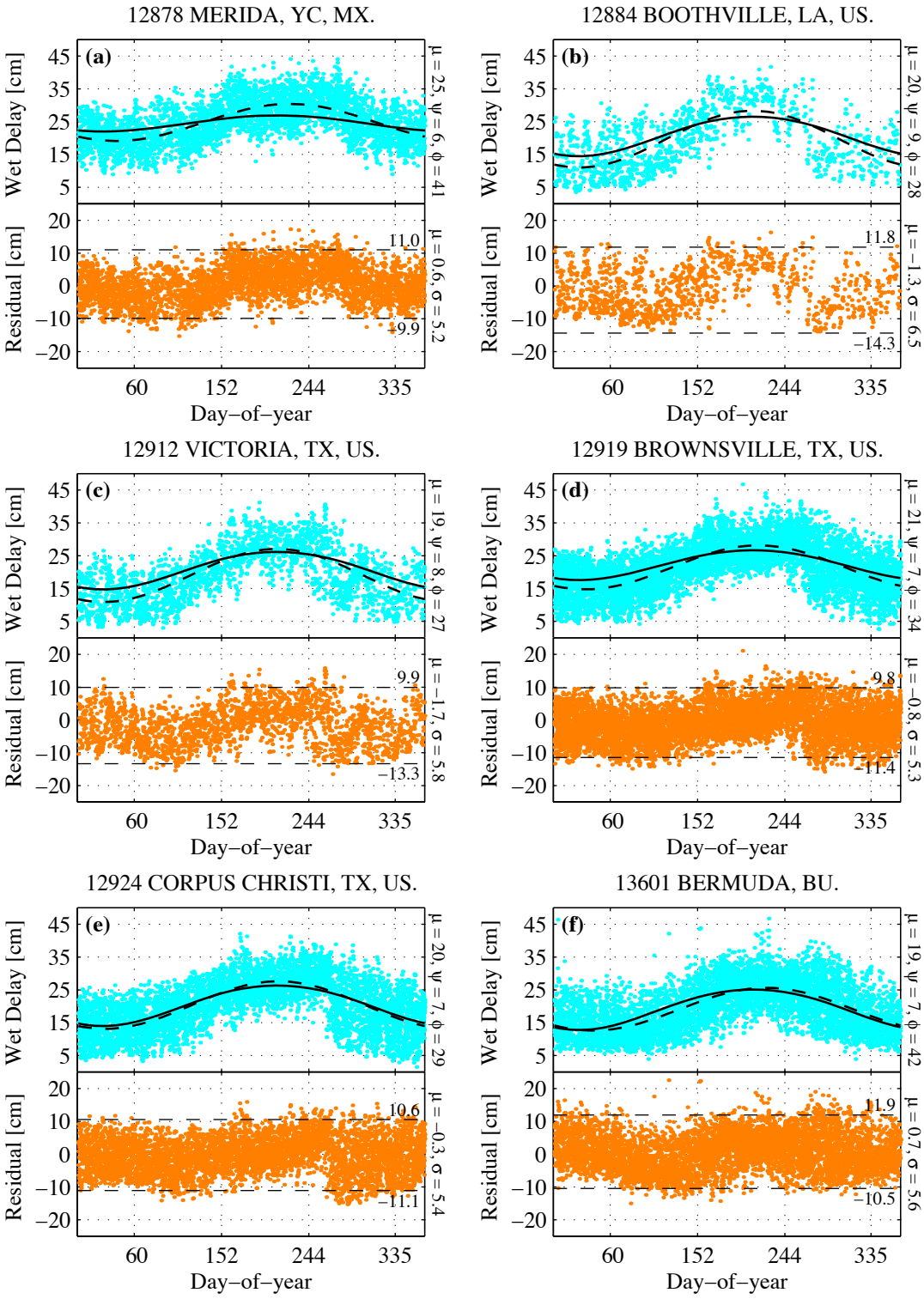

Figure D.11a–f. Wet zenith delays and UNB3 residuals for stations 12878, 12884, 12912, 12919, 12924, and 13601.

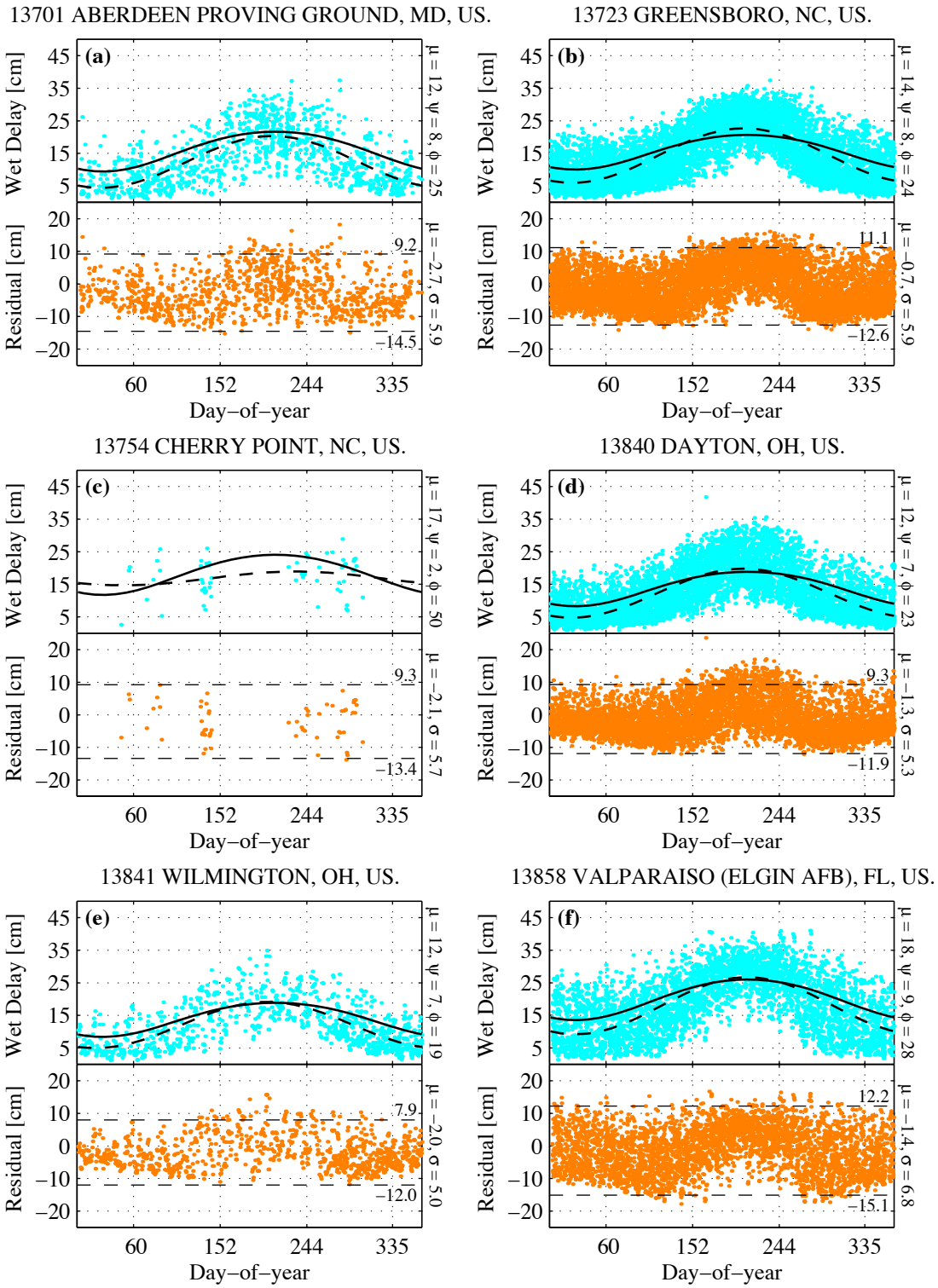

Figure D.12a–f. Wet zenith delays and UNB3 residuals for stations 13701, 13723, 13754, 13840, 13841, and 13858.

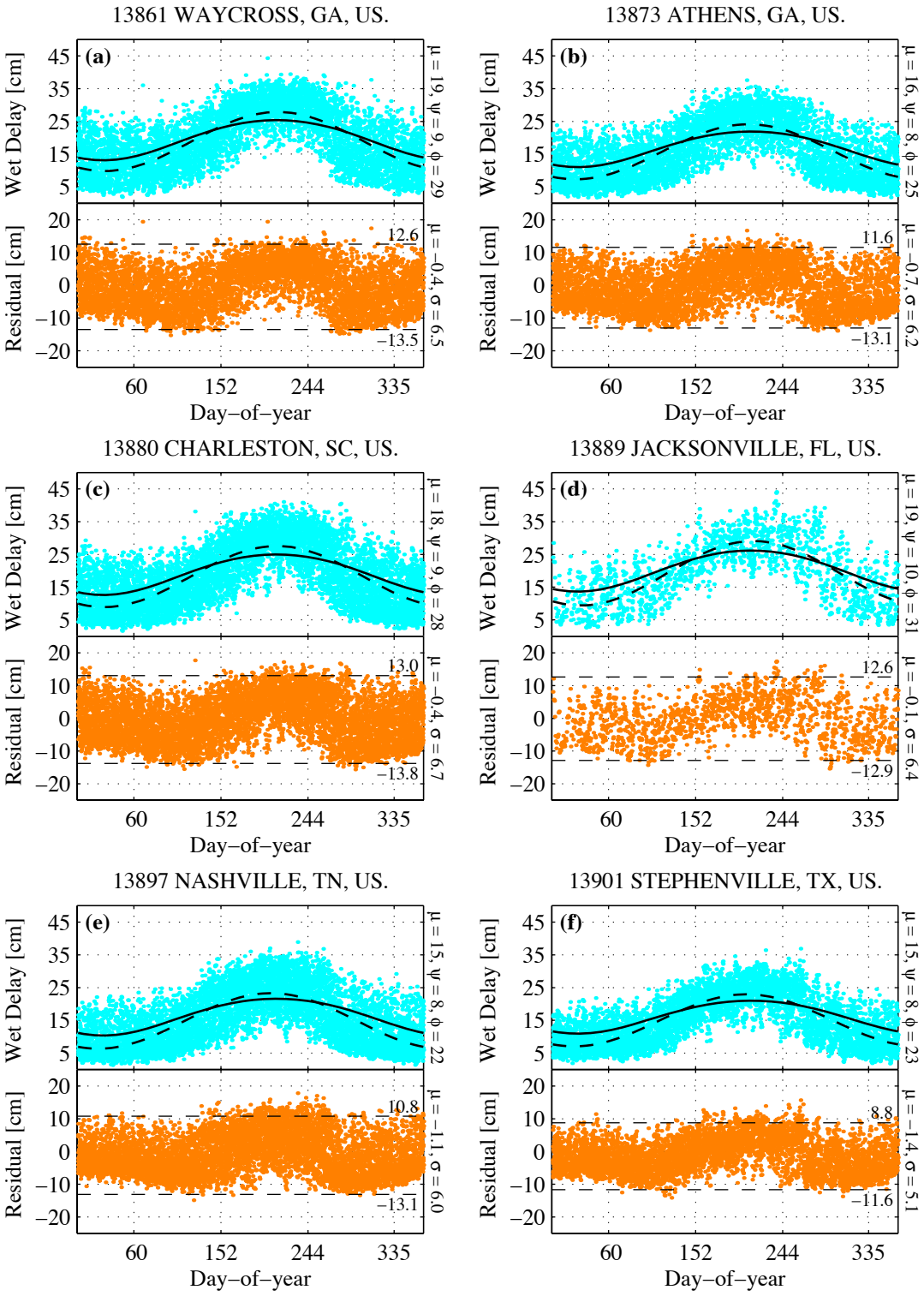

Figure D.13a–f. Wet zenith delays and UNB3 residuals for stations 13861, 13873, 13880, 13889, 13897, and 13901.

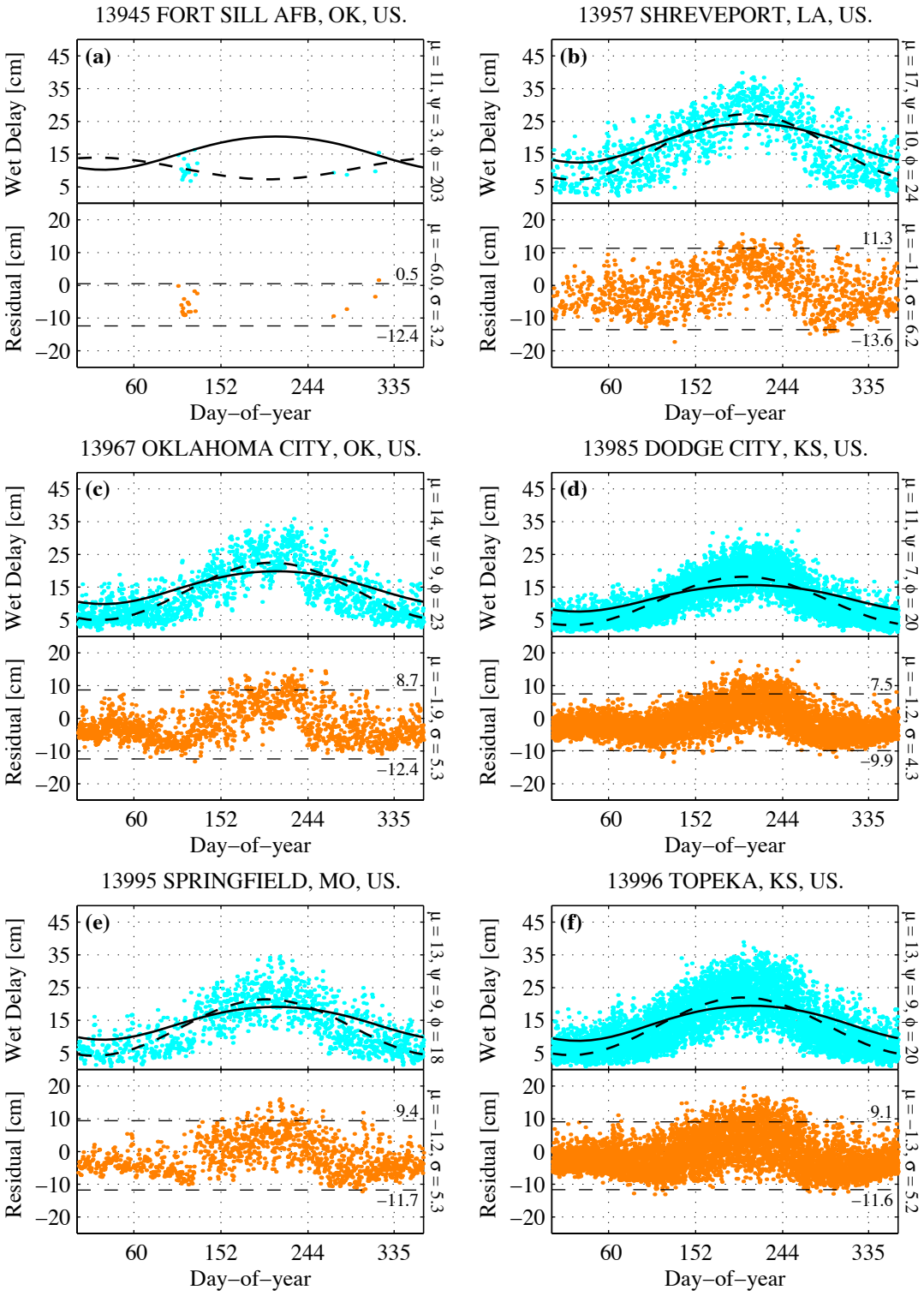

Figure D.14a–f. Wet zenith delays and UNB3 residuals for stations 13945, 13957, 13967, 13985, 13995, and 13996.

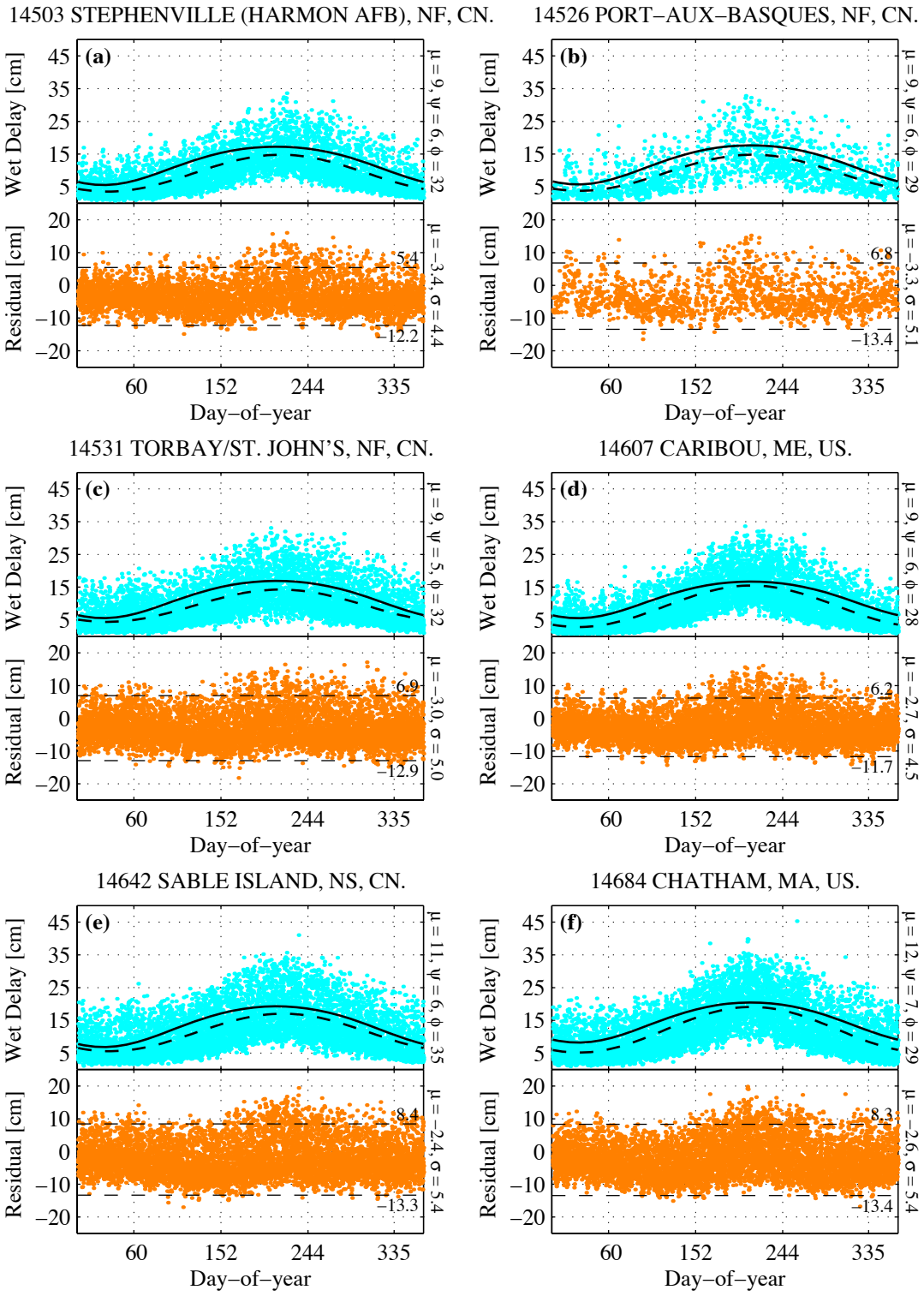

Figure D.15a–f. Wet zenith delays and UNB3 residuals for stations 14503, 14526, 14531, 14607, 14642, and 14684.

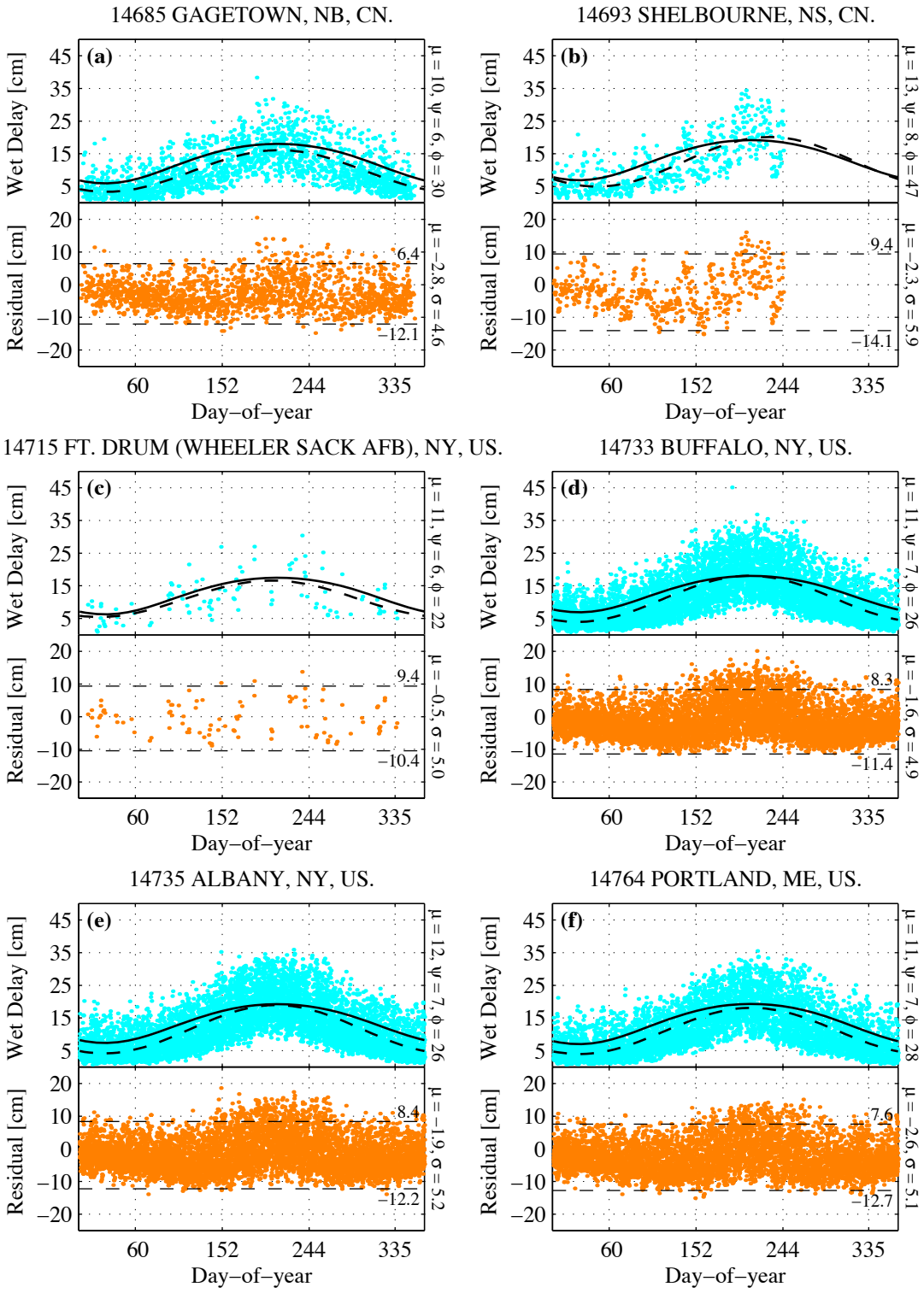

Figure D.16a–f. Wet zenith delays and UNB3 residuals for stations 14685, 14693, 14715, 14733, 14735, and 14764.

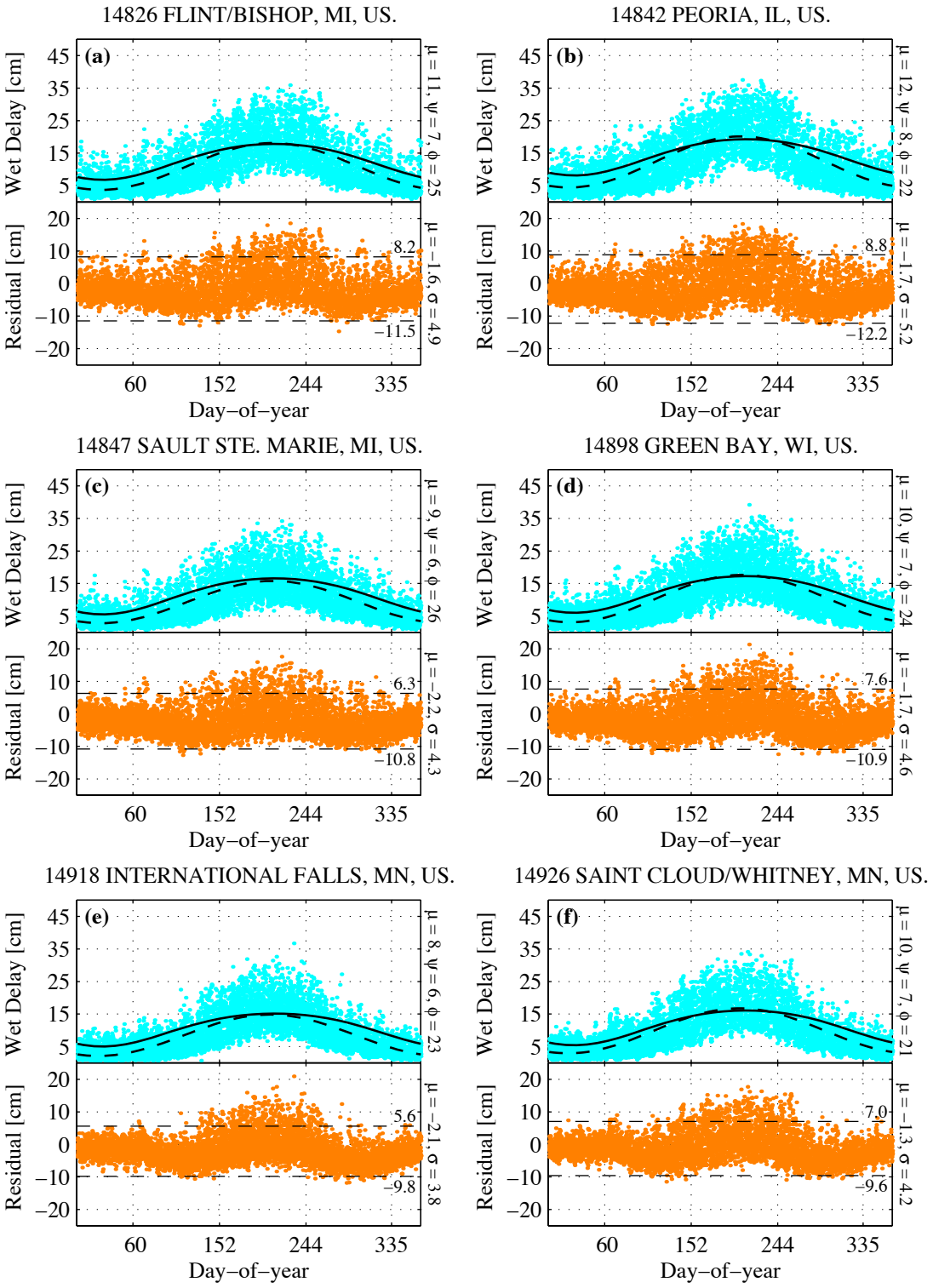

Figure D.17a–f. Wet zenith delays and UNB3 residuals for stations 14826, 14842, 14847, 14898, 14918, and 14926.

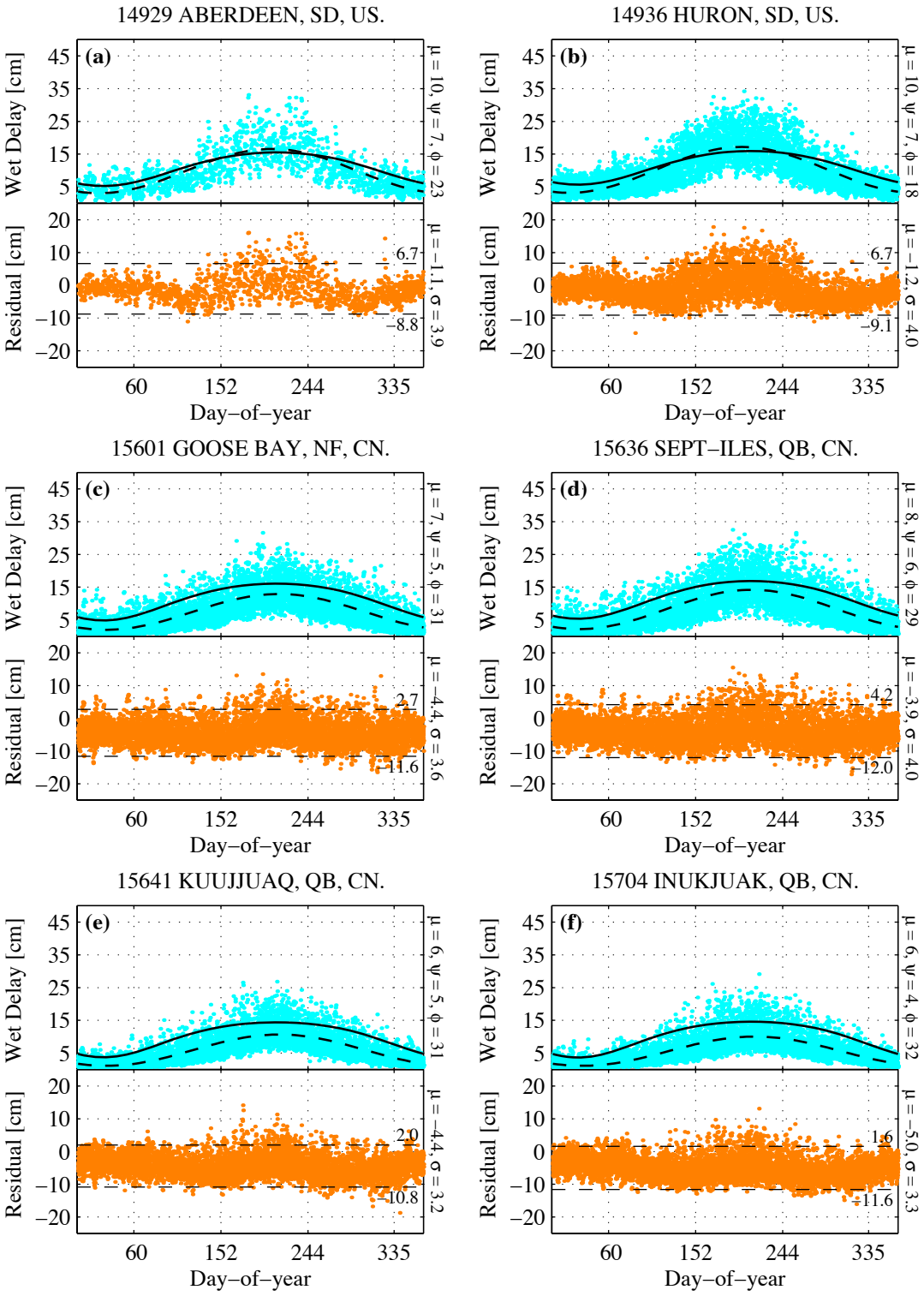

Figure D.18a–f. Wet zenith delays and UNB3 residuals for stations 14929, 14936, 15601, 15636, 15641, and 15704.

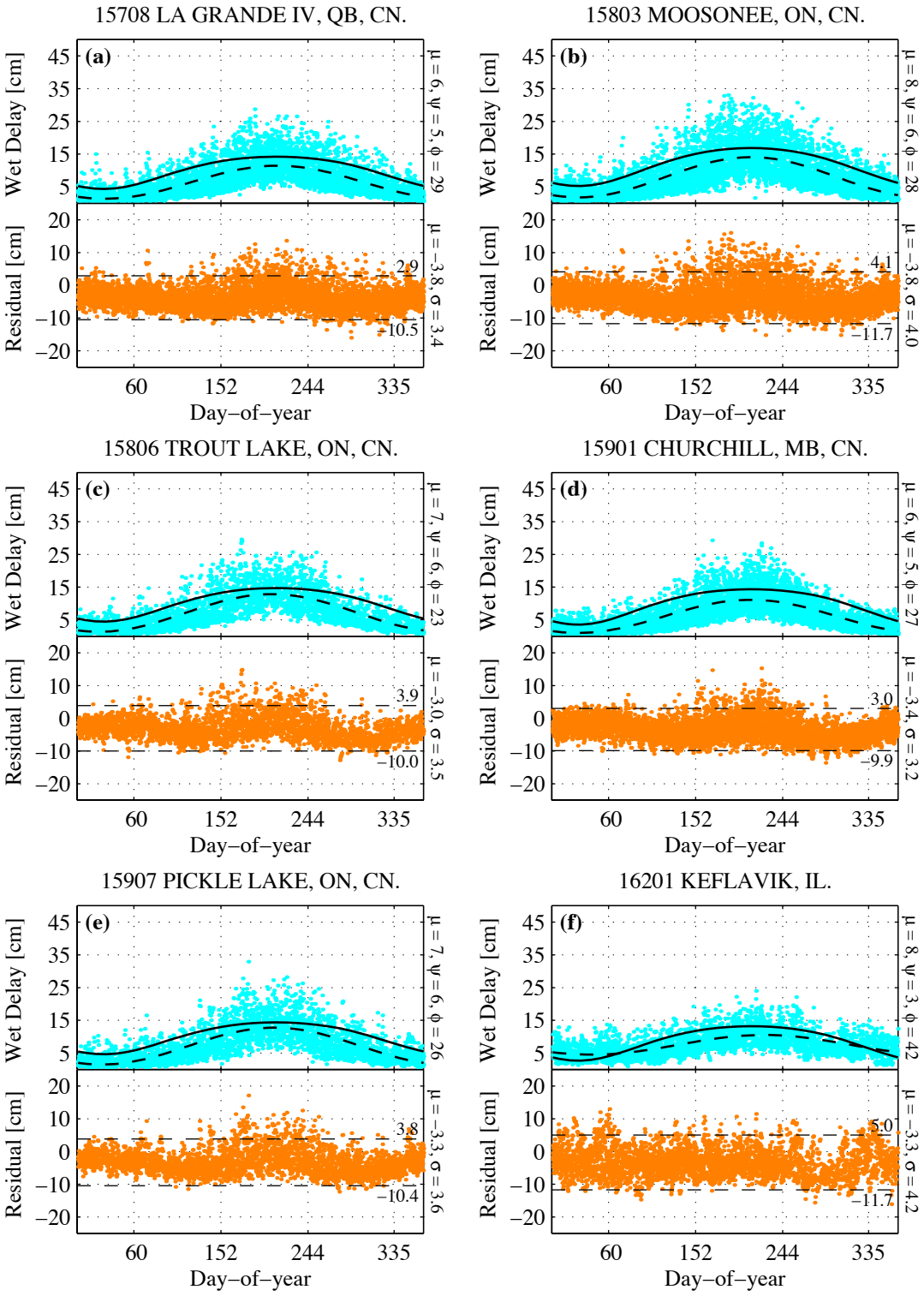

Figure D.19a–f. Wet zenith delays and UNB3 residuals for stations 15708, 15803, 15806, 15901, 15907, and 16201.

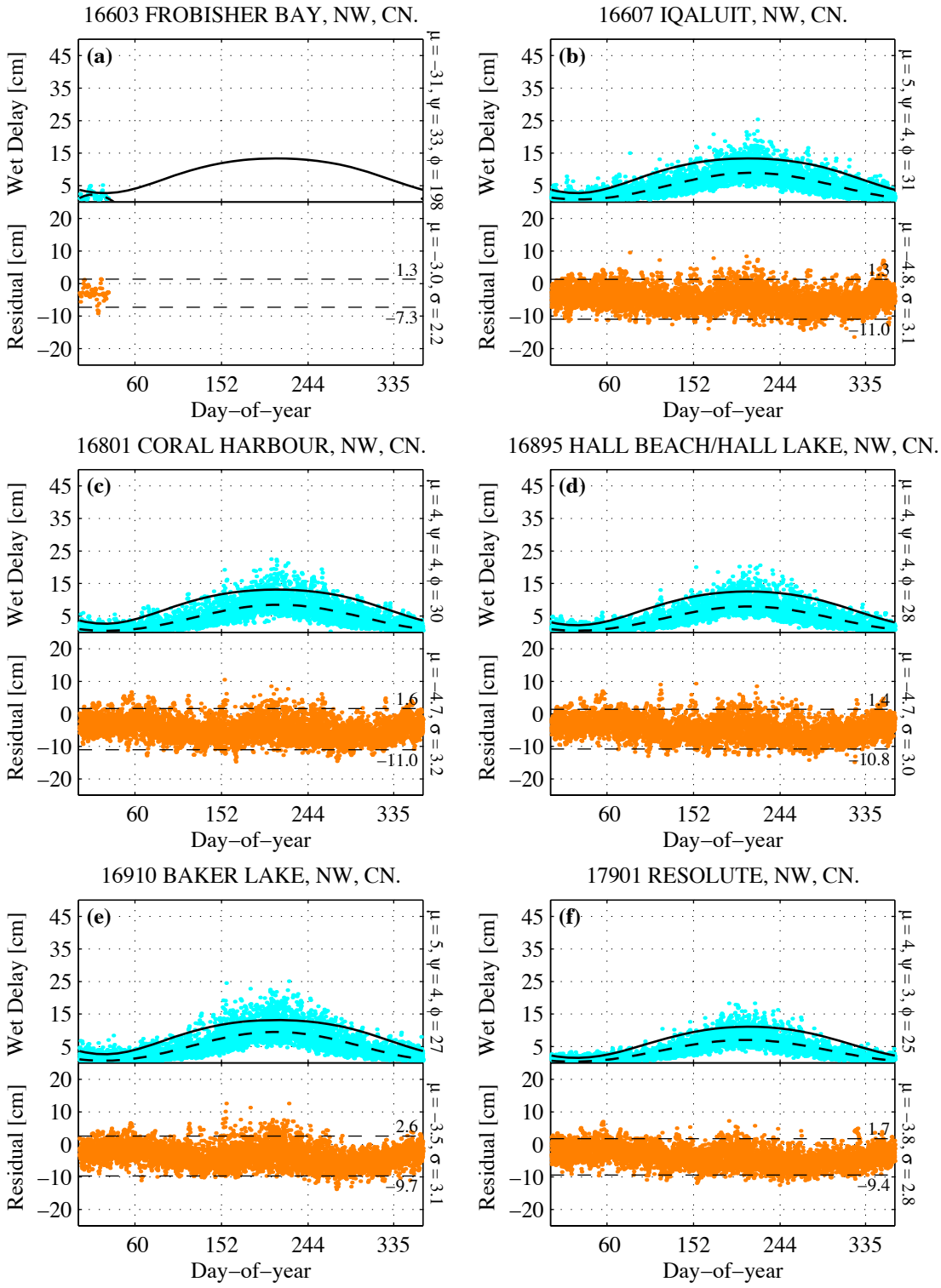

Figure D.20a–f. Wet zenith delays and UNB3 residuals for stations 16603, 16607, 16801, 16895, 16910, and 17901.

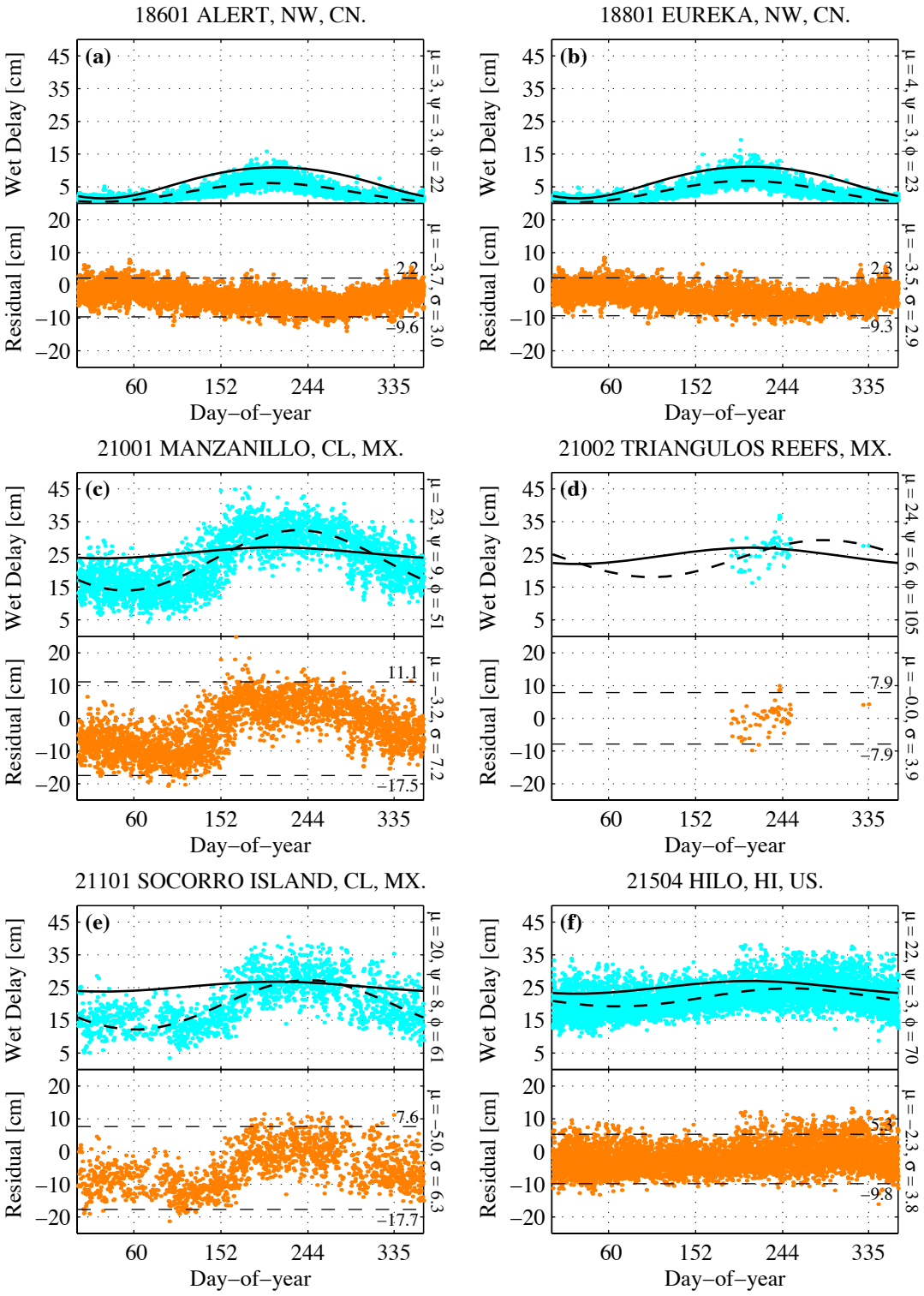

Figure D.21a–f. Wet zenith delays and UNB3 residuals for stations 18601, 18801, 21001, 21002, 21101, and 21504.

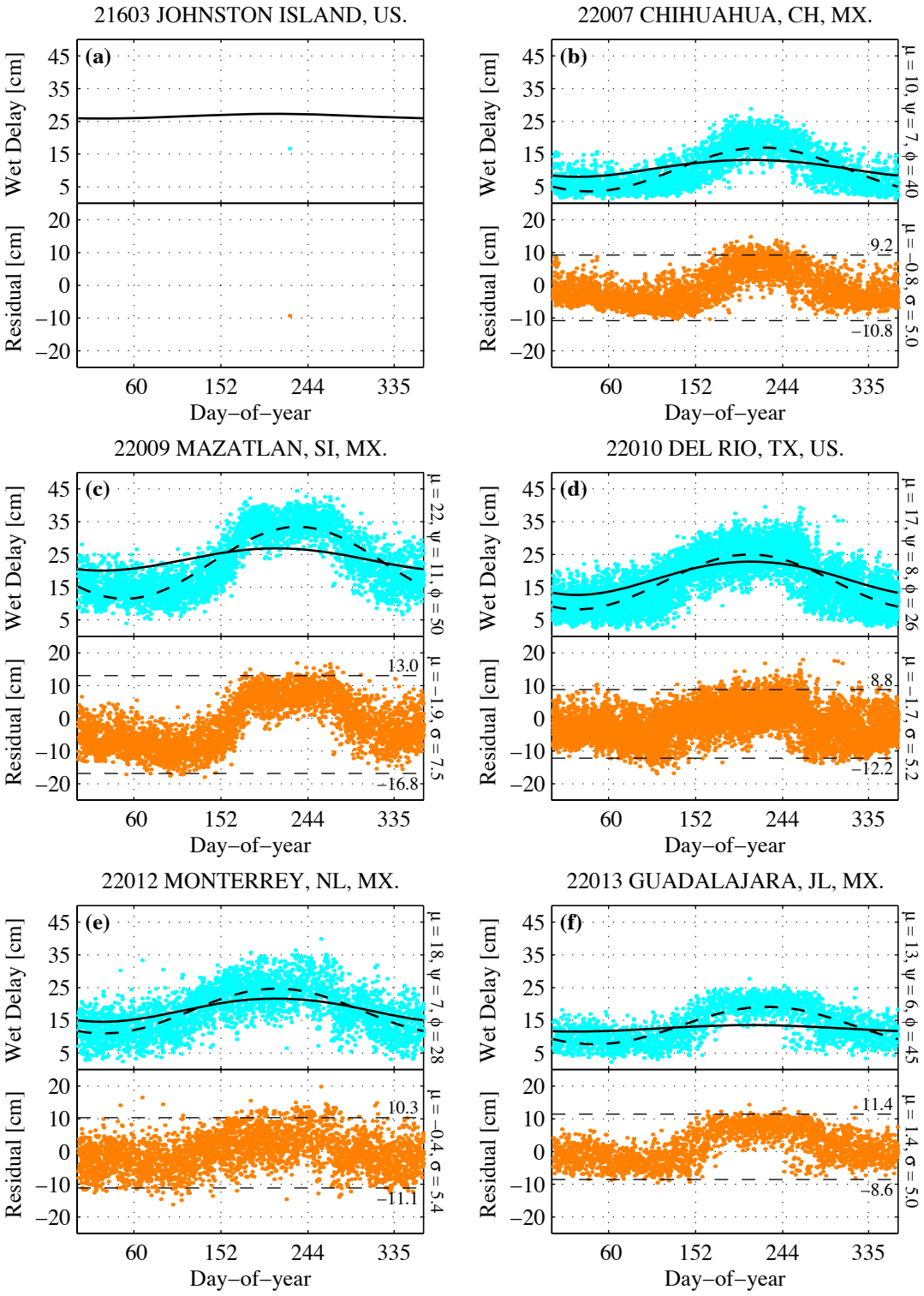

Figure D.22a–f. Wet zenith delays and UNB3 residuals for stations 21603, 22007, 22009, 22010, 22012, and 22013.

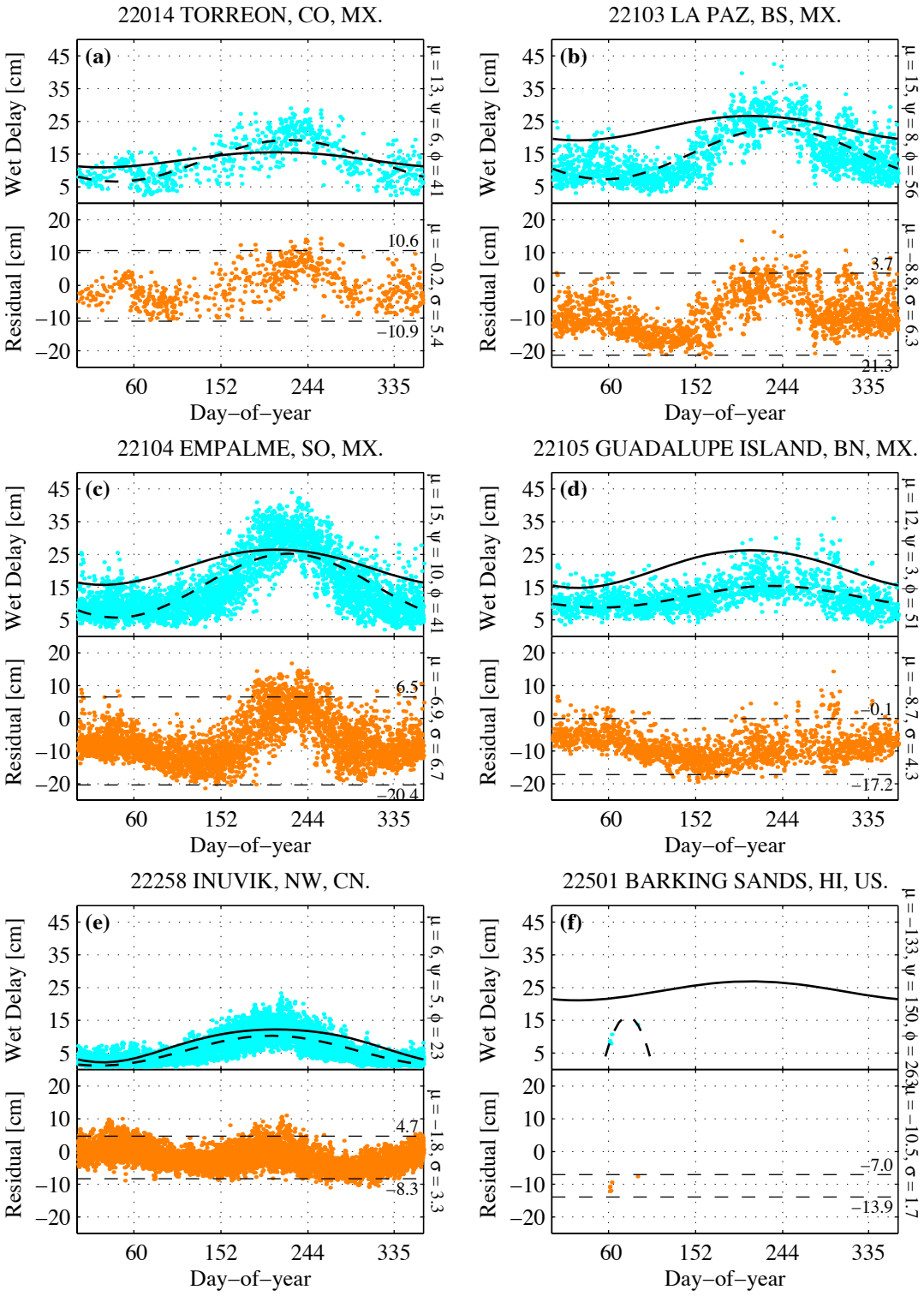

Figure D.23a–f. Wet zenith delays and UNB3 residuals for stations 22014, 22103, 22104, 22105, 22258, and 22501.

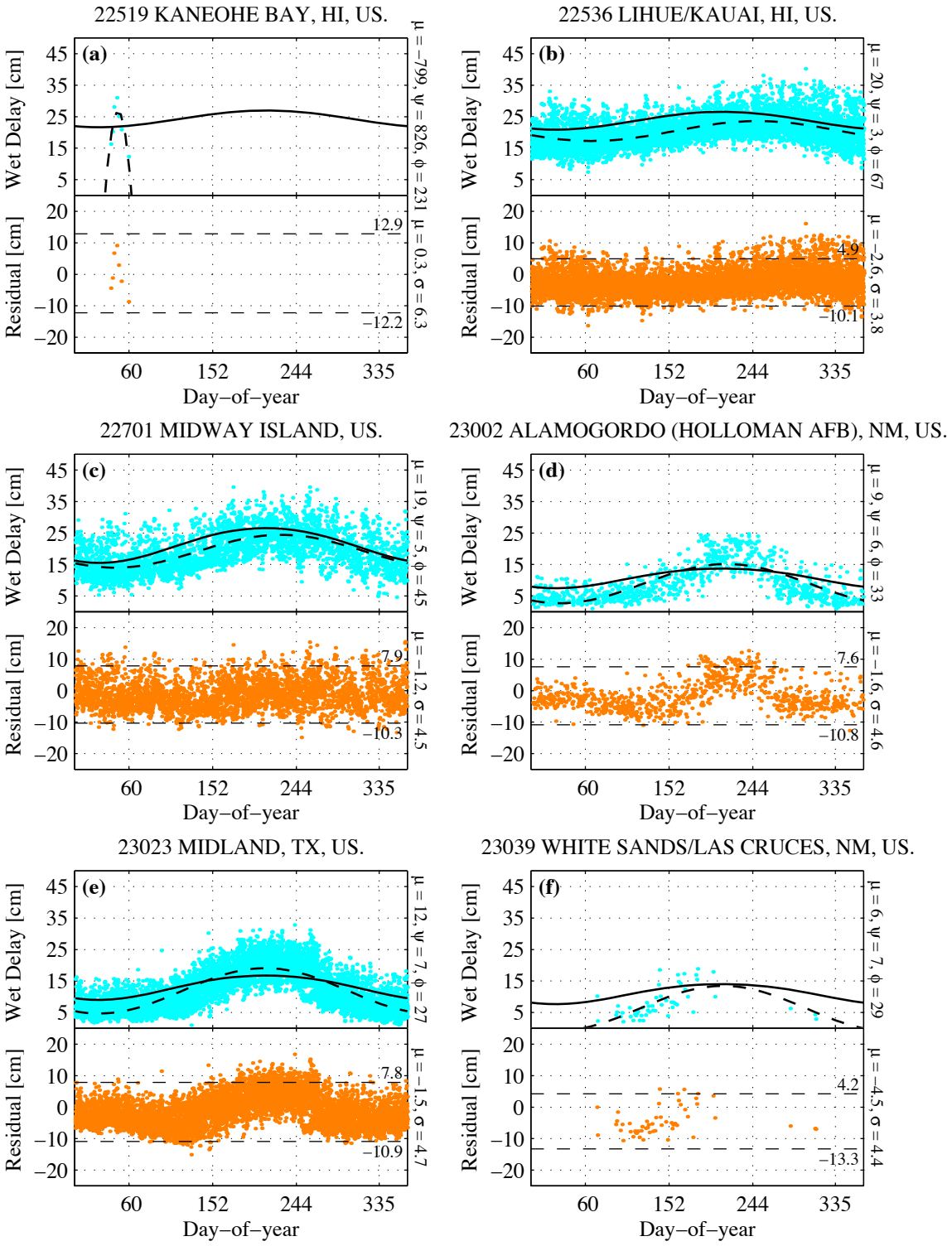

Figure D.24a–f. Wet zenith delays and UNB3 residuals for stations 22519, 22536, 22701, 23002, 23023, and 23039.

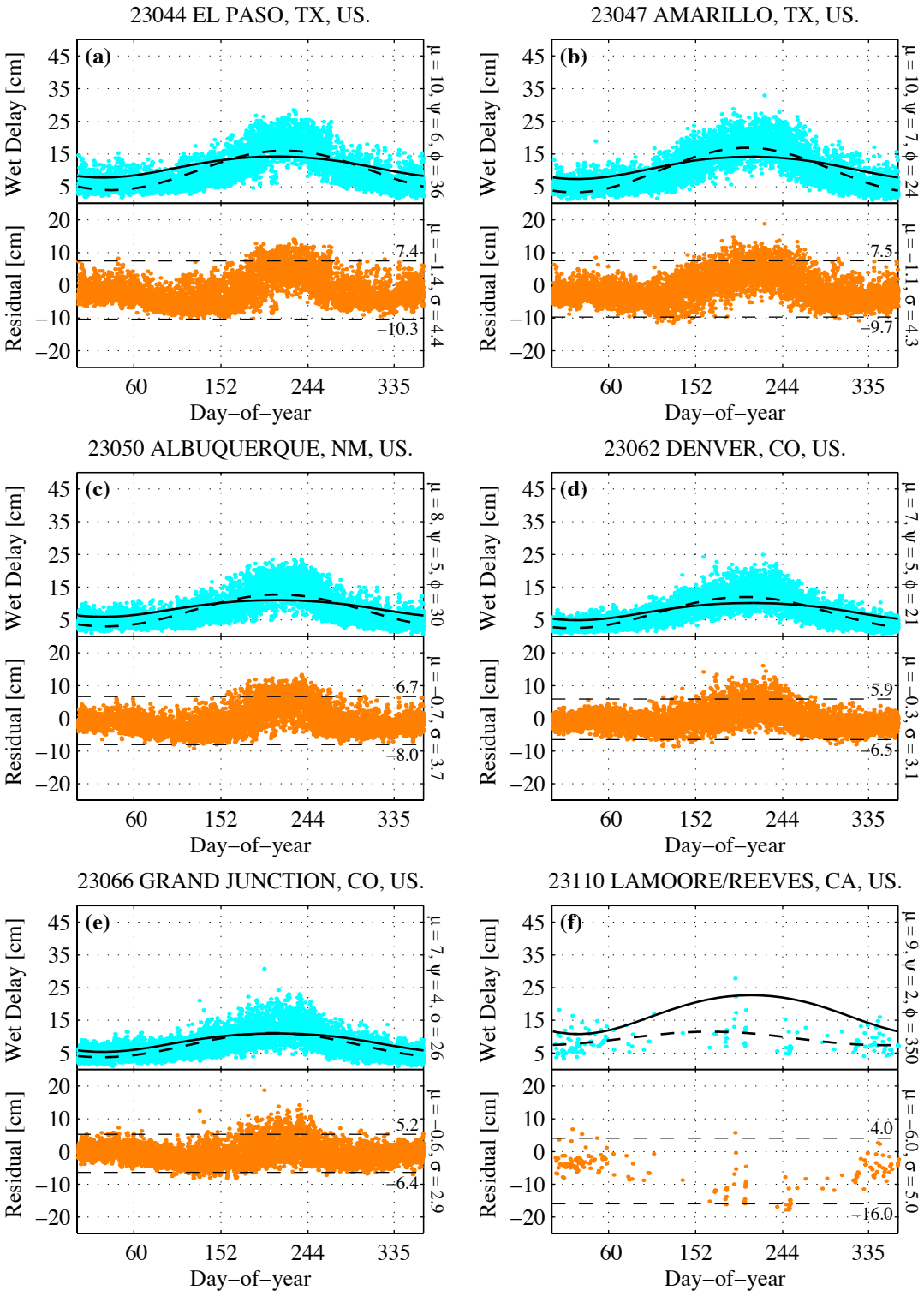

Figure D.25a–f. Wet zenith delays and UNB3 residuals for stations 23044, 23047, 23050, 23062, 23066, and 23110.

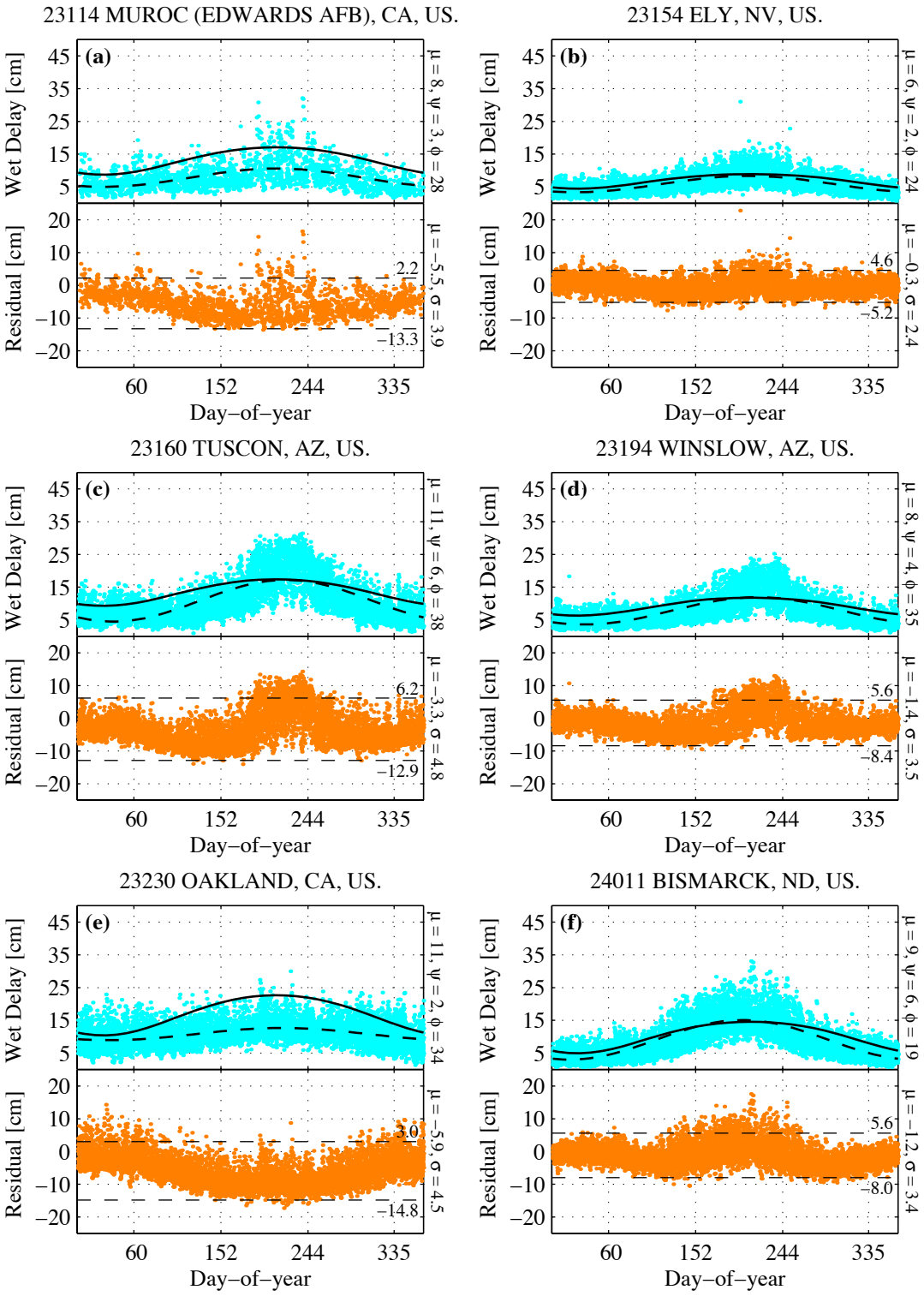

Figure D.26a–f. Wet zenith delays and UNB3 residuals for stations 23114, 23154, 23160, 23194, 23230, and 24011.

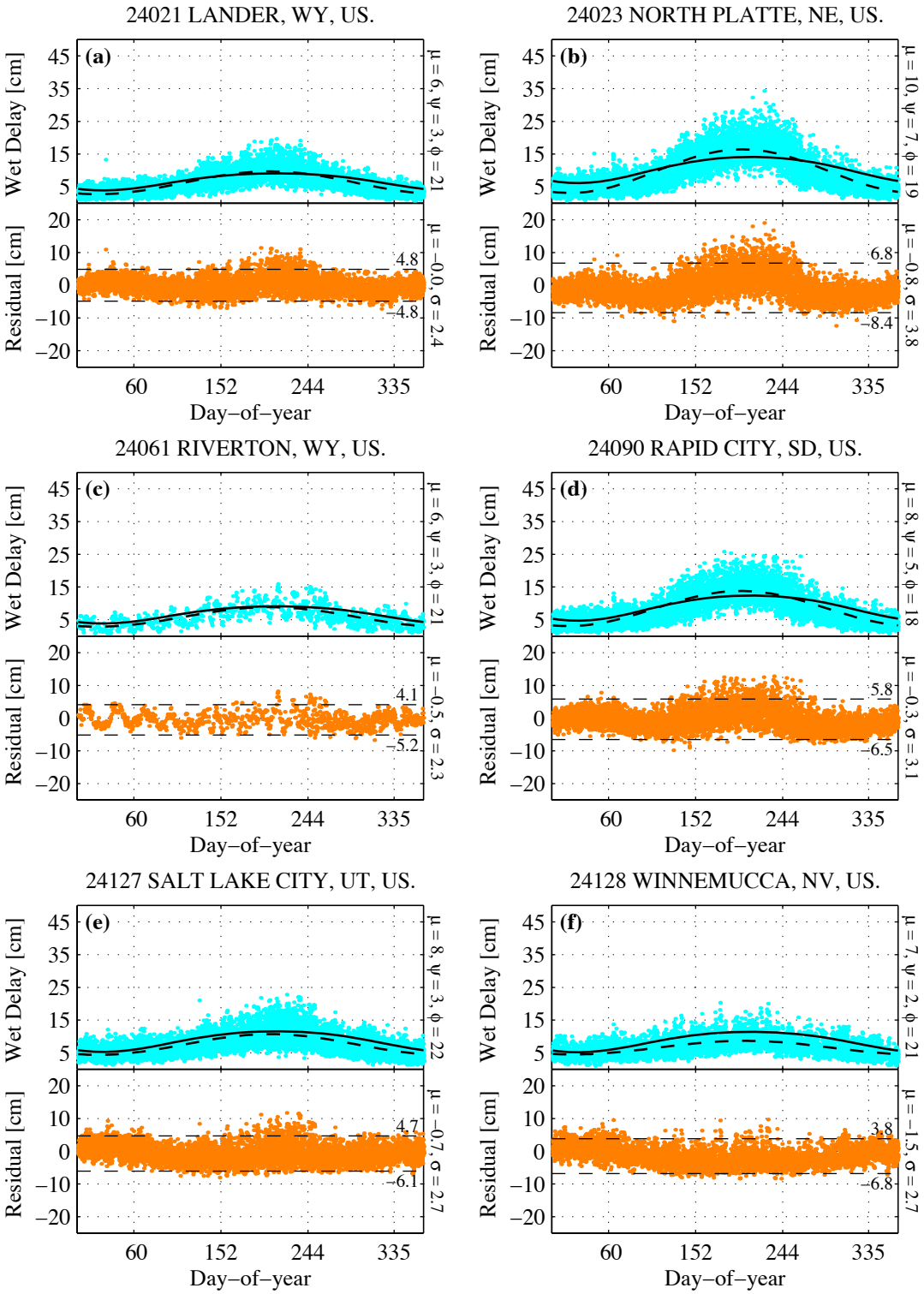

Figure D.27a–f. Wet zenith delays and UNB3 residuals for stations 24021, 24023, 24061, 24090, 24127, and 24128.

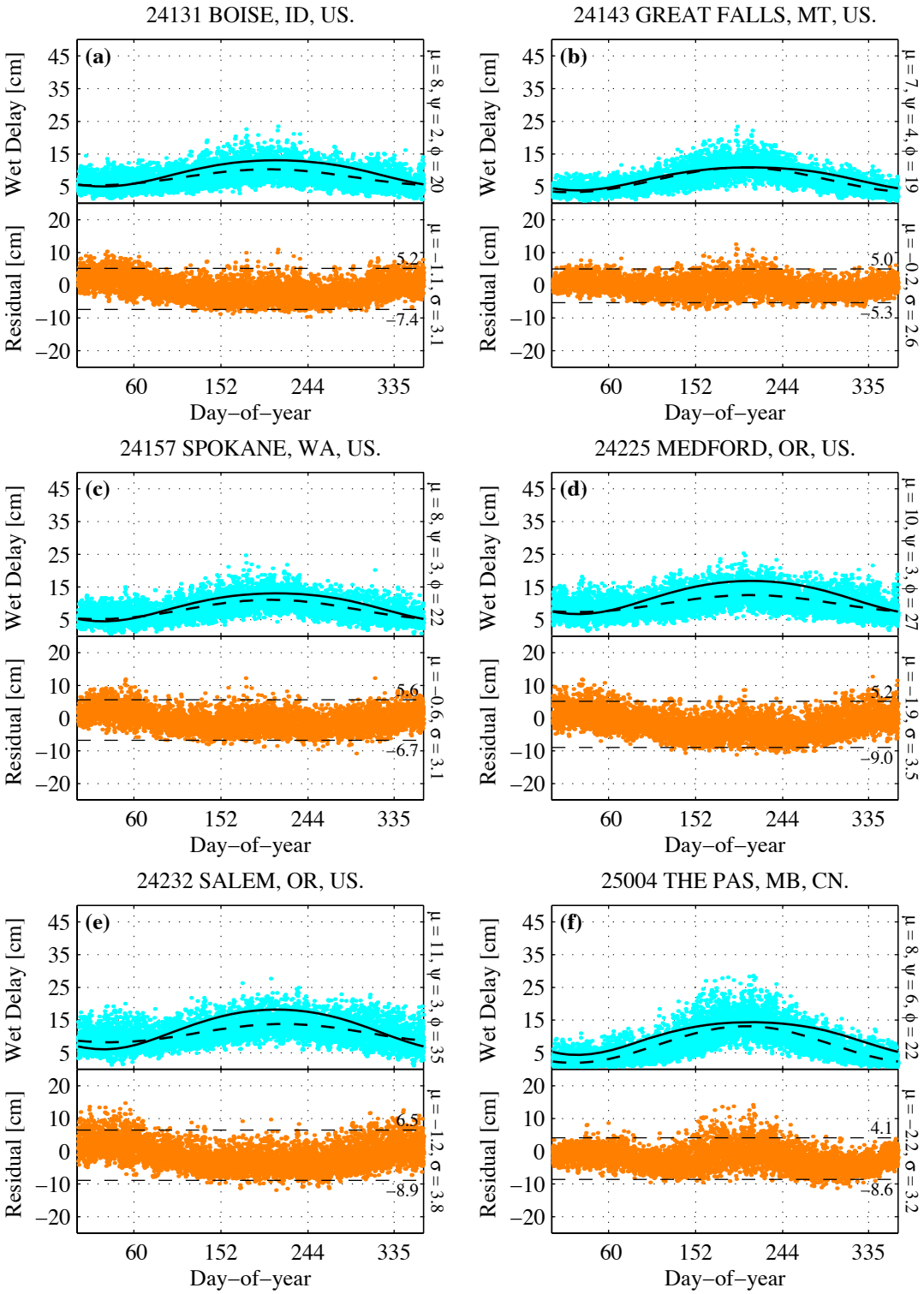

Figure D.28a–f. Wet zenith delays and UNB3 residuals for stations 24131, 24143, 24157, 24225, 24232, and 25004.

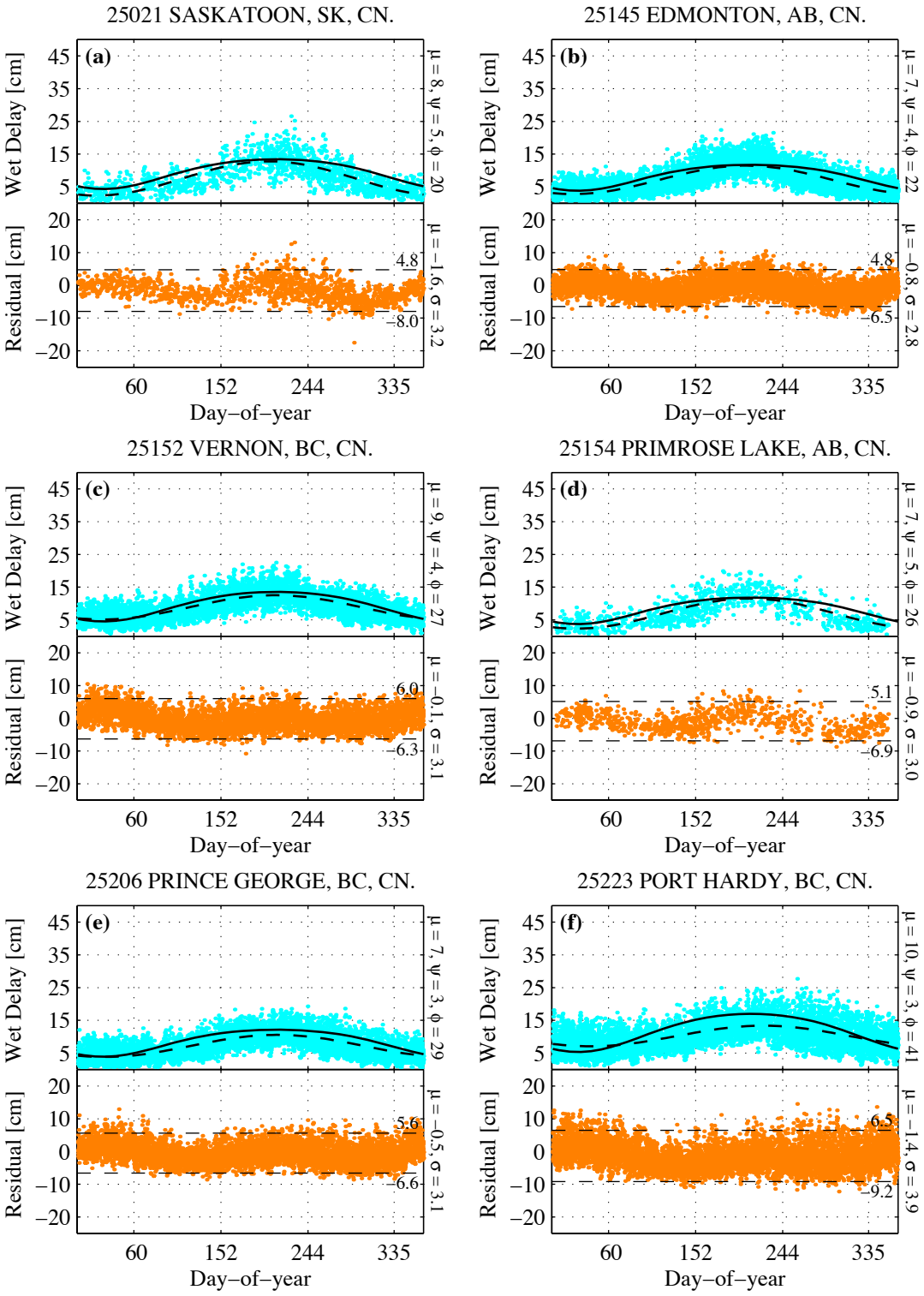

Figure D.29a–f. Wet zenith delays and UNB3 residuals for stations 25021, 25145, 25152, 25154, 25206, and 25223.

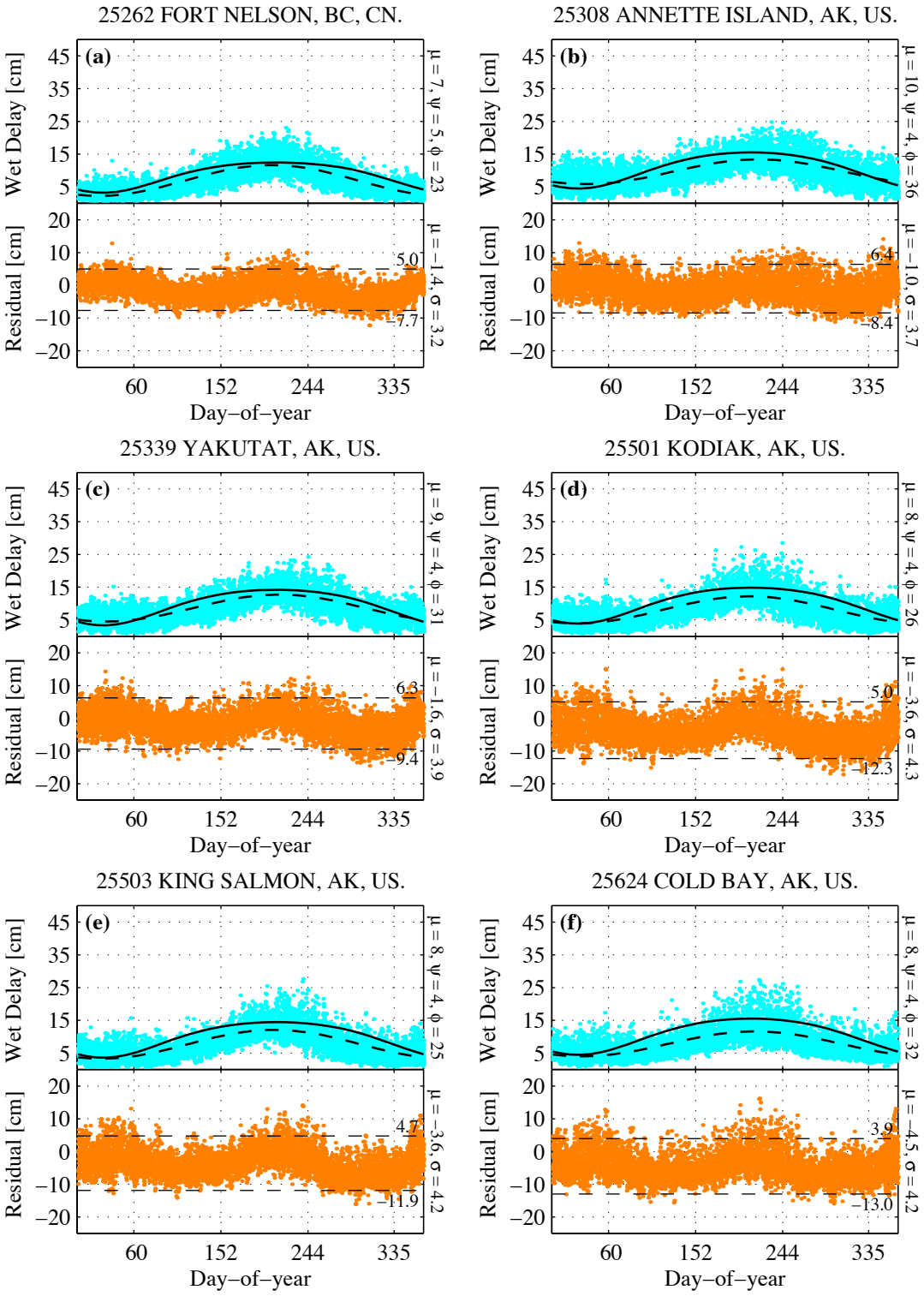

Figure D.30a–f. Wet zenith delays and UNB3 residuals for stations 25262, 25308, 25339, 25501, 25503, and 25624.

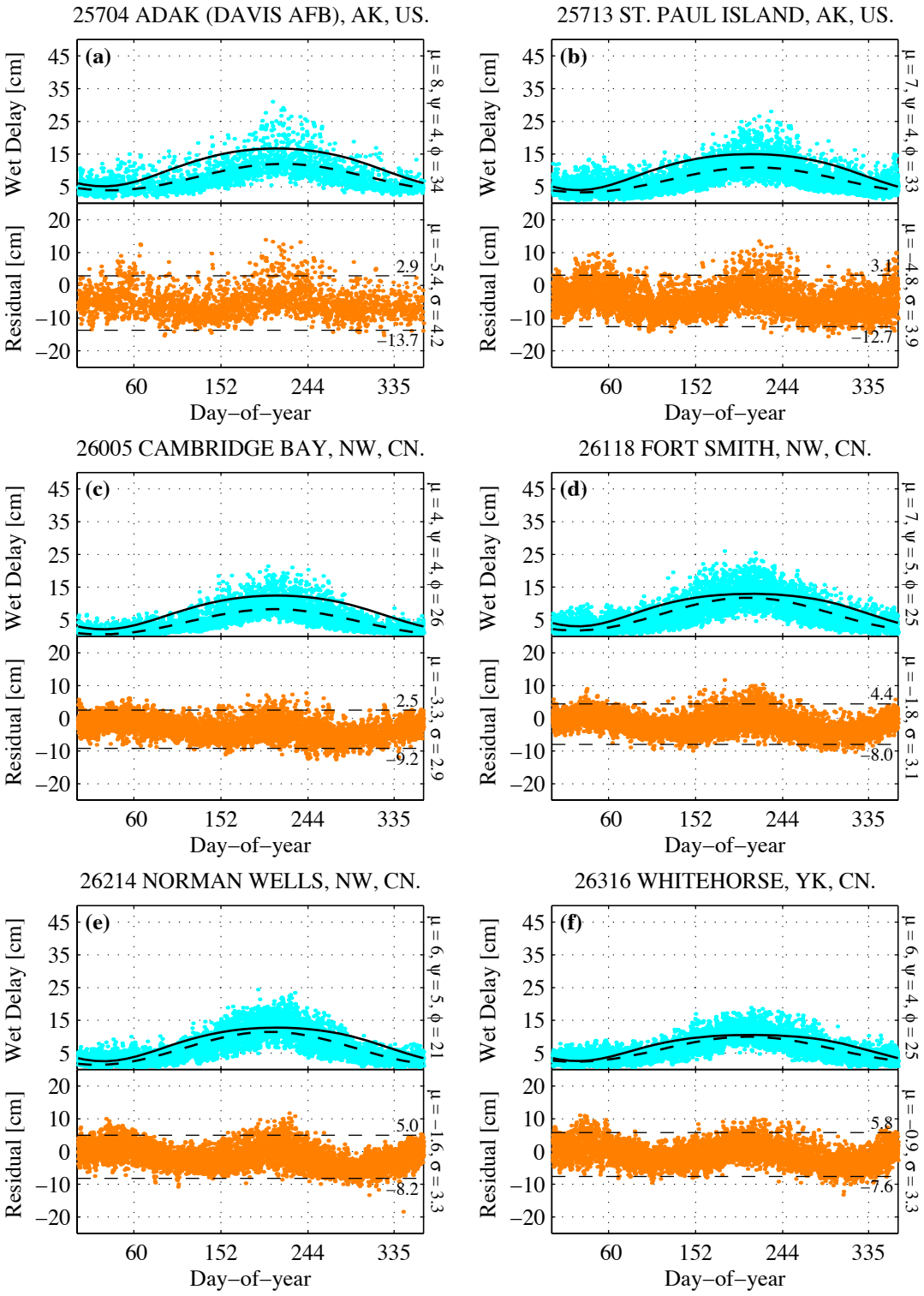

Figure D.31a–f. Wet zenith delays and UNB3 residuals for stations 25704, 25713, 26005, 26118, 26214, and 26316.

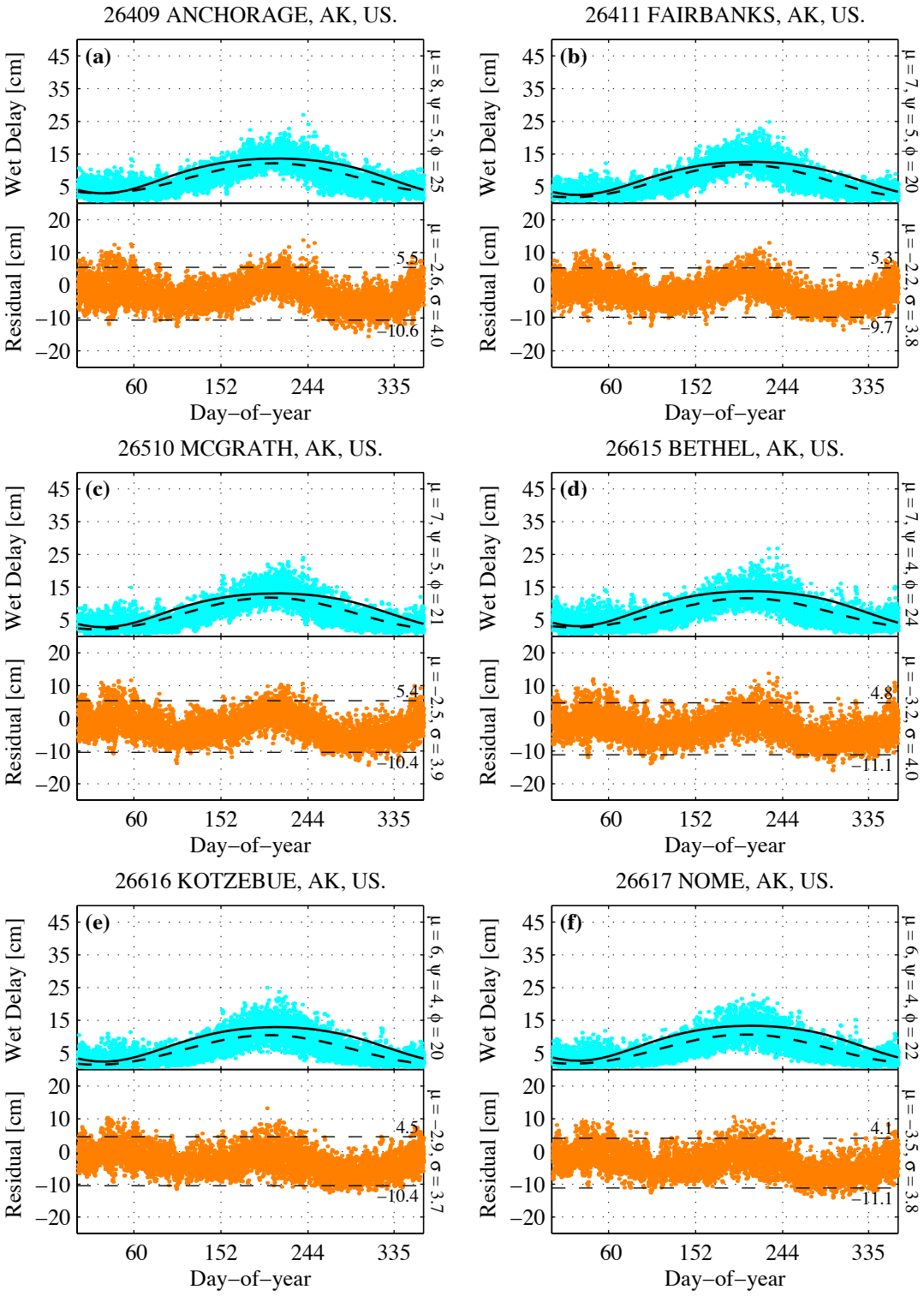

Figure D.32a–f. Wet zenith delays and UNB3 residuals for stations 26409, 26411, 26510, 26615, 26616, and 26617.

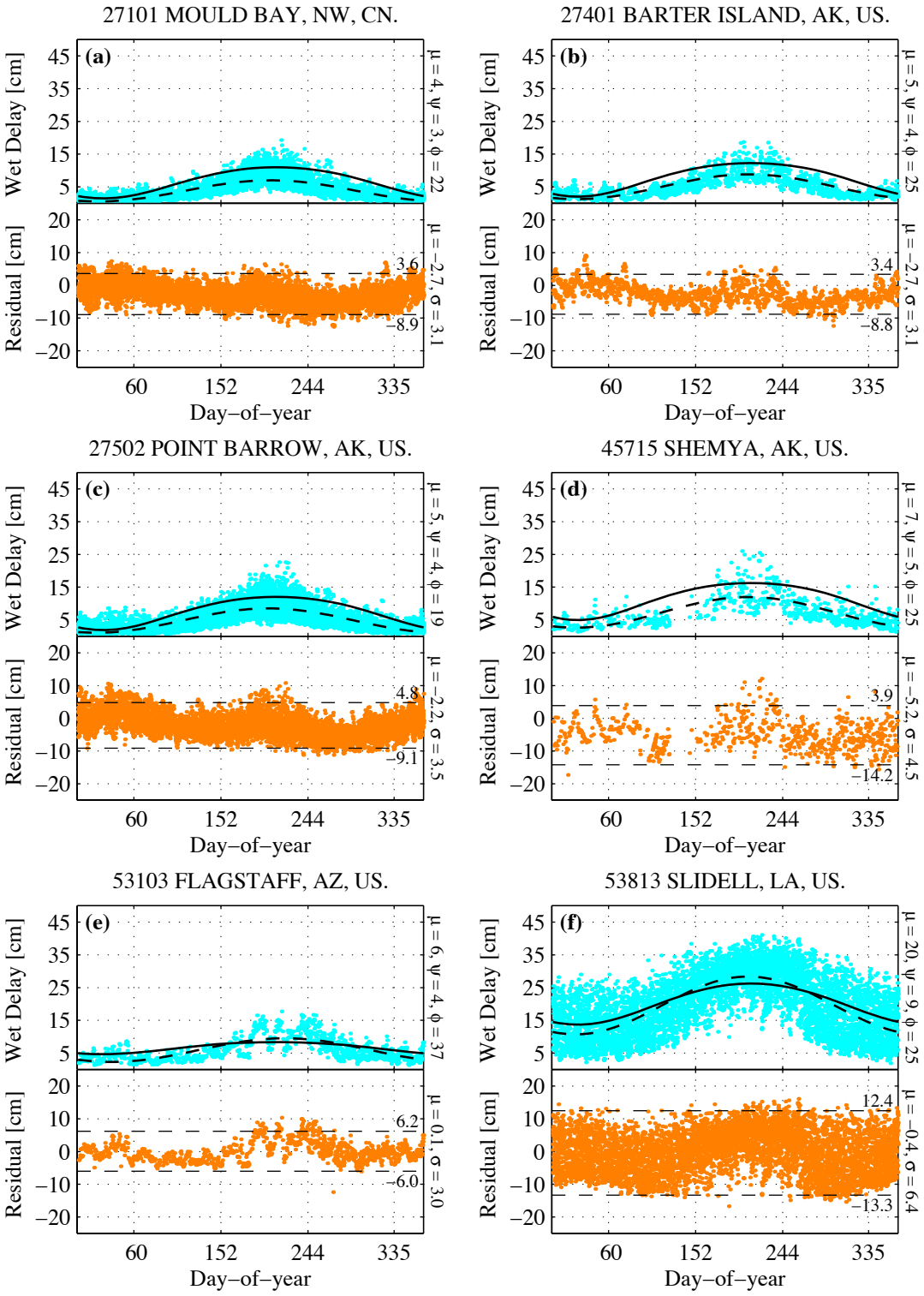

Figure D.33a–f. Wet zenith delays and UNB3 residuals for stations 27101, 27401, 27502, 45715, 53103, and 53813.

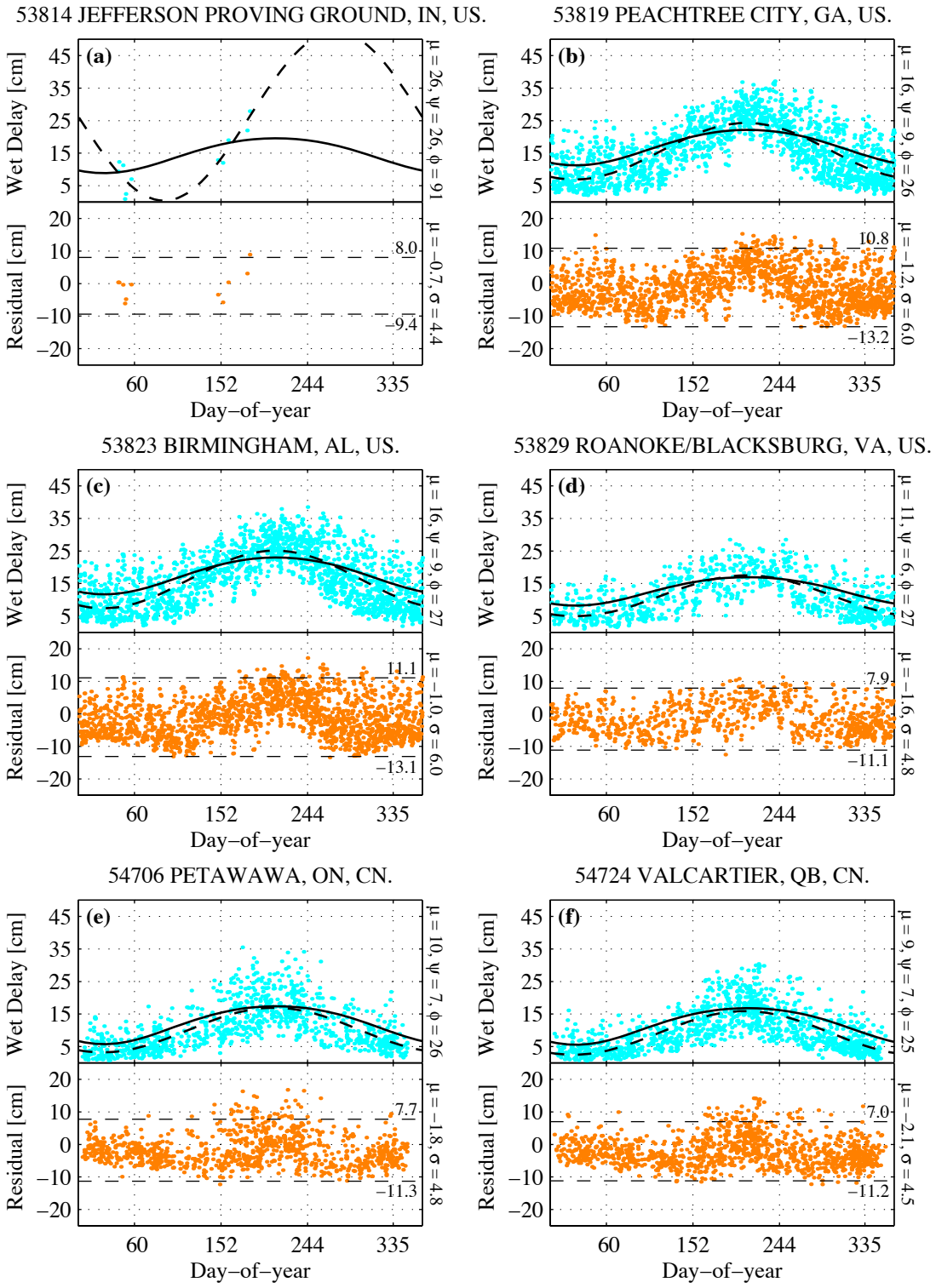

Figure D.34a–f. Wet zenith delays and UNB3 residuals for stations 53814, 53819, 53823, 53829, 54706, and 54724.

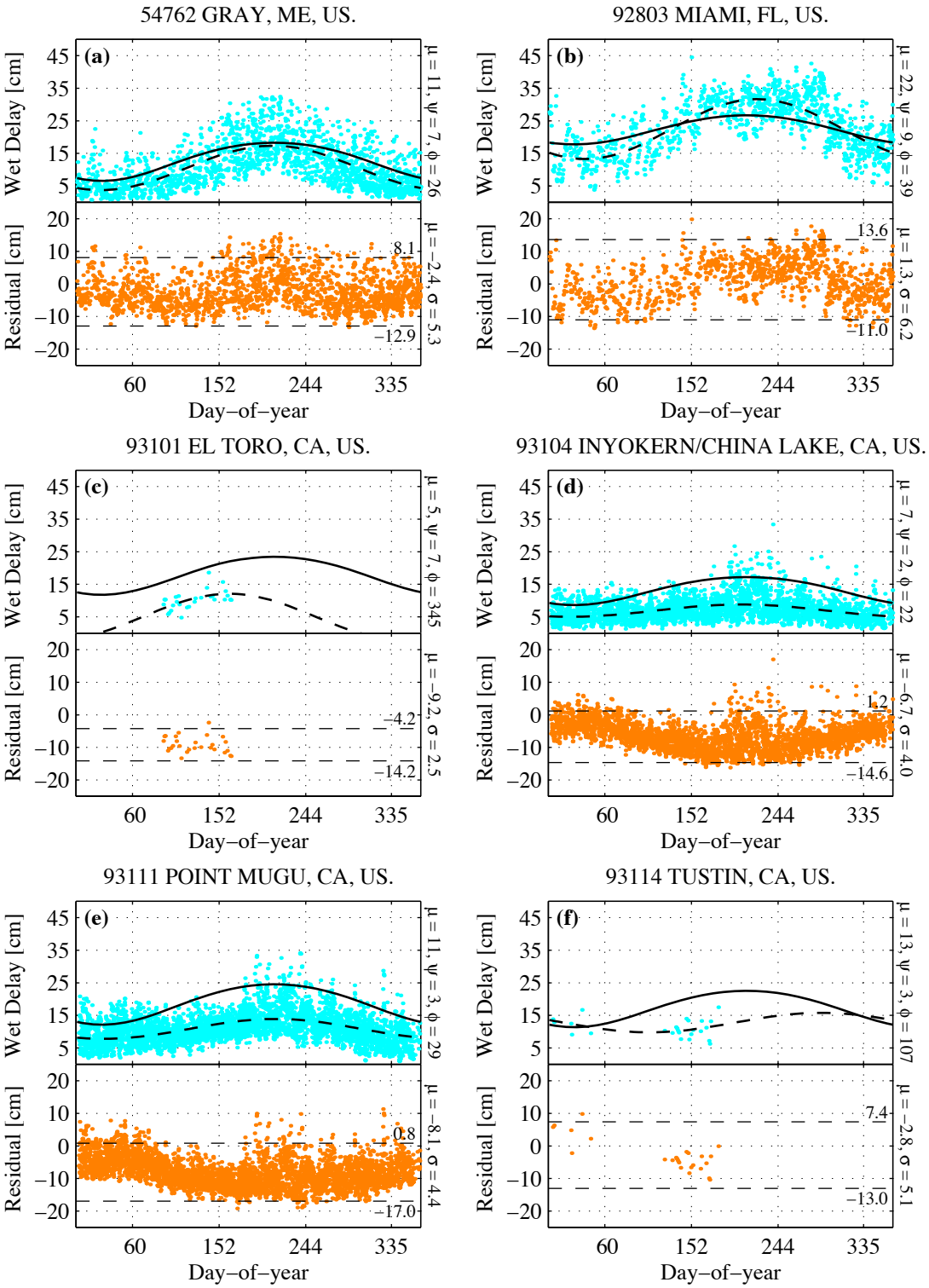

Figure D.35a–f. Wet zenith delays and UNB3 residuals for stations 54762, 92803, 93101, 93104, 93111, and 93114.

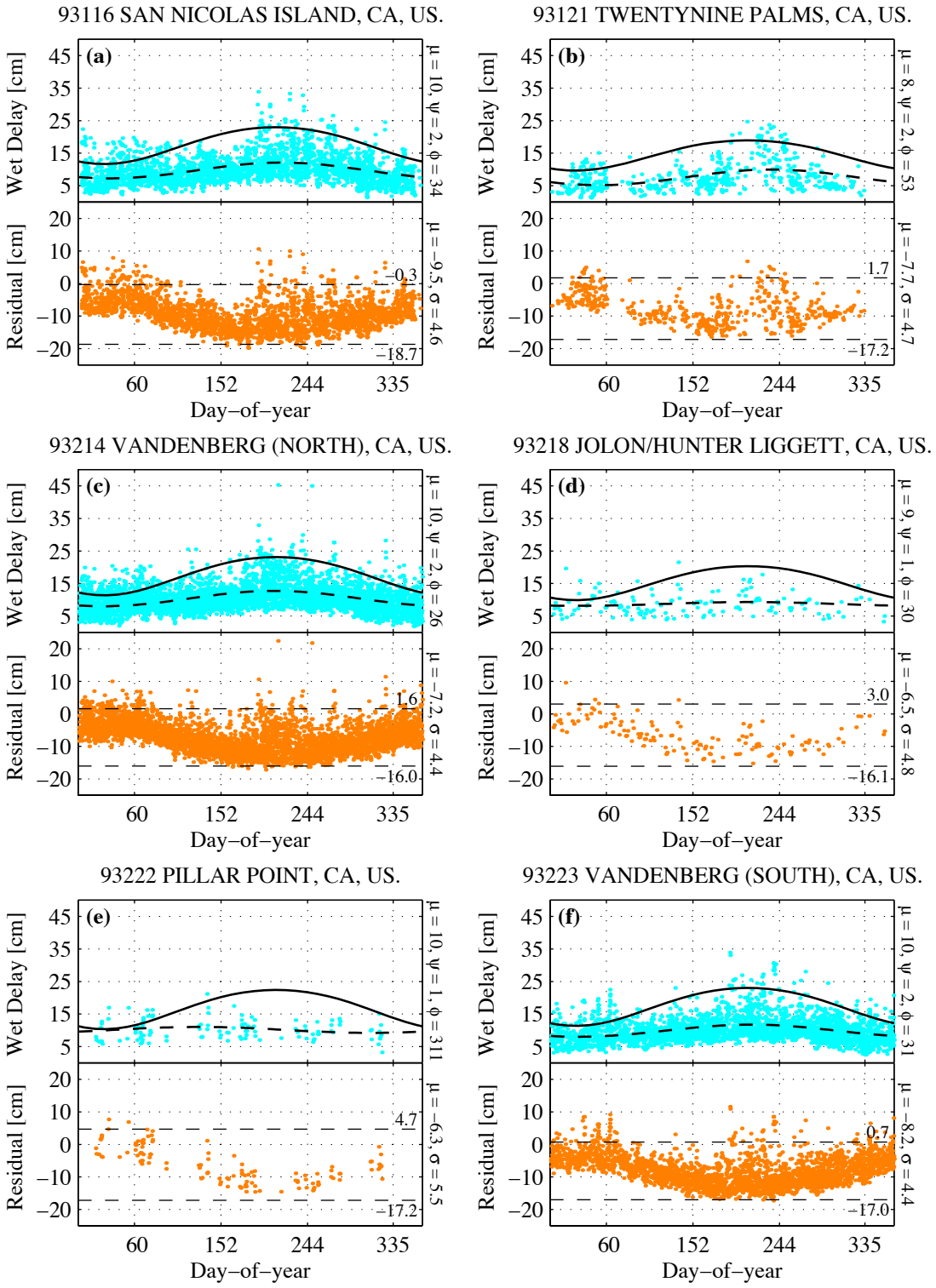

Figure D.36a–f. Wet zenith delays and UNB3 residuals for stations 93116, 93121, 93214, 93218, 93222, and 93223.

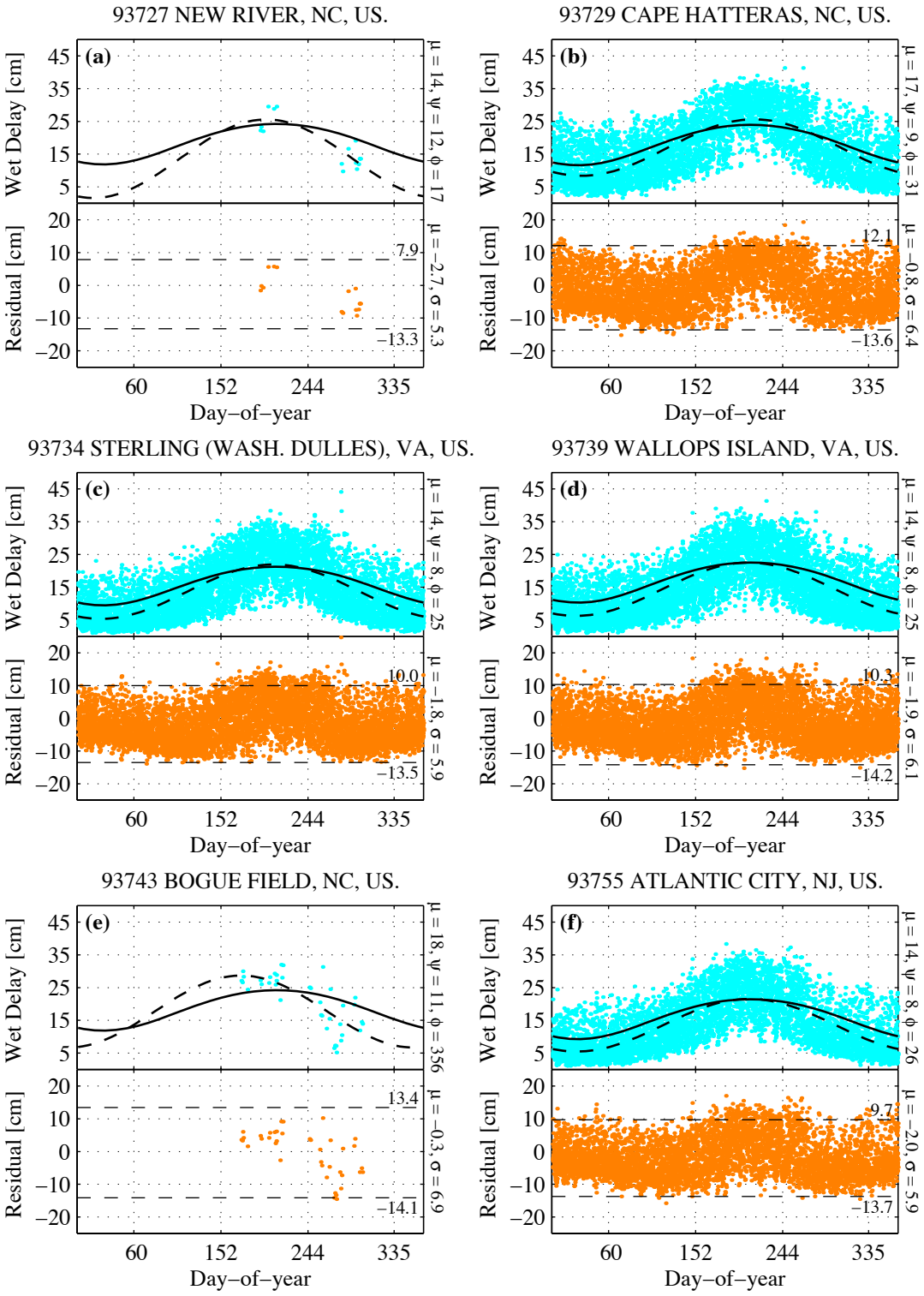

Figure D.37a–f. Wet zenith delays and UNB3 residuals for stations 93727, 93729, 93734, 93739, 93743, and 93755.

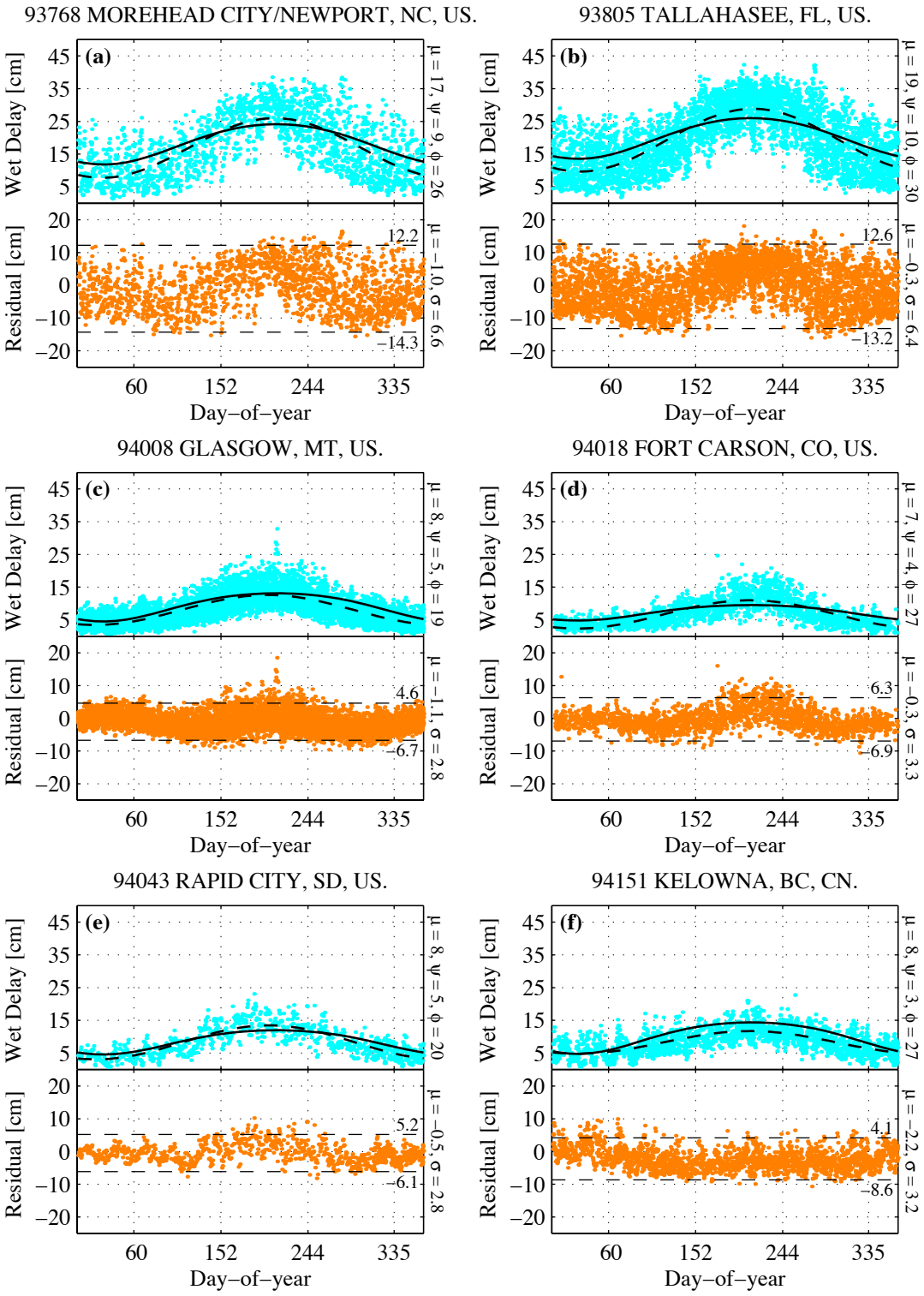

Figure D.38a–f. Wet zenith delays and UNB3 residuals for stations 93768, 93805, 94008, 94018, 94043, and 94151.

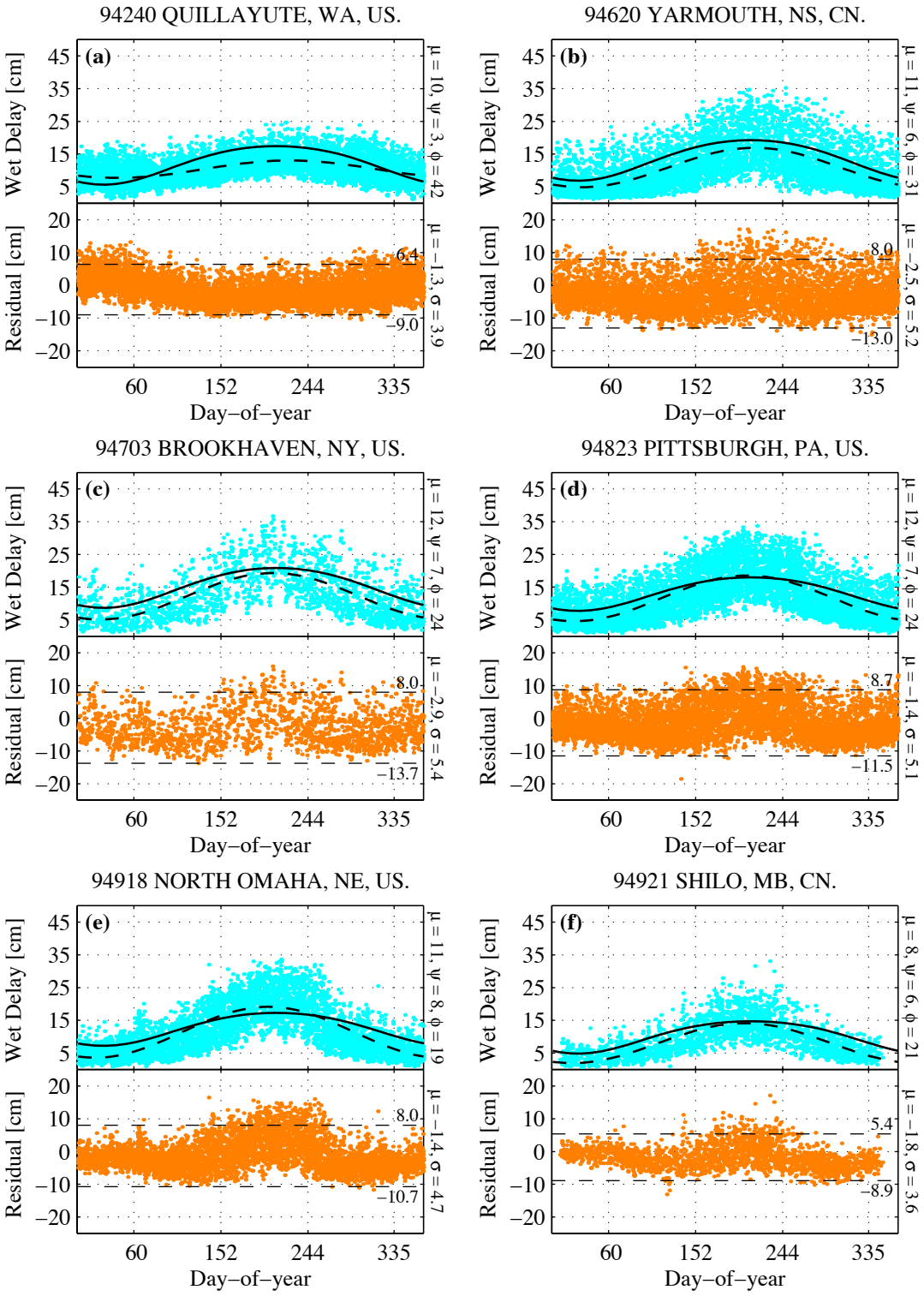

Figure D.39a–f. Wet zenith delays and UNB3 residuals for stations 94240, 94620, 94703, 94823, 94918, and 94921.

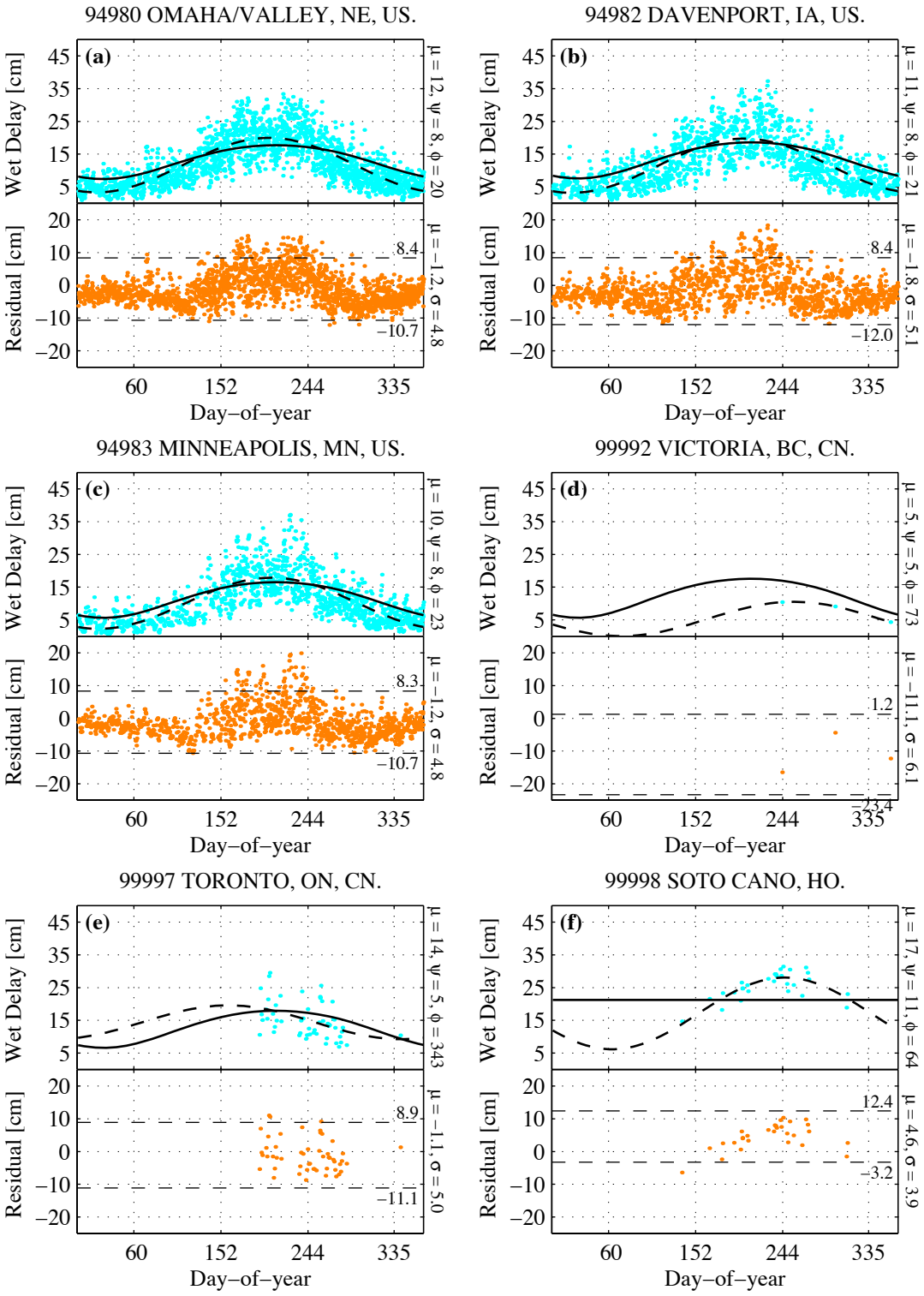

Figure D.40a–f. Wet zenith delays and UNB3 residuals for stations 94980, 94982, 94983, 99992, 99997, and 99998.

APPENDIX E.

MISCELLANEOUS REPORTS

The following consultation papers were written during the course of this contract in response to various requests for information and input arising from the results of our previous contract. It should be noted that the ray-trace data referred to in two of these papers is the thirteen station data set used for the analyses discussed in our previous report.

Contents:

Consideration of the differential GPS range delay due to the troposphere: a brief analysis.

J.P. Collins and R.B. Langley, University of New Brunswick, Canada.
e-mail: k4eo@unb.ca, phone: 506-453-5088.

Figure 1 illustrates the impact of various model atmospheres on differential GPS pseudoranges measured in the zenith direction. As the user descends through the troposphere towards the surface, the amount of the atmosphere through which the signal traverses increases. The maximum is reached at the surface, where it will be equal (ignoring horizontal gradients) to that at the reference station. Hence, the differential delay (in the sense of reference station minus aircraft) will increase with height.

The zenith delay models used to compute the differential delays are the refined versions of Saastamoinen as used in the UNB3 model. The algorithms are driven with meteorological values representing a variety of 'standard' and extreme atmospheric conditions. These conditions are tabulated in Figure 1. The differential zenith delays can be multiplied by 10 to obtain the approximate differential range error at an elevation angle of 5 degrees and the corresponding height position error (in an unweighted least-squares solution) due to ignoring the tropospheric effect on GPS ranges measured at this elevation angle.

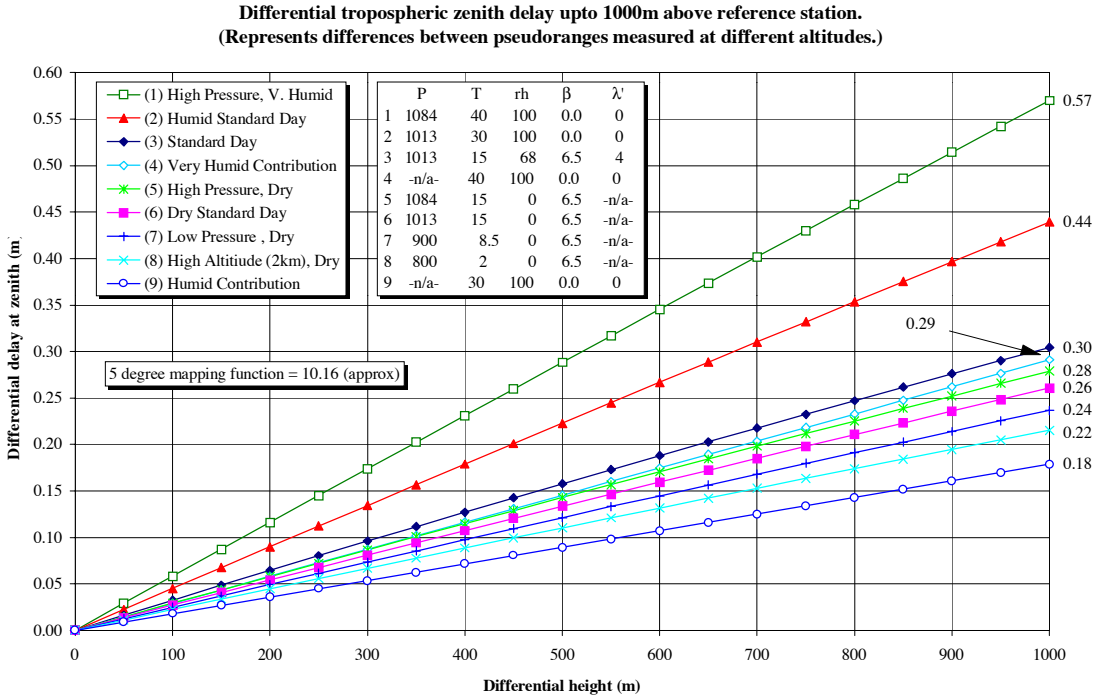

Figure 1. The impact of various atmospheric conditions on differential GPS ranges in the zenith direction.

The pressure of 1084 mbar represents the highest ever recorded and is used as an upper bound on the range delay due to the hydrostatic component of the tropospheric delay. For a lower bound, 900 mbar can be used. This pressure also represents the altitude of 1 km above sea level, and 800 mbar represents that of 2 km. The bounds of the tropospheric wet delay is provided by a 'dry' atmosphere (i.e. no water vapour whatsoever) and two upper limits taking temperatures of 30°C and 40°C with 100% relative humidity. These values are then considered constant through the atmosphere. True atmospheric conditions could only support these values to heights of approximately 2.5 and 1.5 kilometres respectively. It is felt that the first limit is more reasonable. Figure 1 shows that the contribution of these conditions alone can approach that of a very dry, high altitude atmosphere.

The errors indicated by Figure 1 however, will be greatly reduced through the use of a common tropospheric delay model at the reference station and aircraft receivers. As an example, we could use the 'Standard Day' model from Figure 1 which is equivalent to the UNB1 model. The effect of the other atmospheric conditions can be examined by differencing the 'Standard Day' results from the other curves in Figure 1. This process is equivalent to differencing pseudoranges and tropospheric delays at a reference station to form "tropo. free" pseudorange corrections which are then differenced from pseudoranges recorded at the aircraft. These pseudoranges would also have to be corrected for the tropospheric delay. The results are presented in Figure 2.

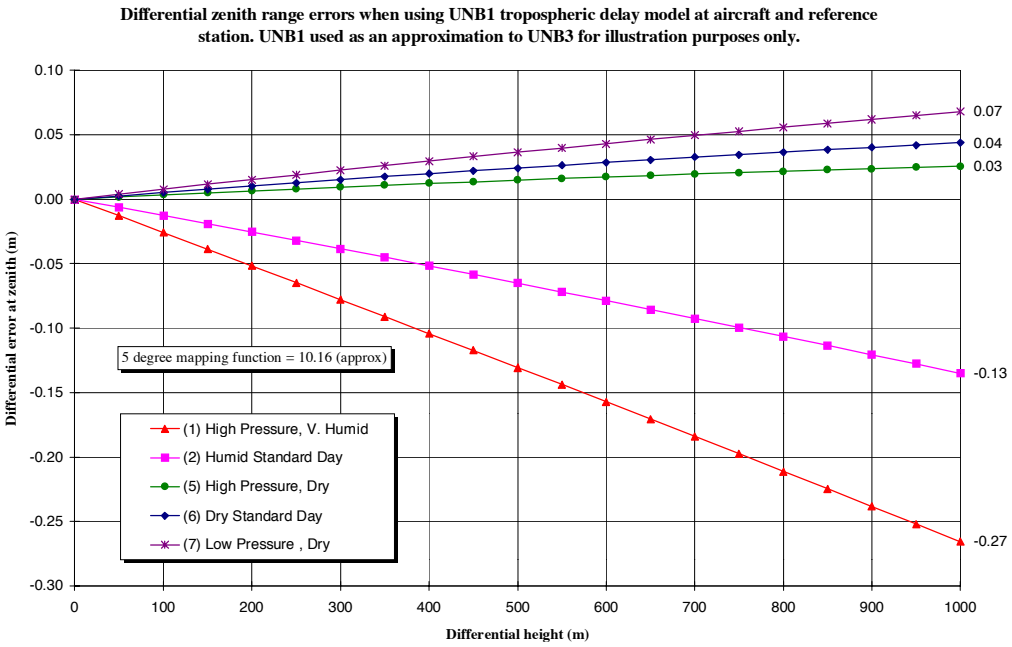

Figure 2. Differential pseudorange errors due to extreme atmospheric conditions when using a tropospheric delay model without real-time input. (Note: legend numbers refer to atmospheric conditions in the table in Figure 1.)

Note that all of the tropospheric delay determination can be done at the aircraft, provided knowledge of the reference station height and latitude is known. The aircraft receiver can compute the reference station tropospheric delay as well as its own and therefore the total differential tropospheric delay.

Figure two shows that as long as the same tropospheric delay model is used at both the reference station and the aircraft, with the correct care taken to scale the atmospheric values that drive the model, then the user position error will not exceed 2.7 metres at 1 km under very extreme conditions for a solution computed with some satellites at an elevation angle of 5 degrees. A more realistic 'extreme' is provided by the "Humid Standard Day" curve of 1.3 metres at 1 km.

A brief report on the comparison of the performance of the Niell and Black and Eisner tropospheric delay mapping functions.

J.P. Collins and R.B. Langley, University of New Brunswick, Canada.
e-mail: k4eo@unb.ca, phone: 506-453-5088.

The primary result of this investigation is that the maximum difference between UNB3 (using Niell) and UNB3 (using B&E) is 16 cm at five degrees elevation angle (see Figure 1). This decreases with variations in latitude/altitude/day-of-year. However, using B&E in UNB3 always over-predicts the delay, compared to Niell. Given real time measurements of the hydrostatic and wet zenith delays the 5 degree difference between the mapping functions could theoretically approach 30 cm.

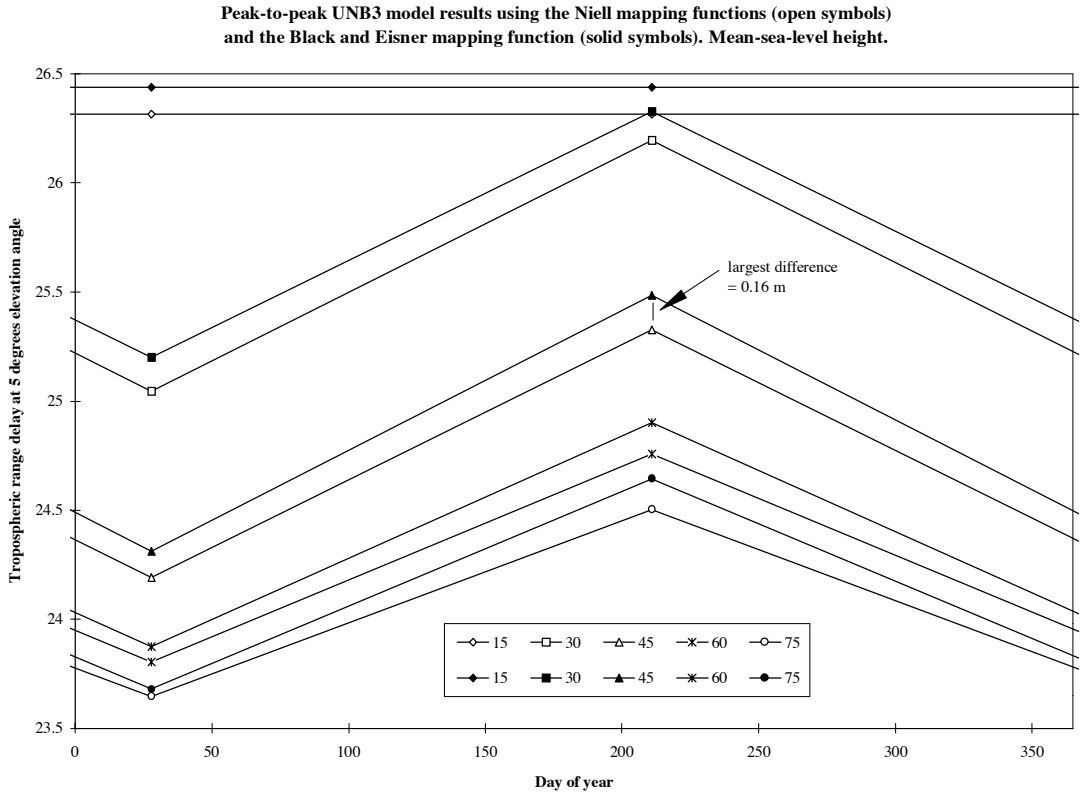

Figure 1. Annual peak to peak values of the UNB3 tropospheric delay model using both Black and Eisner and Niell mapping functions for various latitudes.

From the ray-trace data, at 5 degrees elevation angle the min/max results with UNB3(Niell) are −1.53 m/+1.47 m with a mean = −0.19 m. For UNB3(B&E) they are −1.67 m/+1.32 m with a mean = −0.30 m. These results are in the sense of "model minus raytrace".

The explanation for these results is that the B&E mapping function values lie between the Niell hydrostatic and wet mapping function values. Hence it will overpredict the hydrostatic delay but at the same time underpredict the wet delay (see Figure 2). The effect is to cancel out some (but not all) of the error. The 30 cm error occurs with very high pressure (1084 mbar) and a completely dry water vapour profile. As you increase the amount of water vapour the total range differences between the two models decreases to just a few cm with a very saturated profile (80 mm Precipitable Water).

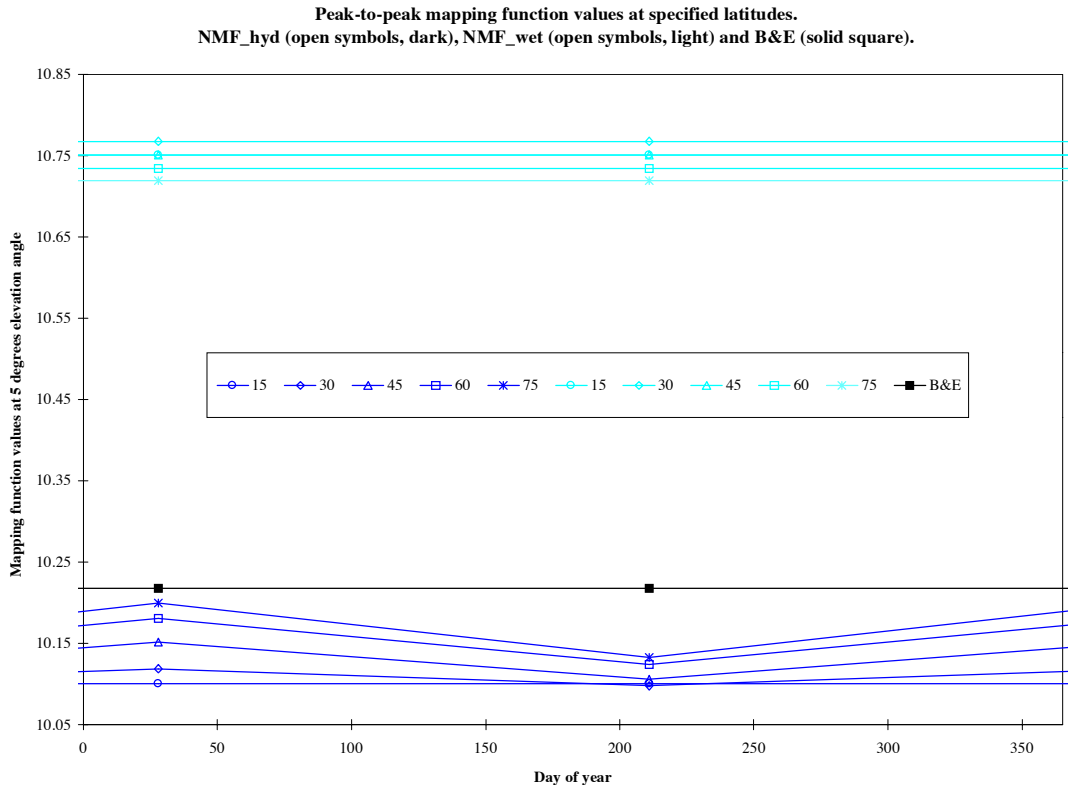

Figure 2. Annual peak-to-peak numerical values of the Niell hydrostatic and wet mapping functions and the Black and Eisner 'total delay' mapping function for various latitudes.

Hence if 16 cm range error is not a concern, but a "messy looking" function is, then you would go with Black and Eisner. As a concession however, it might be possible to specify the Niell hydrostatic mapping function without the height correction. This would leave both Niell functions as "simple" continued fractions.

This height correction increases the hydrostatic mapping function value by 0.022 per kilometer at 5 degrees elevation angle. However the range change is not constant because of the decrease in hydrostatic zenith delay with height (due to the pressure fall off, see Figure 3). The effect at 1.5 km (the approximate altitude of Denver and Grand Junction,

two of our radiosonde sites) is approximately 6-7 cm at 5 degrees elevation angle. This is confirmed by raytrace results of this modified model.

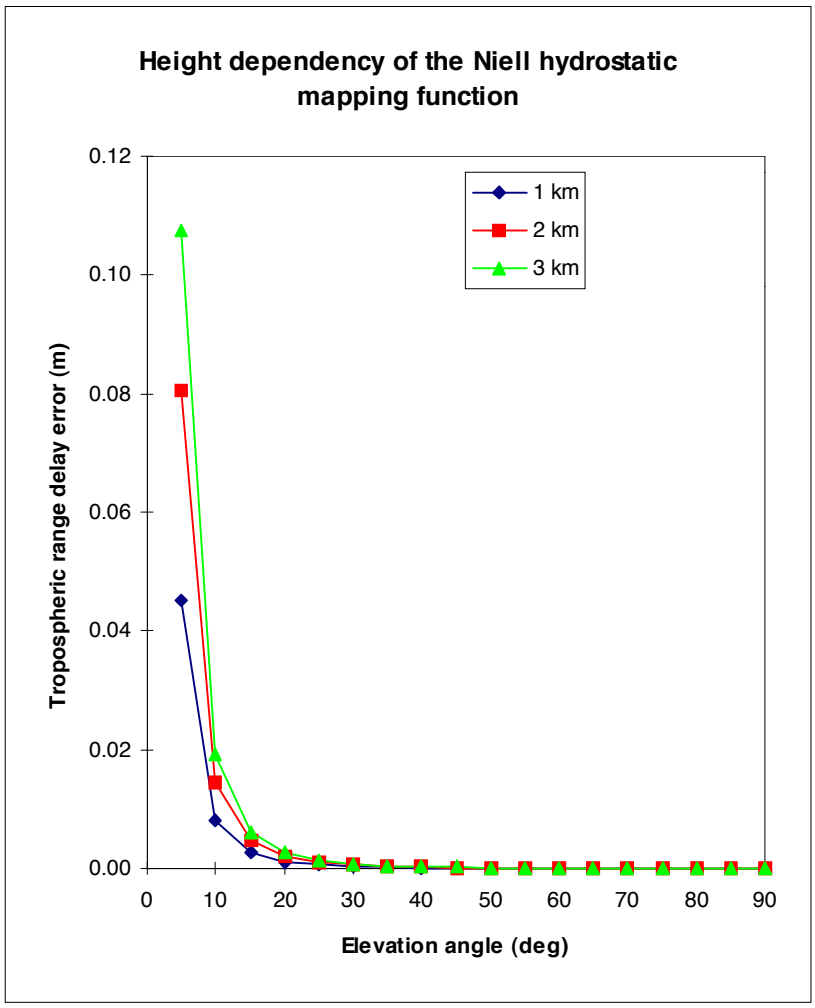

Figure 3. Range equivalent height correction for the Niell hydrostatic mapping function for various aircraft heights.

The general difference between using this modified version of the Niell hydrostatic mapping function in UNB3 and the old one is to introduce sub-centimeter range differences at 5 degrees elevation angle for stations below 200 m altitude. The statistics for the whole set of raytrace data are all at the 1 cm level of the original UNB3 model (see Table 1).

Table 1. Raytrace statistics for UNB3 model with various mapping functions. Units are metres.

UNB3(Niell)					
Elevation Angle	MEAN	STDEV	MIN	MAX	RANGE
90	–0.02	0.04	–0.14	0.14	0.28
30	–0.04	0.09	–0.28	0.28	0.56
20	–0.05	0.12	–0.41	0.41	0.82
15	–0.07	0.16	–0.54	0.53	1.07
10	–0.10	0.24	–0.80	0.78	1.58
5	–0.19	0.45	–1.53	1.47	3.00
UNB3(modified Niell)					
Elevation Angle	MEAN	STDEV	MIN	MAX	RANGE
90	–0.02	0.04	–0.14	0.14	0.28
30	–0.04	0.09	–0.28	0.28	0.56
20	–0.05	0.13	–0.41	0.41	0.82
15	–0.07	0.16	–0.54	0.53	1.07
10	–0.10	0.24	–0.80	0.79	1.58
5	–0.18	0.45	–1.53	1.48	3.01
UNB3(B&E)					
Elevation Angle	MEAN	STDEV	MIN	MAX	RANGE
90	–0.02	0.04	–0.14	0.14	0.28
30	–0.04	0.09	–0.28	0.28	0.56
20	–0.06	0.13	–0.42	0.40	0.82
15	–0.09	0.16	–0.56	0.51	1.07
10	–0.16	0.24	–0.86	0.72	1.58
5	–0.30	0.45	–1.67	1.33	3.00

On a possible form for the WAAS tropospheric delay residual error model.

J.P. Collins and R.B. Langley, University of New Brunswick, Canada.
e-mail: k4eo@unb.ca; lang@unb.ca, phone: 506-453-5088; 506-453-5142.

A proposal has been made to use the following equation to derive the residual error due to unmodelled portions of the tropospheric delay for use in the Vertical Protection Level (VPL) equation:

$$\sigma^2_{tropo} = \left(0.0016 + \left[\frac{d^z_{wet}}{3} \right]^2 \right) \cdot \left(m(E) \right)^2 . \qquad (1)$$

This equation assumes that the error in the zenith delay is predominantly due to mis-modelling of the wet portion of the tropospheric delay (almost always true) and that the amount of error is proportional to the total amount of water vapour. This is not necessarily true. For example, there is generally a greater percentage variation in water vapour content in the mid-latitudes than either the tropics or the polar regions. However the total amount of water vapour is generally much greater in the tropics than at the poles.

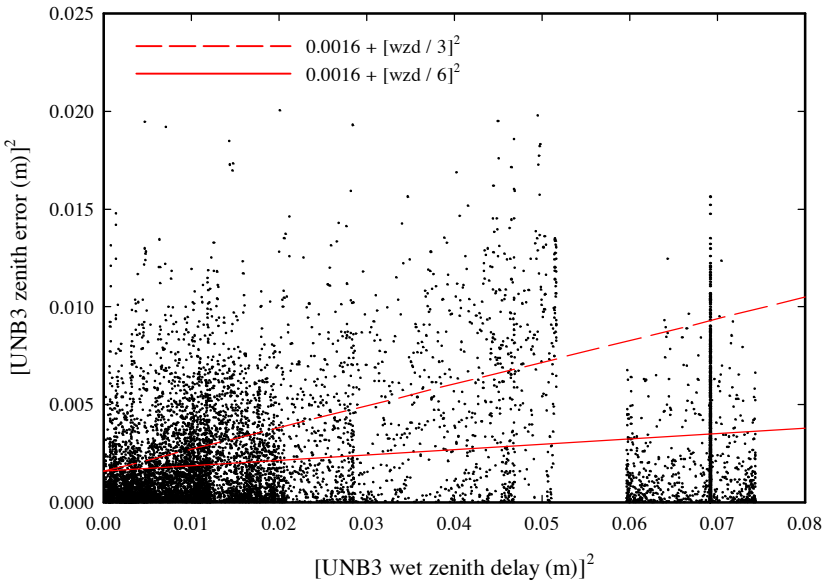

Figure 1. Scatter plot of ray-traced zenith residuals from the UNB3 model. Dashed line: equation (1); solid line: linear regression.

In an attempt to examine this assumption and give some theoretical justification for this equation, we have looked at the ray-trace residuals and statistics used in our previous report. Figure 1 shows this equation plotted through the square of the zenith residuals

after using the UNB3 model at all 13 radiosonde stations (9393 points). Note that by using the zenith residuals, the particular mapping function ($m(E)$) used in equation (1) is irrelevant, as long as it is reasonably accurate down to low elevation angles.

The values plotted on the x-axis above $0.06m^2$ are from the two tropical stations. The scatter here is clearly less than the mid-latitude and arctic stations. The apparent vertical scatter at ~$0.07m^2$ is from station Guam, which lies below 15°N and for which UNB3 provides only a constant wet zenith delay due to the lack of annual variation in the model at this latitude.

We note that a simple linear regression through the data leaves the intercept unchanged, but suggests that the factor dividing the wet zenith delay in equation (1) is too large, and a more suitable value would be '6'. It is possible that with more tropical stations, the slope of the line could tend toward equation (1), however by how much is only something that can be investigated with more data. In general there is a lot of scatter and neither equation adequately represents the plot. It is also unlikely that an equation of another form will be able to adequately represent this plot.

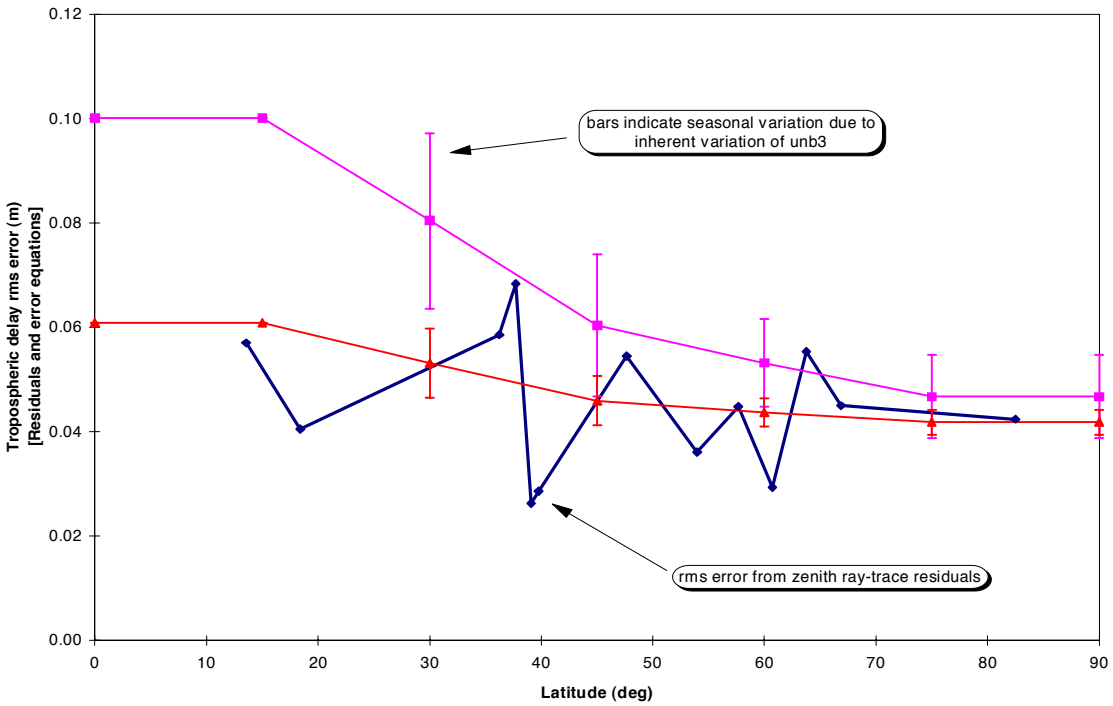

Figure 2. RMS ray-traced zenith residuals from UNB3 model and proposed error equations. Squares: $\sqrt{(0.0016 + [wzd/3]^2)}$, Triangles: $\sqrt{(0.0016 + [wzd/6]^2)}$.

To try and condense the information in Figure 1, we can consider Figure 2, which shows the root-mean-square (rms) value of the zenith residuals for the thirteen stations and the

values from the two forms of the error equation computed at the tabulation latitudes in UNB3. The results are plotted versus latitude, with which the significant trends are associated. Plotting the data versus the stations' altitudes reveals no significant trends.

Nevertheless, if an equation of the form of equation (1) is to be recommended immediately then we suggest the following modification:

$$\sigma^2_{tropo} = \left(0.0016 + \left[\frac{d^z_{wet}}{6} \right]^2 \right) \cdot \left(m(E) \right)^2 . \qquad (2)$$

The form of this equation is something that can be confirmed with the larger data set we intend to process in the coming months. However, as Figure 1 indicates, it is unlikely that any equation will adequately represent the scatter of the residual tropospheric delay error.